Advanced Signal Processing Solutions for ATR and Spectrum Sharing in Distributed Radar Systems

---

Domenico Gaglione

A thesis submitted for the degree of

Doctor of Philosophy

Centre for Signal and Image Processing

Department of Electronic and Electrical Engineering

University of Strathclyde

Glasgow

2017

Declaration

This thesis is the result of the author's original research. It has been composed by the author and has not been previously submitted for examination which has led to the award of a degree.

Domenico Gaglione 10th May 2017

To my Mum and Dad,
Claudia and Paola,
and Annachiara.

Acknowledgements

This work and this entire experience would have not been possible without the contribution and the support of many people.

First and foremost, I would like to thank my first supervisors Prof John Soraghan and Dr Carmine Clemente, for giving me the opportunity to carry out an exciting and novel research, for the endless support and patience, for the useful comments and suggestions, and for the never-ending flow of ideas. Despite the hard work, thank you for letting me enjoy my time here.

I am also thankful to my second supervisor Dr Stephan Weiss, for his technical support and help, as well as priceless optimism and enthusiasm.

I would also like to thank Prof Ian Proudler for the precious advice and the inspiring talks, Prof Antonio De Maio, Prof Chris Baker, Prof Li Gang and their research groups for the fruitful collaboration.

Thanks to all the Academics, Researchers, Students and external Experts of the LSSCN Consortium of the UK MoD University Defence Research Collaboration (UDRC) in Signal Processing.

A special thank you goes to the guys from the Sensor Signal Processing for Defence (SSPD) Laboratories: Christos, Adriano, Alessio and Jianlin, and more recently William and Hlias; great friends first, and then colleagues. And thanks to all the other people from the Centre for Signal and Image Processing (CeSIP).

My deepest and heartfelt gratitude goes to my family, my Mum and Dad, my sisters, my brothers-in-law, my nieces, for their unconditional love and encouragement.

A big thank you to my old friends Tommaso, Dario and Pietro, for being, despite the distance, constantly present and supportive.

Thanks to my “glaswegian” friends Giovanni, Luigi, Giuseppe and Ciro, and all the other folks met in this journey.

Thank you to the lions and lionesses of the Amatori Rugby Torre del Greco, and to the members of the Polo Scientifico, Cristian, Luca, Pasquale, Raffaele and Silvio.

My final and greatest thank you goes to Annachiara. Thank you for being such an amazing person, for the love, for the patience, for your kind understanding. Thanks for always believing in me and for all the good memories.

Abstract

This Thesis presents advanced signal processing solutions for Automatic Target Recognition (ATR) operations and for spectrum sharing in distributed radar systems.

Two Synthetic Aperture Radar (SAR) ATR algorithms are described for full- and single-polarimetric images, and tested on the GOTCHA and the MSTAR datasets. The first one exploits the Krogager polarimetric decomposition in order to enhance peculiar scattering mechanisms from man-made targets, used in combination with the pseudo-Zernike image moments. The second algorithm employs the Krawtchouk image moments, that, being discrete defined, provide better representations of targets' details. The proposed image moments based framework can be extended to the availability of several images from multiple sensors through the implementation of a simple fusion rule.

A model-based micro-Doppler algorithm is developed for the identification of helicopters. The approach relies on the proposed sparse representation of the signal scattered from the helicopter's rotor and received by the radar. Such a sparse representation is obtained through the application of a greedy sparse recovery framework, with the goal of estimating the number, the length and the rotation speed of the blades, parameters that are peculiar for each helicopter's model. The algorithm is extended to deal with the identification of multiple helicopters flying in formation that cannot be resolved in another domain. Moreover, a fusion rule is presented to integrate the results of the identification performed from several sensors in a distributed radar system. Tests performed both on simulated signals and on real signals acquired from a scale model of a helicopter, confirm the validity of the algorithm.

Finally, a waveform design framework for joint radar-communication systems is presented. The waveform is composed by quasi-orthogonal chirp sub-carriers generated through the Fractional Fourier Transform (FrFT), with the aim of preserving the radar performance of a typical Linear Frequency Modulated (LFM) pulse while embedding data to be sent to a cooperative system. Techniques aimed at optimise the design parameters and mitigate the Inter-Carrier Interference (ICI) caused by the quasi-orthogonality of the chirp sub-carriers are also described. The FrFT based waveform is extensively tested and compared with Orthogonal Frequency Division Multiplexing (OFDM) and LFM waveforms, in order to assess both its radar and communication performance.

Contents

List of Figures

List of Tables

List of Abbreviations

AF - Ambiguity Function
AWGN - Additive White Gaussian Noise
ATR - Automatic Target Recognition

BER - Bit Error Ratio
BPSK - Binary Phase Shift Keying

C/A - Coarse/Acquisition Code
CNN - Convolutional Neural Network
CoRadar - Communicating-Radar System
CPI - Coherent Processing Interval
CTD - Coherent Target Decomposition
CVD - Cadence Velocity Diagram
CW - Continuous Wave

ECC - Error Correcting Code
ESD - Energy Spectral Density

FFT - Fast Fourier Transform
FMCW - Frequency Modulated Continuous Wave
FPGA - Field-Programmable Gate Array
FrFT - Fractional Fourier Transform
FT - Fourier Transform

ICI - Inter-Carrier Interference
ICTD - Incoherent Target Decomposition

IFFT - Inverse Fast Fourier Transform
IFrFT - Inverse Fractional Fourier Transform
IQ - In-phase/Quadrature
IRT - Inverse Radon Transform
ISAR - Inverse Synthetic Aperture Radar
ISI - Inter-Symbol Interference

k**-NN** - k-Nearest Neighbour Classifier
Kr/pZ - Krogager pseudo-Zernike
Kraw - Krawtchouk

LFM - Linear Frequency Modulated
LFMCW - Linear Frequency Modulated Continuous Wave
LoS - Line of Sight

mD - micro-Doppler
MIMO - Multiple-Input Multiple-Output
MSK - Minimum Shift Keying
MTI - Moving Target Indicator

NI-USRP - National Instruments Universal Software Radio Peripheral

OFDM - Orthogonal Frequency Division Multiplexing
OMP - Orthogonal Matching Pursuit

PCA - Principal Component Analysis
PN - Pseudo Noise
POMP - Pruned Orthogonal Matching Pursuit
PRF - Pulse Repetition Frequency
PRI - Pulse Repetition Interval
PSK - Phase Shift Keying
pZ - pseudo-Zernike

QPSK - Quadrature Phase Shift Keying

RCMC - Range Cell Migration Correction

RCS - Radar Cross Section

RDA - Range Doppler Algorithm

RF - Radio Frequency

ROC - Receiver Operating Characteristic

RRC - Root Raised Cosine Filter

RSM - Range Side lobe Modulation

S/P - Serial-to-Parallel

SAR - Synthetic Aperture Radar

SDR - Software Defined Radio

SFCW - Stepped Frequency Continuous Wave

SINR - Signal-to-Interference plus Noise Ratio

SIR - Signal-to-Interference Ratio

SLL - Side Lobe Level

SNR - Signal-to-Noise Ratio

STFT - Short Time Fourier Transform

SVM - Support Vector Machine

TFMCW - Trapezoidal Frequency Modulated Continuous Waveform

TMA - Time Modulated Array

UAV - Unmanned Aerial Vehicle

UWB - Ultra-Wide Band

WV - Wigner-Ville

List of Symbols

$\mathbb{C}$	Set of complex numbers.
$\mathbb{N}$	Set of natural numbers.
$\mathbb{N}_0$	Set of natural numbers, 0 included.
$\mathbb{R}$	Set of real numbers.
$\mathbb{Z}$	Set of integer numbers.
$\lvert\cdot\rvert$	Magnitude of a complex number.
$(\cdot)^*$	Complex conjugate operator.
$(\cdot)^+$	Moore-Penrose inverse operator.
$(\cdot)^T$	Transpose operator.
$(\cdot)^\dagger$	Complex conjugate transpose operator.
$(\cdot)_k$	Pochhammer operator.
$\lfloor\cdot\rfloor$	Largest integer not greater than the argument.
$\lVert\cdot\rVert_0$	ℓ_0-norm.
$\lVert\cdot\rVert_1$	ℓ_1-norm.
$\lVert\cdot\rVert_2$	ℓ_2-norm.
$\lfloor\cdot\rceil$	Nearest integer to the argument.
$a\left(\cdot\right)$	C/A code.

$\boldsymbol{s}$	Score vector of a k-NN classifier.
d_i	Element of the set $\mathcal{D}_e$.
$f\left(\cdot,\cdot\right)$	Real-valued image.
$f_D\left(\cdot\right)$	Time-varying Doppler frequency shift.
f_s	Sampling frequency.
$f_{D_{\max}}$	Maximum Doppler frequency shift.
j	Imaginary unit.
$\boldsymbol{k}_s$, $\boldsymbol{k}_d$, $\boldsymbol{k}_h$	Matrices containing the Krogager components derived from a full polarimetric SAR image.
$\hat{k}$, $\hat{u}$, $\hat{v}$	Versors of the reference system (K, U, V).
k_s, k_d, k_h	Components of the Krogager CTD.
$k_{n,m}$	Krawtchouk moment of order (n, m).
$n^{\star}$	Sample index of the location of a flash.
$n_h^{\star}$	Sample index of the location of the h-th flash.
p	Shift parameter of the Krawtchouk polynomials.
$p\left(\cdot\right)$	Pilot waveform of the FrFT based pulse.
p_{mod}	Probability error of a modulation scheme.
$\boldsymbol{r}$	Residual vector in a sparse signal recovery problem.
$\boldsymbol{r}_0$	Target's position vector.
$\boldsymbol{r}_i^{(l)}$	Residual vector referring to the couple d_i at iteration l.
$\text{sinc}\left(\cdot\right)$	Sinc function.
$\overline{v}$	Estimated class in ATR algorithms.

$w_{n,l}$	Pseudo-Zernike moment of order $n \geq \lvert l \rvert$.
$\boldsymbol{x}$	Sparse vector.
$\boldsymbol{x}_i^{\mathcal{R}}$	Portion of the sparse vector $\boldsymbol{x}$ referring to the couple d_i.
$\hat{x}$, $\hat{y}$, $\hat{z}$	Versors of the reference system (X, Y, Z).
$\hat{x}'$, $\hat{y}'$, $\hat{z}'$	Versors of the reference system (X', Y', Z').
$\boldsymbol{y}_\eta$	Vector containing the samples of the signal $y_\eta(\cdot)$.
$\tilde{y}(\cdot)$	Normalised signal received from a helicopter's rotor and synchronised to the first flash.
$\tilde{y}_h(\cdot)$	Normalised signal received from a helicopter's rotor and synchronised to the h-th flash.
$y(\cdot)$	Signal received from a helicopter's rotor and synchronised to the first flash.
$y_h(\cdot)$	Signal received from a helicopter's rotor and synchronised to the h-th flash.
$y_\eta(\cdot)$	Model of the signal scattered by a helicopter's rotor hub.
$z(\cdot)$	Signal received from a helicopter's rotor hub.
α	Order of the FrFT.
α_H, β_H	Angles identifying the orientation of the helicopter.
α_L, β_L	Azimuth and elevation angles of the LoS.
β	Roll-off coefficient of the RRC filter.
γ_b	Energy per bit to noise power spectral density ratio.
γ_u	Angle between the position vector $\boldsymbol{r}_0$ and the versor $\hat{u}$.
γ_v	Angle between the position vector $\boldsymbol{r}_0$ and the versor $\hat{v}$.

δ_{fus}	Fusion threshold.
δ_{ω}	Step size used to discretise the range of rotation speeds.
δ_{ρ}	Step size used to discretise the range of lengths of the blades.
ε	Threshold used for the generation of the subsets $\mathcal{H}_f^g$.
ζ	Geometry-dependent angle in $y_{\eta}\left(\cdot\right)$.
η	Number of blades of a helicopter.
θ_0, θ_s, η_0	Angular components of the Krogager CTD.
ι	Threshold used for the generation of the subsets $\mathcal{H}_f$.
κ	Parameter that controls the speed of pruning of $\tilde{\boldsymbol{Y}}$.
λ	Carrier wavelength.
μ	Periodicity of the flashes that appear in a signal received from rotating blades.
μ_s, ν_s	Scale and shape parameters of the Gamma distribution.
$\mu_{\boldsymbol{F}}$	Feature vector's mean.
ν	Parameter that controls the speed of pruning of the dictionary $\boldsymbol{\Psi}$.
ν_{guard}	Fraction of the sub-carriers overlap that defines τ_{guard}.
$\boldsymbol{\xi}$	Complex symmetric zero-mean Gaussian random vector.
ξ	Complex symmetric zero-mean Gaussian random variable.
ξ_c	Compound-Gaussian random variable.
ρ	Length of the blades of a helicopter.
$\rho_{\min}$, $\rho_{\max}$	Smallest and largest lengths of the blades.
$\sigma_{\boldsymbol{F}}$	Feature vector's standard deviation.

τ	Duration of a waveform.
τ_i	Duration of the i-th sub-waveform when employing the adaptive duration technique.
τ_{guard}	Guard time.
τ_{plus_i}	Fraction of additional time w.r.t. the duration of the pulse, τ, when employing the adaptive duration technique.
υ	Threshold for the definition of the set $\mathcal{W}^{\upsilon}$.
ϕ	Rotation angle of the FrFT.
ϕ_0	Initial angular position of the helicopter's blades.
ϕ_i	Rotation angle of the i-th sub-waveform when employing the adaptive duration technique.
χ	Threshold for the overlap degree Q when designing the FrFT waveform.
ψ	Inter-carrier separation angle.
$\psi_{i,k}\left(\cdot\right)$	Atom of the dictionary $\mathbf{\Psi}$, referring to the i-th couple d_i and the k-th length of the blades.
$\tilde{\psi}_{i,k}\left(\cdot\right)$	Normalised atom of the dictionary $\mathbf{\Psi}$, referring to the i-th couple d_i and the k-th length of the blades.
ω	Rotation angular speed.
$\tilde{\omega}_k$	Nominal rotation speed of the k-th helicopter of interest.
BER_{lb}	Lower bound of the BER.
B_S	Number of bits per symbol (modulation scheme).
B_w	Bandwidth of a waveform.
$B_{w,sub}$	Bandwidth of a sub-waveform.

C	Number of sub-carriers.
C_{im}	Number of columns in a SAR image.
$\mathcal{D}$	Set of the helicopters of interest.
$\mathcal{D}_e$	Overall extended set containing the parameters of the helicopters of interest.
$\mathcal{D}_e^k$	Extended set of the k-th helicopter of interest.
E_b	Energy per bit.
F	Number of subsets $\mathcal{H}_f$.
$\boldsymbol{F}$	Feature vector.
$\tilde{\boldsymbol{F}}$	Normalised feature vector.
${}_2F_1\left(\cdot,\cdot,\cdot;\cdot\right)$	Gauss hypergeometric function.
G	Number of subsets $\mathcal{H}_f^g$.
G_b	Guard bits.
H	Number of chunks (portion of the received signal) used for the identification of multiple helicopters.
$\mathcal{H}^{(l)}$	Set of the indices identifying the potential uncorrelated chunks at iteration l.
$\mathcal{H}_f$	f-th subset of $\mathcal{H}$, containing the indices of correlated chunks.
$\mathcal{H}_f^g$	g-th subset of $\mathcal{H}_f$, containing the indices of the chunks that present the same periodicity.
I	Length in samples of the Krawtchouk polynomials.
$\boldsymbol{I}_{HH}, \boldsymbol{I}_{VV}$	Linear co-polarised SAR images.
$\boldsymbol{I}_{HV}, \boldsymbol{I}_{VV}$	Linear cross-polarised SAR images.

$\boldsymbol{I}_{RL}$, $\boldsymbol{I}_{LR}$	Circular cross-polarised SAR images.
$\boldsymbol{I}_{RR}$, $\boldsymbol{I}_{LL}$	Circular co-polarised SAR images.
$\mathcal{I}^{(l)}$	Set of active candidate couples d_i at iteration l.
J	Length of the discrete-time signal $z\left(\cdot\right)$.
$K_n\left(\cdot;p,I\right)$	Krawtchouk polynomial of degree n, length I and shift parameter p.
$K_\alpha\left(u,t\right)$	Kernel of the FrFT of order α.
$\left(K,U,V\right)$	Reference system centred in the helicopter's rotor hub and rotated such as K is its rotation axis.
$\tilde{K}_n\left(\cdot;p,I\right)$	Weighted Krawtchouk polynomial of degree n, length I and shift parameter p.
L	Number of potential targets in ATR algorithms.
L_b	Length of the Barker code.
M	Cardinality of the set $\mathcal{D}_e$.
M_S	Cardinality of the alphabet of the modulation scheme.
M_k	Cardinality of the set $\mathcal{D}_e^k$.
N	Number of samples of a discrete time signal.
N_b	Number of bits transmitted per pulse.
N_{ord}, M_{ord}	Maximum moments order.
P	Cardinality of the set $\mathcal{P}$.
P_D	Probability of detection.
P_s	Power of the transmitted pulse.
P_{FA}	Probability of false alarm.

$P_{\triangle}$, $P'_{\triangle}$	Cardinality of the sets $\mathcal{R}_{\triangle}$ and $\mathcal{R}'_{\triangle}$.
Q	Sub-carriers overlap degree.
$R\left(\cdot\right)$	Time-varying radar-target range.
R_0	Initial range of a target.
R_b	Bit rate of a system designed to send a continuous waveform.
R_u	Up-sampling factor of the multirate RRC filter.
R_{det}	Detection rate.
R_{fa}	False alarm rate.
R_{im}	Number of rows in a SAR image.
R_{miss}	Missing rate.
$\boldsymbol{R}_i^{(l)}$	Matrix containing the residual vectors for each chunk, referring to the couple d_i at iteration l.
$\mathcal{R}$	Set of possible lengths of the blades.
$\mathcal{R}_{\triangle}$, $\mathcal{R}'_{\triangle}$	Extensions of the set $\mathcal{R}$.
S	Number of targets present in a radar cell of interest.
SNR_c	SNR at the communication receiver.
SNR_r	SNR at the radar receiver.
T	Number of sensors in a distributed radar system.
T_s	Sampling period.
$\boldsymbol{V}$	Matrix of residual errors.
$\tilde{\boldsymbol{V}}$	Matrix of residual errors, with zero-mean along the columns.

$\tilde{\boldsymbol{V}}'$	Matrix of residual errors, with zero-mean and unit variance along the columns.
$W_{n,l}\left(\cdot,\cdot\right)$	Pseudo-Zernike polynomial of degree $n \geq \lvert l \rvert$.
$\boldsymbol{X}$	Matrix composed by H sparse columns.
$\boldsymbol{X}_i^{\mathcal{R}}$	Portion of the sparse matrix $\boldsymbol{X}$ referring to the couple d_i.
(X', Y', Z')	Reference system centred in the helicopter's rotor hub.
(X, Y, Z)	Reference system centred in the radar.
$\tilde{\boldsymbol{Y}}$	Matrix containing the normalised chunks $\tilde{y}_h\left(\cdot\right)$.
Γ	Gamma random variable.
Δ	Geometry-dependent factor in $y_\eta\left(\cdot\right)$.
Δ_f	OFDM sub-carrier spacing.
$\Lambda_i^{(l)}$	Support of the matrix $\boldsymbol{\Phi}_{\Lambda_i}$ at iteration l.
$\boldsymbol{\Xi}$	Complex symmetric zero-mean Gaussian random matrix.
$\boldsymbol{\Sigma}_H$	Correlation matrix of the chunks in the $\mathcal{D}_e$ domain.
Υ	Figure of merit for ATR algorithms.
$\boldsymbol{\Phi}_{\Lambda_i}$	Portion of the dictionary $\boldsymbol{\Psi}$ referring to the couple d_i and identified by the support Λ_i.
$\boldsymbol{\Psi}$	Dictionary of a parametric sparse model.
$\boldsymbol{\Psi}_i^{\mathcal{R}}$	Portion of the dictionary $\boldsymbol{\Psi}$ referring to the couple d_i.
$\boldsymbol{\Omega}$	Pre-processed real-valued SAR image.
$\tilde{\boldsymbol{\Omega}}$	Normalised real-valued SAR image.

Chapter 1

Introduction

1.1 Preface

The authorship of the RAdio Detection And Ranging (RADAR) system is often attributed to Christian Hülsmeyer in 1904 [1], although its *Telemobiloskop* was not able to measure the range from a metallic object, but only to detect it [2]. Since then, the concept of radar has evolved, and it is today considered a complex system capable of several operations, such as detecting, ranging, tracking, identifying, imaging, and classifying targets, for both military and civilian applications [3].

Of particular interest is the capability of creating high resolution images from radar returns, exploiting the Doppler history, that is the variation of the Doppler shift over time, of stationary targets. This technology was introduced in the radar community with the name of Synthetic Aperture Radar (SAR) by an employee of the Goodyear Aircraft Corporation in 1951, Carl Wiley [4]. At that time, the acquired signal was recorded on a black and white film, and processed real-time with optical lenses and diffraction gratings to obtain a focussed image [5]. Optical SAR processors produced well-focused images, but needed high quality lenses, precise alignment and the supervision of an operator. The advent of digital processors allowed researchers and engineers to develop automatic algorithms for SAR image focussing; furthermore, the flexibility introduced by digital signal processing techniques, promoted the emergence of a variety of SAR operation modes and applications. One of the first application, direct consequence of the high-resolution nature of SAR images, was their use for Automatic Target Recognition (ATR). The complex SAR phenomenology and the several degrees of freedom that a SAR system offers in terms of operation mode, wavelength, aspect angle, polarisation, continue to encourage the research in this field, with the objective of improving the accuracy and the reliability of the ATR algorithms.

ATR is not only limited to radar imagery. Recently, micro-Doppler based techniques aimed at target recognition have attracted lots of interest [6]. First described to the radar community by Victor Chen [7], the micro-Doppler effect identifies the time-varying modulation of the main Doppler of the received radar echo due to secondary motions that a target exhibits in addition to its bulk motion. These secondary motions, such as swinging limbs of a human walking or rotating blades of a helicopter's main and tail rotors, are characteristic of the observed object itself, and can be exploited for recognition purposes.

ATR techniques may also benefit from the spatial diversity offered by the observation of the target of interest from multiple perspective [8], since it is intuitively clear that these may provide additional information about the target. Multiple viewpoints of an observed object can be obtained with an aircraft flying past the scene of interest, or with a network of cooperative radars [9]. The use of a network of sensors in a distributed radar system clearly enhances the recognition capability but, on the other hand, increases the complexity of the entire system. For example, nodes in a distributed radar system with functions of detection and classification of targets also need the additional capability of communicating each other or, at least, with a fusion centre, in order to share information about, for example, the location and the nature of potential targets. This can be achieved by providing each node with a secondary communication channel, at cost of allocating dedicated bandwidth, power and hardware resources to this task. In this context, a joint radar-communication technology enabling the different sensors to sense the environment while sending data to cooperative systems represents an ideal solution for sharing the resources between the two tasks. NASA first introduced this concept in 1978 with its Space Shuttle Orbiter [10], giving a new inspiration to the radar community.

1.2 Motivation

The research presented in this Thesis is motivated by recent advances in SAR and micro-Doppler signal processing, with particular reference to ATR operations. Moreover, with the increased potential of modern radar systems from the employment of a network of distributed sensors, the scope of this Thesis is twofold: propose novel advanced signal processing solutions to improve the recognition of both civilian and military vehicles in SAR systems and enhance the micro-Doppler based identification of helicopters; propose an efficient spectrum sharing enabling technology that allows nodes in a distributed radar system to communicate.

Objectives of the research presented in this Thesis are: improvement of a SAR ATR algorithm through the exploitation of polarimetric information and the use of novel image moments; development of a model-based micro-Doppler algorithm for the identification of helicopters; development of a waveform design framework for a joint radar-communication system.

1.3 Contribution

The research detailed in this Thesis includes original contributions to the fields of SAR ATR, micro-Doppler based ATR and spectrum sharing for joint radar-communication systems. These contributions are as follows:

1. Enhancement of the SAR ATR algorithm presented in [11, 12] by further exploiting the information provided by the full-polarimentric SAR image of the target of interest. Krogager polarimetric components are introduced in the framework, in order to emphasise the scattering from single bounce, double bounce and volumetric scattering, becoming particularly suitable for man-made target recognition. Moreover, the property of roll invariance of Krogager components makes the algorithm robust with respect to the acquisition elevation angle.

2. Development of an image moments based SAR ATR algorithm that uses the Krawtchouk polynomials. Being discrete defined, the Krawtchouk moments bet-

ter represent the details of a target, providing higher capabilities in discriminating vehicles in different configurations.

3. Development of a model-based micro-Doppler algorithm for identification of helicopters. The algorithm is independent of both the orientation of the aircraft with respect to the radar Line of Sight (LoS), and the initial position of the blades. Moreover, an information fusion approach is developed, that merges the identification outputs coming from multiple sensors with the objective of enhancing performance.

4. Extension of the capability of the model-based micro-Doppler algorithm to the identification of multiple helicopters in the radar cell of interest. The algorithm is able to both estimate the number of helicopters and identify their model.

5. Development of a waveform design framework for joint radar-communication systems based on the Fractional Fourier Transform (FrFT). The proposed technique allows a radar system to use the same waveform to both sense the environment and send data to other cooperative systems, saving bandwidth, power and hardware resources.

1.4 Thesis Organisation

The remainder of this Thesis is divided into six chapters, whose organisation is explained as follows: Chapter 2 provides an overview of the most recent advances in SAR ATR and micro-Doppler based ATR. In the first part, the basics of SAR technology, such as geometry, image formation and polarimetry, are presented, followed by a review of recently developed SAR ATR algorithms. In the second part, preceded by an introduction on micro-Doppler theory and analysis, an overview of recent micro-Doppler based ATR techniques is provided, with a particular focus on the challenging problem of helicopters identification.

Chapter 3 focuses on the problem of spectrum congestion, arisen for the ever greater demand on bandwidth for different kind of Radio Frequency (RF) applications, and provides a review of recent spectrum sharing solutions for radar and communication systems. In particular, the discussion is first focussed on solutions that allow the coexistence of radar and legacy communication systems, then enabling technologies for joint radar-communication systems are presented. The FrFT is also introduced as tool for waveform design.

In Chapter 4, the two SAR ATR algorithms that enhance the framework previously introduced in [11, 12] are presented. The first one includes additional features, represented by the components of the Krogager polarimetric decomposition, in order to increase the information content providing a more accurate description of the targets. The second algorithm, instead, exploits the high capability of the Krawtchouk moments in characterising targets within the same framework. Performance assessment for the two algorithms is performed on real SAR images, from the GOTCHA and the MSTAR datasets, respectively.

In Chapter 5 the model-based micro-Doppler algorithm for helicopters identification is presented. It is based on the estimation of the helicopter's micro-Doppler parameters achieved by finding the solution of a sparse recovery problem, obtained through a modified version of the Pruned Orthogonal Matching Pursuit (POMP) [13], a previously developed greedy sparse recovery framework. The proposed algorithm is able to identify either single or multiple targets in the radar cell of interest, and its performance is evaluated on both simulated and real data.

Chapter 6 presents the FrFT based joint radar-communication system. Waveform design and optimisation are explained in details, followed by the description of the system implementation on a Software Defined Radio (SDR) device. Performance of the proposed waveform design framework, and comparison results with Orthogonal Frequency Division Multiplexing (OFDM) waveforms for joint radar-communication system, are finally provided.

Chapter 7 includes a summary and conclusions of this Thesis, along with a discussion of its limitations and suggestion of potential areas for further future work. Appendix A provides the mathematical derivation of the nonlinear relationship between order and rotation angle of the FrFT used in Chapter 6. A list of the author's publications is also provided.

Chapter 2

Automatic Target Recognition

2.1 Introduction

Automatic Target Recognition (ATR) represents the capability of a system to reliably distinguish different targets. Radar systems are particularly suitable for this function, being used in any weather condition and in day or night, effective for long range operations and capable of almost instantaneous response to threats [1]. ATR technologies find use in several civilian scenarios, although the military sector represents the driver for recent and future development. Several systems are currently used for recognition of cooperative targets, such as the Identification Friend or Foe (IFF) system, also called Secondary Surveillance Radar (SSR), used by military and civilian authorities for the identification of aircraft. However, the ability to automatically distinguish between friend, hostile and neutral targets in a non cooperative environment is a much more valuable feature for any radar, as well as challenging. Particularly in a battlefield scenario, if a target can be accurately classified, an appropriate countermeasure can be deployed in order to successfully neutralise the threat. Reliability of the decision is also key, to avoid potential casualties caused by friendly fire.

The ATR capability of radars comes from the interactions between the target and the electromagnetic wave generated and sent by the systems. The reflected signal from the target contains information that can be extracted through signal processing techniques, and exploited to perform the classification. The nature of this information is various, and also depends on the actual radar systems that is employed [1]. For example, radar imagery systems, such as Synthetic Aperture Radars (SARs), provide images of potential targets from which discriminative features, such as shape, size and reflectivity, can be extracted. Advanced methods also combine multiple images acquired, for example, with polarimetric or multi-frequency sensors, or during a wide temporal window. Geometric characteristics of a target of interest can also be retrieved from the High Resolution Range Profile (HRRP), a one dimensional range representation of the time domain signal reflected from the object. Besides spatial attributes, a target can also be identified by evaluating the characteristics of its moving parts. Indeed, these generate a peculiar frequency modulation of the received signal, known as micro-Doppler (mD), that can be analysed by means of time-frequency techniques and used for classification purposes.

In this Chapter, ATR in radar is discussed with particular focus on SAR systems and mD based techniques. The terminology used throughout this Chapter, as well as the whole Thesis, is first clarified in Section 2.2. In Section 2.3, the basics of SAR technology, such as geometry, image formation and polarimetry, are presented; then, recent advances in SAR ATR are reviewed. Finally, mD theory is introduced in Section 2.4, followed by an overview of the mD based ATR techniques that represent the current state of the art.

2.2 Terminology

The terminology used in the field of ATR may be sometimes ambiguous. Several terms, such as classification, recognition, identification and characterisation, are often used interchangeably, but sometimes they are also meant to indicate different levels of discrimination. Throughout this Thesis, the used terminology is in accordance with the NATO AAP-6 Glossary Terms and Definitions:

- with *recognition*, is meant the ability to give a type/category to a target, e.g. car or truck, tank or personnel carrier, fighter aircraft or helicopter;

- *identification* regards the capability to assign the target to a subclass, e.g. compact car or SUV, Eurofighter Typhoon or F-16 Fighting Falcon;

- *characterisation* takes into account the class variants or target configurations, e.g. Porsche 911 Carrera coupé or Porsche 911 Carrera cabriolet.

The term *classification*, instead, is used in this work to describe the general process of assigning objects to categories, whatever the detail level.

2.3 Synthetic Aperture Radar

Synthetic Aperture Radar (SAR) is a type of imagery radar that exploits the movement of the platform on which it is placed (spaceborne, airborne, etc.) to create an image of the illuminated area. The word *synthetic* comes from this movement, that synthesises a longer antenna than the physical one, which, in turn, provides finer resolution with respect to a Real Aperture Radar (RAR). In this Section, the basic principles of SAR are provided, followed by a review of the recent advances in SAR ATR. The review provides an insight of two classes of ATR techniques: *model-based* and *feature-based* [14, 15]. Algorithms that fall in the first category, use bright points, corners, line segments that correspond to identifiable parts of a target as features, and the classification depends on matching these parts with a reference. Algorithms from the second category, instead, use features that result from the application of transforms to the SAR image of the target.

2.3.1 SAR Geometry and Image Formation

The typical geometry of a SAR system is shown in Figure 2.1. The illustration depicts a SAR platform that flies along a straight line path[1] while sensing the scene, composed, in this simple case, by a single point scatterer. The radar transmits a pulse, generally a Linear Frequency Modulated (LFM) signal or *chirp*, with a cadence equal to the Pulse Repetition Interval (PRI), and receives the echoes reflected by the scatterer on the ground. The received signal is sampled, discretised and stored in a two-dimensional domain, namely the *range-azimuth domain*[2]. As the platform moves, the point scatterer

---

[1] Other paths can be considered, such as circular.

[2] The range-azimuth domain is also called *slow time-fast time domain*, since the range dimension is driven by the light speed, while the azimuth dimension is controlled by the platform speed.

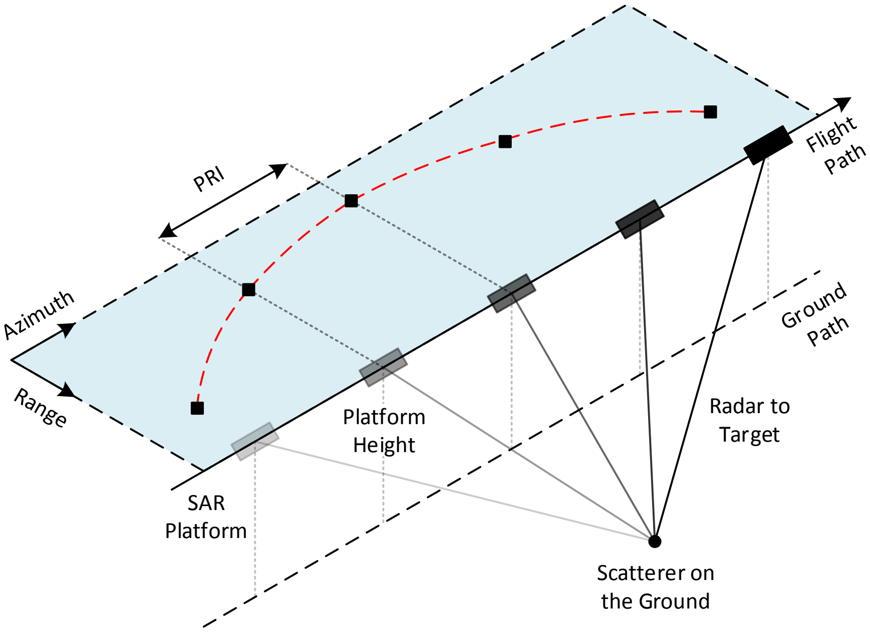

Figure 2.1: Synthetic Aperture Radar (SAR) geometry.

first approaches and then goes away from the radar: this causes the *range migration* of the point scatterer response in the range-azimuth domain, as highlighted in Figure 2.1 by the red dashed line.

Any SAR focussing algorithm needs to deal with this distortion in order to produce the final image. One of the most common and used approach is the Range Doppler Algorithm (RDA) [5], consisting of 3 main steps. Figure 2.2 shows (a) the unfocussed SAR image, and (b)-(d) the output of each of the three steps in the range-azimuth domain. The first stage is the *range compression*, that consists in matched filtering the received echo signal, that is the range signal. This operation despreads the acquired signal, providing the image with a fine range resolution[3]. Then, the range migration distortion is compensated, assuming that the point scatterer is in the middle of the illuminated scene when it is closest to the radar, that is when its Doppler shift is zero[4]: this phase is called *Range Cell Migration Correction (RCMC)*. The last step is the *azimuth compression*, obtained by matched filtering portions of the signal along the azimuth domain with a reference function. Indeed, the motion of the platform ensures that the azimuth signal is a chirp-like signal, which, once matched filtered, provides

---

[3] Hence, the range resolution of a SAR system depends on the bandwidth on the transmitted chirp.
[4] This is true only if the SAR is side-looking, with no squint angle forward or backward.

a fine resolution. These two last steps are efficiently implemented in the frequency domain; for this reason, a Fast Fourier Transform (FFT) is computed before the RCMC, and reversed after the azimuth compression.

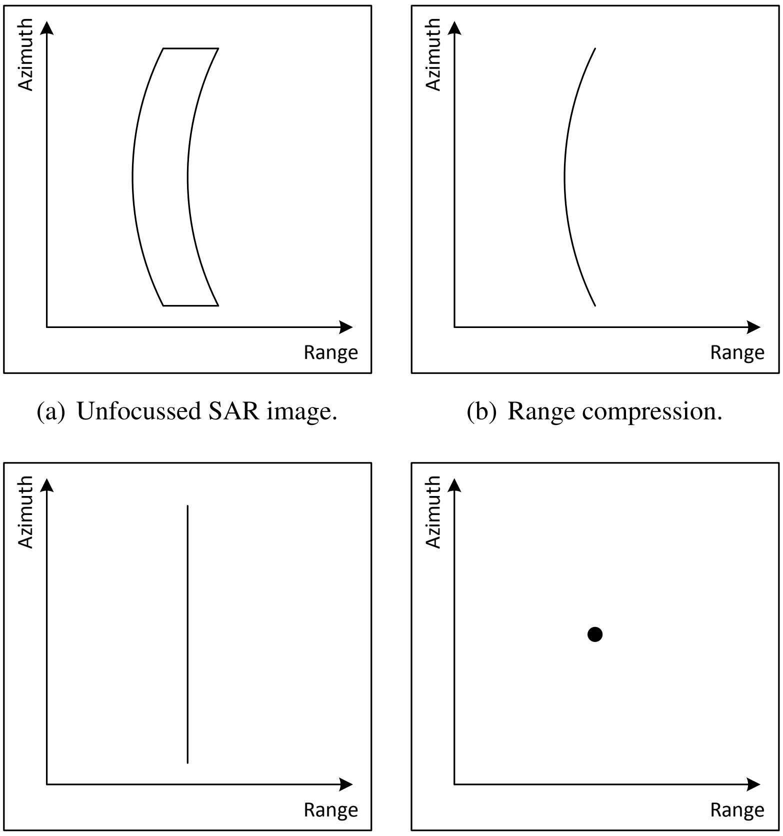

(a) Unfocussed SAR image. (b) Range compression.

(c) RCMC. (d) Azimuth compression.

Figure 2.2: Range-Doppler Algorithm (RDA), (a) input and (b)-(d) outputs of each of the three steps.

2.3.2 PolSAR and Polarimetric Decompositions

The first SAR systems were designed to provide images in single polarisation, that is the electromagnetic wave was transmitted on one polarisation, either horizontal (H) or vertical (V), and received on the same polarisation. Recently developed SAR systems, instead, can provide images either in single, or dual, or full polarisation. An example is given by the TerraSAR-X, a German spaceborne SAR launched in 2007 [16]. The dual polarisation mode is achieved by transmitting the signal on either the H or V polarisation, and electronically dividing the antenna in reception in order to get both of them. The quad polarisation, or *full-polarimetric* mode, instead, is possible with an additional modification, consisting in alternating the transmission of pulses on the horizontal and vertical polarisation.

The additional information provided by the polarisation can be exploited for classification purposes, since objects interact differently based on the polarisation on the incident wave. A full-polarimetric SAR image is completely characterised by the scattering matrix $\boldsymbol{S}$, defined as follows [3]:

$$\boldsymbol{S}_{(H,V)} = \begin{bmatrix} S_{HH} & S_{HV} \\ S_{VH} & S_{VV} \end{bmatrix} \in \mathbb{C}^{2\times 2} \tag{2.1}$$

where $\mathbb{C}$ is the set of complex numbers, S_{HH} and S_{VV} are the linear co-polarised terms, and S_{HV} and S_{VH} the linear cross-polarised terms[5]. Accordingly, in the case of circular polarised waves, the scattering matrix can be expressed as:

$$\boldsymbol{S}_{(R,L)} = \begin{bmatrix} S_{RR} & S_{RL} \\ S_{LR} & S_{LL} \end{bmatrix} = \frac{1}{2}\begin{bmatrix} 1 & j \\ 1 & -j \end{bmatrix}\begin{bmatrix} S_{HH} & S_{HV} \\ S_{VH} & S_{VV} \end{bmatrix}\begin{bmatrix} 1 & 1 \\ j & -j \end{bmatrix} \in \mathbb{C}^{2\times 2} \tag{2.2}$$

where $j = \sqrt{-1}$ is the imaginary unit, $(\cdot)^T$ indicates the transpose of a matrix, S_{RR} and S_{LL} are the circular co-polarised terms, and S_{RL} and S_{LR} the circular cross-polarised terms, respectively.

The interpretation of a full-polarimetric SAR image can often be extremely difficult, for this reason decomposition techniques are employed in order to obtain a different representation of the data that has a direct physical interpretation. These polarimetric decomposition techniques can be divided in two main classes. Incoherent Target Decomposition (ICTD) methods are used to represent *distributed targets* through a second order characterisation of the scattering matrix (i.e. coherency matrix or covariance matrix). Distributed targets, in fact, are highly affected by speckle noise[6], and their characterisation cannot merely relies on intensity values picked from the full-polarimetric SAR image. However, ICTD techniques suffer from the estimation

---

[5] Note that, in the monostatic case, the cross-polarised terms are equal due to the reciprocity theorem.

[6] Speckle noise is the pixel-to-pixel variation in intensity caused by the phase fluctuations of the waves reflected by the large number of scatterers that are contained in a resolution cell [17].

of either the coherency matrix or the covariance matrix through $\boldsymbol{S}$, and for the same reason they cannot maintain the full resolution of the SAR image [18, 19][7]. On the other hand, Coherent Target Decomposition (CTD) methods are suitable for the representation of point targets, also called *pure targets*. Their objective is to express the scattering matrix as a combination of canonical objects which present an easier physical interpretation. Furthermore, since the CTDs are directly computed from $\boldsymbol{S}$, they maintain the full resolution of the SAR image. ICTD techniques are generally used to characterise natural targets, such as forests, agriculture areas, water, etc., while CTD methods are suitable for the extraction of features from man-made targets [20, 21]; dealing with the classification of man-made targets, hereafter the focus is on this last class of polarimetric decompositions.

2.3.2.1 Coherent Target Decompositions

As mentioned before, a CTD can be expressed as [17]:

$$\boldsymbol{S} = \sum_{n=0}^{N_S-1} c_n \boldsymbol{S}_n \tag{2.3}$$

where $\boldsymbol{S}_n$ is the response of the n-th canonical object, c_n indicates the weight of $\boldsymbol{S}_n$ in the combination leading to $\boldsymbol{S}$ and N_S is the number of components. The most common polarimetric decomposition, which also represents the basis for the coherency matrix formulation, is the *Pauli decomposition*, defined as [17]:

$$\begin{aligned}\boldsymbol{S}_{(H,V)} &= \frac{c_0^{(P)}}{\sqrt{2}}\boldsymbol{S}_0^{(P)} + \frac{c_1^{(P)}}{\sqrt{2}}\boldsymbol{S}_1^{(P)} + \frac{c_2^{(P)}}{\sqrt{2}}\boldsymbol{S}_2^{(P)} + \frac{c_3^{(P)}}{\sqrt{2}}\boldsymbol{S}_3^{(P)} = \\ &= \frac{c_0^{(P)}}{\sqrt{2}}\begin{bmatrix}1 & 0\\ 0 & 1\end{bmatrix} + \frac{c_1^{(P)}}{\sqrt{2}}\begin{bmatrix}1 & 0\\ 0 & -1\end{bmatrix} + \frac{c_2^{(P)}}{\sqrt{2}}\begin{bmatrix}0 & 1\\ 1 & 0\end{bmatrix} + \frac{c_3^{(P)}}{\sqrt{2}}\begin{bmatrix}0 & -j\\ j & 0\end{bmatrix}\end{aligned} \tag{2.4}$$

---

[7] Generally, the degradation of the resolution is traded with the accuracy of the estimation of the second order characterisation.

where

$$\begin{aligned} c_0^{(P)} &= \frac{S_{HH}+S_{VV}}{\sqrt{2}}, \quad c_1^{(P)} = \frac{S_{HH}-S_{VV}}{\sqrt{2}} \\ c_2^{(P)} &= \frac{S_{HV}+S_{VH}}{\sqrt{2}}, \quad c_3^{(P)} = j\frac{S_{HV}-S_{VH}}{\sqrt{2}} \end{aligned} \tag{2.5}$$

The four components represent the scattering mechanism from four canonical objects. The first one is interpreted as sphere, plate or trihedral, since it takes into account single or odd bounce scattering. The second and the third components are seen as un-rotated and $45°$-rotated dihedrals, respectively, representing double or even bounce scattering. The last one includes all the antisymmetric components of the scattering matrix $\boldsymbol{S}$, representing a non reciprocal target. A basis proportional to the Pauli matrices is also the starting point for the definition of the *Cameron decomposition*, defined as [22]:

$$\boldsymbol{S}_{(H,V)} = c_0^{(C)}\boldsymbol{S}_{\text{sym}}^{\max} + c_1^{(C)}\boldsymbol{S}_{\text{sym}}^{\min} + c_2^{(C)}\boldsymbol{S}_{\text{non-rec}} \tag{2.6}$$

where

$$\begin{aligned} c_0^{(C)} &= \left\|\boldsymbol{S}_{(H,V)}\right\| \cos\theta_{\text{rec}} \cos\tau_{\text{sym}} \\ c_1^{(C)} &= \left\|\boldsymbol{S}_{(H,V)}\right\| \cos\theta_{\text{rec}} \sin\tau_{\text{sym}} \\ c_2^{(C)} &= \left\|\boldsymbol{S}_{(H,V)}\right\| \sin\theta_{\text{rec}} \end{aligned} \tag{2.7}$$

The Cameron decomposition is based on the two concepts of reciprocity and symmetry [17]: a scatterer is reciprocal if it obeys to the reciprocity principle such that its scattering matrix is symmetric, while it is symmetric if it has an axis of symmetry in the plane orthogonal to the radar Line of Sight (LoS). The angle θ_{rec} separates the reciprocal ($\theta_{\text{rec}} \leq \pi/4$) and non reciprocal ($\theta_{\text{rec}} > \pi/4$) components of the scattering matrix, while τ_{sym} further divides the former one in a symmetric ($\tau_{\text{sym}} \leq \pi/8$) and an asymmetric ($\tau_{\text{sym}} > \pi/8$) component.

When the reciprocity principle is satisfied, the *Krogager decomposition* may also be applied. It is another example of CTD and it is defined by means of the circular polarization scattering matrix $\boldsymbol{S}_{(R,L)}$, introduced in equation (2.2), as [23]:

$$\boldsymbol{S}_{(R,L)} = e^{j\theta_0} \left\{ k_s e^{j\theta_s} \begin{bmatrix} 0 & j \\ j & 0 \end{bmatrix} + k_d \begin{bmatrix} e^{j2\eta_0} & 0 \\ 0 & -e^{-j2\eta_0} \end{bmatrix} + k_h \begin{bmatrix} e^{j2\eta_0} & 0 \\ 0 & 0 \end{bmatrix} \right\} \tag{2.8}$$

where k_s, k_d and k_h are real-valued quantities which can be interpreted as scattering coefficients from a sphere, a diplane and a helix, respectively[8]. Moreover, θ_0 is the absolute phase term which depends on the distance between the target and the sensor, θ_s represents the displacement of the sphere with respect to the diplane and the helix components, and η_0 is their orientation angle. The scattering coefficients k_s, k_d and k_h may be computed as follows [18]:

$$\begin{aligned} k_s &= |S_{RL}| \\ k_d &= \min\left(|S_{RR}|, |S_{LL}|\right) \\ k_h &= ||S_{RR}| - |S_{LL}|| \end{aligned} \tag{2.9}$$

where $|\cdot|$ represents the magnitude of a complex number. An important property of this decomposition is the roll invariance of the components k_s, k_d and k_h, demonstrated in [24]. Consequently they do not depend on the orientation of the target in roll (meaning invariance with respect to observations from platforms with different incidence angles).

The capability of the polarimetric decompositions of representing the scattering mechanism of the illuminated objects, makes them highly effective in target recognition from radar imagery. Comparisons between different methods, both coherent and incoherent, were carried out in [18, 19]. In the first work, Pauli, Cameron and Krogager decompositions were tested on the classification of several urban and non urban areas (water, houses, roads, trees, grass, crops) from real full-polarimetric SAR images acquired with the German E-SAR system, and compared with ICTD techniques. Results showed that the Krogager and Cameron decompositions outperformed all the other techniques, with an overall accuracy of $87\,\%$ and $76\,\%$, respectively. On the other hand, the Pauli decomposition did not result in better performance than using the

---

[8] This decomposition is also known as Sphere, Diplane and Helix (SDH) decomposition.

original elements of the scattering matrix S. In the later work, classification performance of the Krogager decomposition was evaluated on Radarsat-2 full-polarimetric images and compared with ICTD techniques. The dataset consisted of images of crops acquired in different days of the year; once again, the Krogager decomposition gave the best results, with an overall accuracy of $78\,\%$. The authors of both the comparison studies ascribed the better performance of the Krogager decomposition over the ICTD techniques to the fact that, being a coherent decomposition, it maintains the full resolution during the feature extraction process. Recent advances in wide-band full-polarimetric SAR system have further revived the employment of coherent decomposition techniques for target recognition, with particular focus on the classification of civilian vehicles [25].

2.3.3 Model-Based ATR Techniques

As mentioned before, model-based ATR algorithms exploit identifiable parts of the target, such as bright points or line segments, as features to be used into the classification step. The first attempt in this direction is represented by [26]. Novak et al. proposed an algorithm consisting of three stages, namely detection, or prescreening, discrimination and classification. In the first step, single pixels belonging to potential targets were discerned from clutter by means of a two-parameter Constant False Alarm Rate (CFAR) detector. The discrimination stage dealt with the estimation of both the position and orientation of the target, and extracted textural, size, contrast and polarimetric features from the 2D image, then combined into a single discrimination statistic. The final classification was performed through a Mean-Squared Error (MSE) pattern-matching classifier.

Length, height and width were used in [27] for reliable classification of ships. The SAR ship silhouette was modelled as ellipsoid-ellipse, from which the 3D geometrical features were extracted assuming that the elevation angle of the target was known.

Park and Kim in [28] proposed a Modified Polar Mapping Classifier (M-PMC), which, in its original version, was used for classification of Inverse SAR (ISAR) images [29]. The algorithm projected the SAR image from Cartesian coordinates onto polar coordinates, namely radius and angle, removing the need of pose estimation.

This representation was both compressed undergoing a Principal Component Analysis (PCA), and further projected onto the radius obtaining a 1D image. The polar projection was preceded by a translation operation, aimed to find and compensate the centre of the target. Indeed, a random selection of the origin of the polar coordinates could bias the final classification, performed with a k-Nearest Neighbour (k-NN) classifier. The algorithm was tested on the MSTAR dataset [30, 31], achieving very high accuracy, in particular in terms of characterisation. However, the interpolation stage needed for the polar projection, as well as the translation operation, could introduce errors leading to misclassification.

Locations of dominant scatterers, such as edges or corners, have been extensively used in SAR ATR [32, 33] as discriminative features, but their direct use shows high variability and may negatively affect classification performance. To overcome this problem, Doo et al. [34, 35] proposed a grid cell structure in order to group dominant scatterers, with the immediate advantages of reducing the variability and lowering the complexity, since the number of groups was much smaller than the number of dominant scatterers. However, the variability of the dominant scatterers was not completely neglected, it was rather extracted through the process described in Figure 2.3 and used as feature. The SAR image taken into consideration belonged to the MSTAR dataset,

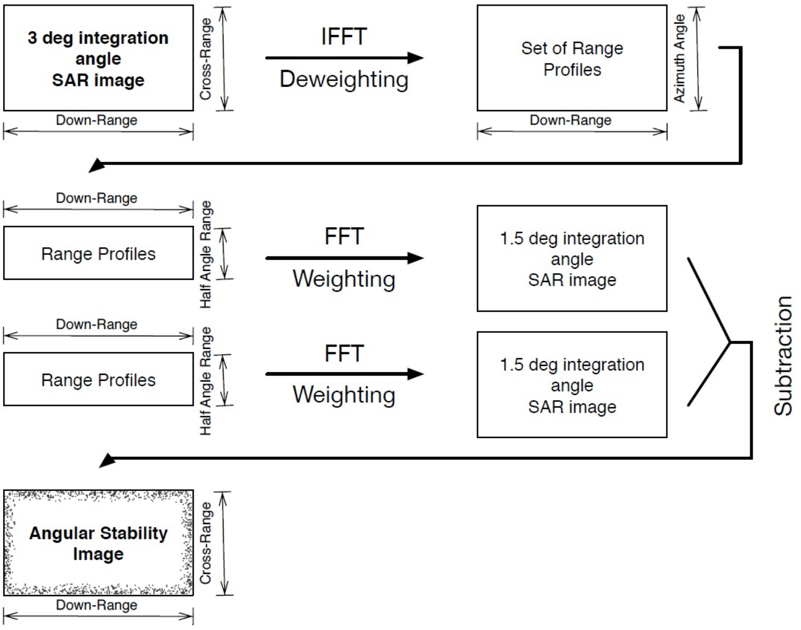

Figure 2.3: From [34], angular stability extraction process.

a collection of circular SAR images focussed over a 3° azimuth angle. The angular stability image, containing information about the variability of the dominant scatterers, was obtained by defocussing the image of the target along the azimuth domain and generating two different images with 1.5° integration angle. These images were then subtracted to highlight the variations in the aspect angle of the dominant scatterers. This approach is very effective, but suffers from potential shifts of the target on the scene, as well as rotation of its pose. Hence, a pose and translation estimation step is still needed [36].

2.3.4 Feature-Based ATR Techniques

Feature-based ATR algorithms rely on the effectiveness of the features extracted from the SAR image in well representing the target itself. The features are not directly related to physical or statistical characteristics of the object, they are rather obtained through the application of a transform or a projection onto a selected basis.

The algorithm developed by Srinivas et al. [37] belongs to this category since the features of the target were extracted by means of the Wavelet transform[9]. It decomposed the image in four sub-images, containing low and high frequency components of the SAR image in both the horizontal and vertical direction. Then, a probabilistic graphical model, able to represent conditional dependences between the features, was used for redundancy reduction and for the actual classification.

Leveraging on recent advances in *machine learning*, Chen et al. [38] and Wagner [39] proposed two approaches for automatically learning hierarchies of features from large quantity of data. This means that the type of feature was not selected a priori, and this task was assigned to the algorithm itself. Chen et al. used a Convolutional Neural Network (CNN), with sparsely connected layers to avoid the overfitting due to limited training images, that could be directly applied to SAR images. Wagner, instead, proposed the combination of a CNN for the automatic generation of the features, and a Support Vector Machine (SVM) for decision making.

---

[9] However, authors stated that their proposed framework readily generalised to any other suitable choice of feature sets that offered complementary benefits.

2.3.4.1 Image Moments

A class of feature-based ATR algorithms for SAR images employs image moments as tool for the extraction of targets' characteristics. As in mathematics and statistics, image moments are scalar quantities defined as weighted averages of the image pixels' intensities.

The first example of use of image moments for target recognition from SAR is given in [40]. Yan et al. used seven Hu moments [41] in combination with a SVM for the classification of planes and tanks. The authors exploited the rotational, translational and scaling invariance of Hu moments [42], achieving an overall recognition accuracy of $96\,\%$ on noise-free simulated images. Hu moments were also used in [43] in combination with intensity, texture and scattering features. The feature extraction phase was followed by a feature selection stage, aimed to remove those with low stability, low discriminability and low correlation, and a k-NN classifier. The approach was tested on real SAR images of three types of ships from TerraSAR-X, obtaining an overall accuracy of $91.54\,\%$.

Amoon et al. proposed in [44] the use of the Zernike moments, obtained as projection of the SAR image on Zernike polynomials with different orders. Zernike polynomials are orthogonal on the unit circle, and this orthogonality makes the moments independent, decreasing the intrinsic redundancy of the features. Moreover, Zernike moments are rotational invariant, but not translational and scale invariant. This means that a variation in the pose or dimension of the target can negatively affect the classification, therefore position and size normalisation were needed in [44]. After these pre-processing steps, moments were extracted from both the shape (binary image) and the intensity image of the target and used with a SVM. The algorithm was tested on the MSTAR dataset, reaching an average accuracy of $96.48\,\%$.

Clemente et al. presented in [11, 12] a novel algorithm for classification of civilian vehicles from SAR based on the use of pseudo-Zernike (pZ) moments [45]. The pZ moments inherit the orthogonality of the Zernike moments [46], and similarly to the Hu moments, they own valuable geometric properties, such as invariance to scale [47], rotation and translation [48, 49]. Moreover, they are less sensitive to noise [46, 50] compared to the Zernike moments[10], and this makes them reliable features in recognition systems for different kind of applications, both in image processing [51, 52, 53, 54] and radar processing [55].

The complex-valued pZ moment $w_{n,l}$ of an image $f(x,y) \in \mathbb{R}$, with $f(x,y) \geq 0$ and (x,y) indices of the pixels, is defined as its projection on the pZ polynomial $W_{n,l}(r,\vartheta)$ of degree $n \geq |l|$, $n \in \mathbb{N}_0$, $l \in \mathbb{N}_0$ with $\mathbb{N}_0$ the set of natural numbers, 0 included:

$$w_{n,l} = \frac{n+1}{\pi} \int_0^{2\pi} \int_0^1 W^*_{n,l}(r,\vartheta) f(r\cos\vartheta, r\sin\vartheta)\, r dr d\vartheta \tag{2.10}$$

where $(\cdot)^*$ indicates the complex conjugate operator, $r = \sqrt{x^2+y^2}$, $\vartheta = \tan^{-1}(y/x)$ and

$$W_{n,l}(r,\vartheta) = \sum_{m=0}^{n-|l|} \frac{r^{n-m}(-1)^m (2n+1-m)!}{m!\,(n+|l|+1-m)!\,(n-|l|-m)!} e^{jl\vartheta} \tag{2.11}$$

The orthogonality condition of the pZ polynomials is reported below, and applies on the unit disc, that is for $r \leq 1$:

$$\int_0^{2\pi} \int_0^1 W^*_{n,l}(r,\vartheta) W_{m,k}(r,\vartheta)\, r dr d\vartheta = \frac{\pi}{n+1} \delta_{n,m} \delta_{l,k}, \tag{2.12}$$

where

$$\delta_{n,m} = \begin{cases} 1 & n = m \\ 0 & n \neq m \end{cases} \tag{2.13}$$

is the Kronecker delta. Therefore, since the number of orthogonal polynomials is $(n+1)^2$ (once n is given), this is also the number of independent pZ moments, where with independence is meant low information redundancy among the moments [56].

The block diagram of the algorithm presented in [11, 12] is reported in Figure 2.4. The SAR image to process, of dimensions $R_{\text{im}} \times C_{\text{im}}$ that contained a detected target[11], was assumed to be full-polarimetric with complex-valued components $\boldsymbol{I}_{HH}(x,y)$,

---

[10] With sensitivity to noise it is meant the variance of the moments when noise is added to an image. Therefore, low sensitivity means that moments computed on a noise-free and a noisy version of the same image, are similar in a defined metric.

[11] The dimensions R_{im} and C_{im} are chosen according to the resolutions of the SAR image and to the physical dimensions of the expected target.

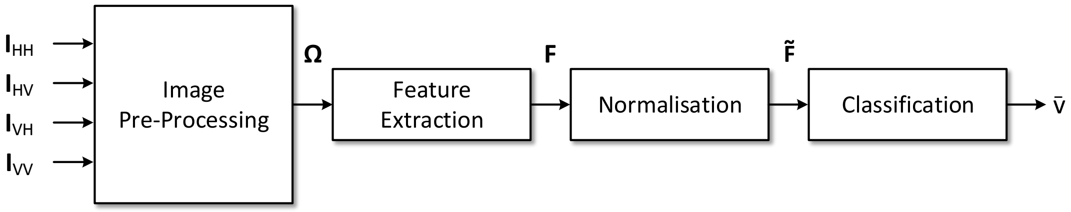

Figure 2.4: Block diagram of the pseudo-Zernike (pZ) based SAR ATR algorithm proposed in [11, 12].

$\boldsymbol{I}_{HV}\left(x,y\right)$, $\boldsymbol{I}_{VH}\left(x,y\right)$ and $\boldsymbol{I}_{VV}\left(x,y\right)$. The pre-processing block consisted of two steps. First, $\tilde{\boldsymbol{\Omega}} \in \mathbb{R}^{R_{\text{im}}\times C_{\text{im}}}$ was obtained as scaled sum of the magnitude of the four polarimetric components:

$$\tilde{\boldsymbol{\Omega}}\left(x,y\right)=\log_{10}\left(\left|\boldsymbol{I}_{HH}\left(x,y\right)\right|+\left|\boldsymbol{I}_{HV}\left(x,y\right)\right|+\left|\boldsymbol{I}_{VH}\left(x,y\right)\right|+\left|\boldsymbol{I}_{VV}\left(x,y\right)\right|\right) \quad (2.14)$$

where the logarithm was performed to reduce the dynamic range of the final image. Then, $\tilde{\boldsymbol{\Omega}}$ was normalised such that its intensity was restricted in the range $[0,1]$, in order to obtain features that were independent of different intensity levels:

$$\boldsymbol{\Omega}\left(x,y\right)=\frac{\tilde{\boldsymbol{\Omega}}\left(x,y\right)-\min_{(x,y)}\tilde{\boldsymbol{\Omega}}\left(x,y\right)}{\max_{(x,y)}\left[\tilde{\boldsymbol{\Omega}}\left(x,y\right)-\min_{(x,y)}\tilde{\boldsymbol{\Omega}}\left(x,y\right)\right]} \quad (2.15)$$

The feature extraction consisted in projecting the image $\boldsymbol{\Omega}\left(x,y\right)\in\mathbb{R}$, with $\boldsymbol{\Omega}\left(x,y\right)\geq 0$, onto the pZ polynomials as in equation (2.10), which could be precomputed, stored and used when necessary since they only depended on the size of the image to process, that is $R_{\text{im}}\times C_{\text{im}}$[12]. The feature vector $\boldsymbol{F}\in\mathbb{R}^{(N_{\text{ord}}+1)^2}$ finally contained the magnitude of the pZ moments up to the order N_{ord}, that is:

$$\boldsymbol{F}=\left[\left|w_{0,0}\right|,\ldots,\left|w_{N_{\text{ord}},-N_{\text{ord}}}\right|\right]^T \quad (2.16)$$

Note that, in order to avoid information loss due to the fact that the pZ polynomials in equation (2.11) are defined on the unit circle, the support of $\boldsymbol{\Omega}\left(x,y\right)$ was scaled before computing the pZ moments. This scaling consisted in inscribing the rectangular image

---

[12] Without loss of generality, this framework can also be applied to single polarisation SAR images. In fact, the feature extraction is applied on just one real-valued image, which may be the magnitude of a single polarisation image.

in the unit circle, while setting to zero the pixels between the image edges and the unit circumference. The feature vector was then normalised to zero-mean and unit variance, in order not to affect the classification with polarised features [57]:

$$\tilde{\boldsymbol{F}} = \frac{\boldsymbol{F} - \mu_{\boldsymbol{F}}}{\sigma_{\boldsymbol{F}}} \tag{2.17}$$

where $\mu_{\boldsymbol{F}}$ and $\sigma_{\boldsymbol{F}}$ are mean and standard deviation of $\boldsymbol{F}$, respectively. The final step was the classification, performed with a k-NN classifier, that returned a score vector $\boldsymbol{s} = [s_1, \dots, s_L] \in \mathbb{R}^L$ whose elements were the occurrences (normalised to k) of each class among the k nearest neighbours to $\tilde{\boldsymbol{F}}$, and L was the number of possible classes. Clemente et al. [11, 12] also proposed a fusion rule when more than one SAR image of the target under test was available, as in a multi-sensor system. Let $\boldsymbol{s}_i$ be the score vector obtained by testing the features extracted from the i-th image, with $i = 0, \dots, T-1$. The proposed fusion rule simply consisted of adding up the score vectors and deciding for the class that presented the largest overall score, that is:

$$\overline{v} = \begin{cases} \underset{v \in \{1,\dots,L\}}{\arg\max} \sum_{i=0}^{T-1} \boldsymbol{s}_i & \text{if } \exists! \underset{v \in \{1,\dots,L\}}{\max} \left(\sum_{i=0}^{T-1} \boldsymbol{s}_i \right) > \delta_{\text{fus}} \\ \textit{unknown} & \text{otherwise} \end{cases} \tag{2.18}$$

where δ_{fus} was a fixed threshold. Whether more than one class presented the same largest score, the decision was not taken and an unknown was declared. The algorithm was tested on the GOTCHA dataset, a collection of real full-polarimetric circular SAR images acquired by an airborne X-band sensor, and compared with the ℓ_2-norm-based algorithm reported in [58]. The results are shown in Figure 2.5 and Figure 2.6, with the blue lines that refer to the pZ moments based approach and the black lines that refer to the ℓ_2-norm-based algorithm. In the first case, the classifiers were trained with observations of the targets chosen from 30 different equally spaced aspect angles, while in the second case 10 aspect angles were selected. Moreover, dashed lines refer to the single sensor case (i.e. only one SAR image of the target was available), while dotted lines and solid lines refer to the 2 and 3 sensors cases, respectively. Given the number of sensors, the pZ moments based algorithm outperformed the ℓ_2-norm-

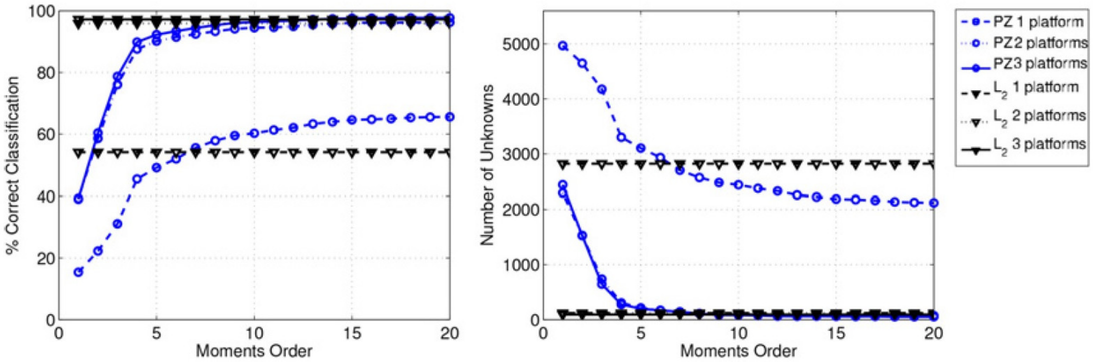

Figure 2.5: From [12], performance comparison between (blue) the pseudo-Zernike (pZ) based SAR ATR algorithm on varying the moments order and (black) the ℓ_2-norm-based algorithm. Images from 30 aspect angles were selected for the training of the classifiers.

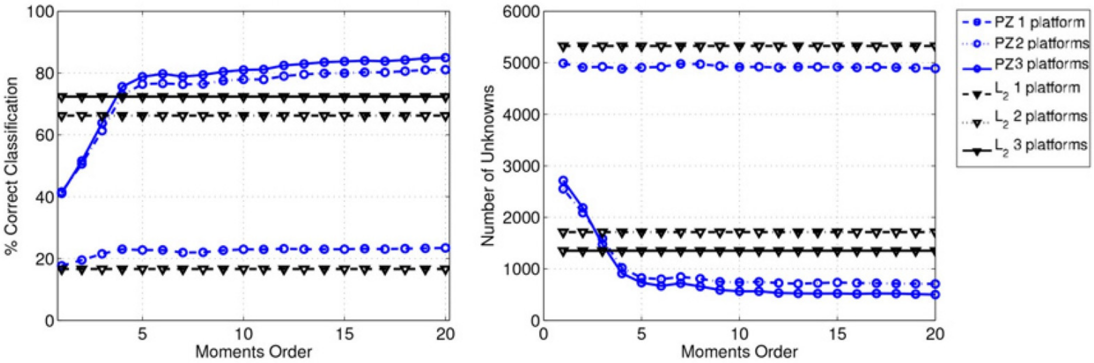

Figure 2.6: From [12], performance comparison between (blue) the pseudo-Zernike (pZ) based SAR ATR algorithm on varying the moments order and (black) the ℓ_2-norm-based algorithm. Images from 10 aspect angles were selected for the training of the classifiers.

based algorithm when fewer training images were used, both in terms of accuracy and unknowns. When the training was performed with images selected from 30 aspect angles, comparable results were obtained with moments order equal or greater than 10; however, as highlighted by the authors, the dimension of the feature vector was 20 times smaller.

2.4 Micro-Doppler Effect in Radar

The frequency shift present in the radar signal reflected back by a moving target is known as Doppler frequency and is proportional to the variation of the radar-target range, that is[13]:

$$f_D\left(t\right) = -\frac{2}{\lambda}\frac{\partial}{\partial t}R\left(t\right) \tag{2.19}$$

where λ is the wavelength and $R\left(t\right)$ is the time-varying radar-target range. Hence, whether the range decreases, namely the target gets closer to the radar, the Doppler frequency is positive, otherwise it is negative. Moreover, if the target is moving towards the radar with constant velocity v_{tg}, such that $R\left(t\right) = R_0 - v_{\text{tg}}\,t$, the Doppler frequency shift is constant and equal to:

$$f_D = 2\frac{v_{\text{tg}}}{\lambda} \tag{2.20}$$

where R_0 is the initial radar-target distance at $t = 0$. Instead, if the target is still moving with constant velocity v_{tg}, but with an angle $\theta_{\text{tg}}\left(t\right)$ with respect to the radar, the frequency shift is:

$$f_D\left(t\right) = 2\frac{v_{\text{tg}}}{\lambda}\cos\left(\theta_{\text{tg}}\left(t\right)\right) \tag{2.21}$$

However, in the general case the target would present a nonlinear movement that would exhibit secondary motions, also known in literature as *micro-motions*. Micro-Doppler (mD) effect identifies the time-varying characteristic of the Doppler frequency shift due to these micro-motions of the observed target. This concept was first introduced in coherent Light (or Laser) Detection and Ranging (LiDAR) systems, as reported in [59], and then also studied and analysed in radar systems [7]. The mD may be due to swinging arms and legs of a human being while walking or running, or to moving legs or flapping wings of animals. Source of micro-motions can also be a rotating propeller of a fixed-wing aircraft, or rotating rotor blades of a helicopter. All these micro-motions are peculiar of each target, and generate different mD signatures that may be used for classification purposes.

Until the joint time-frequency analysis was introduced in radar signal processing, not much attention was given to the time-varying characteristic of the Doppler frequency shift [60]. In the following Sections, the main time-frequency tools for mD analysis, as well as mD based ATR techniques exploiting such tools, are presented. Then, a recent technique based on a parametric sparse representation of the mD signal and its recovery aimed at estimating the mD parameters, will be introduced. Finally

---

[13] This definition is valid for a mono-static radar.

the discussion will focus on the challenge of helicopters identification.

2.4.1 Time-Frequency Analysis and ATR Techniques

Time-frequency analysis comprises a set of techniques that provide a two-dimensional representation of a non-stationary time-domain signal. They represent a useful tool for the characterisation of a signal in the time and in the frequency domain simultaneously.

The most common and intuitive time-frequency transform is the Short Time Fourier Transform (STFT). The STFT of a generic continuous signal, $x\left(t\right)$, is defined as the Fourier Transform (FT) of $x\left(t\right)$ multiplied by a sliding window, $w\left(t\right)$, such as [61]:

$$X_{\mathrm{STFT}}\left(t,f\right)=\int_{-\infty}^{\infty}x\left(t'\right)w\left(t'-t\right)e^{-j2\pi ft'}dt' \tag{2.22}$$

This transform can be seen as a time-varying FT, since it provides details of the frequency content of a signal as the time proceeds. The choice of the window and its length are crucial to determine both the time and the frequency resolution. The type of window affects the frequency resolution and the side lobe levels, in the same way it does for the usual FT. Regarding its length, the larger the window, the finer the frequency resolution while the poorer the time resolution. However, the selection of the length of the window also depends on the observed phenomenon. Indeed, in order for slow phenomenon to be appreciable, larger windows are necessary. The *spectrogram* of the signal $x\left(t\right)$, defined as the squared magnitude of its STFT, is often used in mD based ATR algorithms, as in [62]. Fioranelli et al. exploited the diversity that the mD exhibits on varying the aspect angle in order to enhance the classification accuracy of different human gaits. To achieve that, some features were extracted from the spectrograms computed from signals acquired by several sensors in a multi-static configuration. Such features were the bandwidth of the mD, the mean period, the main Doppler offset and the Radar Cross Section (RCS) ratio of limbs and body. Figure 2.7(a) and Figure 2.7(b) show the spectrograms of a signal reflected back by a human, walking towards two different directions, respectively, identified by the aspect angle θ_{tg}. In Figure 2.7(a) the mD spread is wider than in Figure 2.7(b), in agreement with equation (2.21). The spectrogram was also used in [63], where the authors proposed a

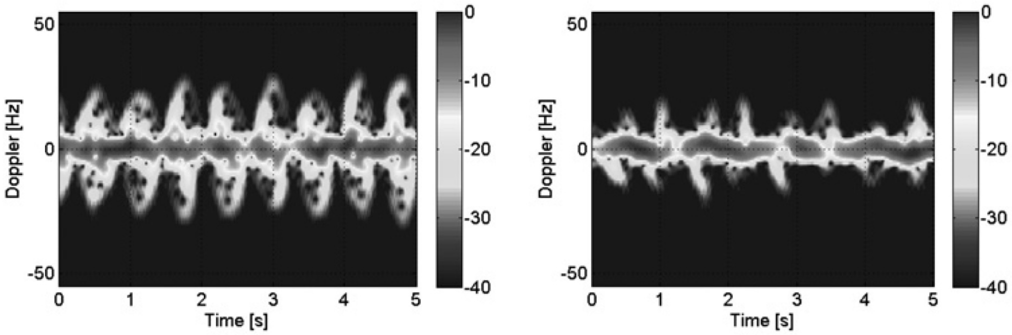

(a) Aspect angle $\theta_{\mathrm{tg}} = 0$. (b) Aspect angle $\theta_{\mathrm{tg}} = 2\pi/3$.

Figure 2.7: From [62], spectrograms of a signal reflected back by a human, walking in direction (a) $\theta_{\mathrm{tg}} = 0$ and (b) $\theta_{\mathrm{tg}} = 2\pi/3$.

CNN for the classification of hand-gestures. The CNN, fed by the spectrogram of the received signal, had three layers, each composed by a convolutional filter, an activation function and a pooling operation.

The Cadence Velocity Diagram (CVD) is another two-dimensional representation of a time-domain signal. It is defined as the FT of the spectrogram along each frequency bin, and results in a frequency-frequency representation. Hence, despite not presenting a time reference, it is widely used in mD analysis, since it provides a measure of how often the different frequencies repeat. Figure 2.8 from [64] shows the pair spectrogram-CVD of a signal received from a running human being, where (a) the mD modulation and (b) the main cadences are clearly visible. In the same way as described in Section 2.3.4.1 for SAR images, the method proposed by Clemente et al. [64] used

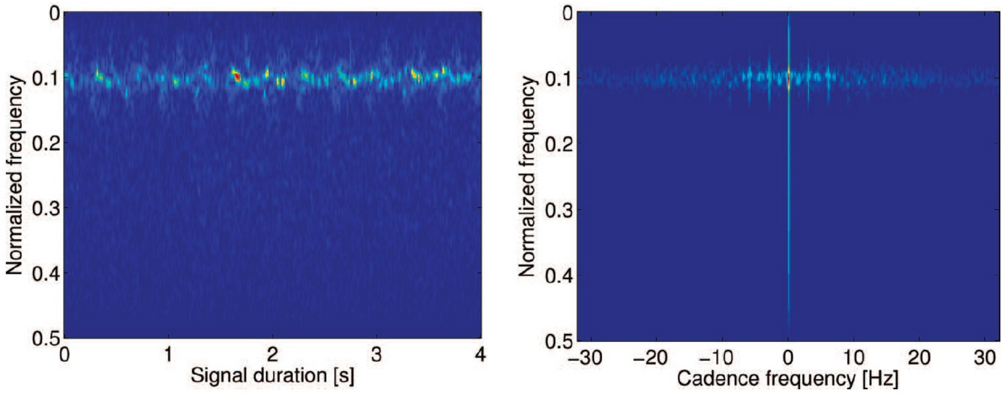

(a) Spectrogram. (b) Cadence Velocity Diagram (CVD).

Figure 2.8: From [64], (a) spectrogram and (b) Cadence Velocity Diagram (CVD) of a signal reflected from a running person.

the pZ moments on the CVD for the classification of several types of target, such as helicopters, and different human's and animal's gaits. Same approach, but with different image moments, was also used in [65] for Ballistic Missile (BM) recognition.

The Wigner-Ville (WV) distribution is an example of quadratic time-frequency transform, defined as [61]:

$$X_{\mathrm{WV}}\left(t,f\right)=\int_{-\infty}^{\infty}x\left(t+\frac{t'}{2}\right)x^{*}\left(t-\frac{t'}{2}\right)e^{-j2\pi ft'}dt' \tag{2.23}$$

and related to the STFT from the following expression [66][14]:

$$X_{\mathrm{WV}}\left(t,f\right)=\int_{-\infty}^{\infty}X_{\mathrm{STFT}}\left(t,f+\frac{f'}{2}\right)X_{\mathrm{STFT}}^{*}\left(t,f-\frac{f'}{2}\right)e^{j2\pi f't}df' \tag{2.24}$$

It provides a high resolution time-frequency representation but, being nonlinear, it exhibits artefacts, called interference or cross terms, that may hamper its interpretation. The S-Method is another quadratic time-frequency transform tightly related to the WV distribution, that keeps its high-resolution while mitigating the cross terms. It is defined as follows [66]:

$$X_{\mathrm{S}}\left(t,f\right)=\int_{-\infty}^{\infty}Q\left(f'\right)X_{\mathrm{STFT}}\left(t,f+\frac{f'}{2}\right)X_{\mathrm{STFT}}^{*}\left(t,f-\frac{f'}{2}\right)e^{j2\pi f't}df' \tag{2.25}$$

where $Q\left(f'\right)$ is a narrow frequency domain window. In [67] this time-frequency representation was used for the classification of human motions. Features were first extracted with log-Gabor filters with different scales and orientations, and then reduced with either a two-directional 2D PCA or a two-directional 2D Linear Discriminant Analysis (LDA).

Harmanny et al. [68] also proposed the use of the *cepstrogram* for the classification of Unmanned Aerial Vehicles (UAVs), defined as the inverse FT of the natural logarithm of the STFT along the frequency domain, that is:

$$X_{\text{cep}}\left(t,t_{Q}\right)=\frac{1}{2\pi}\int_{-\infty}^{\infty}\ln\left|X_{\mathrm{STFT}}\left(t,f\right)\right|^{2}e^{j2\pi ft_{Q}}df \tag{2.26}$$

---

[14] This definition differs from the one given in [66] by the exponential and the constant factors. This is due to the different expression of the STFT.

The cepstrogram is particularly valuable when long integration intervals are used with respect to the velocity of the observing phenomenon, as it could be the rotation of rotor blades of an UAV, as shown in Figure 2.9. Indeed, Figure 2.9(a) shows the spectrogram of a simulated signal reflected from a UAV with 6 rotors and 2 blades for each rotor, which are rotating with different speeds. The mD signature is not clearly visible, because the phenomenon, which is the rotation of the blades in this case, happens too quickly. However, by means of the cepstrogram, shown in Figure 2.9(b), it is still possible to recognise the presence of the 6 rotors.

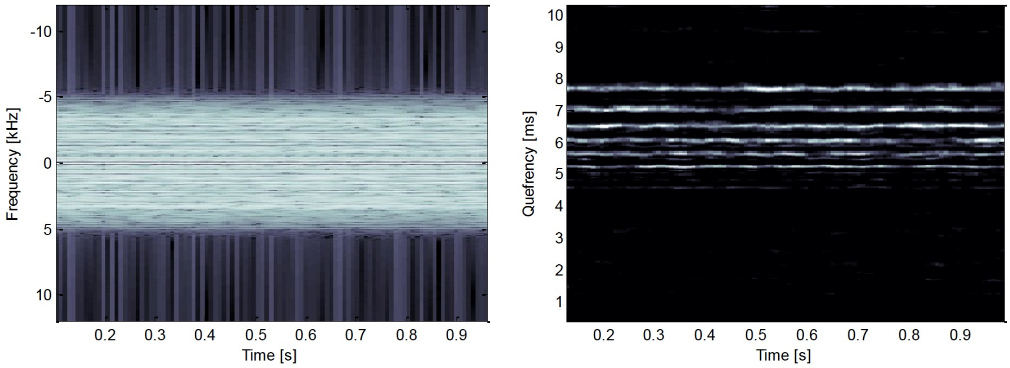

(a) Spectrogram. (b) Cepstrogram.

Figure 2.9: From [68], (a) spectrogram and (b) cepstrogram of a steady Unmanned Aerial Vehicle (UAV) whose 6 two-bladed rotors are spinning with different rates.

2.4.2 Parametric Sparse Representation and POMP

Recent developments in signal sparse representation, especially driven by Compressed Sensing (CS), have led to the application of such techniques for the estimation of mD parameters.

Li and Varshney [13] presented a parametric sparse representation aimed at modelling a mD signal from a rigid body, and an algorithm called Pruned Orthogonal Matching Pursuit (POMP) used to find the solution of such a sparse representation. From the parametric sparse representation of the mD signal, based on the geometric model of the target of interest, a dictionary was built and used by the POMP to estimate the mD parameters, supposed unknown, of a generic signal reflected from a target of the same kind. The authors considered a coning target, whose radar echo can be expressed as [59]:

$$y_{\text{con}}\left(n\right)=\sum_{l=0}^{K_{\text{sc}}-1}a_{l}e^{j\frac{4\pi}{\lambda}d_{l}\sin\left(\omega nT_{s}+\theta_{l}\right)} \tag{2.27}$$

with $n=0,\ldots,N-1$, where N is the number of time samples, T_s is the sampling period, K_{sc} is the number of dominant scatterers and a_l their complex reflectivity. The mD parameters to estimate were d_l and θ_l, that identify the spatial position of each scatterer, and ω, that refers to the angular velocity of the target, supposed equal for all the scatterers. The parametric representation of $y_{\text{con}}\left(n\right)$ was obtained by discretising the domains that d_l, θ_l and ω belong to, that is $d_l\in\left\{d_0,\ldots,d_m,\ldots,d_{M_d-1}\right\}$, $\theta_l\in\left\{\theta_0,\ldots,\theta_{m'},\ldots,\theta_{M_\theta-1}\right\}$ and $\omega\in\left\{\omega_0,\ldots,\omega_{m''},\ldots,\omega_{M_\omega-1}\right\}$. In this way, the expression in (2.27) could be rewritten as:

$$\boldsymbol{y}_{\text{con}}=\boldsymbol{\Psi}\boldsymbol{x} \tag{2.28}$$

where $\boldsymbol{y}_{\text{con}}=\left[y_{\text{con}}\left(0\right),\ldots,y_{\text{con}}\left(N-1\right)\right]^{T}\in\mathbb{C}^{N\times1}$, $\boldsymbol{\Psi}\in\mathbb{C}^{N\times\left(M_dM_\theta M_\omega\right)}$ is called *dictionary* and $\boldsymbol{x}\in\mathbb{C}^{\left(M_dM_\theta M_\omega\right)\times1}$ is a sparse vector. Each column of the dictionary, called *atom*, was equal to:

$$\psi\left(d_m,\theta_{m'},\omega_{m''};n\right)=e^{j\frac{4\pi}{\lambda}d_m\sin\left(\omega_{m''}nT_s+\theta_{m'}\right)} \tag{2.29}$$

such that if $d_m=d_l$, $\theta_{m'}=\theta_l$ and $\omega_{m''}=\omega$, the corresponding element of the sparse vector $\boldsymbol{x}$ was non-zero and equal to a_l. Therefore, from another point of view, the recovering of the sparse signal $\boldsymbol{x}$ allowed to retrieve the mD parameters d_l, θ_l and ω. The sparse signal recovery problem was stated as follows:

$$\overline{\boldsymbol{x}}=\arg\min_{\boldsymbol{x}}\left\|\boldsymbol{x}\right\|_0 \quad \text{s.t.} \quad \left\|\boldsymbol{r}\right\|_2^2\leq\epsilon \tag{2.30}$$

where $\left\|\cdot\right\|_0$ and $\left\|\cdot\right\|_2$ represent the ℓ_0- and the ℓ_2-norm, respectively, $\boldsymbol{r}\triangleq\boldsymbol{y}_{\text{con}}-\boldsymbol{\Psi}\boldsymbol{x}$ and ϵ is the error threshold on the residual $\boldsymbol{r}$. The ℓ_0 minimisation problem in (2.30) is highly non-convex, however it has been demonstrated [69, 70, 71] that, under certain conditions, the ℓ_0-norm can be replaced by the ℓ_1-norm, therefore the problem can be solved through traditional convex optimisation techniques. Solutions can also be obtained iteratively. This class of approaches is referred to as greedy algorithms, such as the Orthogonal Matching Pursuit (OMP) [72], which iteratively selects the atoms that present the largest correlation coefficients with the residual and update the sparse solution, until the energy of the residual is smaller than the error threshold. The Pruned OMP developed by Li and Varshney, and proposed in [13], exploits the fact that all the scatterers have the same angular velocity ω. It combines the traditional iterative approach of the OMP, which is applied on smaller portions of the dictionary, with a pruning process, that progressively reduces the dimension of the dictionary $\boldsymbol{\Psi}$ avoiding unnecessary computations corresponding to wrong atoms.

2.4.3 Helicopters Identification

In this Section, the discussion focuses on the challenging problem of mD based helicopters identification. The capability to identify the model of a helicopter by analysing its mD signature was first investigated in [73], after that in [74] was demonstrated that the theoretical return signal from propeller blades depends on the number, η, the length, ρ, and the rotation speed, ω, of the blades themselves. Moreover, since the RCS from the tail blades is smaller than the RCS from the main rotor blades [1], the majority of the methods only relies on the mD information extracted from the main rotor blades.

According to [60], the return signal from a rotor blades can be modelled as[15]:

$$\begin{aligned} y_{\text{rotor}}(n) = {} & \rho\, e^{-j\frac{4\pi}{\lambda}R_0} \times \\ & \times \sum_{l=0}^{\eta-1} \operatorname{sinc}\left(\frac{2}{\lambda}\rho\cos\beta_L\cos\left(\omega n T_s + \frac{2\pi}{\eta}l + \phi_0\right)\right) \times \\ & \times e^{-j\frac{2\pi}{\lambda}\rho\cos\beta_L\cos\left(\omega n T_s + \frac{2\pi}{\eta}l + \phi_0\right)} \end{aligned} \tag{2.31}$$

with $n = 0, \ldots, N-1$, where R_0 is the range of the helicopter, ϕ_0 is the initial position of the blades and β_L is the elevation angle. Note that, the maximum Doppler

---

[15] It is assumed that the segment identifying the LoS, and the rotor rotation axis, lie on the same plane.

shift depends on the length of the blades, ρ, and their rotation speed, ω, as follows:

$$f_{D_{\max}} = 2\frac{\omega\rho}{\lambda} \tag{2.32}$$

Figure 2.10(a) shows an example of a simulated time signal received from the rotor of a *Mil Mi-2 Hoplite* with a Signal-to-Noise Ratio (SNR) of $20\,d$B. It has $\eta = 3$ blades of length $\rho = 7.30$ meters rotating at nominal speed of $\omega = 25.76\,rad/s$. The spectrogram in Figure 2.10(b) is in normalised frequency, and clearly shows the characteristic mD signature of the helicopter. The *flashes* that appear in the time signal are due to the blades when they, approaching or receding from the radar, get perpendicular to the LoS [73]. Simultaneously, the velocity vector becomes parallel to the LoS, generating the maximum, positive or negative, Doppler shift. The time distance, μ, between two flashes, that is the periodicity of the flashes, can be computed as:

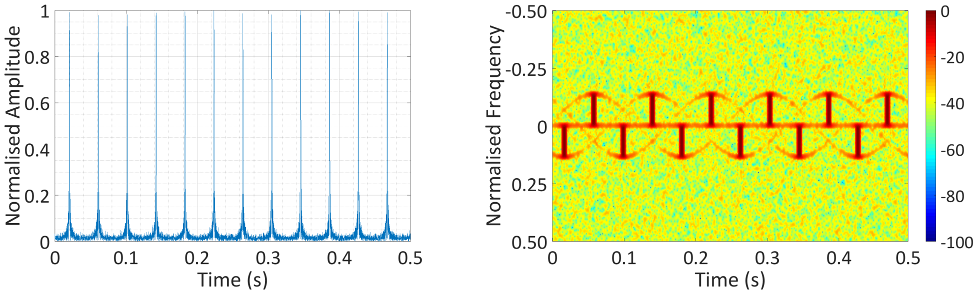

(a) Time signal. (b) Spectrogram.

Figure 2.10: Example of a simulated radar signal received from the rotor of a Mil Mi-2 Hoplite: (a) time-domain signal and (b) its spectrogram.

$$\mu = \begin{cases} \dfrac{2\pi}{\omega\eta} & \text{if } \eta \text{ is even} \\ \dfrac{\pi}{\omega\eta} & \text{if } \eta \text{ is odd} \end{cases} \tag{2.33}$$

The first algorithm aimed to identify helicopters was developed in [75]: it was based on the computation of the ρ/η-quotient, that is characteristic of each helicopter, obtained from the relations (2.32) and (2.33) as:

$$\frac{\rho}{\eta} = \begin{cases} \dfrac{\mu f_{D_{\max}}}{4\pi}\lambda & \text{if } \eta \text{ is even} \\ \dfrac{\mu f_{D_{\max}}}{2\pi}\lambda & \text{if } \eta \text{ is odd} \end{cases} \tag{2.34}$$

where μ and $f_{D_{\max}}$ could be estimated from the time-domain received signal and its spectrum, respectively. Note that, the ambiguity about which expression to be used for the computation of quotient in (2.34), was solved by inspecting the spectrum of the received signal. Indeed, it is symmetric if η is even, asymmetric otherwise. The main drawback of this technique is that two different models of helicopter that share the same ρ/η-quotient cannot be distinguished. Moreover, in low SNR conditions the estimate of $f_{D_{\max}}$ could be very difficult.

Further improvements to this algorithm can be obtained by exploiting one of the time-frequency representations presented in Section 2.4.1. Specifically, in [76] the STFT was used to better estimate $f_{D_{\max}}$ in low SNR conditions and to easily distinguish between an even or an odd number of blades. Furthermore, in [77] after the estimation of the periodicity of the flashes and of the maximum Doppler shift, a mask was generated and used to distinguish between helicopters that presented the same ρ/η-quotient. An example is given in Figure 2.11, where the spectrograms of the signals reflected from two helicopters with same ρ/η-quotient, but with (a) 2 and (b) 4 blades, are shown. It is evident that the region between two consecutive flashes is different, and is exploited as discriminative characteristic. In a similar way, in [78] the authors proposed either a coherent or an incoherent mask to be applied on the slow time-fast time matrix obtained from a High Resolution Linear Frequency Modulated Continuous Wave (LFMCW) radar.

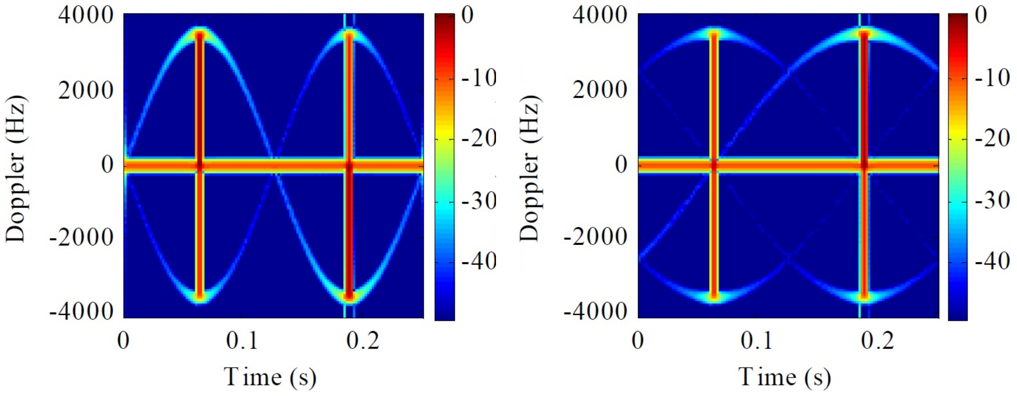

(a) Spectrogram the two-bladed helicopter. (b) Spectrogram the four-bladed helicopter.

Figure 2.11: From [77], spectrograms of signals reflected from two helicopters with same ρ/η-quotient, but with (a) 2 and (b) 4 blades.

Zhang et al. [79] proposed a helicopters identification method based on the estimation of the periodicity of the flashes, μ, and the number of blades, η. The periodicity was determined by measuring the time distance between two consecutive peaks in the autocorrelation function of the received signal. The estimation of the number of blades was performed in two steps, in order to remove the ambiguity on the parity. First a time-domain correlation coefficient between the received signal and a synthetic signal generated with either an odd or an even number of blades was calculated. Then, a time-frequency correlation coefficient was computed to obtain the actual value of η.

A different approach, based on a joint time-frequency and tomographic technique, is presented in [80]. The time-varying Doppler frequency shift due to a single blade, neglecting any initial offset, can be written as:

$$f_D\left(n\right) = -2\frac{\omega\rho}{\lambda}\sin\left(\omega n T_s\right) \tag{2.35}$$

Therefore the authors recognised that, besides the factor $2\omega/\lambda$, the Doppler shift could be seen as a projection of the cross-range coordinate of the blade tip of an angle $\omega n T_s$. Since series of such projections form the spectrogram of the signal reflected from the rotor blades, the application to the spectrogram of the Inverse Radon Transform (IRT), with a proper selection of the angle for each projection[16], led to the formation of an image from which number and length of the blades could be estimated. Note that, the correct angular rate was estimated through a linear search method and using the IRT image focus as fitness criteria. Figure 2.12 shows an example of application of the IRT to the spectrogram. Figure 2.12(a) shows the spectrogram of a signal acquired from an AS-350B Squirrel. This helicopter has 3 blades rotating at 390 rpm. The IRT was applied to the spectrogram with different angular rates, each associated to different rotation speeds selected within a range. The linear search, based on the image focus as fitness criteria, led to an estimate of the rotation speed of 390 rpm. The IRT applied to the spectrogram with this angular rate is shown in Figure 2.12(b), from which 3 bright points (in black) are clearly visible, identifying the tips of the 3 blades.

---

[16] The angle of each projection is estimated as a linear function versus time with unknown slope, due to the unknown rotation speed ω.

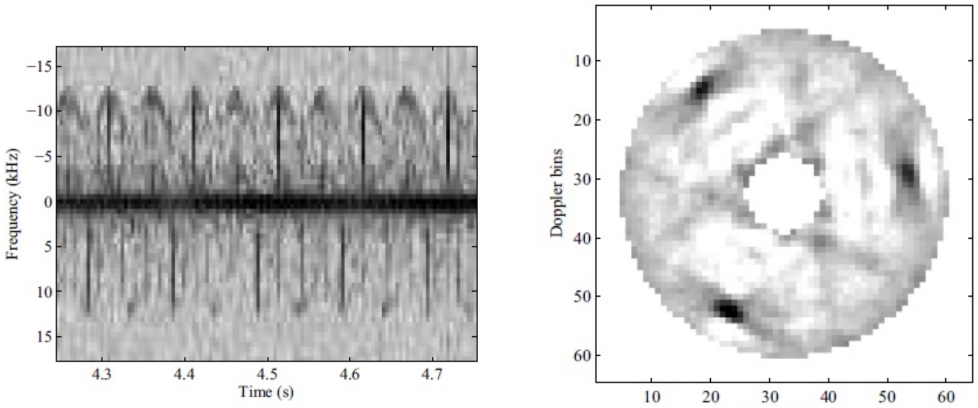

(a) Spectrogram. (b) Inverse Radon Transform (IRT).

Figure 2.12: From [80], (a) spectrogram of a signal acquired from an AS-350B Squirrel, whose nominal rotation speed is 390 rpm, and (b) tomographic result, that is the Inverse Radon Transform (IRT), obtained selecting a rotation speed of 392 rpm.

2.5 Conclusion

In this Chapter, recent Automatic Target Recognition (ATR) techniques were discussed with particular focus on Synthetic Aperture Radars (SARs) and micro-Doppler (mD) processing.

SAR ATR algorithms were presented as divided into two categories, with the first ones, *model-based* presented in Section 2.3.3, that use identifiable parts of the target as discriminative features to be used during the classification process. Such features, being based on the direct observation of the SAR images, depend on and are sensitive to the location and the orientation of the target on the scene. Therefore, they need a prior step aimed at estimating the position and the pose of the object, that could introduce errors leading to misclassification. *Feature-based* ATR algorithms described in Section 2.3.4, instead, either project the SAR image in a domain different from the spatial one, which may also be rotational and/or translational invariant, or leave the computation and selection of the features to the algorithm itself. In this context, image moments based SAR ATR techniques have been demonstrated to be very effective. In Chapter 4 two novel SAR ATR algorithms based on the pseudo-Zernike (pZ) moments framework presented in Section 2.3.4.1 are introduced.

The second part of the Chapter was focussed on the mD effect in radar and on mD based ATR techniques, designed at classifying target by exploiting peculiar micro-motions that they exhibit. This is particularly effective for helicopters identification, as reported in Section 2.4.3. Most of the techniques developed with this objective, however, use time-frequency analysis tools that are computationally expensive and need some parameters to be properly set, according to the dynamic of the motion. Moreover, they do not take into consideration the variation of a helicopter's mD signature due to its orientation with respect to the radar. In Chapter 5 a novel automatic model-based algorithm for helicopters identification is presented, which is independent of the orientation of the target and of the initial position of the blades. Moreover, it can be implemented in a distributed radar system to further enhance the identification process, and it is also able to identify multiple helicopters flying in formation that cannot be distinguished in any other common radar domain, i.e. range, angle, Doppler, etc.

Chapter 3

Waveform Design for Radar-Comms Systems

3.1 Introduction

In several applications there is the dual need for a system to perform radar operations while sending data to another cooperative system. Examples are vehicles in an Intelligent Transportation System (ITS) that need to share information in a rapidly changing environment [81]; Synthetic Aperture Radar (SAR) systems that need to share sensed data with ground stations [82]; nodes in a Multiple-Input Multiple-Output (MIMO) radar system with purposes of surveillance or navigation aid [83]. These dual-function systems are known in literature as joint radar-communication, or Communicating-Radar (CoRadar), systems.

In this Chapter the focus is on the problem of spectrum congestion, which is increasingly becoming a significant issue, due to the ever greater demand on bandwidth for different kind of Radio Frequency (RF) applications. In this context, CoRadar technology provides a clever solution for the sharing of bandwidth resources, as well as power and hardware resources, between the radar and the communication task. The problem is introduced in Section 3.2, while a review about current solutions providing spectrum sharing are presented in Section 3.3. Specifically, the discussion is first focussed on solutions that allow the coexistence of radar and legacy communication systems, then enabling technologies for joint radar-communication systems are presented. Finally, the Fractional Fourier Transform (FrFT), used in the following of the Thesis as a waveform design tool, is presented in Section 3.4.

3.2 Spectrum Congestion

The radio spectrum is a finite resource, and as such there is ever greater competition for accessing it as the demand continues to grow [84]. The increasing demand comes from both the continuous introduction of new wireless technology, and the fact that almost any remote service needs access to wider bandwidth. In the specific case of radar systems, higher bandwidth means finer range resolution, that is superior sensing capability, while for communication systems it translates into higher data rates. To better exploit the available bandwidth, many users are forced to coexist in the same band. Indeed, allocated frequency bands are often interleaved or, in some cases, shared between different services. This means that a radar may represent an interference for other systems, or even for other radars, and, on the other hand, it may be affected by other interfering systems. In [85], the performance degradation of an S-band long range weather radar system due to interference caused by Orthogonal Frequency Division Multiplexing (OFDM) communication signals, used in systems as WiMAX and LTE, was examined. The study showed that under an interfering OFDM signal with bandwidth of $5\,MHz$, after the application of a notch filter for its mitigation and the coherent integration of 64 radar pulses, the increase in SNR to achieve a detection probability of 0.5 (with a fixed probability of false alarm of 10^{-4}) was of about $60\,d\mathrm{B}$ with respect to the no interference case. Kodituwakku et al. [86] evaluated the degradation in detection performance for a radar, either in L- or S-band, in presence of LTE communication signals, reporting an average loss of $1.3 - 1.4\,d\mathrm{B}$ at detection probability of 0.5, with an interference level of $-6\,d\mathrm{B}$ below the noise floor. In the worst case, the detection loss increased up to $4.7\,d\mathrm{B}$[17].

The effect of interfering radar signals on communication systems was analysed in [87] and [88]. Pasya et al. [87] studied the interference of Ultra-Wide Band (UWB) radar signals on OFDM communication system. This was based on the IEEE802.16

---

[17] The difference in the outcomes between studies [85] and [86] is most likely due to the different interference-to-noise level analysed, which, in the first article, is not clearly reported.

standards, while the radar signal was designed to have a bandwidth of $5\ GHz$. Results showed an increase of the Bit Error Ratio (BER) as effect of the interfering radar signal. Specifically, by fixing the energy per bit to noise power spectral density ratio at $10\,d\mathrm{B}$, the BER, which was equal to $2 \cdot 10^{-6}$ without interference, increased up to $3 \cdot 10^{-4}$ with a Signal-to-Interference Ratio (SIR) of $15\,d\mathrm{B}$. The authors in [88], instead, evaluated the throughput loss in a LTE systems when transmitting either HTTP or FTP packets and in presence of an interfering radar signal. As reported in the study, the throughput loss was as high as $50\,\%$ and $75\,\%$ when FTP packets were transmitted for the uplink and downlink, respectively, and for $SIR = 47\,d\mathrm{B}$.

All the above mentioned results show how the spectrum congestion problem in the context of coexistence of radar and communication systems is severe, and motivate the recent research in this area.

3.3 Spectrum Sharing

The Defense Advanced Research Projects Agency (DARPA) has recently launched the Shared Spectrum Access for Radar and Communications (SSPARC) program [89], with the scope of development of enabling technologies for joint spectrum access for both radar and communications systems. Two of the main task areas of the SSPARC program are *coexistence* and *codesign* [90]. Coexistence regards the development of techniques that allow the sharing of the spectrum between radar and legacy communication systems, while codesign refers to the concept of jointly designing the systems, radar and communications, such that they incorporate spectrum sharing operations from inception. Following this categorisation, an overview of the most recent solutions in both these areas is presented in the next Sections.

3.3.1 Radar and Legacy Comms Systems: Coexistence

Researchers have extensively worked to present solutions for the coexistence of radar and communication systems, by proposing techniques for the design of radar waveforms that present spectral constraints and do not interfere with legacy communication systems. Aubry et al. [91] proposed a waveform design technique formalised as an optimisation problem aimed at forcing spectral constraints in agreement with a priori information provided by a Radio Environmental Map (REM). The optimisation problem, whose objective was the maximisation of the Signal-to-Interference plus Noise Ratio (SINR), consisted in finding the code of a coherent burst of slow-time coded pulse such that both a similarity constraint with a reference signal, and spectral constraints in order for the radar waveform not to interfere with pre-existing emitters, were met. The spectral compatibility was enhanced in [92] enabling different interference levels in different spectral bands, so-called local design. Figure 3.1 illustrates an example scenario: the frequency bands occupied by the legacy communication systems are highlighted in grey, while the unoccupied spectral bands, available to the radar system, are shown in white. Moreover, the Energy Spectral Densities (ESDs) of the reference signal and the constrained waveforms obtained with either a global or a local design are depicted in green, red and blue, respectively. The energy of the waveform obtained as solution of the global optimisation problem is concentrated in the white areas, while it is more than $10\,d\mathrm{B}$ lower in the grey areas, in order not to interfere with the operations of the communication systems. Moreover, when the local design is considered, different interference levels are obtained depending on the transmission power of each communication system. The optimisation framework was further extended in [93] to account for the Doppler filter bank, thus jointly optimising both the code of the transmitted waveform and the weights of the filters. Huang et al. [94] used a different approach, maximising the the mutual information between the target impulse response,

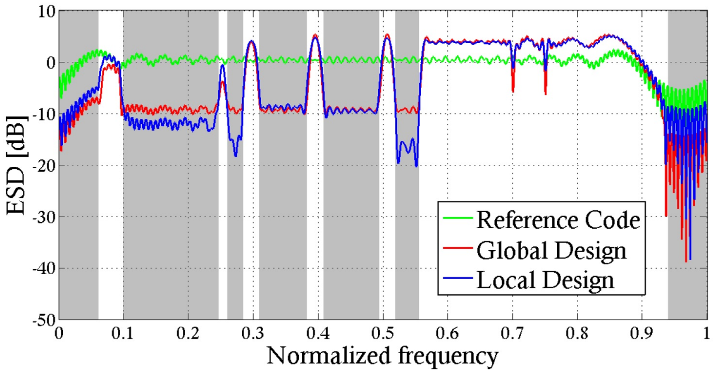

Figure 3.1: From [92], Energy Spectral Density (ESD) versus normalized frequency of the reference signal, in green, and the constrained waveforms, globally (red) and locally (blue) designed, respectively.

that is the channel between the radar and the target, and the radar signal returns [95], while constraining the spectrum of the radar waveform in order to ensure a minimum level of service to the communication systems.

Cognitive solutions are also suitable in this context, with radar waveforms that can dynamically adapt to the presence of communication systems. La Manna et al. [96] proposed a cognitive radar for operation in spectrally dense environments. The problem to address was the design of a wide-band radar waveform in presence of narrowband communication signals. The main idea was to provide the radar signal with a set of notches located where the communication systems operate. The proposed radar system was able to first sense the environment, estimating the occupied frequency bands and the power transmitted by the communication systems [97], and then to design the radar waveform accordingly. At the receiver side, a specifically designed processing chain was developed to compensate the high range sidelobes introduced by the discontinuities in the signal spectrum.

3.3.2 Joint Radar-Comms (CoRadar) Systems

The joint design of radar and communication systems represents another approach for tackling the spectrum sharing problem. Unlike the techniques presented in Section 3.3.1, rather than designing the radar waveform such that it does not interfere with legacy communication systems, both the radar and the communication signals are designed from inception in order not to collide. Codesign techniques can be used - but they are not limited - to enable a communication channel within a radar system that needs to share information with one or multiple cooperative systems. The concept of attaching information in the radar signal is becoming ever more interesting and appealing to the radar community, and it is now seen as a potential feature in future radar systems [98].

In the following, the discussion is split into *dynamic spectrum allocation* and *information embedding techniques*. In the first case, radar and communication signals are generated independently and then merged, while, in the second case, the bits to be transmitted are directly embedded in the radar waveform.

3.3.2.1 Dynamic Spectrum Allocation

Turlapaty and Jin [99] proposed the joint optimised allocation of the power spectral density for a wide-band radar waveform and an OFDM communication signal whose spectra partially overlap. This was done by maximising the total mutual information, which, in turn, translated into the maximisation of the data rate for the communication channel and of the SNR for the radar system, while reducing the mutual interference.

A technique for enabling a communication channel between several nodes in a network of UWB noise radars[18] is described in [100]. Authors exploited the noise-like spectrum of an OFDM signal, which can be included in a frequency portion of the radar waveform (noise-like by construction) without affecting its spectral characteristics.

3.3.2.2 Information Embedding Techniques

Besides the above mentioned spectrum sharing approaches, design techniques that directly embed data into the transmitted radar waveform have been reported [101]. A time-domain duplex technique was proposed in [102]. The transmitted signal consisted of a radar cycle, based on a Trapezoidal Frequency Modulated Continuous Waveform (TFMCW), followed by a single frequency carrier modulated by information data using common modulation techniques, such as Phase Shift Keying (PSK). The system, developed for automotive application, was able of sending data at $75\,Mb/s$, with a BER of 10^{-6}, while detecting target at a maximum unambiguous range of $100\,m$, with probability of detection and false alarm of 0.9 and 10^{-6}, respectively. Xu et al., instead, proposed a technique based on the Direct Sequence Code Division Multiple Access (DS-CDMA) [103] to avoid mutual interference between radar and communication signals: the two signals were mixed in time and frequency, but made orthogonal by means of Pseudo Noise (PN) codes. Performance analysis showed that the BER was not affected by the interfering radar waveform but, on the other hand, the authors did not provide any results on how the system behaved on a radar perspective. The orthogonality between radar and communication signals was achieved in [104] by using an up- and a down-chirp. Specifically, the radar waveform was associated to a down-

---

[18] A noise radar transmits a noise, or noise-like, waveform and, as consequence, meets the requirements for Low Probability of Interception (LPI) and Low Probability of Detection (LPD) systems.

chirp, while a sequence of up-chirp signals (with the first one that overlaps with the radar waveform) were modulated by $\pi/4$-Differential Quadrature Phase Shift Keying ($\pi/4$-DQPSK) data symbols, as explained in [105]. The implementation of the system was later reported in [106]: it operated with a bandwidth of $500\,MHz$ and a Pulse Repetition Frequency (PRF) of $150\,kHz$, capable of transmitting $1\,Mb/s$ (BER less than 10^{-5}) and detecting targets with probability 0.99 and false alarm 0.07.

Alternative methods are based on the modulation of a LFM carrier. Chen et al. [107] analysed the Ambiguity Function (AF) of a Minimum Shift Keying (MSK) modulated LFM carrier, without, however, providing information in terms of communication performance. Zhao and Jiang [108], instead, proposed a Binary Phase Shift Keying (BPSK) modulated LFM where constraints on the number of symbols per waveform were set to ensure that the amplitude of transmitted signal was continuous. These resulted in the number of transmitted bits, N_b, to be bounded by the square root of the time-bandwidth product, that is $N_b \leq \sqrt{\tau \cdot B_w}$, where τ is the pulse width and B_w its bandwidth. BPSK was also used in [109] to modulate a Stepped Frequency Continuous Waveform (SFCW) acting as carrier.

The use of multi-carrier signals [110], widely investigated in radar literature for their high time-bandwidth product and flexibility, also represents a natural solution for the implementation of an integrated radar-communication system. The idea was first introduced in [111], where Donnet and Longstaff combined a co-located MIMO radar with OFDM communications by employing a step-frequency technique [112], such that one or multiple OFDM sub-carriers were transmitted from one antenna at time. The authors proposed a candidate system using an overall bandwidth of $40\,MHz$, divided into 512 sub-carriers, and arranged such that the maximum unambiguous range was $74.88\,km$ and the data rate was $384.6\,kb/s$. An OFDM system concept for joint radar and communications operations was also proposed in [113]. The authors exploited a previously described OFDM radar signal processing technique performed in the *modulation symbol domain*, which consisted in: 1) comparing the transmitted and the received OFDM symbols before channel equalisation in order to obtain the channel frequency response; and 2) computing the radar range profile as Inverse Fast Fourier Transform (IFFT) of the channel frequency response. This processing aimed at removing the dependency from the transmitted data and circumventing the high side-lobes problem that arises when performing usual radar processing. However, as consequence of sampling the spectrum, the resulting radar range profile was periodic in time. In [81] the authors extended this concept to the radar Doppler processing, and presented a real system able of transmitting $20\,Mb/s$ with a maximum unambiguous range of $1650\,m$.

Approaches based on the joint use of waveform diversity and side lobe control have been recently reported. In [114] a dual-function radar-communication system based on Time Modulated Array (TMA)[19] was proposed, which implemented the radar function in the main lobe while enabling a communication channel in a side lobe direction by exploiting the variations of the beam patterns. In order to allow the radar operations, each beam pattern, synthesised by means of a beamforming weight vector, needed to satisfy several requirements, such as constant directivity and beamwidth of the main beam. This, in turn, limited the number of bits transmitted per pulse, since $N_b = \log_2(K_{\text{pattern}})$, where K_{pattern} is the number of available beamforming vectors satisfying the radar requirements. Hassanien et al. [116] proposed a different approach, augmenting the capability of the system of sending the sequence of bits in several side lobe directions yet needing only two different beam patterns, jointly used with a set of orthogonal waveforms that were sent simultaneously in each radar pulse. Two strategies were reported: in the first one, each of the N_b orthogonal waveforms embedded a single bit, whose actual value (0 or 1) depended on the radiation beam pattern with which the waveform was transmitted. In the second one, a pair of orthogonal waveforms, each transmitted through either the beam patterns, was appointed to the delivery of a single bit. The value of the latter depended on the combination waveform-beam pattern. In both the cases, the data rate was limited by the availability of orthogonal waveforms and, depending on the PRF used, it was in the range of kb/s. Finally, in [117] the information was embedded in the differential phase between two beamforming weight vectors, which did not affect the radar operation in the main beam.

---

[19] The concept of TMA, introduced in [115], consists in changing the set, as well as the number, of antennas switched on over time, producing intermediary radiation patterns.

3.4 Radar Waveform Design Tool: Fractional Fourier Transform

The FT of a time signal provides a representation of the signal itself in the frequency domain, decomposing it as a summation of weighted harmonics. In the time-frequency domain it can be thought as a rotation of the signal by a $\pi/2$ angle. The Fractional Fourier Transform (FrFT), firstly introduced in [118], generalises this concept, providing a representation of a time signal along an intermediate axis between time and frequency, identified by the angle ϕ that it forms with the time domain axis. Letting $x(t)$ be an arbitrary time signal, its α-th order FrFT is defined as [119]:

$$\mathscr{F}^{\alpha}\left\{x(t)\right\}(u) = \int_{-\infty}^{\infty} K_{\alpha}(u,t)\, x(t)\; dt \tag{3.1}$$

where

$$\alpha = \frac{2}{\pi} \times \phi \tag{3.2}$$

and $K_{\alpha}(u,t)$ is the FrFT kernel, defined as:

$$K_{\alpha}(u,t) = \begin{cases} A_0 e^{j\pi\left(u^2+t^2\right)\cot\phi} e^{-j\pi 2ut\csc\phi} & \text{if } \phi \neq m\pi \\ \delta(u-t) & \text{if } \phi = 2m\pi \\ \delta(u+t) & \text{if } \phi = 2m\pi + \pi \end{cases} \tag{3.3}$$

where $A_0 = \frac{e^{j\frac{\phi}{2}}}{\sqrt{j\sin\phi}}$, $\delta(\cdot)$ is the Dirac delta function and $m \in \mathbb{Z}$ is an integer. The FrFT is an invertible linear transform continuous in the angle ϕ, which satisfies the basic conditions for it to be meaningful in the time-frequency plane [120]. Moreover, the FrFT is periodic in α with period 4, and it is straightforward to demonstrate that:

$$\mathscr{F}^{\alpha+2}(u) = \mathscr{F}^{\alpha}(-u) \tag{3.4}$$

Figure 3.2 shows the example of application of the FrFT to a chirp signal sampled with a sampling frequency $f_s = 2\,MHz$, whose expression is:

$$x\left(t\right) = e^{j\pi \frac{B_w}{\tau} t^2} \tag{3.5}$$

$B_w = 1\,MHz$ is its bandwidth and $\tau = 100\,\mu s$ its duration, respectively. The illustration at the centre of the figure shows the spectrogram of the signal, while bottom and left graphs show the time signal (real part and imaginary part) and its spectrum, respectively. The graph on the right, instead, represents the FrFT magnitude of the chirp signal computed selecting the optimum order defined as [121]:

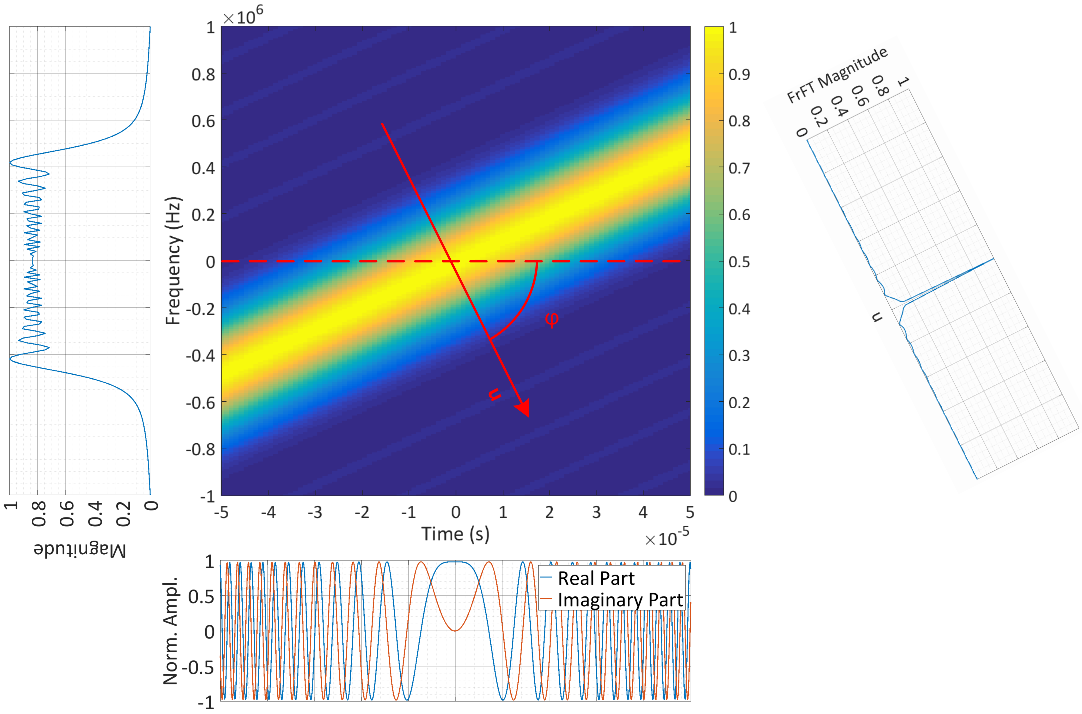

Figure 3.2: Example of application of the Fractional Fourier Transform (FrFT) to a chirp signal. Middle graph shows the spectrogram of the signal; bottom and left diagrams are the time signal and its spectrum, respectively; right graph is the FrFT with order -0.70.

$$\alpha_{\text{opt}} = -\frac{2}{\pi}\tan\left(\frac{f_s^2/N}{B_w\tau}\right) \sim -0.70 \tag{3.6}$$

where N is the number of samples that composes the discrete signal, from which, through equation (3.2), $\phi \sim -63°$.

The FrFT's capability of well identifying the chirp rate of a LFM signal, as shown in Figure 3.2, as well as its capacity to compress or spread a signal, either in time or frequency, simply through a rotation in the time-frequency domain, has opened to a variety of applications to which the FrFT can potentially be used. The capability of reliably detecting a chirp was exploited in [122], where the FrFT was proposed to identify a signal in a complex time-space-frequency-dependent underwater acoustic channel. Similarly, Sha et al. [123] described a FrFT based multiple-access technology. In transmission, an LFM carrier with a unique chirp rate was assigned to each user of the network, practically emulating a spread spectrum technique; at the receiver, the FrFT was employed to effectively despread the signal and retrieve the data. The radar community, which extensively deals with processing of LFM signals, has proposed the FrFT for several purposes, such as enhanced matched filtering [124] and SAR resolution [125], detection of slow-moving target [126] and micro-Doppler based classification [127].

Beside being a tool for signal analysis and processing, the FrFT has also been used to synthesise waveforms. Specifically, frequency-varying basis functions derived from the FrFT were proposed in [128] to generate a multi-carrier signal more suitable for rapidly time-varying channels. Clemente et al. [129], instead, described a novel method of generating a library of phase-coded radar waveforms applying the FrFT with different orders to a seed waveform, such as a Barker code. By selecting the appropriate order spacing, a good level of orthogonality could be achieved, enabling the use of the FrFT waveforms in MIMO radar systems [130, 131].

3.5 Conclusion

This Chapter offered an overview on the problem of spectrum congestion, in Section 3.2, and on several technologies that have been recently proposed for enabling the Spectrum Sharing between radar and communication systems, in Section 3.3. Attention was particularly focussed on techniques for implementing a communication channel exploiting, where possible, bandwidth, power and hardware already allocated for the primary radar system, allowing the latter to transmit data to other cooperative systems. Concepts were proposed based on the embedding of data into Frequency Modulated Continuous Waveforms (FMCWs) or Stepped Frequency Continuous Waveforms (SFCWs), or on the use of multi-carrier signals. These approaches were generally limited by either short unambiguous range or low data rate. Other techniques were based on the joint use of waveform diversity and beam pattern side lobe control. In Chapter 6 a novel waveform design framework based on the Fractional Fourier Transform (FrFT), described in Section 3.4, is presented, able of transmitting data with a bit rate in the range of Mb/s not limiting the unambiguous range and not needing antenna arrays.

Chapter 4

Image Moments Based SAR ATR

4.1 Introduction

In this Chapter, two image moments based Automatic Target Recognition (ATR) algorithms for Synthetic Aperture Radar (SAR) images are presented. The first one improves the approach presented in [11, 12] and recalled in Section 2.3.4.1 by including additional target features in order to increase the information content which leads to the final classification. Specifically, the Krogager decomposition, introduced in Section 2.3.2, is embedded in the framework to get these additional target features. The second proposed algorithm uses the same framework introduced in Section 2.3.4.1, while substituting the pseudo-Zernike (pZ) moments with the Krawtchouk moments.

4.2 Enhanced Pseudo-Zernike Based Algorithm

The algorithm presented in this Section is based on the use of both the full-polarimetric image of the target and its Krogager components, which emphasise the single bounce, the double bounce and the volumetric scattering. A block diagram of the proposed approach is illustrated in Figure 4.1. It is possible to recognise two branches of the pZ algorithm presented in Section 2.3.4.1, one applied on the polarimetric components of the SAR image, and another one applied on its Krogager components, $\boldsymbol{k}_s(x, y)$,

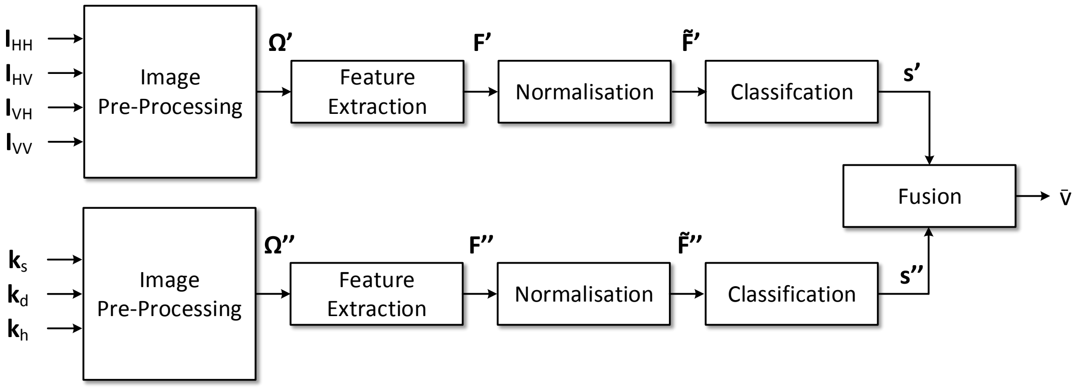

Figure 4.1: Block diagram of the Krogager pseudo-Zernike (Kr/pZ) based SAR ATR algorithm.

$\boldsymbol{k}_d\left(x,y\right)$ and $\boldsymbol{k}_h\left(x,y\right)$, which, according to equation (2.9), are computed as follows:

$$\begin{aligned}\boldsymbol{k}_s\left(x,y\right)&=\left|\boldsymbol{I}_{RL}\left(x,y\right)\right|\\\boldsymbol{k}_d\left(x,y\right)&=\min\left(\left|\boldsymbol{I}_{RR}\left(x,y\right)\right|,\left|\boldsymbol{I}_{LL}\left(x,y\right)\right|\right)\\\boldsymbol{k}_h\left(x,y\right)&=\left|\left|\boldsymbol{I}_{RR}\left(x,y\right)\right|-\left|\boldsymbol{I}_{LL}\left(x,y\right)\right|\right|\end{aligned}\tag{4.1}$$

with $\boldsymbol{I}_{RR}\left(x,y\right)$, $\boldsymbol{I}_{LL}\left(x,y\right)$ and $\boldsymbol{I}_{RL}\left(x,y\right)$ being the circular polarimetric components of the SAR image of the target, obtained from the linear polarimetric components $\boldsymbol{I}_{HH}\left(x,y\right)$, $\boldsymbol{I}_{VV}\left(x,y\right)$ and $\boldsymbol{I}_{HV}\left(x,y\right)$ in accordance to equation (2.2):

$$\begin{aligned}\boldsymbol{I}_{RR}\left(x,y\right)&=\frac{\boldsymbol{I}_{HH}\left(x,y\right)-\boldsymbol{I}_{VV}\left(x,y\right)}{2}+j\boldsymbol{I}_{HV}\left(x,y\right)\\\boldsymbol{I}_{LL}\left(x,y\right)&=\frac{\boldsymbol{I}_{HH}\left(x,y\right)-\boldsymbol{I}_{VV}\left(x,y\right)}{2}-j\boldsymbol{I}_{HV}\left(x,y\right)\\\boldsymbol{I}_{RL}\left(x,y\right)&=\frac{\boldsymbol{I}_{HH}\left(x,y\right)+\boldsymbol{I}_{VV}\left(x,y\right)}{2}\end{aligned}\tag{4.2}$$

The feature extraction blocks always compute the pZ moments of the input images $\boldsymbol{\Omega}'\in\mathbb{R}^{R_{\text{im}}\times C_{\text{im}}}$ and $\boldsymbol{\Omega}''\in\mathbb{R}^{R_{\text{im}}\times C_{\text{im}}}$. The first one is obtained as in (2.14) and (2.15), while similarly $\boldsymbol{\Omega}''$ is:

$$\boldsymbol{\Omega}''\left(x,y\right)=\frac{\tilde{\boldsymbol{\Omega}}''\left(x,y\right)-\min_{(x,y)}\tilde{\boldsymbol{\Omega}}''\left(x,y\right)}{\max_{(x,y)}\left[\tilde{\boldsymbol{\Omega}}''\left(x,y\right)-\min_{(x,y)}\tilde{\boldsymbol{\Omega}}''\left(x,y\right)\right]}\tag{4.3}$$

where

$$\tilde{\boldsymbol{\Omega}}''(x,y) = \log_{10}\left(\boldsymbol{k}_s(x,y) + \boldsymbol{k}_d(x,y) + \boldsymbol{k}_h(x,y)\right) \tag{4.4}$$

The feature vectors, $\boldsymbol{F}' \in \mathbb{R}^{(N_{\text{ord}}+1)^2}$ and $\boldsymbol{F}'' \in \mathbb{R}^{(N_{\text{ord}}+1)^2}$, are then normalised as in (2.17) and used to classify the target with two different k-NN classifiers. The fusion rule used for the overall classification is the one already presented in (2.18) and adapted to the proposed approach, that is:

$$\overline{v} = \begin{cases} \underset{v\in\{1,\ldots,L\}}{\arg\max}\left(\boldsymbol{s}' + \boldsymbol{s}''\right) & \text{if } \exists!\ \underset{v\in\{1,\ldots,L\}}{\max}\left(\boldsymbol{s}' + \boldsymbol{s}''\right) > \delta_{\text{fus}} \\ \textit{unknown} & \text{otherwise} \end{cases} \tag{4.5}$$

where $\boldsymbol{s}' = [s'_1, \ldots, s'_L] \in \mathbb{R}^L$ and $\boldsymbol{s}'' = [s''_1, \ldots, s''_L] \in \mathbb{R}^L$ are the score vectors obtained from the two branches of the framework. Note that, as for the pZ moments based algorithm, this framework can be easily extended to the availability of several images from multiple sensors by simply modifying the fusion rule to accommodate for score vectors coming from multiple branches.

4.2.1 Performance Evaluation

The proposed integrated Krogager pseudo-Zernike (Kr/pZ) algorithm is tested and compared with the original one [11, 12], based on the extraction of the features from only the polarimetric components of the SAR images. The analysis is performed by using the images of the GOTCHA dataset. Furthermore, several noise conditions are considered in order to demonstrate the robustness of the approach.

4.2.1.1 GOTCHA Dataset

The algorithm is tested using the GOTCHA dataset [132], which is a collection of real full-polarimetric circular SAR images acquired by an airborne X-band sensor (carrier frequency $9.6\,GHz$) with a $640\,MHz$ bandwidth at 8 different elevation angles; the set consists of 2880 full-polarimetric images, 360 for each pass, of several civilian vehicles and calibration targets. In particular, the 9 different civil vehicles used in this evaluation and shown in Figure 4.2, can be divided for recognition, identification

Table 4.1: GOTCHA Dataset.

Target	Description	Recognition	Identification	Characterisation
Nissan Sentra	Compact Car	R1	I1	C1
Chevy Prizm	Compact Car			C2
Chevy Malibu	Mid-Size Car		I2	C3
Toyota Camry	Mid-Size Car			C4
Ford Taurus	Full-Size Car		I3	C5
Nissan Maxima	Full-Size Car			C6
Hyundai Santa Fe	SUV		I4	C7
Case Tractor	Industrial Truck	R2	I5	C8
Fork Lift	Industrial Truck			C9

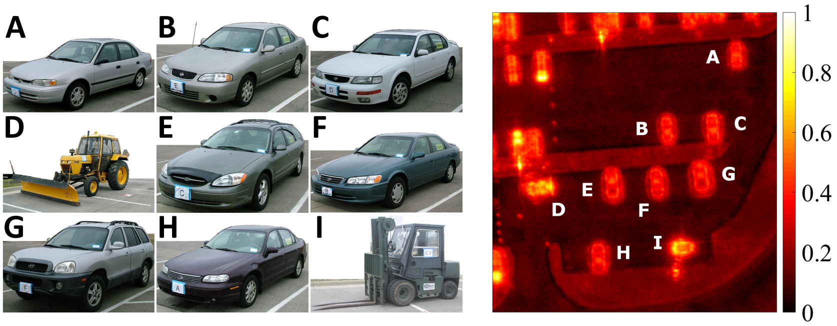

(a) Vehicles. (b) SAR image.

Figure 4.2: GOTCHA Dataset: (a) images of the vehicles used as targets; (b) full-azimuth and full-polarimetric magnitude SAR image of the area of interest containing the 9 vehicles.

and characterisation purposes, respectively, as shown in Table 4.1 The full synthetic aperture (360°) is split into 90 sub-apertures of 4° in azimuth each, in order to have approximately equal range-azimuth resolution cells of 23 cm; thus, the set used is made up of 720 full-polarimetric images for each of the 9 commercial vehicles considered as target. Moreover, equal-sized sub-images, with $R_{\text{im}} = 51$ and $C_{\text{im}} = 46$, containing each vehicle are selected.

Four different analyses are presented, as combination of two configurations for the training set and two configurations for the test set. The training set is formed by images coming from the lowest altitude pass; either 10 or 30 images for each vehicles are used to train the classifiers, selected each 36° or 12° in azimuth, respectively. The test set is formed by all but the images used for the training. Two configurations are considered: in the first scenario, shown in Figure 4.3(a), one image is used in order to classify the target, which is equivalent to having $T = 1$; in the other scenario, depicted in Figure 4.3(b), two images are used ($T = 2$) to show the benefits of the multi-sensor framework.

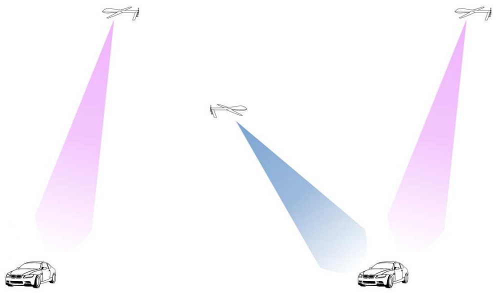

(a) One sensor case. (b) Two sensors case.

Figure 4.3: Test configurations: (a) one and (b) two sensors cases.

4.2.1.2 Noise Conditions

The images of the GOTCHA dataset are real SAR images affected by noise. However, in order to demonstrate the robustness of the approach, additional noise is also considered, both additive and multiplicative. In the first case, the noise is modelled as a compound-Gaussian random variable [133, 134], which can be written in the form:

$$\xi_c = \sqrt{\Gamma}\,\xi \tag{4.6}$$

where ξ is a complex symmetric zero-mean Gaussian variable and Γ is a Gamma variable, whose distribution is:

$$f_\Gamma\left(x\right) = \frac{1}{\Gamma\left(\nu_s\right)}\frac{1}{\mu_s^{\nu_s}}x^{\nu_s-1}e^{-x/\mu_s}, \quad x > 0 \tag{4.7}$$

where $\Gamma\left(\cdot\right)$ is the Gamma function, and μ_s and ν_s are the scale and shape parameters, respectively, set to $\nu_s = 1/\mu_s$ in order to have a Gamma distribution with unit mean; specifically, ν_s is chosen equal to 0.5. Equations (4.6) and (4.7) ensure that the amplitude probability density function of ξ_c is K-distributed. In the multiplicative noise case, instead, each pixel is multiplied with a square root of a Gamma random variable.

4.2.1.3 Results

The assessment of the performance is carried out by means of a Monte-Carlo simulations with 100 tests. The results are presented in terms of Characterisation and Identification accuracies[20], defined as the number of targets correctly classified normalized to the total number of targets under test and expressed as percentage. Moreover, the percentage of unknowns is also shown, defined as the ratio of the number of targets declared unknown following the rule in (4.5) to the total number of tests (the chosen thresholds δ_{fus} are summarised in Table 4.2). For the case of one sensor, all the available images are used for the testing, that is 710 images for each target if the training is performed with 10 images, 690 images for the 30 training images case. For the case of 2 sensors, 71000 or 69000 couples are chosen randomly, depending on the training configurations. Moreover, the analysis is performed for different values of the degree of the pZ polynomial, different SNRs and using a 3-NN classifier; this value of k resulted to be the most effective in [12].

Table 4.2: Fusion rule threshold δ_{fus}.

	1 Sensor	**2 Sensors**
pZ	$1/3$	$2/3$
Kr/pZ	$2/3$	$4/3$

Figure 4.4 shows the results in the noise-free case on varying the moments order. Cross markers refer to the characterisation accuracy, circles represent the identification accuracy, while straight lines are used to identify the percentage of unknowns. Figure 4.4(a) and Figure 4.4(b) compare the performance of the Kr/pZ algorithm (red solid lines) with the original approach (dashed blue lines), in the case of classification with one sensor and the use of either 10 or 30 training images, respectively. No differences can be appreciated between characterisation and identification, while improvements are seen between the two approaches, pZ and Kr/pZ, both when the training is performed with 10 images per target, and when it is carried out with 30 images. Focussing on the moments orders equal or above 8 and up to 23, these improvements can

---

[20] Recognition accuracy is not taken into consideration, since it involves only two classes: car and industrial truck.

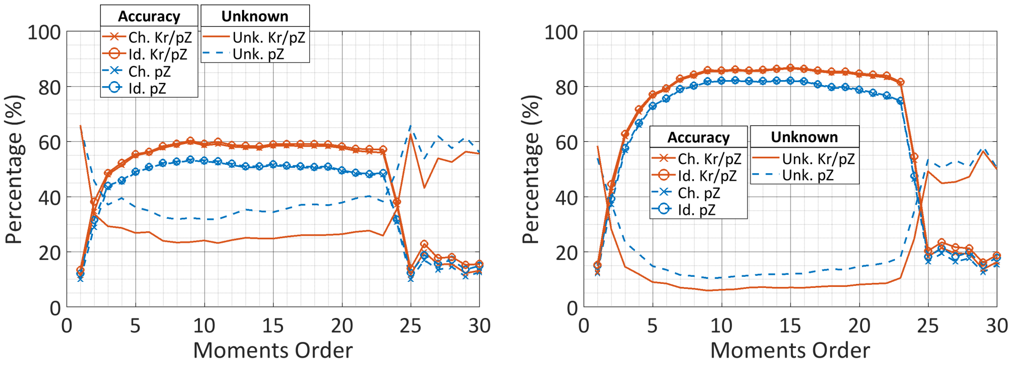

(a) One sensor, 10 training images. (b) One sensor, 30 training images.

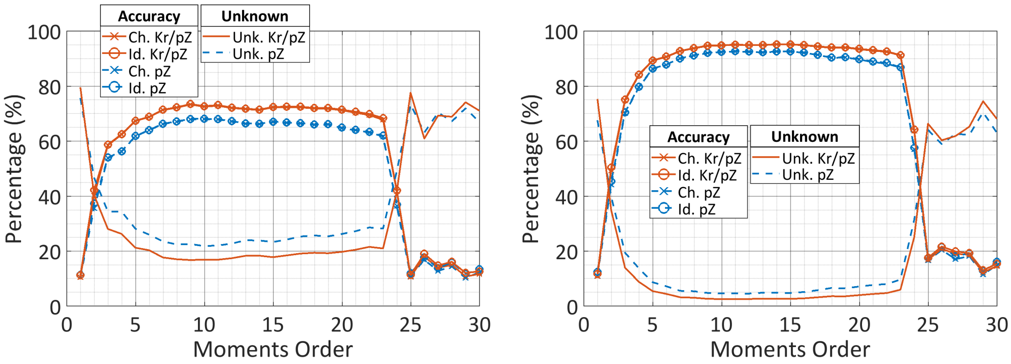

(c) Two sensors, 10 training images. (d) Two sensors, 30 training images.

Figure 4.4: Comparative analysis between Krogager pseudo-Zernike (Kr/pZ) and pseudo-Zernike (pZ) only approaches, noise-free case. Results in terms of characterisation (Ch.) and identification (Id.) accuracy, and percentage of unknowns (Unk.), on varying the number of training images (left-right), the number of sensors (top-bottom) and the moments order.

be quantified in terms of characterisation accuracy in $7.26\,\%$ and $4.51\,\%$, when 10 and 30 images are used for the training, respectively, and in $10\,\%$ and $5.22\,\%$ in terms of percentage of unknowns. The maximum achieved accuracy is $60\,\%$ in the first case, and $87\,\%$ in the second case for the integrated Kr/pZ method, compared to $53.5\,\%$ and $82.3\,\%$ for the pZ algorithm.

Overall better performance is obtained when the classification is performed by using images acquired from two sensors, as shown in Figure 4.4(c) and Figure 4.4(d). Improvements due to the integrated Kr/pZ approach over the original algorithm are also visible in this case: the improvement is of approximately $5.43\,\%$ in terms of characterisation accuracy and $5.73\,\%$ in terms of percentage of unknowns, when 10 images are used for the training, and of $2.90\,\%$ and $2.40\,\%$ for accuracy and unknowns, respectively, when the classifiers are trained with 30 images per target. In this scenario, the maximum accuracy is 73.5 % and 68 % for Kr/pZ and pZ, respectively, when the training is performed with 10 images, while it is 95.2 % and 92.6 %, respectively, when 30 images are used.

Interesting is that for moments orders larger than 23, both the pZ and the Kr/pZ algorithms fail in correctly classifying the targets, with the percentage of accuracy that drops below 20 % independently of both the number of sensors and the number of training images. This is caused by the numerical instability at the edge of the unit circle and the numerical approximation that is applied when computing the pZ polynomials, effects that are more evident as the order increases. Figure 4.5 shows the magnitude of some pZ polynomials computed on either a grid of 688 × 688 pixels, top row, or a grid of 69 × 69 pixels, bottom row, also used during the tests. All the high resolution

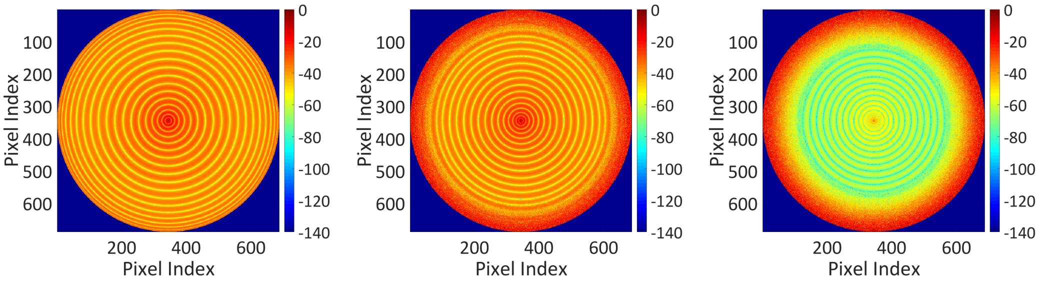

(a) High res., $W_{20,0}(\rho,\theta)$. (b) High res., $W_{23,0}(\rho,\theta)$. (c) High res., $W_{25,0}(\rho,\theta)$.

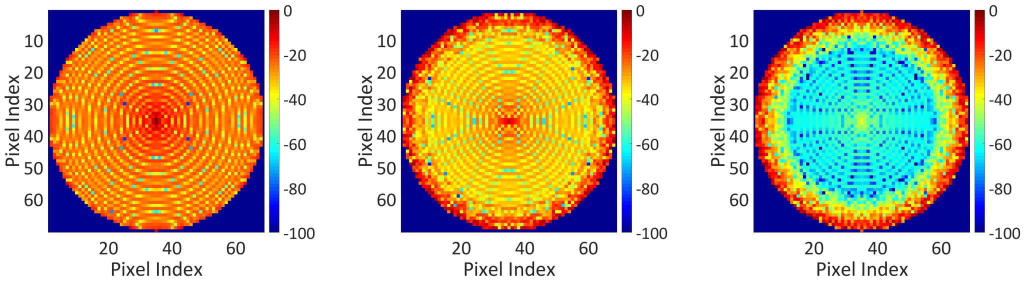

(d) Low res., $W_{20,0}(\rho,\theta)$. (e) Low res., $W_{23,0}(\rho,\theta)$. (f) Low res., $W_{25,0}(\rho,\theta)$.

Figure 4.5: Magnitude of the pseudo-Zernike polynomials (left) $W_{20,0}(\rho,\theta)$, (middle) $W_{23,0}(\rho,\theta)$ and (right) $W_{25,0}(\rho,\theta)$, on a grid of either (top) 688 × 688 or (bottom) 69 × 69 pixels.

polynomials $W_{20,0}(\rho,\theta)$, $W_{23,0}(\rho,\theta)$ and $W_{25,0}(\rho,\theta)$ depicted in Figure 4.5(a), Figure 4.5(b) and Figure 4.5(c), respectively, present a particular pattern with concentric circles, which increase in the number as the degree raises. Moreover, especially for the polynomial of degree 25, undesired edge effects also appear. Comparing the high resolution polynomials with the low resolution ones, the pattern of concentric circles can be still distinguished for $W_{20,0}\left(\rho,\theta\right)$ and $W_{23,0}\left(\rho,\theta\right)$, in Figure 4.5(d) and Figure 4.5(e), while it does disappear for $W_{25,0}\left(\rho,\theta\right)$ in Figure 4.5(f). This behaviour makes the high degrees polynomials unable to extract distinctive features from the different targets, which are then misclassified. For this reason, in the following only polynomials up to the degree 20 are considered.

Results similar to the noise-free case are obtained when compound-Gaussian noise is added to the images, as observed from Figure 4.6, where characterisation accuracy, identification accuracy and percentage of unknowns are shown on varying the SNR, namely the variance of the complex Gaussian variable in (4.6), and fixing the moments order to 10. The accuracy increases as the SNR increases, while the percentage of unknown decreases. As expected, better performance is obtained when using

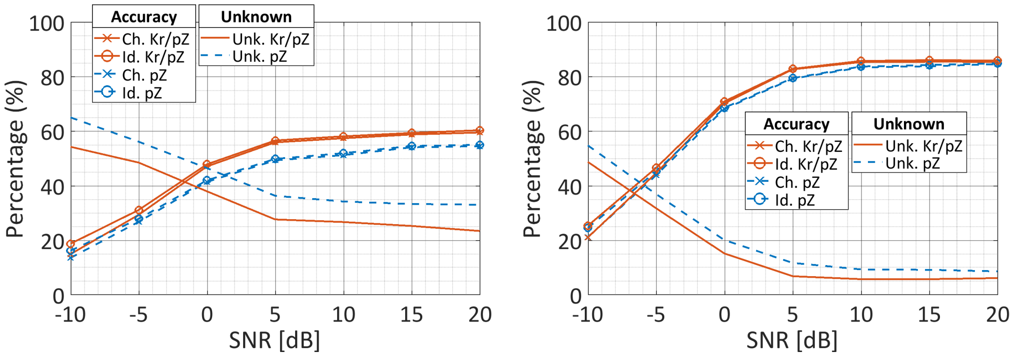

(a) One sensor, 10 training images. (b) One sensor, 30 training images.

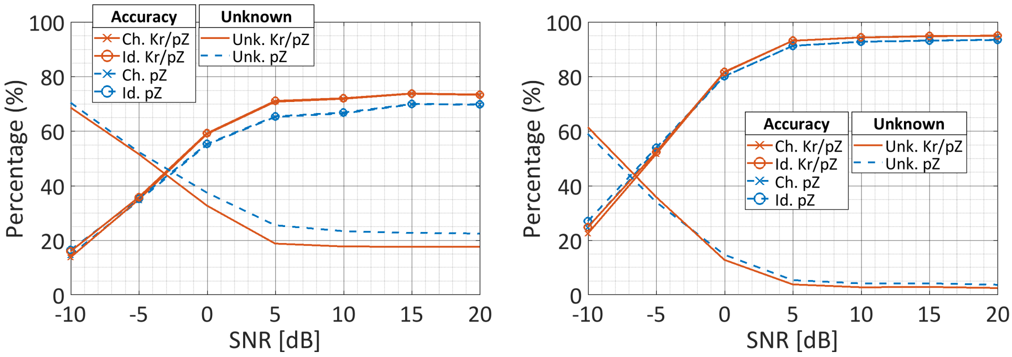

(c) Two sensors, 10 training images. (d) One sensor, 30 training images.

Figure 4.6: Comparative analysis between Krogager pseudo-Zernike (Kr/pZ) and pseudo-Zernike (pZ) only approaches, additive compound-Gaussian noise case. Results in terms of characterisation (Ch.) and identification (Id.) accuracy, and percentage of unknowns (Unk.), on varying the number of training images (left-right), the number of sensors (top-bottom) and the SNR while fixing the moments order to 10.

more images for training the classifiers, as shown in Figure 4.6(b) and Figure 4.6(d), however larger improvements of the integrated Kr/pZ algorithm over the pZ moments based approach are visible when the training is performed with 10 images, as depicted in Figure 4.6(a) and Figure 4.6(c), confirming the effectiveness of the proposed algorithm especially when fewer images are available for training, as already demonstrated in the noise-free scenario. In the most likely scenario, that is when 10 images per target are available for training and the classification is performed with only one sensor, for SNR above $0\,dB$ the average improvement is of about $5.63\,\%$ in terms of accuracy and $8.48\,\%$ in terms of percentage of unknowns.

The last analysis evaluates the effect of multiplicative noise. Performance on varying the moments order is shown in Figure 4.7. In agreement with the results obtained in

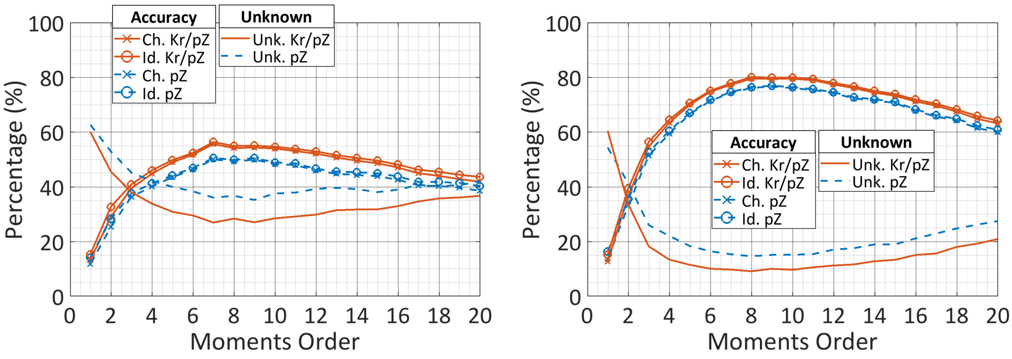

(a) One sensor, 10 training images.
(b) One sensor, 30 training images.

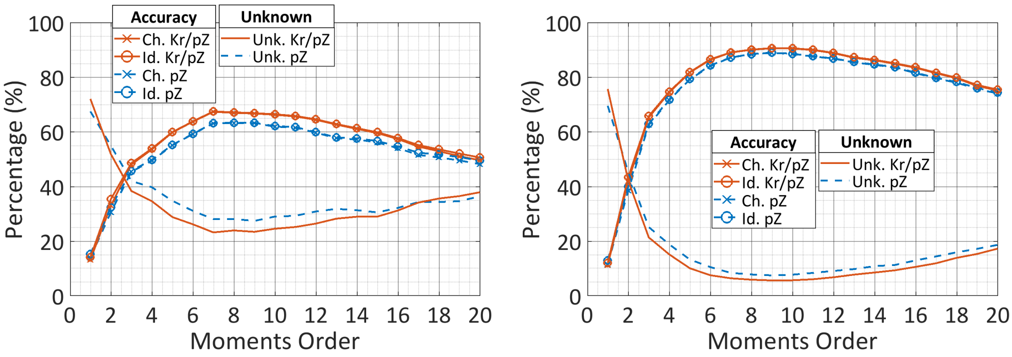

(c) Two sensors, 10 training images.
(d) Two sensors, 30 training images.

Figure 4.7: Comparative analysis between Krogager pseudo-Zernike (Kr/pZ) and pseudo-Zernike (pZ) only approaches, multiplicative noise case. Results in terms of characterisation (Ch.) and identification (Id.) accuracy, and percentage of unknowns (Unk.), on varying the number of training images (left-right), the number of sensors (top-bottom) and the moments order.

the previous analyses, higher accuracy and lower percentage of unknowns are achieved when 30 images are used for the training and the classification is performed by using images acquired by two sensors. However, in all the analysed cases, the proposed combined Kr/pZ approach outperforms the original algorithm. Finally, it is worth highlighting that both the approaches are very sensitive to the multiplicative noise in particular when the moments order is high. It is clear that the optimum value of the order for this scenario is between 7 and 10.

Hence, the proposed approach presents better performance for all the configurations in which it has been tested. In particular the best improvements are achieved in the case in which 10 images for the training are used; this means that in order to reach the same performance, the Kr/pZ approach requires less a priori information compared to the pZ algorithm, which implies less cost, since the acquisition of a targets database is often expensive and time consuming. In addition to the general increase of accuracy, the decrease of the percentage of unknowns makes the Kr/pZ approach even more reliable than the pZ method. Moreover, the pZ moments properties of translation and rotation independence, combined with the roll invariant characteristic of the Krogager decomposition, makes the algorithm robust with respect to both the target orientation in the image plane and the acquisition elevation angle. Note that these improvements are obtained only at cost of a small computational increase, since no additional information is required as input of the algorithm with respect to the pZ only approach.

4.3 Krawtchouk Moments Based Algorithm

The second feature-based ATR technique presented in this Chapter, uses the same framework presented in Section 2.3.4.1 and reported in Figure 4.8, where the feature extraction is achieved by means of the Krawtchouk polynomials. First the analytical

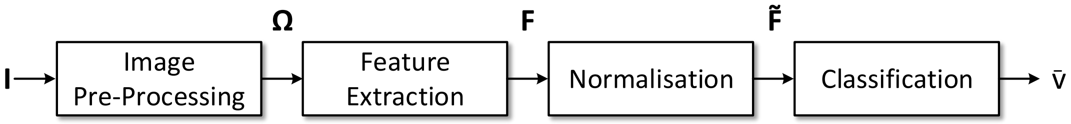

Figure 4.8: Block diagram of the Krawtchouk based SAR ATR algorithm.

formulation of the Krawtchouk polynomials is provided, then performance is evaluated and compared with the pZ based approach.

4.3.1 Krawtchouk Moments

The Krawtchouk polynomials are a set of polynomials associated with the binomial distribution first introduced in [135]. The classical Krawtchouk polynomial of degree $n \in \mathbb{N}_0$, $n \leq I$, is defined as [136]:

$$K_n\left(x;p,I\right) = {}_2F_1\left(-n,-x;-I;\frac{1}{p}\right) \tag{4.8}$$

where $x \in \mathbb{N}_0$, $x \leq I$, $I \in \mathbb{N}$ is its support, $\mathbb{N}$ the set of natural numbers, $p \in (0,1)$, and ${}_2F_1$ the Gauss hypergeometric function, defined as:

$${}_2F_1\left(a,b;c;z\right) = \sum_{k=0}^{\infty} \frac{\left(a\right)_k\left(b\right)_k}{\left(c\right)_k}\frac{z^k}{k!} \tag{4.9}$$

where $\left(\cdot\right)_k$ is the Pochhammer symbol given by:

$$\left(a\right)_k = a\left(a+1\right)\ldots\left(a+k-1\right) = \frac{\Gamma\left(a+k\right)}{\Gamma\left(a\right)} \tag{4.10}$$

The classical formulation of Krawtchouk polynomials suffers from numerical instability, since the range of values of the polynomials expands rapidly as the degree increases. In order to overcome this problem, weighted Krawtchouk polynomials were introduced in [136], defined as:

$$\tilde{K}_n\left(x;p,I\right) = K_n\left(x;p,I\right)\sqrt{\frac{w'\left(x;p,I\right)}{w''\left(n;p,I\right)}} \tag{4.11}$$

where

$$w'\left(x;p,I\right) = \binom{I}{x}p^x\left(1-p\right)^{I-x} \tag{4.12}$$

$$w''\left(n;p,I\right) = \left(-1\right)^n\left(\frac{1-p}{p}\right)^n\frac{n!}{\left(-I\right)_n} \tag{4.13}$$

The polynomials defined in (4.11) are orthogonal, since:

$$\sum_{x=0}^{N} \tilde{K}_n\left(x;p,I\right)\tilde{K}_m\left(x;p,I\right) = \delta_{n,m}, \quad \forall p, I \tag{4.14}$$

Furthermore, the parameter p represents a shift parameter. Indeed, as p deviates from the value 0.50 by Δp, the weighted Krawtchouk polynomials are approximately shifted by $I\Delta p$ [136]. Figure 4.9 is an illustration of the weighted Krawtchouk polynomials of degree (a) $n = 0$ and (b) $n = 2$ for $I = 100$, which also shows the effect of the shift parameter p, equal to 0.25 and 0.75.

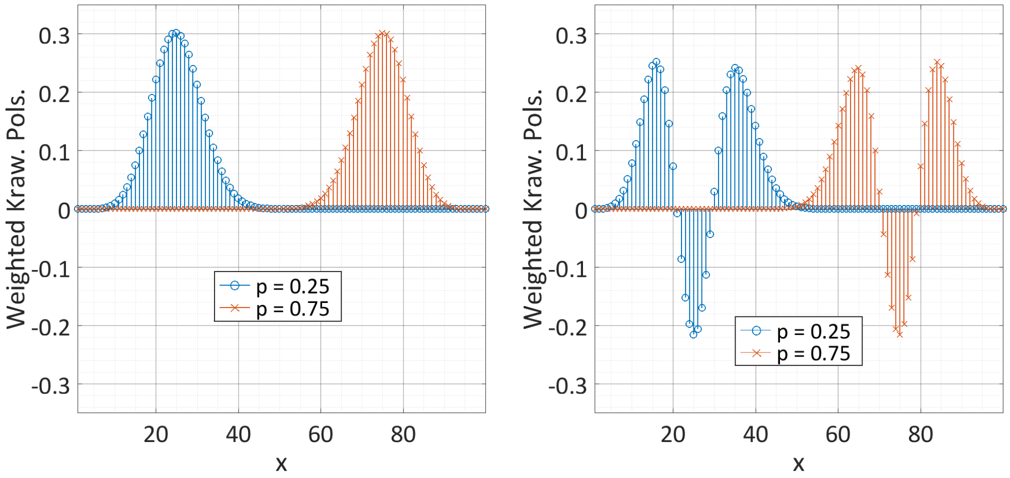

(a) Degree $n = 0$.

(b) Degree $n = 2$.

Figure 4.9: Illustration of the weighted Krawtchouk polynomials of degree (a) $n = 0$ and (b) $n = 2$, for $I = 100$ and $p = 0.25, 0.75$, in blue and red, respectively.

The Krawtchouk moments are defined as any other image moments as weighted averages of the image pixels' intensity. Therefore, let $f\left(x,y\right) \in \mathbb{R}$, $f\left(x,y\right) \geq 0$, be an image with $R_{\text{im}} \times C_{\text{im}}$ pixels; the Krawtchouk moment of order (n,m) is defined as:

$$k_{n,m} = \sum_{x=0}^{R_{\text{im}}-1}\sum_{y=0}^{C_{\text{im}}-1} \tilde{K}_n\left(y;p_1,R_{\text{im}}-1\right)\tilde{K}_m\left(x;p_2,C_{\text{im}}-1\right) f\left(x,y\right) \tag{4.15}$$

The moments in (4.15) provide a powerful tool for representing 2D functions with a limited set of values and have been previously used for image compression [46]. Furthermore, thanks to the orthogonality of the polynomials and to the capability to focus on a specific area within an image by means of the parameter p, Krawtchouk moments are also widely used in image processing for pattern recognition [137, 138, 139]. Therefore, the proposed ATR algorithm is based on the computation of the Krawtchouk moments on the intensity SAR image of the target. The moments form the feature vector $\boldsymbol{F} \in \mathbb{R}^{(N_{\text{ord}}+1)\times(M_{\text{ord}}+1)}$, where N_{ord} and M_{ord} are the maximum degree of the two Krawtchouk polynomials in (4.15); this feature vector, after normalisation, is used to perform the classification.

4.3.2 Performance Evaluation

The proposed algorithm is tested on the MSTAR dataset, a collection of SAR images of military targets. In the next Sections, first the dataset is described, then performance is evaluated in different noise conditions.

4.3.2.1 MSTAR Dataset

The MSTAR dataset is a collection of circular SAR images of 14 different military targets [30, 31], some of which are the same target in different configurations, such as the BMP2 and the T72. The images, with a resolution of $30\,cm \times 30\,cm$, were acquired with an X-band SAR system with two different depression angles, $15°$ and $17°$, and they were supposed to cover the full $360°$ azimuth angle. However, due to missing images in the dataset, the total number of observations does not always cover each aspect angle. In addition, different targets have different number of images. Table 4.3 summarises the number of available images for each target and each depression angle, together with the division in groups based of the definition of recognition, identification and characterisation given in Section 2.2.

4.3.2.2 Results

In the performance analysis 191 samples are used as the minimal number of images available for all the targets. The training images are selected randomly from the ones acquired with $15°$ of depression angle. Furthermore, in order to investigate the robustness of the algorithm for different training sets, the selection of the images used for testing and those used for training is randomized in each run. Specifically, a total of

Table 4.3: MSTAR Dataset.

Target	**Type**	**# of Images** $15^\circ - 17^\circ$	**Rec.**	**Ident.**	**Charac.**
BMP2 9563	Tank	195 - 233	R1	I1	C1
BMP2 9566	Tank	196 - 232			C2
BMP2 C21	Tank	196 - 233			C3
T72 132	Tank	196 - 232		I2	C4
T72 812	Tank	195 - 231			C5
T72 S7	Tank	191 - 228			C6
2S1	Tank	276 - 299		I3	C7
T62	Tank	273 - 299		I4	C8
ZSU	Tank	274 - 299		I5	C9
BTR70 C71	Personnel Carrier	196 - 233	R2	I6	C10
BTR60	Personnel Carrier	195 - 256		I7	C11
ZIL131	Truck	274 - 299	R3	I8	C12
BRDM	Reconn. Vehicle	274 - 298	R4	I9	C13
D7	Bulldozer	274 - 299	R5	I10	C14

100 Monte-Carlo runs are performed for each analysis in order to be able to randomly draw a wider set of training and test images for the targets with more than 191 images available. The results of the Krawtchouk moments based algorithm (blue solid lines) are compared to those obtained using the pZ moments [11, 12] presented in Section 2.3.4.1 (red dashed lines). In the experiments a 3-NN classifier and $p_1 = p_2 = 0.5$ for the computation of the Krawtchouk polynomials have been used.

Figure 4.10 shows the results of the noise-free analysis. Performance in terms of characterisation, identification and recognition accuracy, as well as percentage of unknowns, are shown on varying the moments order. The Krawtchouk moments based algorithm achieves the best performance for the highest order, that is $N_{\text{ord}} = M_{\text{ord}} = 20$. Specifically, the accuracy is $81.1\,\%$, $88\,\%$ and $90\,\%$ for characterisation, identification and recognition, respectively. The improvement over the pZ moments based approach is of approximately $6\,\%$, $5.40\,\%$ and $4.45\,\%$ for the three levels of classification; moreover, the maximum accuracy for the pZ moments algorithm does not occur always for the same order, which highlights a higher sensitivity to the choice of the moments or-

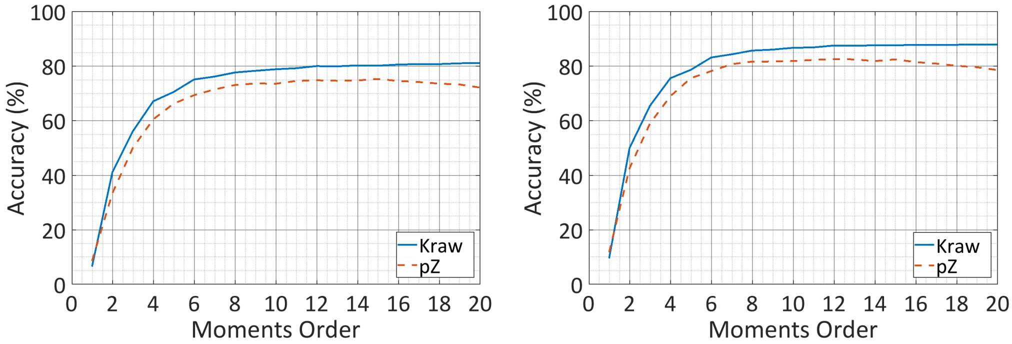

(a) Characterisation. (b) Identification.

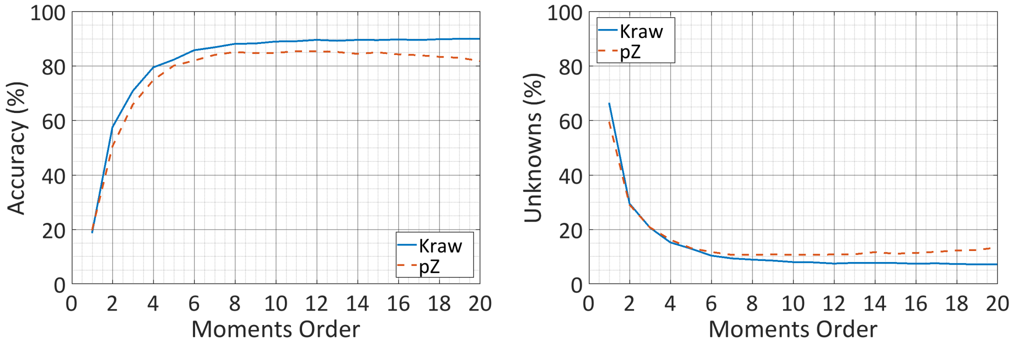

(c) Recognition. (d) Unknowns.

Figure 4.10: Comparative analysis between Krawtchouk (Kraw) and pseudo-Zernike (pZ) moments based approaches, noise-free case. Results in terms of (a) characterisation, (b) identification and (c) recognition accuracy, and (d) percentage of unknowns, on varying the moments order.

der. The Krawtchouk moments approach outperforms the pZ moments algorithm also in terms of unknowns, with a reduction in the percentage of about $3.5\,\%$.

Stress analyses are also conducted under different noise conditions. In the first one, additive compound-Gaussian noise, already introduced in Section 4.2.1.2, is generated and added to the intensity SAR images. The results are reported in Figure 4.11, in terms of accuracies and percentage of unknowns, on varying the SNR, the parameter ν_s of the Gamma distributed random variable in (4.7), and fixing the moments order to 10. No appreciable difference can be observed when changing the parameters ν_s from 0.5 (impulsive noise) to 10. The Krawtchouk moments based algorithm outperforms the pZ approach with respect to all the figures of merit considered. For example, at $0\,d$B the accuracies are $73.8\,\%$, $82\,\%$ and $84.8\,\%$ in terms of characterisation, identification and recognition, while the percentage of unknowns is $11.8\,\%$, with improvements of approximately $17.5\,\%$, $17.4\,\%$, $15\,\%$ and $10.3\,\%$, respectively, with respect to the pZ

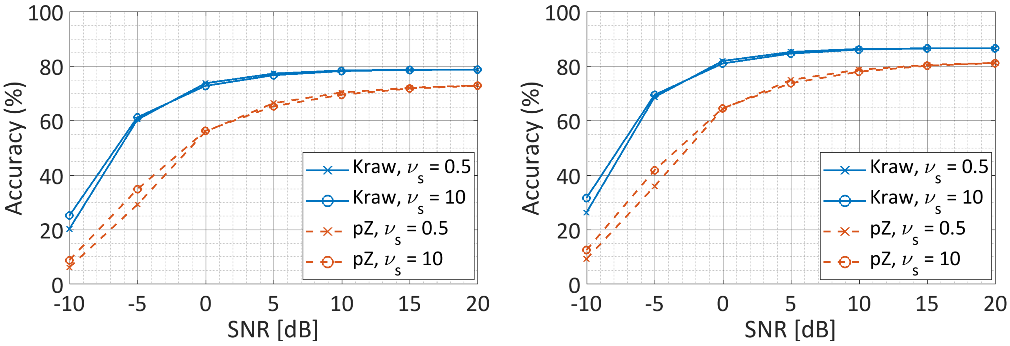

(a) Characterisation. (b) Identification.

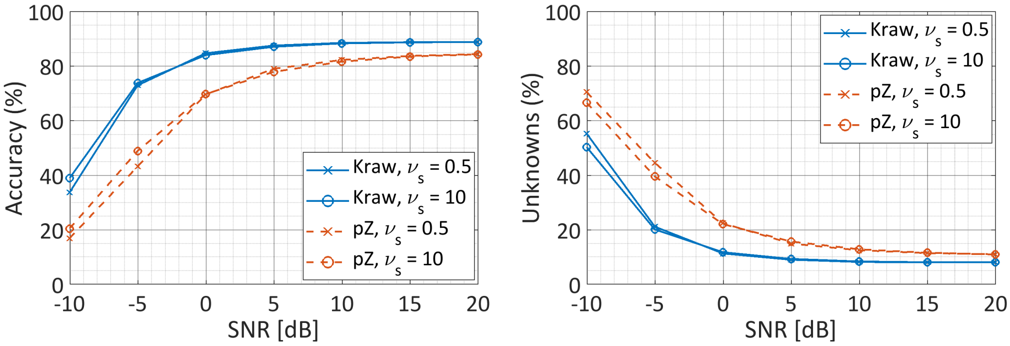

(c) Recognition. (d) Unknowns.

Figure 4.11: Comparative analysis between Krawtchouk (Kraw) and pseudo-Zernike (pZ) moments based approaches, additive compound-Gaussian noise case. Results in terms of (a) characterisation, (b) identification and (c) recognition accuracy, and (d) percentage of unknowns, on varying the SNR and for two values of ν_s, while fixing the moments order to 10.

algorithm. Another figure of merit for the overall performance of ATR algorithms introduced in [1] and referred as $\Upsilon \in [0, \infty)$ throughout this Thesis, considers the ratio of the sum of the values along the diagonal of the confusion matrix, to the sum of the off-diagonal values. With reference to Table 4.4 and Table 4.5, that report the confusion matrices for the Krawtchouk and the pZ moments based approach, respectively, in terms of characterisation accuracy when $SNR = 0\,d$B and $\nu_s = 0.5$, the figure of merit Υ is equal to $\Upsilon_{\text{Kraw}} = 4.70$ and $\Upsilon_{\text{pZ}} = 2.52$, confirming the superiority of the Krawtchouk moments based algorithm. The 3×3 sub-matrices highlighted in grey, refer to the variants of the targets BMP2 and T72 as listed in Table 4.3, with values reported in red and blue, respectively. Both these sub-matrices exhibit a more *diagonal* behaviour in the Krawtchouk case than in the pZ one, and this is confirmed by Υ that, computed for the Krawtchouk moments based approach is equal to $\Upsilon_{\text{Kraw}}^{\text{BMP2}} = 1.71$ and

Table 4.4: Confusion matrix showing the characterisation accuracy (%) using the Krawtchouk moments based approach. Additive compound-Gaussian noise case, $SNR = 0\,d\text{B}$, $\nu_s = 0.5$.

	C1	**C2**	**C3**	**C4**	**C5**	**C6**	**C7**	**C8**	**C9**	**C10**	**C11**	**C12**	**C13**	**C14**
C1	59.8	9.3	15.8	0.1	0.6	0.2	0.9	0.1	0.0	0.1	0.0	0.0	0.1	0.9
C2	19.7	53.7	8.4	0.1	0.6	0.6	0.2	0.2	0.4	1.2	0.2	0.0	0.1	0.0
C3	25.9	11.9	41.7	0.5	0.5	0.1	0.5	0.1	0.1	0.4	0.0	0.1	0.1	0.0
C4	0.3	0.2	0.7	80.3	3.0	4.0	0.0	0.2	1.3	0.0	0.0	0.4	0.0	0.0
C5	0.2	0.3	0.6	2.6	71.2	11.1	0.0	0.6	1.1	0.1	0.0	0.1	0.0	0.0
C6	0.1	0.9	0.5	6.9	11.1	64.5	0.0	0.2	0.7	0.1	0.1	0.7	0.0	0.0
C7	0.6	1.5	1.2	0.1	0.3	0.1	81.1	0.1	0.1	2.8	0.4	0.5	0.3	0.4
C8	1.2	0.7	1.5	1.9	1.3	1.4	1.9	67.8	1.6	0.4	0.2	0.4	0.6	0.2
C9	0.2	0.3	0.4	1.1	0.0	0.1	0.3	1.8	85.7	0.4	0.1	0.0	0.1	1.0
C10	0.1	0.2	0.4	0.0	0.3	0.0	0.3	0.0	0.0	90.5	2.1	0.5	0.7	0.0
C11	0.3	0.2	0.7	0.1	0.0	1.0	0.1	0.2	0.9	2.8	84.7	0.3	0.9	0.2
C12	1.5	0.5	0.7	0.5	0.3	0.9	4.3	0.4	0.2	1.8	0.2	73.7	2.5	0.1
C13	0.8	1.1	0.8	0.5	0.4	0.8	2.2	1.0	1.9	2.6	0.7	0.6	72.4	0.7
C14	0.2	0.3	0.4	0.0	0.0	0.0	0.1	0.1	0.2	0.0	0.3	0.0	0.5	95.6

Table 4.5: Confusion matrix showing the characterisation accuracy (%) using the pZ moments based approach. Additive compound-Gaussian noise case, $SNR = 0\,d\text{B}$, $\nu_s = 0.5$.

	C1	**C2**	**C3**	**C4**	**C5**	**C6**	**C7**	**C8**	**C9**	**C10**	**C11**	**C12**	**C13**	**C14**
C1	40.2	10.0	16.7	0.8	0.3	0.9	1.3	0.3	0.1	1.5	0.2	0.7	0.8	0.2
C2	17.6	33.0	12.5	0.9	0.7	1.5	0.8	0.2	0.1	1.8	0.3	0.4	0.5	0.0
C3	21.1	12.1	29.9	0.4	0.3	1.3	1.1	0.4	0.1	1.2	0.3	0.3	0.7	0.2
C4	1.3	1.2	1.4	57.4	3.4	6.9	0.2	1.3	0.7	0.2	0.6	1.1	0.3	0.4
C5	1.2	1.1	0.8	4.2	46.4	14.7	0.5	1.0	0.8	0.4	0.6	0.7	0.1	0.4
C6	0.7	1.6	1.0	6.2	6.6	51.8	0.2	0.5	0.7	0.8	0.4	1.3	0.2	0.8
C7	0.9	3.9	1.6	0.3	0.7	0.9	53.5	0.7	2.2	8.3	0.1	3.3	0.2	0.8
C8	2.6	1.7	4.7	2.4	1.2	2.1	2.6	38.7	1.5	1.5	1.0	0.8	1.2	1.4
C9	0.3	0.2	0.5	0.8	0.1	0.4	0.4	4.9	72.1	0.0	0.2	0.1	0.4	5.7
C10	1.4	1.2	1.3	0.1	0.0	0.0	0.9	0.2	0.0	81.5	0.7	0.5	1.4	0.0
C11	0.6	1.0	1.0	0.6	0.1	0.9	0.4	0.6	0.5	6.9	70.0	0.5	1.4	0.4
C12	0.7	1.1	1.6	1.5	0.9	0.7	4.4	1.5	0.1	5.1	2.2	56.0	0.9	0.4
C13	0.8	1.5	0.5	0.4	0.2	0.5	2.1	1.1	0.7	3.3	2.3	0.6	68.2	1.4
C14	0.8	0.1	0.8	0.4	0.1	1.4	0.6	1.2	3.9	0.0	0.1	0.1	0.3	76.3

$\Upsilon^{\text{T72}}_{\text{Kraw}} = 5.59$, while for pZ results in $\Upsilon^{\text{BMP2}}_{\text{pZ}} = 1.15$ and $\Upsilon^{\text{T72}}_{\text{pZ}} = 3.71$.

In the last analysis, multiplicative noise is considered, modelled as a square root Gamma random variable. Figure 4.12 shows the effect on the performance of the multiplicative noise with two values of the parameters ν_s, on varying the moments order and in terms of accuracies and percentage of unknowns. Unlike the additive compound-Gaussian noise, in this case the parameters ν_s highly affects the results, with the impulsive noise, $\nu_s = 0.5$, that degrades more the accuracy and the percentage of unknowns than $\nu_s = 10$. However, as already observed in the previous analyses,

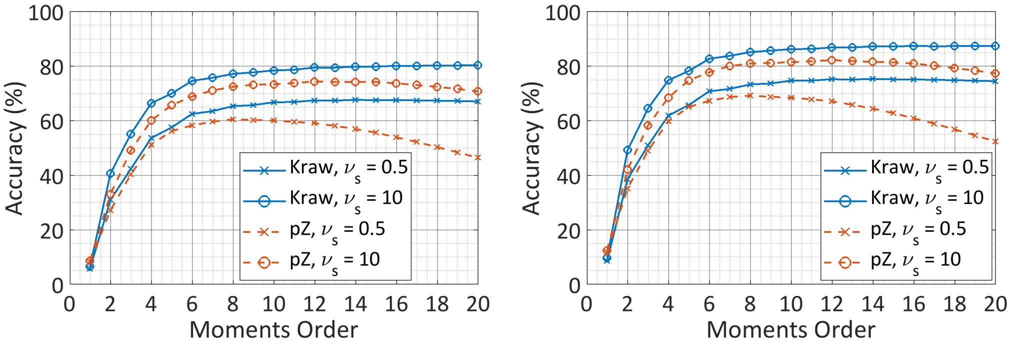

(a) Characterisation. (b) Identification.

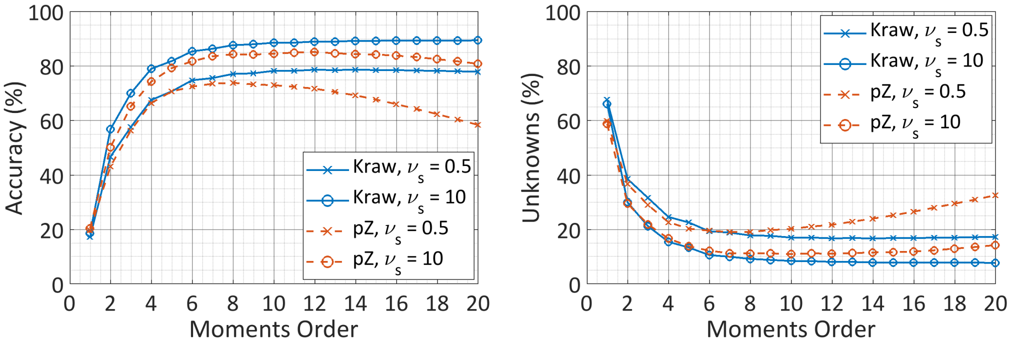

(c) Recognition. (d) Unknowns.

Figure 4.12: Comparative analysis between Krawtchouk (Kraw) and pseudo-Zernike (pZ) moments based approaches, multiplicative noise case. Results in terms of (a) characterisation, (b) identification and (c) recognition accuracy, and (d) percentage of unknowns, on varying the moments order and for two values of ν_s.

the Krawtchouk moments based algorithm always outperforms the pZ approach. In the worst case, that is for $\nu_s = 0.5$, the maximum accuracy for the Krawtchouk method is reached for moments order equal to 20, and it is equal to $67\,\%$, $74.5\,\%$ and $78\,\%$, for characterisation, identification and recognition, respectively. Assuming the same noise condition, the pZ algorithm achieves the best performance for moments order 8, and it is equal to $60.5\,\%$, $69.2\,\%$ and $73.9\,\%$, with improvements of $6.5\,\%$, $5.3\,\%$ and $4.1\,\%$, respectively. When the noise is less severe, that is for $\nu_s = 10$, the pZ moments based algorithm achieves its best performance for moments order 12. Comparing the two methods while fixing this moments order, the Krawtchouk moments approach outperforms the pZ one of approximately $5.1\,\%$, $4.7\,\%$ and $3.8\,\%$, for characterisation, identification and recognition, respectively. The reduction in performance of the pZ algorithm when the moments order is above 12, compared to the continuous increment of the accuracies for the Krawtchouk approach, shows the higher robustness

Table 4.6: Confusion matrix showing the characterisation accuracy (%) using the Krawtchouk moments based approach. Multiplicative noise case, order 8, $\nu_s = 0.5$.

	C1	**C2**	**C3**	**C4**	**C5**	**C6**	**C7**	**C8**	**C9**	**C10**	**C11**	**C12**	**C13**	**C14**
C1	46.8	10.0	15.3	0.6	0.8	0.4	0.8	0.3	0.3	0.1	0.3	0.1	0.3	0.8
C2	15.6	46.4	10.7	0.5	0.4	1.1	0.5	0.3	0.6	0.4	0.1	0.1	0.2	0.1
C3	20.0	13.0	34.7	0.5	0.4	0.2	0.9	0.8	0.3	0.3	0.1	0.3	0.4	0.5
C4	0.4	0.6	0.8	66.9	3.6	5.3	0.1	0.7	2.3	0.0	0.2	0.9	0.0	0.1
C5	0.3	0.6	0.8	3.1	60.9	12.5	0.1	0.9	1.8	0.1	0.1	0.4	0.0	0.0
C6	0.4	1.2	0.5	6.7	10.5	54.4	0.1	0.3	1.5	0.3	0.1	1.1	0.2	0.1
C7	0.8	1.5	1.3	0.1	0.3	0.3	73.9	0.6	0.3	3.1	0.3	0.9	0.2	0.8
C8	1.0	0.8	1.5	2.0	1.9	1.7	2.0	56.3	4.1	0.2	0.6	0.8	0.8	0.9
C9	0.3	0.3	0.5	0.7	0.0	0.2	0.4	1.8	82.9	0.1	0.2	0.0	0.2	2.1
C10	0.6	0.3	0.3	0.1	0.6	0.1	1.8	0.2	0.1	81.2	2.4	0.6	1.0	0.0
C11	0.5	0.4	0.4	0.3	0.1	0.7	0.4	0.7	1.1	3.1	76.8	0.5	0.7	1.0
C12	1.0	0.7	0.8	0.7	0.6	1.0	5.2	1.0	0.3	1.5	0.5	65.1	1.3	0.7
C13	1.5	1.1	0.9	0.3	0.1	0.9	3.0	1.2	2.8	2.0	1.5	0.4	61.7	0.7
C14	0.2	0.1	0.5	0.1	0.0	0.1	0.1	0.1	0.9	0.0	0.1	0.1	0.3	93.9

Table 4.7: Confusion matrix showing the characterisation accuracy (%) using the pZ moments based approach. Multiplicative noise case, order 8, $\nu_s = 0.5$.

	C1	**C2**	**C3**	**C4**	**C5**	**C6**	**C7**	**C8**	**C9**	**C10**	**C11**	**C12**	**C13**	**C14**
C1	38.0	11.6	16.9	1.1	0.2	1.0	1.3	0.5	0.1	1.4	0.4	0.4	0.9	0.7
C2	15.0	36.7	14.3	0.8	0.9	2.1	0.6	0.4	0.3	1.5	0.4	0.4	0.3	0.0
C3	18.9	13.2	31.9	0.8	0.3	1.3	1.1	0.2	0.1	0.8	0.6	0.5	0.4	0.7
C4	1.0	0.6	1.1	58.6	4.1	8.5	0.2	1.2	0.7	0.1	0.5	0.9	0.1	0.5
C5	0.3	0.6	0.6	5.5	46.7	15.5	1.0	2.1	0.7	0.1	0.2	1.0	0.0	0.5
C6	0.6	1.2	0.7	7.0	6.8	49.1	0.6	1.3	1.0	0.4	0.3	2.8	0.0	1.1
C7	0.6	2.2	2.0	0.2	0.9	1.3	60.7	0.9	0.5	5.3	0.3	3.0	0.2	0.4
C8	0.7	0.3	1.3	2.6	1.3	2.8	4.1	54.9	2.2	0.2	0.8	1.4	0.1	1.3
C9	0.0	0.1	0.0	0.3	0.0	0.3	0.1	4.8	78.8	0.0	0.1	0.4	0.1	7.2
C10	1.6	1.8	1.2	0.1	0.0	0.1	1.6	0.3	0.0	79.5	1.5	0.2	1.6	0.0
C11	1.0	0.7	1.2	0.5	0.3	1.1	0.6	1.1	0.7	5.3	70.6	0.3	0.8	0.4
C12	0.2	0.5	0.8	0.6	0.6	1.3	4.5	2.2	0.3	1.3	1.2	68.3	0.5	0.7
C13	1.3	1.0	0.6	0.6	0.4	0.6	1.7	1.0	0.6	3.9	0.6	0.4	74.0	1.2
C14	0.2	0.0	0.3	0.2	0.0	0.6	0.3	0.8	5.9	0.0	0.0	0.5	0.1	82.7

of the latter with respect to the selection of the number of features to be extracted from the SAR image, as already observed during the noise-free analysis. For completeness, confusion matrices are reported when the moments order is 8 and $\nu_s = 0.5$ in Table 4.6 and Table 4.7, for the Krawtchouk and the pZ algorithm, respectively. The figure of merit Υ for the overall confusion matrices is $\Upsilon_{\text{Kraw}} = 3.69$ and $\Upsilon_{\text{pZ}} = 2.81$, while, for the specific cases of the targets BMP2 and T72, it is equal to $\Upsilon_{\text{Kraw}}^{\text{BMP2}} = 1.51$, $\Upsilon_{\text{Kraw}}^{\text{T72}} = 4.38$, $\Upsilon_{\text{pZ}}^{\text{BMP2}} = 1.19$ and $\Upsilon_{\text{pZ}}^{\text{T72}} = 3.26$.

Results shown in this Section demonstrate superior performance and robustness of the Krawtchouk based algorithm over the approach using pZ moments. The Krawtchouk moments, being defined in discrete, do not present any discretisation errors, which translates in higher capabilities in discriminating between different configurations of the same vehicle (like BMP2 and T72) and in noisy environments. Unlike the pZ moments, however, they are not rotational and translational invariant, although the shift parameter p may be used for this last purpose. Therefore a priori step of pose estimation is required.

4.4 Conclusion

In this Chapter two Synthetic Aperture Radar (SAR) Automatic Target Recognition (ATR) algorithms based on the pseudo-Zernike (pZ) framework, presented in Section 2.3.4.1, were introduced. The first one, reported in Section 4.2, attempted to further exploit the polarimetric information provided by a full-polarimetric SAR image. It consisted in extracting the pZ moments from both the full-polarimetric SAR image of the target, and its Krogager components, described in Section 2.3.2. The properties of rotation and translation invariance of the pZ moments, combined with the roll invariance property of the Krogager components, made the algorithm robust with respect to the orientation of the target and to the acquisition elevation angle, with no need of either position or pose estimation. Moreover, the framework could be easily extended whether images from multiple sensors were available. In such a case, the information that the nodes have to share within the network or with a fusion centre, only regards the score vectors, operation that would require low complexity and bandwidth. The algorithm was tested on the real full-polarimetric circular SAR images of the GOTCHA dataset. Results showed that the integrated Krogager pseudo-Zernike (Kr/pZ) framework outperformed the original one in all the analysed case, namely noise-free, additive compound-Gaussian noise and multiplicative noise. In particular, larger improvements were appreciable when fewer images were used for training the classifiers, which means that, in order to reach the same performance, the Kr/pZ approach would need less a priori information compared to the pZ only algorithm. This comes at cost of just a slight increase in the computational complexity, since no additional information is required as input of the algorithm.

The second algorithm, presented in Section 4.3, was still based on the pZ framework, but made use of the Krawtchouk polynomials instead. Unlike the pZ polynomials, these are discrete defined, which removes the discretisation error that builds up as the order increases, limiting the accuracy of the moments. The performance of the proposed algorithm was assessed using the real MSTAR dataset, that contains different vehicles in various configurations. The experimental results demonstrated superior performance and robustness of the Krawtchouk moments based algorithm over the pZ only approach, in particular on the characterisation of targets and in noisy environment. However, this was achieved while renouncing to the rotational and translational invariance of the pZ moments.

Chapter 5

Micro-Doppler Model Based Identification of Helicopters

5.1 Introduction

As described in Section 2.4.3, micro-Doppler (mD) signature is a peculiar characteristic of any helicopter model, since its modulation depends on the number, η, the length, ρ and the rotation speed, ω, of the helicopter's rotor blades, therefore it can be exploited for identification purposes. The mD model based identification algorithm described in this Chapter, relies on a sparse representation of the discrete-time radar signal received from a helicopter's rotor, and its recovery through the resolution of a sparse signal recovery problem, aimed at estimating the mD parameters of the target. The algorithm is independent of the orientation of the target with respect to the radar Line of Sight (LoS) and of the initial position of the blades. Moreover, it does not use any time-frequency analysis tool, reviewed in Section 2.4.1, which may be computationally expensive and needs some parameters to be properly set depending of the dynamic of the micro-motions.

In the following of this Chapter, the general model of the signal received from a helicopter's rotor, and its parametric sparse representation are derived and reported in Section 5.2. Then, a modified version of the Pruned Orthogonal Matching Pursuit (POMP), previously described in Section 2.4.2 for the estimation of mD parameters of a coning target, is introduced in Section 5.3, while in Section 5.4 the algorithm for the identification of single-targets present in the radar cell of interest is finally described. In Section 5.5 the framework is further developed for the identification of multiple-targets that cannot be separated in any other domain, i.e. range, angle, Doppler, etc. Furthermore, an information fusion technique is presented (for both the single-target and the multi-target scenario) when several sensors are operating simultaneously, in order to enhance the identification capability on the entire system. Performance assessment of the algorithms is reported in Section 5.6 and Section 5.7, with analyses performed on simulated and real data, respectively.

5.2 Radar Return from Rotor Blades

In this Section the model of the signal returned from a helicopter's rotor is derived in the general case, that is, unlike (2.31), no assumption is made on the position and orientation of the target. First the distance from the radar to a point scatterer on a generic blade is geometrically calculated as the blade rotates, and then the radar signal received from the helicopter's rotor is modelled as superimposition of the returns from each blade.

5.2.1 Geometry of Rotating Blades

Let us consider the Cartesian coordinate system shown in Figure 5.1. The system (X, Y, Z) is centred in the radar, while (X', Y', Z') is centred in the main rotor hub of the helicopter. The position vector $\boldsymbol{r}_0$, in red, is:

$$\boldsymbol{r}_0 = R_0 \left(\cos\beta_L \cos\alpha_L \,\hat{x} + \cos\beta_L \sin\alpha_L \,\hat{y} + \sin\beta_L \,\hat{z}\right) \tag{5.1}$$

where R_0 is the distance radar-helicopter, α_L and β_L are the azimuth and elevation angles, respectively, identifying the LoS of the radar, and $\hat{x}$, $\hat{y}$ and $\hat{z}$ are the versors of the coordinate system, respectively. Moreover, let us consider the coordinate system (K, U, V) centred in O' and rotated of $-\beta_H$ and α_H about the Y' and Z' axes, respectively, using the right-hand rule. Specifically, the overall rotation matrix can be

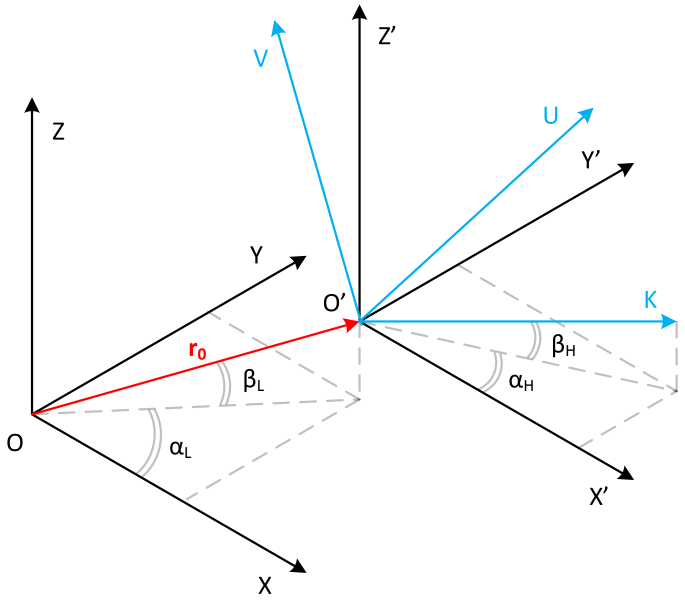

Figure 5.1: Geometry of rotating blades: reference system.

expressed as:

$$\begin{aligned}
\boldsymbol{R}(\alpha_H,\beta_H) &= \boldsymbol{R}_{Z'}(\alpha_H)\,\boldsymbol{R}_{Y'}(-\beta_H) = \\
&= \begin{bmatrix} \cos\alpha_H & -\sin\alpha_H & 0 \\ \sin\alpha_H & \cos\alpha_H & 0 \\ 0 & 0 & 1 \end{bmatrix} \begin{bmatrix} \cos\beta_H & 0 & -\sin\beta_H \\ 0 & 1 & 0 \\ \sin\beta_H & 0 & \cos\beta_H \end{bmatrix} = \\
&= \begin{bmatrix} \cos\alpha_H\cos\beta_H & -\sin\alpha_H & -\cos\alpha_H\sin\beta_H \\ \sin\alpha_H\cos\beta_H & \cos\alpha_H & -\sin\alpha_H\sin\beta_H \\ \sin\beta_H & 0 & \cos\beta_H \end{bmatrix}
\end{aligned} \tag{5.2}$$

The versors of the rotated reference system (K, U, V) are also reported:

$$\hat{k} = \cos\alpha_H\cos\beta_H\,\hat{x}' + \sin\alpha_H\cos\beta_H\,\hat{y}' + \sin\beta_H\,\hat{z}' \tag{5.3}$$

$$\hat{u} = -\sin\alpha_H\,\hat{x}' + \cos\alpha_H\,\hat{y}' \tag{5.4}$$

$$\hat{v} = -\cos\alpha_H\sin\beta_H\,\hat{x}' - \sin\alpha_H\sin\beta_H\,\hat{y}' + \cos\beta_H\,\hat{z}' \tag{5.5}$$

where $\hat{x}' \equiv \hat{x}$, $\hat{y}' \equiv \hat{y}$ and $\hat{z}' \equiv \hat{z}$.

The axis identified by the versor $\hat{k}$ is assumed to be the rotation axis of the rotor blades[21], while $\hat{u}$ and $\hat{v}$ identify the plane on which the blades lie. Let $\boldsymbol{b}$ be the position vector in (K, U, V) of a point scatterer, B, at distance b from the hub on a generic blade:

$$\boldsymbol{b} = b \cos \phi_0 \, \hat{u} + b \sin \phi_0 \, \hat{v} \tag{5.6}$$

where ϕ_0 is the initial offset of the blade with respect to $\hat{u}$. Moreover, let $\boldsymbol{b}_\theta$ be the position vector of the point B_θ, which is the point scatterer B rotated of an angle θ about the axis $\hat{k}$, as shown in Figure 5.2. By means of the Rodrigues' rotation formula,

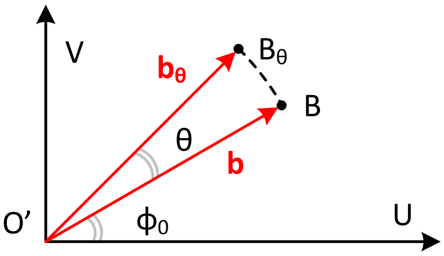

Figure 5.2: Representation of the point scatterer B_θ.

$\boldsymbol{b}_\theta$ can be written as:

$$\boldsymbol{b}_\theta = \boldsymbol{b} \cos \theta + \left(\hat{k} \times \boldsymbol{b} \right) \sin \theta + \hat{k} \left(\hat{k} \cdot \boldsymbol{b} \right) (1 - \cos \theta) \tag{5.7}$$

Since the rotation axis, $\hat{k}$, and the vector identifying the generic blade, $\boldsymbol{b}$, are orthogonal, their inner product is zero, while the result of their cross product is a vector, named $\boldsymbol{b}'$, orthogonal to both:

$$\boldsymbol{b}' = \hat{k} \times \boldsymbol{b} = -b \sin \phi_0 \, \hat{u} + b \cos \phi_0 \, \hat{v} \tag{5.8}$$

Hence, the vector $\boldsymbol{b}_\theta$ in (5.7) can be expressed as:

$$\boldsymbol{b}_\theta = \boldsymbol{b} \cos \theta + \boldsymbol{b}' \sin \theta = b \cos (\theta + \phi_0) \, \hat{u} + b \sin (\theta + \phi_0) \, \hat{v} \tag{5.9}$$

The squared distance between the radar, located in O, and the scatterer point B_θ can

---

[21] This implies that $\pi/2 - \beta_H$ can be interpreted as the helicopter's pitch angle, while α_H identifies its forward direction.

now be derived as:

$$\begin{aligned} R(\theta) = \overline{OB_\theta} &= \|\boldsymbol{b}_\theta + \boldsymbol{r}_0\| = \sqrt{\|\boldsymbol{r}_0\|^2 + \|\boldsymbol{b}_\theta\|^2 + 2\boldsymbol{b}_\theta \cdot \boldsymbol{r}_0} = \\ &= \sqrt{R_0^2 + b^2 + 2R_0 b \left(\cos(\theta + \phi_0)\, \hat{r}_0 \cdot \hat{u} + \sin(\theta + \phi_0)\, \hat{r}_0 \cdot \hat{v}\right)} \end{aligned} \tag{5.10}$$

where $\hat{r}_0 = \boldsymbol{r}_0 / \|\boldsymbol{r}_0\|$. Defining the angles γ_u and γ_v such that:

$$\cos\gamma_u \triangleq \hat{r}_0 \cdot \hat{u} = \cos\beta_L \sin(\alpha_L - \alpha_H) \tag{5.11}$$

$$\cos\gamma_v \triangleq \hat{r}_0 \cdot \hat{v} = -\cos\beta_L \sin\beta_H \cos(\alpha_L - \alpha_H) + \sin\beta_L \cos\beta_H \tag{5.12}$$

the distance $R(\theta)$ in (5.10) can be rewritten as:

$$R(\theta) = \sqrt{R_0^2 + b^2 + 2R_0 b \Delta \cos(\theta + \phi_0 - \zeta)} \tag{5.13}$$

where

$$\Delta = \sqrt{\cos^2\gamma_u + \cos^2\gamma_v} \tag{5.14}$$

$$\tan\zeta = \cos\gamma_v / \cos\gamma_u \tag{5.15}$$

Assuming the helicopter to be in the far field, such as $(b/R_0)^2 \to 0$, the range from the radar to the point scatter B_θ can be approximated as:

$$R(\theta) \approx R_0 + b\Delta\cos(\theta + \phi_0 - \zeta) \tag{5.16}$$

Note that, when $\alpha_L = \alpha_H$ and $\beta_H = \pi/2$:

$$\Delta = \sqrt{\cos^2\gamma_u + \cos^2\gamma_v} = \cos\beta_L \tag{5.17}$$

therefore the expression of $R(\theta)$ in (5.16) falls in the two-dimensional model[22] described in [60].

---

[22] For *two-dimensional model* it is meant that the vector identifying the LoS, $\boldsymbol{r}_0$, and the rotor rotation axis versor, $\hat{k}$, lie on the same plane

5.2.2 Signal Model

Let ω be the rotation speed, in radian per second (rad/s), of the rotor, such that the rotation angle over time of the point scatterer B_θ is $\theta = \omega n T_s$, where T_s is the sampling rate and $n = 0, \ldots, N-1$ is the index of the time sample. Then, from equation (5.16) the discrete-time baseband radar signal received from this point scatterer is derived as:

$$y_B\left(n\right) = e^{-j\frac{4\pi}{\lambda}R(n)} = e^{-j\frac{4\pi}{\lambda}\left[R_0 + b\Delta\cos(\omega n T_s + \phi_0 - \zeta)\right]} \tag{5.18}$$

By integrating (5.18) over the length, ρ, of the blade, the signal becomes [60]:

$$\begin{aligned} y_\rho\left(n\right) = & \int_0^\rho e^{-j\frac{4\pi}{\lambda}\left[R_0 + b\Delta\cos(\omega n T_s + \phi_0 - \zeta)\right]} db = \\ & = \rho\, e^{-j\frac{4\pi}{\lambda}R_0} \operatorname{sinc}\left(\frac{2}{\lambda}\rho\Delta\cos\left(\omega n T_s + \phi_0 - \zeta\right)\right) \times \\ & \times e^{-j\frac{2\pi}{\lambda}\rho\Delta\cos(\omega n T_s + \phi_0 - \zeta)} \end{aligned} \tag{5.19}$$

where $\operatorname{sinc}\left(x\right) = \sin\left(\pi x\right)/\pi x$. Finally, assuming that the helicopter's rotor has η equally spaced blades, the discrete-time baseband radar signal received from the overall helicopter's rotor can be modelled through equation (5.19) by superimposing the returns from each blade:

$$\begin{aligned} y_\eta\left(n\right) = & \rho\, e^{-j\frac{4\pi}{\lambda}R_0} \times \\ & \times \sum_{l=0}^{\eta-1} \operatorname{sinc}\left(\frac{2}{\lambda}\rho\Delta\cos\left(\omega n T_s + \frac{2\pi}{\eta}l + \phi_0 - \zeta\right)\right) \times \\ & \times e^{-j\frac{2\pi}{\lambda}\rho\Delta\cos\left(\omega n T_s + \frac{2\pi}{\eta}l + \phi_0 - \zeta\right)} \end{aligned} \tag{5.20}$$

where the term $\frac{2\pi}{\eta}l$ takes into account the initial rotation angle of each blade. The phase history of the signal represents a characteristic mD signature of the type of helicopter, and can be exploited to identify the helicopter itself.

Taking into account the term Δ, which depends on the aspect angle and on the orientation of the helicopter, the maximum Doppler shift over time can be computed as follows:

$$f_{D_{\max}} = 2\frac{\omega\rho}{\lambda}\Delta \tag{5.21}$$

Since $\Delta \in [0,1]$, the expected maximum Doppler shift is obtained for $\Delta = 1$. Therefore, the sampling frequency, f_s, used to discretise the signal in (5.20) must satisfy the following Nyquist sampling condition:

$$f_s = 1/T_s > 2f_{D_{\max}}\Big|_{\Delta=1} \tag{5.22}$$

5.2.3 Parametric Sparse Signal Model

In this Section a parametric sparse representation of the discrete-time radar signal received from the helicopter's rotor, reported in equation (5.20), is obtained. The sparse domain is defined by the characteristic helicopter's parameters ω, ρ and η.

Let $\mathcal{D}$ be the set of L couples $(\tilde{\omega}_k, \tilde{\eta}_k)$ that identify as many helicopter models of interest:

$$\mathcal{D} = \left\{\tilde{d}_k = (\tilde{\omega}_k, \tilde{\eta}_k), k = 0, \ldots, L-1\right\} \tag{5.23}$$

where $\tilde{\eta}_k$ is the number of blades and $\tilde{\omega}_k$ is the *nominal* rotation speed of the k-th type of target. Note that a helicopter generally flies with constant rotor's rotation speed [140], however in some cases and for some manoeuvres throughout the flight, this can vary within the range $95 - 102\,\%$ of its nominal value[23]. For this reason, for each type of helicopter let us consider an extended set $\mathcal{D}_e^k$, $k = 0, \ldots, L-1$, defined as follows:

$$\mathcal{D}_e^k = \{d_i = (\omega_i, \eta_i), i = 0, \ldots, M_k - 1 \mid \eta_i = \tilde{\eta}_k, 0.95\,\tilde{\omega}_k \leq \omega_i \leq 1.02\,\tilde{\omega}_k\} \tag{5.24}$$

and an overall extended set that results from the union of the sets $\mathcal{D}_e^k$, that is:

$$\mathcal{D}_e = \{d_i = (\omega_i, \eta_i), i = 0, \ldots, M-1\} = \bigcup_{k=0}^{L-1} \mathcal{D}_e^k \tag{5.25}$$

The cardinality of the sets $\mathcal{D}_e^k$, namely M_k, varies on varying k and it is not known a priori. It depends on the step size used to discretise the range $[0.95\,\tilde{\omega}_k, 1.02\,\tilde{\omega}_k]$, which step size is assumed to be equal for all the sets $\mathcal{D}_e^k$. Furthermore, since the sets $\mathcal{D}_e^k$ may

---

[23] Note that the range $95 - 102\,\%$ may also vary among the different types of helicopter, however this is kept fixed throughout the discussion without loss of generality.

be not disjoint, the following relation holds:

$$M \leq \sum_{k=0}^{L-1} M_k \tag{5.26}$$

Moreover, let us also define the set of possible lengths of the blades:

$$\mathcal{R} = \{\rho_k, k = 0, \ldots, P-1 \mid \rho_{\text{min}} \leq \rho_k \leq \rho_{\text{max}}, \rho_{k-1} < \rho_k\} \tag{5.27}$$

where ρ_{min} and ρ_{max} are the smallest and the largest expected lengths, respectively, based on the helicopter models of interest. As for the sets $\mathcal{D}_e^k$, the range $[\rho_{\text{min}}, \rho_{\text{max}}]$ is uniformly discretise, and the step size affects the cardinality of the set P.

The sparse representation of the discrete-time radar signal received from the helicopter's rotor in (5.20) is obtained as:

$$\boldsymbol{y}_\eta = \boldsymbol{\Psi} \boldsymbol{x} \tag{5.28}$$

where $\boldsymbol{y}_\eta = [y_\eta(0), \ldots, y_\eta(N-1)]^T \in \mathbb{C}^N$ contains the time samples, $\boldsymbol{x} \in \mathbb{C}^{P \cdot M}$ is a sparse vector and $\boldsymbol{\Psi} \in \mathbb{C}^{N \times (P \cdot M)}$ is a matrix, called *dictionary*, whose columns are populated based on the sets $\mathcal{D}_e$ and $\mathcal{R}$. Specifically, $\boldsymbol{\Psi}$ is a block matrix organised as follows:

$$\boldsymbol{\Psi} = \left[\boldsymbol{\Psi}_0^{\mathcal{R}}, \ldots, \boldsymbol{\Psi}_i^{\mathcal{R}}, \ldots, \boldsymbol{\Psi}_{M-1}^{\mathcal{R}}\right] \tag{5.29}$$

where each matrix $\boldsymbol{\Psi}_i^{\mathcal{R}} \in \mathbb{C}^{N \times P}$ is:

$$\boldsymbol{\Psi}_i^{\mathcal{R}} = [\psi_{i,0}(n), \ldots, \psi_{i,k}(n), \ldots, \psi_{i,P-1}(n)] \tag{5.30}$$

The function $\psi_{i,k}(n)$ is called *atom* of the dictionary, and it is an instance of the discrete-time signal (5.20) for two specific elements of the sets $\mathcal{D}_e$ and $\mathcal{R}$, respectively.

In particular it can be defined as follows:

$$\begin{aligned}\psi_{i,k}\left(n\right) = {} & \rho_k\, e^{-j\frac{4\pi}{\lambda}R_0}\times\\ & \times\sum_{l=0}^{\eta_i-1}\operatorname{sinc}\left(\frac{2}{\lambda}\rho_k\Delta\cos\left(\omega_i n T_s+\frac{2\pi}{\eta_i}l+\phi_0-\zeta\right)\right)\times\\ & \times e^{-j\frac{2\pi}{\lambda}\rho_k\Delta\cos\left(\omega_i n T_s+\frac{2\pi}{\eta_i}l+\phi_0-\zeta\right)}\\ & \text{with } d_i=\left(\omega_i,\eta_i\right)\in\mathcal{D}_e,\quad \rho_k\in\mathcal{R}\end{aligned} \tag{5.31}$$

Given the block structure of the matrix $\boldsymbol{\Psi}$, the sparse vector $\boldsymbol{x}$ is organised accordingly as follows:

$$\boldsymbol{x}=\left[\left(\boldsymbol{x}_0^{\mathcal{R}}\right)^T,\ldots,\left(\boldsymbol{x}_i^{\mathcal{R}}\right)^T,\ldots,\left(\boldsymbol{x}_{M-1}^{\mathcal{R}}\right)^T\right]^T \tag{5.32}$$

where $\boldsymbol{x}_i^{\mathcal{R}}\in\mathbb{C}^P$ is:

$$\boldsymbol{x}_i^{\mathcal{R}}=\left[x_{i,0},\ldots,x_{i,k},\ldots,x_{i,P-1}\right]^T \tag{5.33}$$

Under the assumption that position and orientation of the helicopter, and initial offset of the blades are known[24], if the couple $d_i=\left(\omega_i,\eta_i\right)$ and the length ρ_k characterise the observed target then $x_{i,k}=1$, otherwise $x_{i,k}=0$.

5.3 Pruned Orthogonal Matching Pursuit

Objective of the algorithm proposed in this Chapter is to first estimate the characteristic parameters of a previously detected helicopter, and then infer the model of helicopter based on the result of the estimate. The estimation process mainly consists of finding the atom, defined in equation (5.31), that best matches the received signal, and this is achieved by solving a sparse signal recovery problem.

Let $y\left(n\right)$, $n=0,\ldots,N-1$ be the discrete-time received radar signal, i.e. a slow-time signal acquired by a pulsed radar with PRI of T_s seconds, or a Continuous Wave (CW) radar signal sampled with sampling rate of T_s seconds. The first sample of the signal, that is for $n=0$, is assumed to coincide with one flash[25], and the main Doppler, due to the bulk motion of the helicopter, is supposed to be already compensated. More-

---

[24] Parameters in equation (5.31) affected by the position and the orientation of the helicopter are R_0, Δ and ζ, while ϕ_0 is the initial offset.

[25] This *synchronisation* is achieved in the first step of the algorithm.

over, the signal is normalised as follows:

$$\tilde{y}(n) = \frac{y(n) - \frac{1}{N}\sum_{n=0}^{N-1} y(n)}{\max_n \left| y(n) - \frac{1}{N}\sum_{n=0}^{N-1} y(n) \right|} \tag{5.34}$$

such that $|\tilde{y}(n)| \in [0,1]$, in order to remove the strong return from the fuselage of the helicopter and to make the estimation independent of the RCS of the target itself. This signal can now be represented in the sparse domain defined by the matrix $\boldsymbol{\Psi}$ in equation (5.29) as follows:

$$\tilde{\boldsymbol{y}} = \boldsymbol{\Psi}\boldsymbol{x} + \boldsymbol{\xi} \tag{5.35}$$

where $\tilde{\boldsymbol{y}} = [\tilde{y}(0), \ldots, \tilde{y}(N-1)]^T \in \mathbb{C}^N$ contains the time samples of the normalised received radar signal, $\boldsymbol{x} \in \mathbb{C}^{P \cdot M}$ is the sparse vector defined in equation (5.32) and $\boldsymbol{\xi} \in \mathbb{C}^N$ is a noise vector. As mentioned at the end of Section 5.2.3, by definition if the observed target has η_i blades of length ρ_k meters rotating at ω_i radians per second, then $x_{i,k}$ is non-zero. Therefore, recovering the sparse signal $\boldsymbol{x}$ gives information on the type of helicopter.

The algorithm proposed in this Thesis is a modified version of the POMP [13] reported in Section 2.4.2 and used for the estimation of the mD parameters of a coning target. The POMP combines the traditional iterative approach of the OMP with a pruning process, that progressively reduces the dimension of the dictionary $\boldsymbol{\Psi}$ avoiding unnecessary computations corresponding to wrong atoms. The algorithm was initially developed for the estimation of the position and the initial phase of the dominant scatterers (whose number is unknown) that compose the coning target, and their common rotation speed. Here it is adapted to the identification of the mD parameters of helicopters, independently of the initial position of the blades and of the orientation of the target itself. Furthermore, the algorithm is extended to the estimation of the mD parameters of multiple targets when they are not resolvable in other domains, and a data fusion approach is introduced when multiple sensors are deployed for enhanced identification.

5.3.1 Remarks on the Design of the Dictionary

Following the high-level description of the algorithm, some clarifications are required about the actual design of the dictionary $\boldsymbol{\Psi}$, hence of the atoms defined in equation (5.31), prior the estimation process.

Firstly, as mentioned above, the signal $\tilde{\boldsymbol{y}}$, input of the estimation process, is normalised as shown in (5.34). For this reason, the atoms must be normalised accordingly. Moreover, the assumption made in Section 5.2.3 of complete knowledge about position and orientation of the observed target, as well as the initial offset of its blades, is not reasonable. This means that when designing the dictionary $\boldsymbol{\Psi}$, the quantities R_0, Δ, ϕ_0 and ζ need to be properly selected.

The angles ϕ_0 and ζ are chosen such that their difference $\phi_0 - \zeta = \pi/2$. This ensures that the first time sample of each atom coincides with a flash.

The range R_0 is selected as $R_0 = \frac{\lambda}{16} + m\frac{\lambda}{8}$, where $m \in \mathbb{Z}$. The choice of this value is driven by the following considerations. Firstly, it only appears in the factor $e^{-j\frac{4\pi}{\lambda}R_0}$ which is periodic with period $\lambda/2$ in R_0. Secondly, it is easy to verify that, when the number of blades is even, the real and imaginary parts of (5.31) are zero for $R_0 = \frac{\lambda}{8} + m\frac{\lambda}{4}$ and $R_0 = m\frac{\lambda}{4}$, respectively. This could bias and degrade the match between the atoms and the discrete-time received signal, while $R_0 = \frac{\lambda}{16} + m\frac{\lambda}{8}$ guarantees that real and imaginary parts of the atom have the same *weight* during the estimation.

Together with the range information, the position of the helicopter is uniquely defined by the azimuth and the elevation angles, α_L and β_L, respectively, of the LoS. These angles, together with α_H and β_H that describe the orientation of the helicopter, are not known and affect the quantity $\Delta \in [0, 1]$, defined in equation (5.14). Note that, Δ always appears multiplied by the length of the blade ρ_k in (5.31). For this reason, the following quantity is considered:

$$\rho_{\Delta,k} = \rho_k \Delta \in [0, \rho_{\text{max}}] \tag{5.36}$$

that implies a redefinition of the set $\mathcal{R}$ made in equation (5.27):

$$\mathcal{R}_\Delta = \{\rho_{\Delta,k}, k = 0, \ldots, P_\Delta - 1 \mid 0 < \rho_{\Delta,k} \leq \rho_{\text{max}}, \rho_{\Delta,k-1} < \rho_{\Delta,k}\} \tag{5.37}$$

A further look at the expression of the atom in (5.31) also suggests the introduction of another degree of freedom. In fact, negative values for $\rho_{\Delta,k}$, despite being physically impossible, allows us to solve an ambiguity when dealing with an odd number of blades. Figure 5.3(a) and Figure 5.3(b) show the same simulated time signal received from the rotor of a three-bladed Mil Mi-2 Hoplite, and synchronised on two consecutive flashes. Apparently, the two signals look very similar, however by inspecting their spectrograms, in Figure 5.3(c) and Figure 5.3(d), respectively, they seem to be flipped along the frequency axis. This flipping occurs because, in the first case, the flash represents a receding blade, while, in the second case, it is due to an approaching blade[26]. Analytically, the two signals are conjugates, but, equivalently, they can be thought to have opposite lengths of the blades. Hence, the set $\mathcal{R}$ can be eventually defined as:

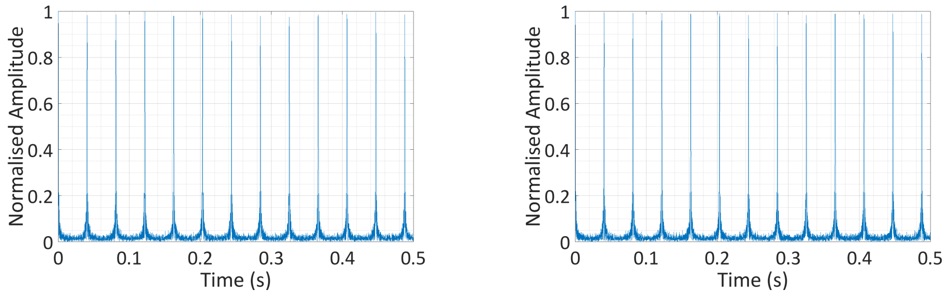

(a) Time signal, synchronised on the 1st flash. (b) Time signal, synchronised on the 2nd flash.

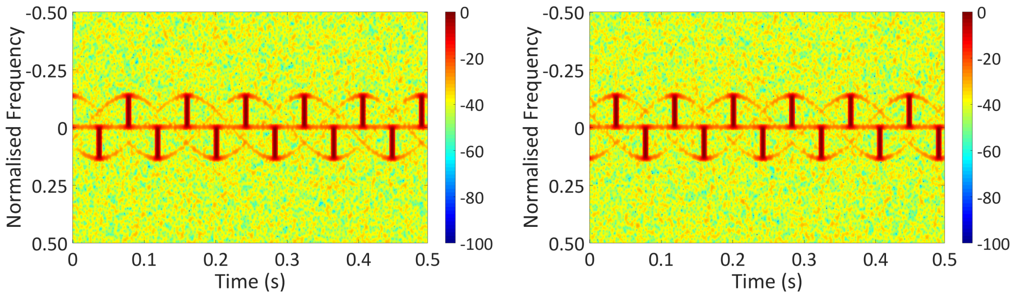

(c) Spectrogram, synchronised on the 1st flash. (d) Spectrogram, synchronised on the 2nd flash.

Figure 5.3: Representation of a simulated time-domain signal, and its spectrogram, received from the rotor of a three-bladed Mil Mi-2 Hoplite ($SNR = 20\,d\mathrm{B}$) and synchronised on two consecutive flashes: (a) and (c) first flash, (b) and (d) second flash.

$$\mathcal{R}'_\Delta = \{\rho_{\Delta,k}, k = 0, \dots, P'_\Delta - 1 \mid |\rho_{\Delta,k}| \leq \rho_{\max}, \rho_{\Delta,k-1} < \rho_{\Delta,k}\} \tag{5.38}$$

---

[26] Note that this effect is not visible when the helicopter has an even number of blades, since approaching blade and receding blade are always coupled.

It is worth mentioning that, given the uniform discretisation of the range $[-\rho_{\max}, \rho_{\max}]$ and the order relation $\rho_{\Delta,k-1} < \rho_{\Delta,k}$, the following holds:

$$\rho_{\Delta,k} = -\rho_{\Delta,P'_{\Delta}-1-k} \tag{5.39}$$

Finally, following the remarks discussed in this Section, the atoms that populate the dictionary $\boldsymbol{\Psi} \in \mathbb{C}^{N\times\left(P'_{\Delta}\cdot M\right)}$ are redefined as follows[27]:

$$\tilde{\psi}_{i,k}(n) = e^{-j\frac{\pi}{4}} \frac{\sum_{l=0}^{\eta_i-1} \operatorname{sinc}\left(\frac{2}{\lambda}\rho_{\Delta,k}\sin\left(\omega_i nT_s + \frac{2\pi}{\eta_i}l\right)\right) e^{j\frac{2\pi}{\lambda}\rho_{\Delta,k}\sin\left(\omega_i nT_s + \frac{2\pi}{\eta_i}l\right)}}{\max_n\left|\sum_{l=0}^{\eta_i-1} \operatorname{sinc}\left(\frac{2}{\lambda}\rho_{\Delta,k}\sin\left(\omega_i nT_s + \frac{2\pi}{\eta_i}l\right)\right) e^{j\frac{2\pi}{\lambda}\rho_{\Delta,k}\sin\left(\omega_i nT_s + \frac{2\pi}{\eta_i}l\right)}\right|}$$
$$\text{with } d_i = (\omega_i, \eta_i) \in \mathcal{D}_e, \quad \rho_{\Delta,k} \in \mathcal{R}'_{\Delta} \tag{5.40}$$

Note that, following equation (5.39), the conditions below hold:

$$\begin{cases} \tilde{\psi}_{i,k}(n) = \tilde{\psi}_{i,P'_{\Delta}-1-k}(n) & \text{if } \eta_i \text{ is even} \\ \tilde{\psi}_{i,k}(n) = \tilde{\psi}^{*}_{i,P'_{\Delta}-1-k}(n) & \text{if } \eta_i \text{ is odd} \end{cases} \tag{5.41}$$

5.4 Single-Target Identification

In this section the mD model based algorithm for helicopters' identification is presented when one target is present in the region of interest. Firstly, each phase of the algorithm is described in detail. Then, an approach of data fusion is proposed when more than one sensor is used to perform the identification.

5.4.1 Algorithm Description

The proposed algorithm consists of three phases, shown in Figure 5.4: synchronisation, estimation process and identification. The synchronisation is performed to make the algorithm independent of the initial position of the blades. In fact, the initial phase offset of the received signal, given by $\phi_0 - \zeta$ in equation (5.20), depends on both the position and the orientation of the helicopter, but also on the instant in which the ac-

---

[27] Given the redefinition of $\mathcal{R}$ into $\mathcal{R}'_{\Delta}$, the dimension P is replaced by P'_{Δ} everywhere.

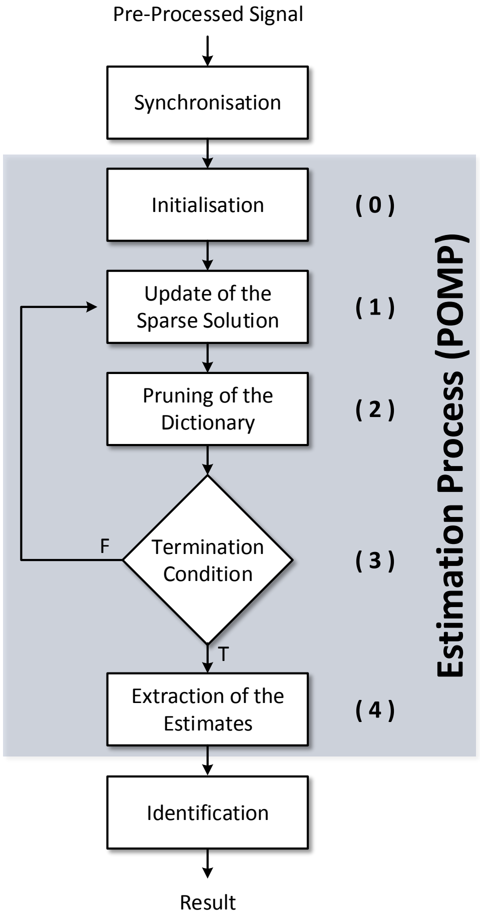

Figure 5.4: Block diagram of the helicopters identification algorithm for the single target scenario.

quisition is triggered, and need to be compensated. The estimation process, composed by 5 steps, is an iterative procedure, based on the POMP, aiming at finding the mD parameters of the observed target through the recovery of the sparse vector $\boldsymbol{x}$. These estimated mD parameters are then used in the last phase for the final identification. The three phases are explained in details in the following three Sections.

5.4.1.1 Synchronisation

Let $z\left(n\right)$, $n = 0, \ldots, J-1$, be the discrete-time acquired radar signal, before synchronisation and normalisation. The sample index $n^{\star}$ where the flash is located, is obtained as position of the first local maximum of $\left|z\left(n\right)\right|$ over a threshold υ. This, in turn, depends on length and maximum value of the acquired signal, $z\left(n\right)$, and the statistical characteristics of the Additive White Gaussian Noise (AWGN), $\xi\left(n\right)$. Specifically, it is computed as:

$$\upsilon = \frac{\left|\max_n |z(n)| - \upsilon'\right|}{4} + \upsilon' \tag{5.42}$$

with:

$$\upsilon' = \sqrt{\sigma_\xi^2 \ln(10J)} \tag{5.43}$$

where σ_ξ^2 is the noise power. Equation (5.43) is equivalent to:

$$\Pr\left(|\xi(n)| > \upsilon'\right) = (10J)^{-1} \tag{5.44}$$

with $\Pr(\cdot)$ indicating the probability. Note that, if no local maximum higher than the threshold υ is found, circumstance that may occur when the SNR is too low, an unknown target is declared. Then, the signal, $y(n)$, input of the estimation process presented in Section 5.3 is defined as:

$$y(n) = z(n + n^\star) \tag{5.45}$$

Note that J has to be sufficiently larger than N, in order to guarantee $J \geq N + n^\star$.

5.4.1.2 Estimation Process

As mentioned before, the estimation process is based on the iteratively estimation of the sparse vector $\boldsymbol{x}$. For each couple $d_i \in \mathcal{D}_e$, the vector $\boldsymbol{x}_i^{\mathcal{R}}$ is estimated and an error is computed, equal to the power of the residual. Then, the columns of the dictionary $\boldsymbol{\Psi}$ that present the largest residual error are removed, until only one couple d_i is left. For clarity, the counter l is introduced, while $\mathcal{I}^{(l)}$ is the set of indices i that identify candidate couples d_i that are still *active* at iteration l; starting from the full dictionary, $\mathcal{I}^{(0)} = \{0, \ldots, M-1\}$, $\left|\mathcal{I}^{(0)}\right| = M$. Other quantities used in the following are: $\boldsymbol{r}_i^{(l)} \in \mathbb{C}^N$ and $\overline{\boldsymbol{x}}_i^{\mathcal{R}} \in \mathbb{C}^{P'_\triangle}$, the recovery residual and the estimate of the vector $\boldsymbol{x}_i^{\mathcal{R}}$, respectively; $\boldsymbol{\Phi}_{\Lambda_i} \in \mathbb{C}^{N \times P'_\triangle}$ the matrix whose columns, specified by the indices in the set $\Lambda_i^{(l)}$, are equal to the corresponding columns $\boldsymbol{\Psi}_i^{\mathcal{R}}$, 0 elsewhere. The estimation procedure is detailed step-by-step in the following.

(0) Initialisation:

- $l = 1$;
- $\mathcal{I}^{(0)} = \{0, \dots, M-1\}$
- $\boldsymbol{r}_i^{(0)} = \tilde{\boldsymbol{y}}$;
- $\Lambda_i^{(0)} = \emptyset$

(1) Update of the sparse solution: for each index $i \in \mathcal{I}^{(l-1)}$

(1.1) The inner product between the residual at the previous step, $\boldsymbol{r}_i^{(l-1)}$, and the block $\boldsymbol{\Psi}_i^{\mathcal{R}}$ is carried out and stored in $\boldsymbol{q}$:

$$\boldsymbol{q} = \left| \left(\boldsymbol{\Psi}_i^{\mathcal{R}}\right)^{\dagger} \boldsymbol{r}_i^{(l-1)} \right| \in \mathbb{C}^{P'_{\Delta}} \tag{5.46}$$

where $(\cdot)^{\dagger}$ is the conjugate transpose.

(1.2) The index of the largest value in $\boldsymbol{q}$ is added to the set $\Lambda_i^{(l)}$:

$$\Lambda_i^{(l)} = \Lambda_i^{(l-1)} \bigcup \underset{0 \le k \le P'_{\Delta}-1}{\arg\max}\; \boldsymbol{q} \tag{5.47}$$

This is equivalent to select the index of the value $\rho_{\Delta,k}$ that best matches the received signal given the couple d_i.

(1.3) The matrix $\boldsymbol{\Phi}_{\Lambda_i}$ is updated accordingly to $\Lambda_i^{(l)}$.

(1.4) The estimate of the vector $\boldsymbol{x}_i^{\mathcal{R}}$ is obtained as follows:

$$\overline{\boldsymbol{x}}_i^{\mathcal{R}} = \boldsymbol{\Phi}_{\Lambda_i}^{+} \tilde{\boldsymbol{y}} \tag{5.48}$$

where $(\cdot)^{+}$ identifies the Moore-Penrose pseudoinverse.

(1.5) The residual $\boldsymbol{r}_i^{(l)}$ is then updated as:

$$\boldsymbol{r}_i^{(l)} = \tilde{\boldsymbol{y}} - \boldsymbol{\Phi}_{\Lambda_i} \overline{\boldsymbol{x}}_i^{\mathcal{R}} \tag{5.49}$$

(2) Pruning of the dictionary: remove E indices i from $\mathcal{I}^{(l-1)}$ that corresponds to the largest residual errors $\left\|\boldsymbol{r}_i^{(l)}\right\|_2^2$ obtaining $\mathcal{I}^{(l)}$, where:

$$E = \left\lfloor \left|\mathcal{I}^{(l-1)}\right| (1-\nu) \right\rfloor \tag{5.50}$$

where $\lfloor\cdot\rfloor$ gives the largest integer not greater than the argument and $\nu \in (0, 0.5]$. That is:

$$\mathcal{I}^{(l)} = \mathcal{I}^{(l-1)} - \mathcal{E}_E \tag{5.51}$$

where the set, $\mathcal{E}_x$, of x indices to remove is defined as:

$$\begin{cases} \mathcal{E}_0 = \emptyset \\ \mathcal{E}_x = \Big\{ i \in \mathcal{I}^{(l-1)} - \mathcal{E}_{x-1} \mid \left\|\boldsymbol{r}_i^{(l)}\right\|_2^2 \geq \left\|\boldsymbol{r}_{i'}^{(l)}\right\|_2^2, \\ \qquad \forall i' \in \mathcal{I}^{(l-1)} - \mathcal{E}_{x-1}, i' \neq i \Big\} \bigcup \mathcal{E}_{x-1} \end{cases} \tag{5.52}$$

(3) Termination condition of the loop: if $\left|\mathcal{I}^{(l)}\right| > 1$, then increment the counter and return to step (1), otherwise go to step (4).

(4) The remaining index in $\mathcal{I}^{(l)}$, say $\bar{\imath}$, identifies the wanted couple:

$$\overline{d} = (\overline{\omega}, \overline{\eta}) \triangleq (\omega_{\bar{\imath}}, \eta_{\bar{\imath}}) = d_{\bar{\imath}} \in \mathcal{D}_e \tag{5.53}$$

Finally, the index:

$$\overline{k} = \underset{0 \leq k \leq P'_\Delta - 1}{\arg\max} \left|\overline{\boldsymbol{x}}_{\bar{\imath}}^{\mathcal{R}}\right| \tag{5.54}$$

identifies the wanted length:

$$\overline{\rho}_\Delta \triangleq \rho_{\Delta,\overline{k}} \in \mathcal{R}'_\Delta \tag{5.55}$$

The estimated number of blades, $\overline{\eta}$, and rotation speed, $\overline{\omega}$, are used to perform the identification of the observed target. The quantity $\overline{\rho}_\Delta$, instead, is not suitable for the identification phase, being an estimate of the length of blades weighted by a factor, Δ, that depends on the aspect angle. However, it will be shown later, in Section 5.4.2, that, when using more than one sensor, and through the knowledge of the angle of arrival of the target, the orientation of the helicopter can be inferred, allowing the estimate of the length to be extracted and exploited for identification.

5.4.1.3 Identification

The last phase of the algorithm is the identification. By definition, the estimated couple $\overline{d} = (\overline{\omega}, \overline{\eta})$ belongs to the set $\mathcal{D}_e$, which, as reported in equation (5.25), is the union of the sets $\mathcal{D}_e^k$, $k = 0, \ldots, L-1$, each of them representing a particular model of helicopter. Objective of the identification phase, then, is to find the set $\mathcal{D}_e^k$ which $\overline{d}$ belongs to. However, since the sets $\mathcal{D}_e^k$ may be not disjoint, the solution to this problem could be not unique, and $\overline{d}$ could belong to different sets, namely the received signal could be associated to different types of target. This ambiguity cannot be solved, which leads to declare the target unknown, unless another discriminative feature is taken into consideration, as the length of the blades. As mentioned before, however, this can only be done if more than one sensor is used, assuming that the angle of arrival of the target is known.

5.4.2 Multi-Sensors: Data Fusion

The exploitation of more than one radar sensor, that see the target with different aspect angles, and the capability of each sensor to infer the angle of arrival, enables the estimation of the orientation of the helicopter, that is the estimation of Δ.

Let us suppose to have a network of T radar sensors. Referring to the reference system presented in Figure 5.1, each sensor locates the target in a specific azimuth-elevation cell identified by the angles α_{L_t} and β_{L_t}, respectively, with $t = 0, \ldots, T-1$. Moreover, each sensor runs the identification algorithm described in Section 5.4.1 locally, leading to different estimates $\overline{d}_t = (\overline{\omega}_t, \overline{\eta}_t)$ and $\overline{\rho}_{\Delta,t}$. In this scenario, the first advantage is that the decision can be made on a majority vote basis with low requirements in terms of communication capabilities between the nodes; more important is the capability to solve the ambiguity that occurs when the estimated couple $\overline{d}_t$ belongs to different sets $\mathcal{D}_e^k$. The exploitation of multiple sensors for the estimation of the orientation of the helicopter, thus of the length of the blades, was first proposed in [141], where the analytical relationship (5.21) was used. The proposed method follows a similar approach, but it does not use the information on the maximum Doppler shift, because not available.

For the sake of simplicity, let us suppose that all the estimates $\overline{d}_t$, $t = 0, \ldots, T-1$, are ambiguous and similar. Here *similarity* means that:

$$\begin{cases} \overline{\eta}_t = \overline{\eta}_{t'} \\ |\overline{\omega}_t - \overline{\omega}_{t'}| \leq \delta_\omega \end{cases} t, t' \in \{0, \ldots, T-1\}, t \neq t' \tag{5.56}$$

where the value δ_ω is the step size used to discretise the range $[0.95\,\tilde{\omega}_k, 1.02\,\tilde{\omega}_k]$ in (5.24). The estimate, from each sensor, of the weighted length of the blade, $\overline{\rho}_{\Delta,t}$, can be written as:

$$\overline{\rho}^2_{\Delta,t} = \rho^2\,\Delta_t^2 = \rho^2\left(\cos^2\gamma_{u,t} + \cos^2\gamma_{v,t}\right) \tag{5.57}$$

where

$$\cos\gamma_{u,t} = \cos\beta_{L_t}\sin\left(\alpha_{L_t} - \alpha_H\right) \tag{5.58}$$

$$\cos\gamma_{v,t} = -\cos\beta_{L_t}\sin\beta_H\cos\left(\alpha_{L_t} - \alpha_H\right) + \sin\beta_{L_t}\cos\beta_H \tag{5.59}$$

In order to remove the true unknown value of the length of the blades from (5.57), the following ratio is considered:

$$\frac{\overline{\rho}^2_{\Delta,t}}{\sum_{t'=0}^{T-1}\overline{\rho}^2_{\Delta,t'}} = \frac{\cos^2\gamma_{u,t} + \cos^2\gamma_{v,t}}{\sum_{t'=0}^{T-1}\left(\cos^2\gamma_{u,t'} + \cos^2\gamma_{v,t'}\right)}, \quad t = 0, \ldots, T-1 \tag{5.60}$$

where the summation is necessary to avoid zero term at the denominator. The unknowns in (5.60) are the helicopter's orientation angles, β_H and α_H, while the number of independent equations is $T-1$: for this reason, in order to be able to solve the system of equations, the number of sensors must satisfy $T \geq 3$. The solution to (5.60) can be found as:

$$\begin{aligned}\left(\overline{\beta}_H, \overline{\alpha}_H\right) = &\arg\min_{(\beta_H,\alpha_H)} \sum_{t=0}^{T-1} \left\{ \frac{\overline{\rho}^2_{\Delta,t}}{\sum_{t'=0}^{T-1} \overline{\rho}^2_{\Delta,t'}} - \frac{\cos^2\gamma_{u,t} + \cos^2\gamma_{v,t}}{\sum_{t'=0}^{T-1}\left(\cos^2\gamma_{u,t'} + \cos^2\gamma_{v,t'}\right)} \right\}^2 \\ &\text{subject to} \\ &\beta_{H,\min} \leq \beta_H \leq \beta_{H,\max} \\ &\alpha_{H,\min} \leq \alpha_H \leq \alpha_{H,\max}\end{aligned} \tag{5.61}$$

by means of a full search algorithm. From the estimates $\overline{\beta}_H$ and $\overline{\alpha}_H$, it follows:

$$\overline{\rho} = \frac{1}{T} \sum_{t=0}^{T-1} \sqrt{\frac{\overline{\rho}^2_{\Delta,t}}{\cos^2\overline{\gamma}_{u,t} + \cos^2\overline{\gamma}_{v,t}}} \tag{5.62}$$

where

$$\cos\overline{\gamma}_{u,t} = \cos\beta_{L_t} \sin\left(\alpha_{L_t} - \overline{\alpha}_H\right) \tag{5.63}$$

$$\cos\overline{\gamma}_{v,t} = -\cos\beta_{L_t} \sin\overline{\beta}_H \cos\left(\alpha_{L_t} - \overline{\alpha}_H\right) + \sin\beta_{L_t} \cos\overline{\beta}_H \tag{5.64}$$

When not all the estimates $\overline{d}_t$, for $t = 0, \ldots, T-1$, are ambiguous, this procedure can be still applied on a subset of sensors, provided that this subset is composed by at least 3 sensors.

5.5 Multi-Target Identification

In this section the mD model based algorithm for helicopters' identification is extended to the estimation and identification of multiple targets. The assumption is that the targets cannot be distinguished in range, Doppler or angle, scenario that is likely to happen when the helicopters fly in formation.

The single target algorithm presented in Section 5.4 highly relies on the synchronisation phase, that deals with the problem of the initial position of the blades. In fact, since the dictionary is built assuming that the first sample of each atom coincides with a flash, also the first sample of the received signal, once pre-processed, must coincide with a flash. This also means that if no flash is picked during the synchronisation phase, the algorithm fails. Moreover, in case of multiple targets present in the scene, even if a flash is selected, only the target which such a flash belongs to is likely to be identified, since the atoms are only synchronised with it.

In order to take this aspect into account, the sparse signal model of the received signal defined in equation (5.35) is modified as follows:

$$\tilde{\boldsymbol{Y}} = \boldsymbol{\Psi}\boldsymbol{X} + \boldsymbol{\Xi} \tag{5.65}$$

The matrix $\boldsymbol{\Psi}$ is the dictionary eventually defined in Section 5.3.1, $\boldsymbol{\Xi} \in \mathbb{C}^{N\times H}$ is a noise matrix while $\boldsymbol{X} \in \mathbb{C}^{\left(P'_{\Delta}\cdot M\right)\times H}$ is a matrix composed by H sparse column vectors. Specifically, it is a block matrix defined as:

$$\boldsymbol{X} = \left[\left(\boldsymbol{X}_0^{\mathcal{R}}\right)^T, \dots, \left(\boldsymbol{X}_i^{\mathcal{R}}\right)^T, \dots \left(\boldsymbol{X}_{M-1}^{\mathcal{R}}\right)^T\right]^T \tag{5.66}$$

where

$$\boldsymbol{X}_i^{\mathcal{R}} = \left[\boldsymbol{x}_{i,0}^{\mathcal{R}}, \dots, \boldsymbol{x}_{i,h}^{\mathcal{R}}, \dots, \boldsymbol{x}_{i,H-1}^{\mathcal{R}}\right] \in \mathbb{C}^{P'_{\Delta}\times H} \tag{5.67}$$

and $\boldsymbol{x}_{i,h}^{\mathcal{R}} \in \mathbb{C}^{P'_{\Delta}}$. Each column vector of the matrix $\tilde{\boldsymbol{Y}} = \left[\tilde{\boldsymbol{y}}_0, \dots, \tilde{\boldsymbol{y}}_h, \dots, \tilde{\boldsymbol{y}}_{H-1}\right] \in \mathbb{C}^{N\times H}$, is a discrete-time signal normalised as follows:

$$\tilde{y}_h\left(n\right) = \frac{y_h\left(n\right) - \frac{1}{N}\sum_{n=0}^{N-1} y_h\left(n\right)}{\max_n \left|y_h\left(n\right) - \frac{1}{N}\sum_{n=0}^{N-1} y_h\left(n\right)\right|} \tag{5.68}$$

where $y_h\left(n\right), n = 0, \dots, N-1$ is the chunk of the received signal synchronised to the h-th flash. Figure 5.5 shows a graphic example of how the matrix $\tilde{\boldsymbol{Y}}$ is constructed. Middle graph is the time-domain received signal, $z\left(n\right)$, in which the first two flashes are marked; the top and bottom graphs represent $y_0\left(n\right)$ and $y_1\left(n\right)$, respectively, that are the chunks synchronised to the first and the second flash. These signals are then normalised through (5.68) and used to populate the first and the second column of $\tilde{\boldsymbol{Y}}$.

Similarly to the single-target identification algorithm, the sparse recovery problem can be stated as follows:

$$\overline{\boldsymbol{x}}_h = \arg\min_{\boldsymbol{x}_h} \left\|\boldsymbol{x}_h\right\|_0 \quad \text{s.t.} \quad \left\|\boldsymbol{r}_h\right\|_2^2 \leq \epsilon \tag{5.69}$$

for $h = 0 \ldots, H-1$, with the additional objective of estimating the number of targets, where $\boldsymbol{r}_h \triangleq \tilde{\boldsymbol{y}}_h - \boldsymbol{\Psi}\boldsymbol{x}_h$ and $\boldsymbol{x}_h = \left[\left(\boldsymbol{x}_{0,h}^{\mathfrak{R}}\right)^T, \ldots, \left(\boldsymbol{x}_{i,h}^{\mathfrak{R}}\right)^T, \ldots, \left(\boldsymbol{x}_{M-1,h}^{\mathfrak{R}}\right)^T\right]^T$ is the h-th column of $\boldsymbol{X}$.

5.5.1 Algorithm Description

Objective of the multi-target identification algorithm is both the estimation of the number of targets, S, present in the radar cell of interest, and the estimation of their mD parameters, $\overline{\omega}_s$, $\overline{\eta}_s$ and $\overline{\rho}_{\Delta,s}$, $s = 0, \ldots, S-1$. Like the single-target algorithm, it consists of three phases, as shown in Figure 5.6. The synchronisation phase aims to extract the chunks from the received signal and build the matrix $\tilde{\boldsymbol{Y}}$. The estimation process presents an additional step that deals with the pruning of the matrix $\tilde{\boldsymbol{Y}}$, with the objective of estimating the correct number of targets. Finally, the identification is performed as for the single-target scenario for the several estimates at the output of the estimation process.

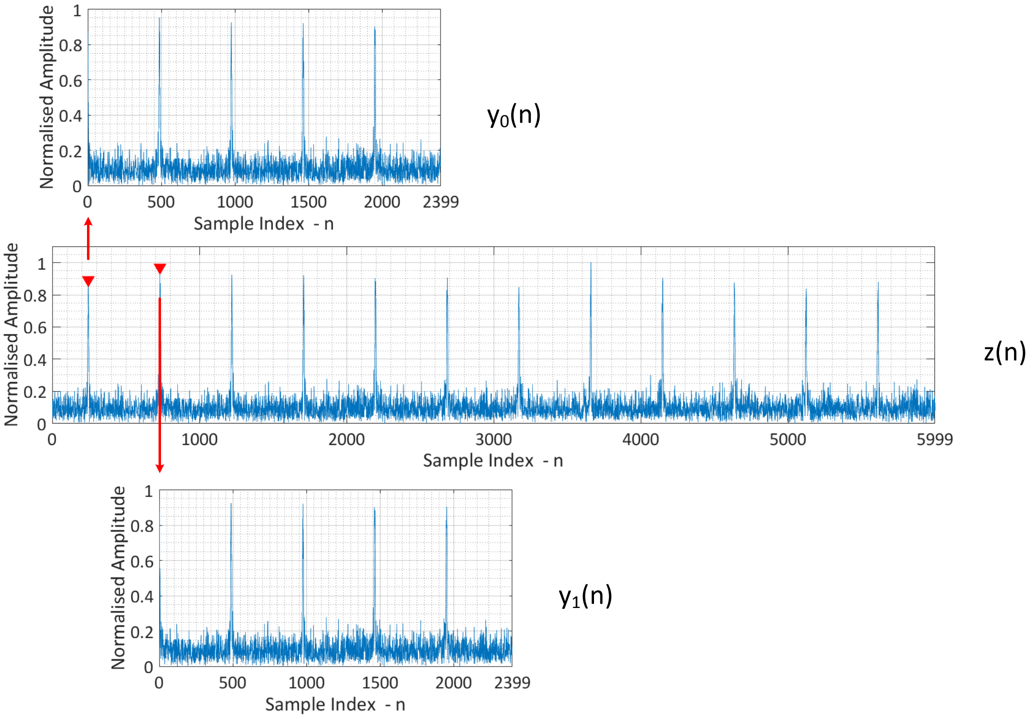

Figure 5.5: Example of construction of matrix $\tilde{\boldsymbol{Y}}$. Middle graph represents the received signal, while top and bottom graphs are the chunks synchronised to the first and second flash, respectively.

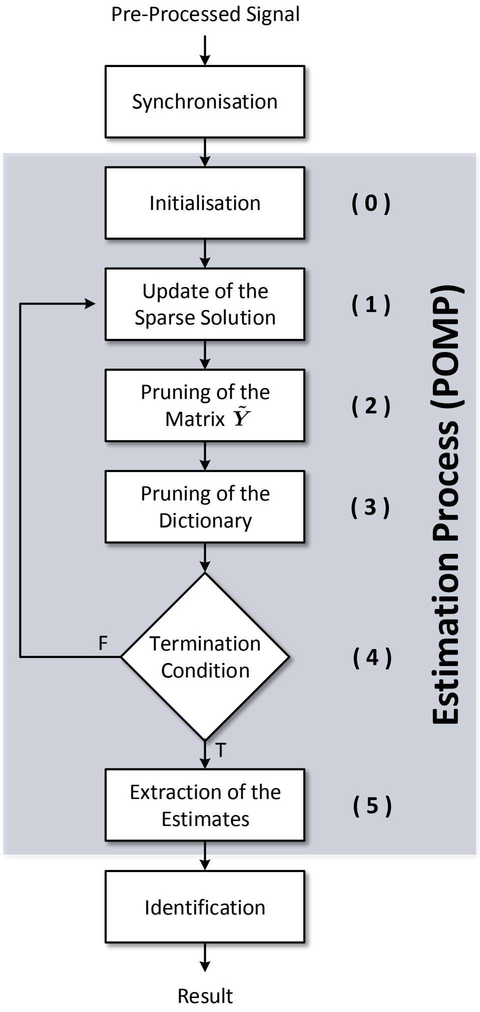

Figure 5.6: Block diagram of the helicopters identification algorithm for the multi target scenario.

5.5.1.1 Synchronisation

The synchronisation is performed as for the single-target algorithm. However, rather than selecting only the location of the first local maximum of $|z\,(n)|$, the locations of at most the first H local maxima are selected. Assuming that these locations are named as $n_h^\star$, $h = 0, \ldots, H-1$, the signals $y_h\,(n)$ that, once normalised, populate the matrix $\tilde{\boldsymbol{Y}}$, are defined as:

$$y_h\,(n) = z\,(n + n_h^\star) \tag{5.70}$$

As for the single-target algorithm, if no local maxima higher than the threshold υ are found, one unknown target is declared independently of the actual number of targets in the scene.

5.5.1.2 Estimation Process

The multi-target estimation process is similar to the single-target one. However, the pruning process does not involve only the dictionary, but also the matrix $\tilde{\boldsymbol{Y}}$. Indeed, each signal $\tilde{y}_h(n)$ that composes the matrix $\tilde{\boldsymbol{Y}}$ is supposed to be uncorrelated with any other, namely it is a portion of the return from a specific helicopter. More likely, however, several chunks are portions of the same return, that is they actually represent the same helicopter. The pruning process applied to $\tilde{\boldsymbol{Y}}$ aims to remove this redundancy and to estimate the correct number of uncorrelated returns, that is the correct number of targets. Meanwhile, couples $d_i \in \mathcal{D}_e$ that characterise the mD signature of the different uncorrelated returns are obtained through the pruning process applied to the dictionary $\boldsymbol{\Psi}$.

As before l is the counter, $\mathcal{I}^{(l)}$ is the set of indices i, associated to the couples $d_i \in \mathcal{D}_e$, that are still active candidates at iteration l, and $\mathcal{H}^{(l)}$ is the set of indices h that identify the potential uncorrelated chunks at iteration l. Starting with the full dictionary and all the chunks extracted from the received signal, $\mathcal{I}^{(0)} = \{0, \ldots, M-1\}$, $\left|\mathcal{I}^{(0)}\right| = M$ and $\mathcal{H}^{(0)} = \{0, \ldots, H-1\}$, $\left|\mathcal{H}^{(0)}\right| = H$. Moreover, $\boldsymbol{R}_i^{(l)} = \left[\boldsymbol{r}_{i,0}^{(l)}, \ldots, \boldsymbol{r}_{i,H-1}^{(l)}\right] \in \mathbb{C}^{N\times H}$ is the matrix of residuals for each chunk, while $\overline{\boldsymbol{X}}_i^{\mathcal{R}} \in \mathbb{C}^{P'_\Delta \times H}$ is the estimate of the matrix $\boldsymbol{X}_i^{\mathcal{R}}$. The estimation process is detailed step-by-step in the following.

(0) Initialisation:

- $l = 1$;
- $\mathcal{I}^{(0)} = \{0, \ldots, M-1\}$
- $\mathcal{H}^{(0)} = \{0, \ldots, H-1\}$
- $\boldsymbol{R}_i^{(0)} = \tilde{\boldsymbol{Y}}$;
- $\Lambda_i^{(0)} = \emptyset$

(1) Update of the sparse solution: for each index $i \in \mathcal{I}^{(l-1)}$

(1.1) The inner product between the matrix of residuals at the previous step, $\boldsymbol{R}_i^{(l-1)}$, and the block $\boldsymbol{\Psi}_i^{\mathcal{R}}$ is carried out and stored in $\boldsymbol{Q} = \left[\boldsymbol{q}_0, \ldots, \boldsymbol{q}_{H-1}\right] \in \mathbb{R}^{P'_\Delta \times H}$:

$$\boldsymbol{Q} = \left|\left(\boldsymbol{\Psi}_i^{\mathcal{R}}\right)^{\dagger} \boldsymbol{R}_i^{(l-1)}\right| \tag{5.71}$$

where the operator $|\cdot|$ is defined for matrices as the magnitude of each complex element of the argument.

(1.2) The index of the largest value in $\boldsymbol{q}_h$, $\forall h \in \mathcal{H}^{(l-1)}$, is added to the set $\Lambda_i^{(l)}$, that is:

$$\Lambda_i^{(l)} = \Lambda_i^{(l-1)} \bigcup \left\{ m_h \mid h \in \mathcal{H}^{(l-1)} \right\} \tag{5.72}$$

where

$$m_h = \underset{0 \le k \le P'_\Delta - 1}{\arg\max}\ \boldsymbol{q}_h \tag{5.73}$$

This is equivalent to select the indices of the values $\rho_{\Delta,k}$ that best match each uncorrelated chunk $\tilde{y}_h(n)$ given the couple d_i.

(1.3) The matrix $\boldsymbol{\Phi}_{\Lambda_i}$ is updated accordingly to $\Lambda_i^{(l)}$.

(1.4) The estimate of the vector $\boldsymbol{X}_i^{\mathcal{R}}$ is obtained as follows:

$$\overline{\boldsymbol{X}}_i^{\mathcal{R}} = \boldsymbol{\Phi}_{\Lambda_i}^{+} \tilde{\boldsymbol{Y}} \tag{5.74}$$

(1.5) The residual $\boldsymbol{R}_i^{(l)}$ is then updated as:

$$\boldsymbol{R}_i^{(l)} = \tilde{\boldsymbol{Y}} - \boldsymbol{\Phi}_{\Lambda_i} \overline{\boldsymbol{X}}_i^{\mathcal{R}} \tag{5.75}$$

(2) Pruning of the matrix $\tilde{\boldsymbol{Y}}$: let $\boldsymbol{V} = [\boldsymbol{v}_0, \ldots, \boldsymbol{v}_{H-1}] \in \mathbb{R}^{M \times H}$ be the matrix that contains the residual errors for each couple d_i, $i \in \mathcal{I}^{(0)}$, and each chunk $\tilde{y}_h(n)$, $h \in \mathcal{H}^{(0)}$, that is:

$$v_{i,h} \triangleq \boldsymbol{V}(i,h) = \begin{cases} \|\boldsymbol{r}_{i,h}\|_2^2 & \text{if } i \in \mathcal{I}^{(l-1)} \text{ and } h \in \mathcal{H}^{(l-1)} \\ 0 & \text{otherwise} \end{cases} \tag{5.76}$$

where $\boldsymbol{r}_{i,h}$ is the h-th column of $\boldsymbol{R}_i^{(l)}$. Moreover, let $\tilde{\boldsymbol{V}} = [\tilde{\boldsymbol{v}}_0, \ldots, \tilde{\boldsymbol{v}}_{H-1}] \in \mathbb{R}^{M \times H}$ and $\tilde{\boldsymbol{V}}' = \left[\tilde{\boldsymbol{v}}'_0, \ldots, \tilde{\boldsymbol{v}}'_{H-1}\right] \in \mathbb{R}^{M \times H}$ be two normalised versions of the matrix $\boldsymbol{V}$, such that:

$$\tilde{\boldsymbol{v}}_h = \boldsymbol{v}_h - \frac{1}{\left|\mathcal{I}^{(l-1)}\right|} \sum_{i \in \mathcal{I}^{(l-1)}} v_{i,h} \tag{5.77}$$

has zero-mean, and

$$\tilde{\boldsymbol{v}}'_h = \tilde{\boldsymbol{v}}_h \left(\sum_{i \in \mathcal{I}^{(l-1)}} \tilde{v}^2_{i,h} \right)^{-\frac{1}{2}} \tag{5.78}$$

has unit variance.

(2.1) Each vector $\boldsymbol{v}_h$ (and its normalised versions $\tilde{\boldsymbol{v}}_h$ and $\tilde{\boldsymbol{v}}'_h$) can be seen as a signature of the h-th chunk $\tilde{y}_h(n)$ in the domain $\mathcal{D}_e$. These signatures are exploited to group the chunks as belonging or not to the same return. For doing this, the correlation matrix $\boldsymbol{\Sigma}_H \in \mathbb{R}^{H \times H}$ is defined as follows:

$$\boldsymbol{\Sigma}_H = \left(\tilde{\boldsymbol{V}}' \right)^T \tilde{\boldsymbol{V}}' \tag{5.79}$$

By definition the value of each element of $\boldsymbol{\Sigma}_H$ is in the range $[-1, 1]$ and indicates how correlated two chunks are in the $\mathcal{D}_e$ domain. Note that, in order for $\boldsymbol{\Sigma}_H$ to be a reliable measure of the correlation between the chunks, the number of active couples d_i must be greater, or at least equal, than the number of chunks and, in general, higher than a threshold set to 10, that is:

$$\left| \mathcal{I}^{(l-1)} \right| \geq \max \left(\left| \mathcal{H}^{(l-1)} \right|, 10 \right) \tag{5.80}$$

Steps (2.2) and (2.3) are only performed if this condition is met.

(2.2) Based on the correlation matrix $\boldsymbol{\Sigma}_H$, F subsets $\mathcal{H}_f$ of the set $\mathcal{H}^{(l-1)}$ are created, according to the following rules:

$$\begin{cases} a \in \mathcal{H}_f \subseteq \mathcal{H}^{(l-1)}, b \in \mathcal{H}_f \subseteq \mathcal{H}^{(l-1)} \iff \exists \boldsymbol{\Sigma}_H(a, b) \geq \iota \\ \mathcal{H}_f = \{a\} \subseteq \mathcal{H}^{(l-1)} \iff \nexists b : \boldsymbol{\Sigma}_H(a, b) \geq \iota \end{cases} \tag{5.81}$$

for $f = 0, \ldots, F-1$. The first rule states that two indices a and b, identifying two chunks $\tilde{y}_a(n)$ and $\tilde{y}_b(n)$, belong to the same group $\mathcal{H}_f$ if and only if their cross-correlation coefficient $\boldsymbol{\Sigma}_H(a, b)$ is higher than a threshold ι. The second rule, on the other hand, asserts that $\mathcal{H}_f$ is a singleton composed by the index a, if and only if it does not exist another chunk with a similar signature.

(2.3) Following the previous step, two chunks, say $\tilde{y}_a(n)$ and $\tilde{y}_b(n)$, that belong to the same group $\mathcal{H}_f$ present a similar signature in the $\mathcal{D}_e$ domain. However, they could be still portions of different returns, circumstance that occurs when helicopters of the same type are flying in formation. In this scenario, the characteristic that can be used to discriminate them is the initial offset of the blades, that is the positions $n_a^\star$ and $n_b^\star$. Firstly, based on their common signature, the periodicity of the flashes is estimated; then, if the distance between the two local maxima, $|n_a^\star - n_b^\star|$ is not a multiple of the estimated periodicity, then the chunks are assumed to belong to the two different returns.

(2.3.1) Find the couple $d_{i^\star} = (\omega_{i^\star}, \eta_{i^\star})$ that characterises the group $\mathcal{H}_f$ as:

$$i^\star = \underset{i \in \mathcal{I}^{(l-1)}}{\arg\min} \sum_{h \in \mathcal{H}_f} \tilde{\boldsymbol{v}}_h \tag{5.82}$$

Thus, following equation (2.33) the periodicity of the flashes, in seconds, can be estimated as:

$$\overline{\mu} = \frac{2\pi}{\omega_{i^\star}\eta_{i^\star}}\left(1 - \frac{\operatorname{mod}(\eta_{i^\star}, 2)}{2}\right) \tag{5.83}$$

where the operator $\operatorname{mod}(\cdot,\cdot)$ is the remainder of the division between the first and the second argument, respectively. The periodicity in samples becomes:

$$\overline{\mu}_s = \left\lfloor \frac{\overline{\mu}}{T_s} \right\rceil \tag{5.84}$$

where the operator $\lfloor \cdot \rceil$ indicates the nearest integer to the argument.

(2.3.2) Based on the estimated periodicity of the flashes, $\overline{\mu}_s$, and on the locations of the local maxima of the received signal, $n_h^\star$, for $h \in \mathcal{H}_f$, G_f

subsets $\mathcal{H}_f^g$ of the set $\mathcal{H}_f$ are created based on the following rules:

$$\begin{cases} a \in \mathcal{H}_f^g \subseteq \mathcal{H}_f, b \in \mathcal{H}_f^g \subseteq \mathcal{H}_f \iff \left| \dfrac{n_a^\star - n_b^\star}{\overline{\mu}_s} - \left\lfloor \dfrac{n_a^\star - n_b^\star}{\overline{\mu}_s} \right\rceil \right| \leq \varepsilon \\ \mathcal{H}_f^g = \{a\} \subseteq \mathcal{H}_f \iff \nexists b : \left| \dfrac{n_a^\star - n_b^\star}{\overline{\mu}_s} - \left\lfloor \dfrac{n_a^\star - n_b^\star}{\overline{\mu}_s} \right\rceil \right| \leq \varepsilon \end{cases} \tag{5.85}$$

for $g = 0, \ldots, G_f - 1$. The first rule states that two indices, namely two chunks, belong to the same group $\mathcal{H}_f^g$ if their distance in the received signal $z(n)$ is a multiple of the estimated periodicity of the flashes. $\mathcal{H}_f^g$ is a singleton, instead, if there is not another chunk such that this condition is satisfied. Note that, by construction, the following expressions hold:

$$\begin{aligned} \bigcap_{g=0,\ldots,G_f-1} \mathcal{H}_f^g = \emptyset, \quad \forall f \\ \bigcap_{f=0,\ldots,F-1} \mathcal{H}_f = \emptyset \end{aligned} \tag{5.86}$$

and

$$\begin{aligned} \mathcal{H}_f &= \bigcup_{g=0,\ldots,G_f-1} \mathcal{H}_f^g, \quad \forall f \\ \mathcal{H}^{(l-1)} &= \bigcup_{f=0,\ldots,F-1} \mathcal{H}_f \end{aligned} \tag{5.87}$$

(2.4) Each set $\mathcal{H}_f^g$ is then a collection of correlated chunks[28], since they potentially belong to the same return. Therefore, in order to mitigate this redundancy, E_f^g indices h that correspond to the largest residual errors $\sum_{i \in \mathcal{I}^{(l-1)}} \tilde{v}_{i,h}$ are removed from $\mathcal{H}_f^g$, obtaining the updated set $\tilde{\mathcal{H}}_f^g$, where

$$E_f^g = \left\lfloor \left| \mathcal{H}_f^g \right| (1 - \kappa) \right\rfloor \tag{5.88}$$

---

[28] Whether the condition (5.80) is not met, and steps (2.2) and (2.3) are not performed, the sets $\mathcal{H}_f^g$ and $\mathcal{H}_f$ refer to the previous iteration of the estimation process.

and $\kappa \in (0, 0.5]$. That is:

$$\tilde{\mathcal{H}}_f^g = \mathcal{H}_f^g - \mathcal{E}_{E_f^g} \tag{5.89}$$

where the set, $\mathcal{E}_x$, of x indices to remove is defined as:

$$\begin{cases} \mathcal{E}_0 = \emptyset \\ \mathcal{E}_x = \left\{ h \in \mathcal{H}_f^g - \mathcal{E}_{x-1} \mid \sum_{i \in \mathcal{I}^{(l-1)}} \tilde{v}_{i,h} \geq \sum_{i \in \mathcal{I}^{(l-1)}} \tilde{v}_{i,h'}, \right. \\ \qquad \left. \forall h' \in \mathcal{H}_f^g - \mathcal{E}_{x-1}, h' \neq h \right\} \bigcup \mathcal{E}_{x-1} \end{cases} \tag{5.90}$$

Moreover, following (5.87), the updated sets $\tilde{\mathcal{H}}_f$ and $\mathcal{H}^{(l)}$ are obtained:

$$\begin{aligned} \tilde{\mathcal{H}}_f &= \bigcup_{g=0,\ldots,G_f-1} \tilde{\mathcal{H}}_f^g, \quad \forall f \\ \mathcal{H}^{(l)} &= \bigcup_{f=0,\ldots,F-1} \tilde{\mathcal{H}}_f \end{aligned} \tag{5.91}$$

Figure 5.7 shows an example of nesting of the sets $\mathcal{H}$, $\mathcal{H}_f$ and $\mathcal{H}_f^g$. The overall set $\mathcal{H}^{(l-1)}$, before the pruning procedure, contains 6 indices, divided in two subsets $\mathcal{H}_0 = \{0, 1, 2\}$ and $\mathcal{H}_1 = \{3, 4, 5\}$. This means that the algorithm has recognised two distinctive signatures in the $\mathcal{D}_e$ domain, one shared between chunks $\tilde{y}_0(n)$, $\tilde{y}_1(n)$, $\tilde{y}_2(n)$ and the other between chunks $\tilde{y}_3(n)$, $\tilde{y}_4(n)$, $\tilde{y}_5(n)$. Moving further, while $\mathcal{H}_1$ coincides with $\mathcal{H}_1^0$, meaning that $\tilde{y}_3(n)$, $\tilde{y}_4(n)$ and $\tilde{y}_5(n)$ are actually portions of the same return,

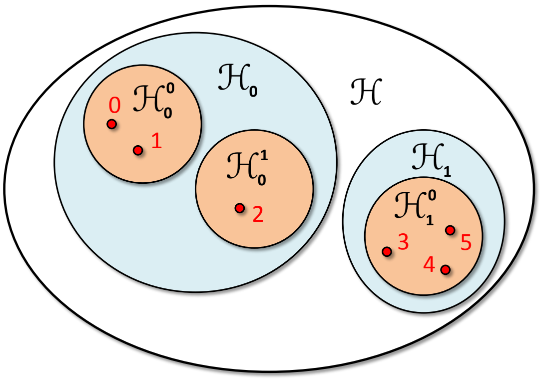

Figure 5.7: Example of nesting of the sets $\mathcal{H}$, $\mathcal{H}_f$ and $\mathcal{H}_f^g$.

namely they are redundant, $\mathcal{H}_0$ is the union of $\mathcal{H}_0^0 = \{0,1\}$ and $\mathcal{H}_0^1 = \{2\}$. Therefore, two helicopters with the same signature in the $\mathcal{D}_e$ domain have been recognised (that is, they have same number of blades and similar rotation speed): $\tilde{y}_0(n)$ and $\tilde{y}_1(n)$ are portions of the return from the first one, while $\tilde{y}_2(n)$ is a portion of the return from the second one. After the pruning process, assuming $\kappa = 0.25$, the updated sets are $\tilde{\mathcal{H}}_0^0 = \{0\}$, $\tilde{\mathcal{H}}_0^1 = \{2\}$ and $\tilde{\mathcal{H}}_1^0 = \{3\}$, which lead to $\tilde{\mathcal{H}}_0 = \{0,2\}$, $\tilde{\mathcal{H}}_1 = \{3\}$ and $\mathcal{H}^{(l)} = \{0,2,3\}$[29].

(3) Pruning of the dictionary: let us consider the mean residual errors for each couple d_i, $i \in \mathcal{I}^{(l-1)}$, and for each subset $\tilde{\mathcal{H}}_f$, $f = 0, \ldots, F-1$, that are the vectors:

$$\tilde{\boldsymbol{v}}_f^{\text{avg}} = \left[\tilde{v}_{f,0}^{\text{avg}}, \ldots, \tilde{v}_{f,i}^{\text{avg}}, \ldots, \tilde{v}_{f,M-1}^{\text{avg}}\right]^T = \frac{\sum_{h \in \tilde{\mathcal{H}}_f} \tilde{\boldsymbol{v}}_h}{\left|\tilde{\mathcal{H}}_f\right|} \in \mathbb{R}^M \tag{5.92}$$

Then, select $E = \left\lfloor \left|\mathcal{I}^{(l-1)}\right| (1-\nu) \right\rfloor$ indices i that correspond to the largest residual errors $\tilde{v}_{f,i}^{\text{avg}}$ and populate the set $\mathcal{E}_E^f$, that is:

$$\begin{cases} \mathcal{E}_0^f = \emptyset \\ \mathcal{E}_x^f = \Big\{ i \in \mathcal{I}^{(l-1)} - \mathcal{E}_{x-1}^f \mid \tilde{v}_{f,i}^{\text{avg}} \geq \tilde{v}_{f,i'}^{\text{avg}}, \\ \qquad \forall i' \in \mathcal{I}^{(l-1)} - \mathcal{E}_{x-1}^f, i' \neq i \Big\} \bigcup \mathcal{E}_{x-1}^f \end{cases} \tag{5.93}$$

where $\nu \in (0, 0.5]$. The remaining indices will then populate the set $\mathcal{U}^f = \mathcal{I}^{(l-1)} - \mathcal{E}_E^f$. Therefore, the set $\mathcal{E}_E^f$ contains the indices to remove from $\mathcal{I}^{(l-1)}$ with respect to the subset $\mathcal{H}_f$, while the indices in $\mathcal{U}^f$ are those to keep for the next iteration. The overall pruning is achieved as follows:

$$\mathcal{I}^{(l)} = \mathcal{I}^{(l-1)} - \left(\bigcup_{f=0}^{F-1} \mathcal{E}_E^f - \bigcup_{f=0}^{F-1} \mathcal{U}^f \right) \tag{5.94}$$

Note that, if $\bigcup_{f=0}^{F-1} \mathcal{E}_E^f - \bigcup_{f=0}^{F-1} \mathcal{U}^f = \emptyset$, the quantity ν is decreased to avoid the estimation process to be stuck in this state.

---

[29] Assuming that $\sum_{i \in \mathcal{I}^{(l-1)}} \tilde{v}_{i,0} \geq \sum_{i \in \mathcal{I}^{(l-1)}} \tilde{v}_{i,1}$ and $\sum_{i \in \mathcal{I}^{(l-1)}} \tilde{v}_{i,3} \geq \sum_{i \in \mathcal{I}^{(l-1)}} \tilde{v}_{i,4} \geq \sum_{i \in \mathcal{I}^{(l-1)}} \tilde{v}_{i,5}$

(4) Termination condition of the loop: if $\left|\mathcal{I}^{(l)}\right| = F$ and the sets $\tilde{\mathcal{H}}_f^g$ are all singleton, then go to step (5), otherwise return to step (1). This ensures that all the remaining chunks are uncorrelated and that the search of the mD parameters for each group $\mathcal{H}_f$ is complete.

(5) Let us define with $\overline{h}_0, \ldots, \overline{h}_s, \ldots, \overline{h}_{\overline{S}-1}$ the remaining indices in $\mathcal{H}^{(l)}$, where

$$\overline{S} = \left|\mathcal{H}^{(l)}\right| = \sum_{f=0}^{F-1} G_f \tag{5.95}$$

is the estimated number of targets. At each index $\overline{h}_s$, i.e. at each chunk $\tilde{y}_{\overline{h}_s}(n)$, is associated a couple $\overline{d}_s \in \mathcal{D}_e$ as:

$$\overline{d}_s = (\overline{\omega}_s, \overline{\eta}_s) \triangleq (\omega_{\overline{\imath}_s}, \eta_{\overline{\imath}_s}) = d_{\overline{\imath}_s} \in \mathcal{D}_e \tag{5.96}$$

where the index $\overline{\imath}_s$ is:

$$\overline{\imath}_s = \arg\max_{i \in \mathcal{I}^{(l)}} \tilde{\boldsymbol{v}}_{\overline{h}_s} \tag{5.97}$$

Finally, the index:

$$\overline{k}_s = \arg\max_{0 \le k \le P'_\Delta - 1} \left|\overline{\boldsymbol{x}}^{\mathcal{R}}_{\overline{\imath}_s, \overline{h}_s}\right| \tag{5.98}$$

identifies the wanted length:

$$\overline{\rho}_{\Delta,s} \triangleq \rho_{\Delta,\overline{k}_s} \in \mathcal{R}'_\Delta \tag{5.99}$$

where $\overline{\boldsymbol{x}}^{\mathcal{R}}_{\overline{\imath}_s, \overline{h}_s}$ is the $\overline{h}_s$-th column of $\overline{\boldsymbol{X}}^{\mathcal{R}}_{\overline{\imath}_s}$.

5.5.1.3 Identification

The identification is performed as for the single-target case for each estimate $\overline{d}_s$, $s = 0, \ldots, \overline{S} - 1$, by looking for the set $\mathcal{D}_e^k$, $k = 0, \ldots, L - 1$ which $\overline{d}_s$ belongs to. As already discussed above, however, this procedure could lead to ambiguous identifications, that can only be solved exploiting the information on the length of the blades, retrieved by using multiple sensors.

5.5.2 Multi-Sensors: Data Fusion

Each of the T sensors runs the identification algorithm described in Section 5.5.1 locally, and this leads to estimate the presence of $\overline{S}_t$ helicopters in the azimuth-elevation cell given by the angles α_{L_t} and β_{L_t}, for $t = 0, \ldots, T-1$. For each helicopter detected by the t-th sensor, the estimated number of blades is given by $\overline{\eta}_{s,t}$, while the estimated rotation speed is $\overline{\omega}_{s,t}$, for $s = 0, \ldots, \overline{S}_t - 1$. As for the single target scenario, the first advantage of the use of multiple sensors is the possibility to make the decision about the model of helicopter on a majority vote basis, while the second one is the capability to solve ambiguous identifications.

However, with respect to the single target scenario, a further consideration must be made. Indeed, the estimated number of target, $\overline{S}_t$, may differ from one sensor to another; for this reason, firstly an overall decision on the number of targets is made on a majority basis, by selecting $\overline{S}_{\text{multi}}$ to be the value, among $\overline{S}_0, \ldots, \overline{S}_{T-1}$, with the largest occurrence. Moreover, let $\mathcal{T}$ be the set of indices t that identify the sensors whose estimates $\overline{S}_t$ are equal to $\overline{S}_{\text{multi}}$, that is:

$$\mathcal{T} = \left\{ t \in \{0, \ldots, T-1\} \mid \overline{S}_t = \overline{S}_{\text{multi}} \right\} \tag{5.100}$$

Then, the ambiguous estimates are grouped based on their *similarity*, as already defined in (5.56). For simplicity, let us suppose that all the estimates $\overline{d}_{s,t} = \left(\overline{\omega}_{s,t}, \overline{\eta}_{s,t}\right)$, for $t \in \mathcal{T}$ and $s = 0, \ldots, \overline{S}_{\text{multi}} - 1$, are ambiguous[30]. Estimates are similar when the following conditions hold:

$$\begin{cases} \overline{\eta}_{s,t} = \overline{\eta}_{s',t'} \\ |\overline{\omega}_{s,t} - \overline{\omega}_{s',t'}| \leq \delta_\omega \end{cases} \tag{5.101}$$

for $t, t' \in \mathcal{T}, t \neq t'$ and $s = 0, \ldots, \overline{S}_{\text{multi}} - 1$. For each of these groups, the procedure already described in Section 5.4.2 for the single target scenario is carried out in order to estimate $\overline{\beta}_{H,s}$ and $\overline{\alpha}_{H,s}$, that lead to $\overline{\rho}_s$, for $s = 0, \ldots, \overline{S}_{\text{multi}} - 1$.

As before, when not all the estimates $\overline{d}_{s,t}$ are ambiguous, this procedure can be still applied by properly grouping the ambiguous estimates, provided that each subsets is

---

[30] Note that the indexing s is sensor-dependent. For example, the estimates $\overline{d}_{0,0}$ and $\overline{d}_{0,1}$ may not refer to the same actual helicopter, even if $s = 0$ for both.

composed by at least 3 sensors.

5.6 Performance Evaluation on Simulated Data

5.6.1 Database and Dictionary Design

The algorithms are tested by simulating discrete-time signals received from $L = 10$ helicopter models in different configurations with an L-band radar, $\lambda \backsim 0.23$ meters. Helicopters' name and mD parameters are listed in Table 5.1. The parametric sparse model introduced in Section 5.2.3, and in particular the creation of the sets $\mathcal{D}_e$ in (5.25) and $\mathcal{R}'_\Delta$ in (5.38), strictly depends on the composition of the database that contains the potential targets to identify. For the following analyses, the step sizes used to discretise the ranges of rotation speeds for the construction of the sets $\mathcal{D}_e^k$, for $k = 0, \dots, 9$, and the range of lengths of the blades for the set $\mathcal{R}'_\Delta$, are equal to $\delta_\omega = \frac{2\pi}{100}$ and $\delta_\rho = 1$, respectively. These, with 5 possible numbers of blades, lead to $M = |\mathcal{D}_e| = 339$ and $P'_\Delta = |\mathcal{R}'_\Delta| = 26$.

Table 5.1: Helicopters' Parameters - Simulated Data

ID (k)	**Name**	**# Blades** (η)	**Rot. Diameter** (2ρ)	**Rot. Speed** $(\tilde{\omega}/2\pi)$
0	AH-1 Cobra	2	14.63 m	4.9 rps
1	Mil MI-2 Hoplite	3	14.60 m	4.1 rps
2	UH-60 Black Hawk	4	16.36 m	4.3 rps
3	AS332 Super Puma	4	15.60 m	4.4 rps
4	*Confuser*	4	10.60 m	4.5 rps
5	AH-64 Apache	4	14.63 m	4.8 rps
6	SA365 Dauphin	4	11.94 m	5.8 rps
7	A109 Agusta	4	11.00 m	6.4 rps
8	MD-500E Defender	5	8.05 m	8.2 rps
9	CH-53 Stallion	7	24.08 m	2.9 rps

While the *AH-1 Cobra* (no. 0), the *Mil Mi-2 Hoplite* (no. 1), the *MD-500E Defender* (no. 8) and the *CH-53 Stallion* (no. 9) have a distinctive number of blades, which also means that the sets $\mathcal{D}_e^k$ for $k = 0, 1, 8, 9$ are disjoint, the other helicopter models present 4 blades. Looking at the graph in Figure 5.8, that shows on the horizontal axis the range of rotation speeds for each of these targets, it is clear that the

SA365 Dauphin (no. 6) and the *A109 Agusta* (no. 7) do not overlap, while the *UH-60 Black Hawk* (no. 2), the *AS332 Super Puma* (no. 3) and the *Confuser*[31] (no. 4) overlap each other, with the latter that also overlaps with the *AH-64 Apache* (no. 5). This may lead to ambiguous identifications, that can be only solved by estimating the orientation of the helicopter and using the length of the blades (vertical axis in Figure 5.8) as discriminative feature.

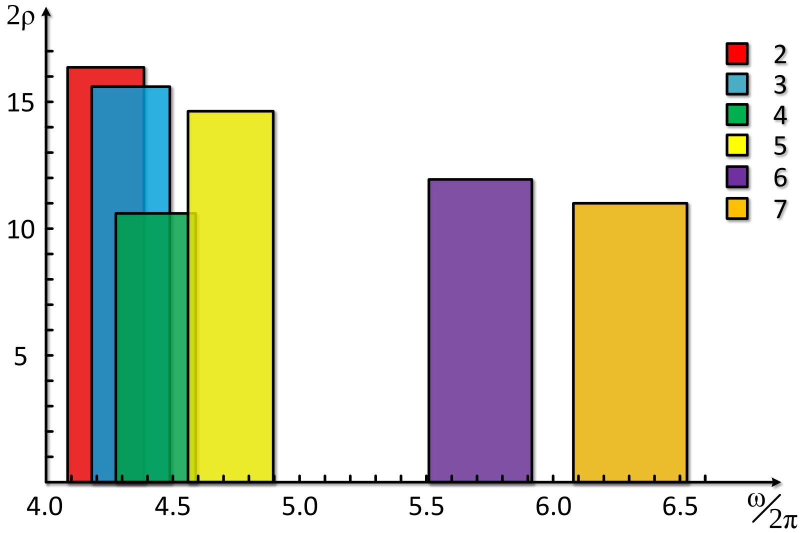

Figure 5.8: Rotation speeds and blades' lengths of the helicopter models no. 2, 3, 4, 5, 6 and 7.

The composition of the database also affects the minimum sampling frequency and the observation time that must be used. Taking into consideration the maximum possible product between rotation speeds and blades' lengths[32], the sampling frequency is chosen equal to $f_s = 12\,kHz$, which satisfies equation (5.22). However, analyses are also performed when f_s is one-fourth of the minimum one, that is $3\,kHz$. This choice is driven by the presence of real pulsed radar surveillance systems operating at L-band with $PRF = 3\,kHz$, such as the AN/SPS-65 [142]. Lastly, it is worth mentioning that with this selection of the sampling frequency, all the signals reflected by the helicopters, except for the Confuser, are likely to experience aliasing. Concerning the observation time, it must be greater than the distance between two flashes, defined

---

[31] Note that, the *Confuser* is not an actual helicopter model, but it is introduced to increase the probability of ambiguous identifications.

[32] Note that, all the possible combinations are considered, not only those presented in the database. This because both the received signal and the atoms of the dictionary must not present aliasing.

in equation (2.33), in the worst case. This ensures that at least two flashes are always visible in the signal to process $y\left(n\right)$. For this reason, the observation time is selected equal to $0.12\,s$, that leads to $N = 0.12/T_s = 1440$ samples. Moreover, the duration of the acquired signal is fixed to $0.60\,s$, leading to $J = 0.60/T_s = 7200$ samples.

The performance of the algorithms is evaluated by means of a Monte-Carlo simulation on varying the SNR on the slow-time signal[33]. The number of Monte-Carlo tests is 220 for each target, in the single-target case, or combination of targets, in the multi-target case. In each iteration the AWGN is randomly generated, as well as the position and orientation of the targets, their actual rotation speed and initial position of the blades. The multi-sensor system is designed as follows: $T = 5$ radar sensors with angular resolution of 5° are equally spaced on a circumference with radius $2500\,m$; the targets are randomly located within a circumference of radius $12\,km$, with a minimum and a maximum altitude of $200\,m$ and $3000\,m$, respectively.

5.6.2 Results: Single-Target Identification

A parameter to be specifically set for the single-target algorithm presented in Section 5.4 is $\nu \in (0, 0.5]$ in equation (5.50), that controls the speed of convergence: the larger ν, the faster the estimation process. For this analysis it is selected equal to 0.5.

Results are shown in Figure 5.9. Figure 5.9(a) and Figure 5.9(b) show the accuracy of the algorithm, with a blue solid line, and the percentage of unknowns, with a red dashed line, for $f_s = 12\,kHz$ and $f_s = 3\,kHz$, respectively. As the SNR increases, the accuracy increases and the percentage of unknowns decreases. With the higher selection for the sampling frequency, the accuracy reaches $83.91\,\%$ for $SNR = -10\,d\mathrm{B}$ and it is above $90\,\%$ for SNR greater than $-5\,d\mathrm{B}$, while the percentage of unknowns is below $1\,\%$. Slightly worst performance is obtained with $f_s = 3\,kHz$, where the maximum accuracy is $85.68\,\%$ and the percentage of unknowns is around $2.5\,\%$ for SNR above $-5\,d\mathrm{B}$. Figure 5.9(c) and Figure 5.9(d) show performance in terms of the figure of merit $\Upsilon \in [0, \infty)$, already introduced in Section 4.3. Specifically, it is used to demonstrate the effectiveness of the algorithm in estimating the factor Δ, and thus

---

[33] The slow-time signal may be the received signal in a CW radar system, or the slow-time signal after compression in a pulsed radar system.

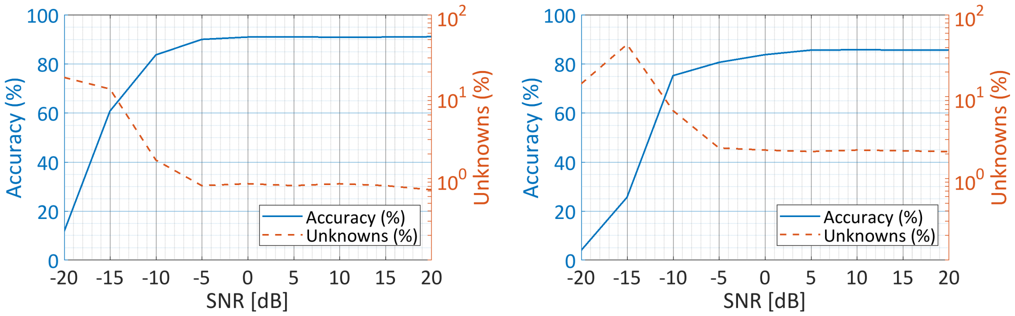

(a) Accuracy and unknowns, $f_s = 12\,kHz$. (b) Accuracy and unknowns, $f_s = 3\,kHz$.

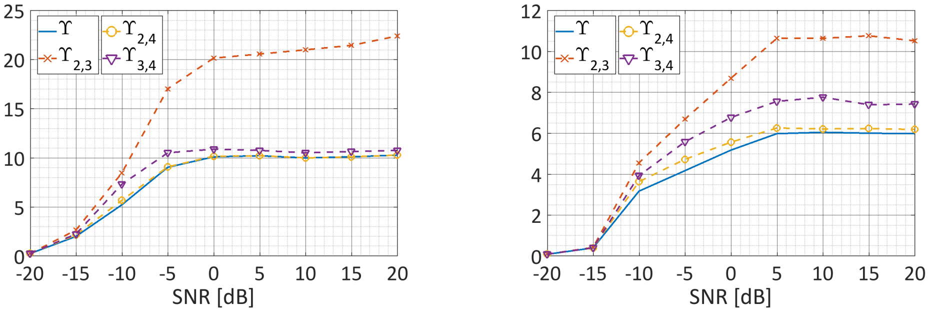

(c) Figure of merit Υ, $f_s = 12\,kHz$. (d) Figure of merit Υ, $f_s = 3\,kHz$.

Figure 5.9: Performance in terms of (a), (b) identification accuracy, unknowns and (c), (d) figure of merit Υ for the single-target algorithm on varying the SNR and for two values of the sampling frequency.

retrieving the length of the helicopter's blades. The figures depict Υ on varying the SNR, as well as $\Upsilon_{2,3}$, $\Upsilon_{2,4}$ and $\Upsilon_{3,4}$. These are computed while considering targets 2 and 3, targets 2 and 4, and targets 3 and 4 as one, respectively for $\Upsilon_{2,3}$, $\Upsilon_{2,4}$ and $\Upsilon_{3,4}$. Figure 5.9(c) refers to the case when $f_s = 12\,kHz$, and shows that $\Upsilon_{2,4}$ and $\Upsilon_{3,4}$ are very close to Υ. This means that the Confuser is unlikely to be confused with both the AS332 Super Puma and the UH-60 Black Hawk. Since they have the same number of blades and their rotation speed ranges overlap, as already shown in Figure 5.8, the discriminative feature used for the identification is the length of their blades, which, in turn, validates the data fusion approach employed for the estimation of Δ. On the other hand, $\Upsilon_{2,3}$ is much larger than Υ, which means that the AS332 Super Puma and the UH-60 Black Hawk are likely to be confused. However, this is expected since, in addition to the number of blades and the rotation speeds, the lengths of their blades are very similar too. Lastly, Figure 5.9(d) shows the same trend of $\Upsilon_{2,3}$, $\Upsilon_{2,4}$ and $\Upsilon_{3,4}$ with respect to Υ when $f_s = 3\,kHz$, even if $\Upsilon_{3,4}$ is further from Υ than before, and this is probably because the Confuser and the AS332 Super Puma have more similar rotation speeds than the Confuser and the UH-60 Black Hawk.

For completeness, an example of confusion matrix is shown in Table 5.2, for $SNR = 0\,d\mathrm{B}$ and $f_s = 12\,kHz$. In this case, $\Upsilon = 10.11$, while $\Upsilon_{2,3} = 20.15$, $\Upsilon_{2,4} = 10.17$ and $\Upsilon_{3,4} = 10.89$. From the confusion matrix, it can also be appreciated that targets 6 and 7 are sometimes confused with target 1, but not vice-versa. This because the algorithm is able to pick the characteristic odd number of blades of the target 1, namely the Mil Mi-2 Hoplite. On the other side, a helicopter with an even number of blades may be confused with one with an odd number of blades if they have a similar periodicity, and this happens for targets 6 and 7, namely SA365 Dauphin and A109 Agusta.

Table 5.2: Confusion matrix (%) obtained with the single-target algorithm, for $SNR = 0\,d\mathrm{B}$ and $f_s = 12\,kHz$.

	0	**1**	**2**	**3**	**4**	**5**	**6**	**7**	**8**	**9**	**Unk.**
0	98.2	0.0	0.0	0.0	0.0	0.0	0.0	0.0	0.0	0.0	1.8
1	0.0	99.5	0.0	0.0	0.0	0.0	0.0	0.0	0.0	0.0	0.5
2	0.0	0.0	93.1	6.4	0.0	0.0	0.0	0.0	0.0	0.0	0.5
3	0.0	0.0	36.4	60.4	3.2	0.0	0.0	0.0	0.0	0.0	0.0
4	0.0	0.0	0.5	2.7	96.8	0.0	0.0	0.0	0.0	0.0	0.0
5	0.0	0.0	0.0	0.0	0.0	100.0	0.0	0.0	0.0	0.0	0.0
6	0.0	10.9	0.0	0.0	0.0	0.0	86.8	0.0	0.0	0.0	2.3
7	0.0	21.4	0.0	0.0	0.0	0.0	0.0	77.2	0.0	0.0	1.4
8	0.0	0.0	0.0	0.0	0.0	0.0	0.0	0.0	99.5	0.0	0.5
9	0.0	0.0	0.0	0.0	0.0	0.0	0.0	0.0	0.0	98.2	1.8

5.6.3 Results: Multi-Target Identification

In addition to ν, equal to 0.25, other parameters that need to be set for the multi-target algorithm are H, ι, ε and κ. H is the maximum number of local maxima selected during the synchronisation stage, and it is set to 20. The thresholds ι and ε control the generation of the subsets $\mathcal{H}_f$ and $\mathcal{H}_f^g$ in (5.81) and (5.85), respectively, and are chosen equal to $\iota = 0.25$ and $\varepsilon = 0.10$. Finally, κ in (5.88) governs the pruning of the matrix $\tilde{\boldsymbol{Y}}$ in the same way in which ν controls the pruning of the dictionary, and it is selected equal to 0.50.

In order to test the effectiveness of the algorithm in estimating both the correct number of helicopters and their model, three scenarios have been considered. In the first one, only one target is supposed to be in the scene, while in the other two scenarios, either two or three helicopters are supposed to fly in formation. As for the single-target algorithm, results obtained with two different values of the sampling frequency are compared.

Figure 5.10 shows the results obtained for the first analysis, in which one target is assumed to be in the region of interest. The top graphs, Figure 5.10(a) and Figure

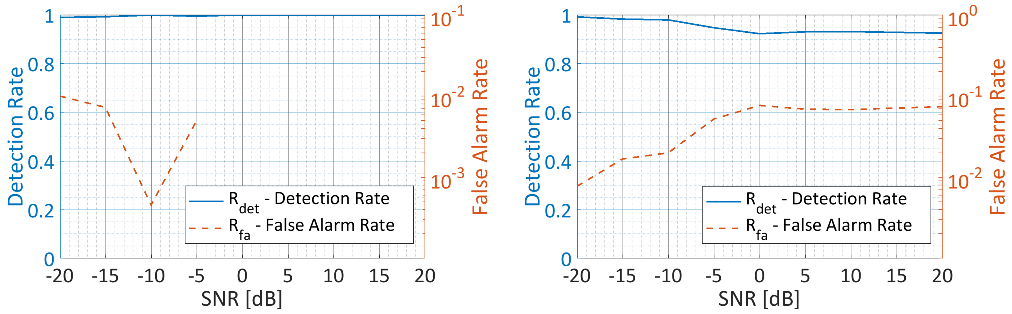

(a) Detection and false alarm, $f_s = 12\,kHz$. (b) Detection and false alarm, $f_s = 3\,kHz$

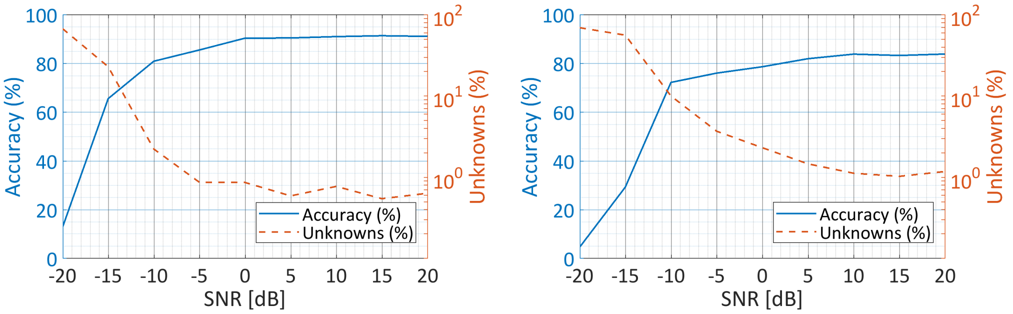

(c) Accuracy and unknowns, $f_s = 12\,kHz$ (d) Accuracy and unknowns, $f_s = 3\,kHz$

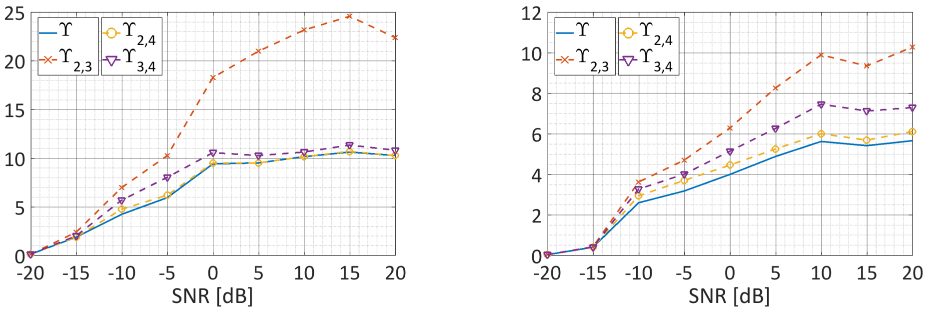

(e) Figure of merit Υ, $f_s = 12\,kHz$ (f) Figure of merit Υ, $f_s = 3\,kHz$

Figure 5.10: Performance in terms of (a), (b) detection rate, false alarm rate, (c), (d) identification accuracy, unknowns and (e), (f) figure of merit Υ for the multi-target algorithm tested on the presence of one target on the scene, on varying the SNR and for two values of the sampling frequency.

5.10(b), show the detection rate and the false alarm rate. The former is the ratio of the number of Monte-Carlo tests in which the number of helicopters has been correctly estimated to the total number of tests, that is:

$$R_{\text{det}} = \frac{\#\text{Monte} - \text{Carlo Tests} \mid \overline{\text{S}} = \text{S}}{\#\text{Monte} - \text{Carlo Tests}} \tag{5.102}$$

The latter is the ratio of the number of Monte-Carlo tests in which the number of helicopters has been overestimated to the total number of tests, namely:

$$R_{\text{fa}} = \frac{\#\text{Monte} - \text{Carlo Tests} \mid \overline{\text{S}} > \text{S}}{\#\text{Monte} - \text{Carlo Tests}} \tag{5.103}$$

Note that, at least one helicopter is always detected, which means that for this analysis $R_{\text{det}} + R_{\text{fa}} = 1$. The rate of detection for $f_s = 12\,kHz$ is close to 1 across all the values of SNR. When $f_s = 3\,kHz$, instead, it slightly decreases between $-10\,d\text{B}$ and $0\,d\text{B}$. This is due to the fact that, during the synchronisation stage, even if no peaks are above the threshold defined in equation (5.42), at least one target is always detected and identified as unknown; from this, the high percentage of unknowns in Figure 5.10(d). As the SNR increases, more peaks are selected in the synchronisation stage, and this lead to an increase of the false alarm rate and, consequently, to a reduction of the detection rate. Figure 5.10(c) and Figure 5.10(d) show accuracy and percentage of unknowns on varying the SNR, for the two choices of sampling frequency. Note that these quantities are conditional to the correct estimation of the number of targets, which means that, in order to get the overall accuracy and overall percentage of unknowns, they must be multiplied by R_{det}. Maximum accuracy is about $90\,\%$ for $f_s = 12\,kHz$ and above $80\,\%$ for $f_s = 3\,kHz$, in agreement with the results obtained with the single-target algorithm. Finally, Figure 5.10(e) and Figure 5.10(f) show the figure of merit Υ, and its related quantities $\Upsilon_{2,3}$, $\Upsilon_{2,4}$ and $\Upsilon_{3,4}$. As for the single-target algorithm, the sensitive difference between $\Upsilon_{2,3}$ and Υ, and, in the same time, the strong correlation between $\Upsilon_{2,4}$, $\Upsilon_{3,4}$ and Υ, demonstrates the goodness of of the fusion approach used for the estimation of Δ and, consequently, of the length of the blades.

During the second analysis, two helicopters are supposed to fly in formation, that is their returns are superimposed. They could be either the same or different models.

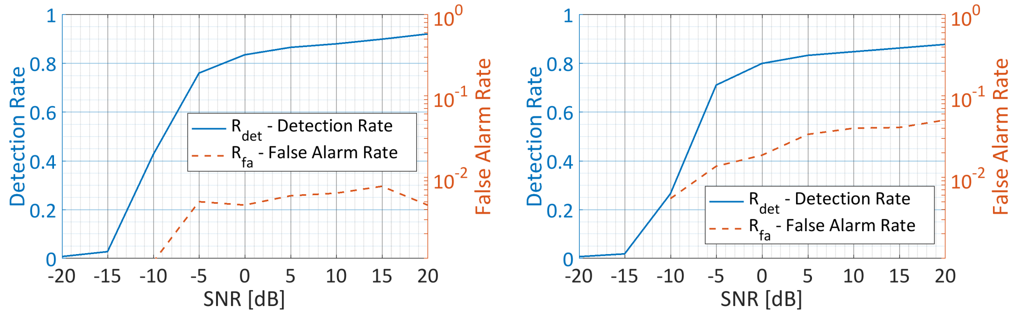

(a) $f_s = 12\,kHz$. (b) $f_s = 3\,kHz$.

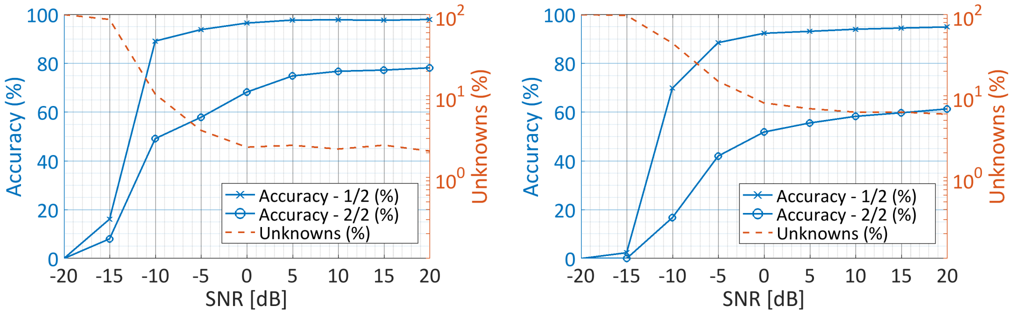

(c) $f_s = 12\,kHz$. (d) $f_s = 3\,kHz$.

Figure 5.11: Performance in terms of (a), (b) detection rate, false alarm rate, (c), (d) identification accuracy and unknowns for the multi-target algorithm tested on the presence of two targets on the scene, on varying the SNR and for two values of the sampling frequency.

Figure 5.11 shows the results. Top graphs, Figure 5.11(a) and Figure 5.11(b), show the detection and false alarm rates, which satisfy the condition $R_{\text{det}} + R_{\text{fa}} + R_{\text{miss}} = 1$, where R_{miss} is the rate of missing, that is the ratio of the number of Monte-Carlo tests in which the number of helicopters has been underestimated to the total number of tests. The rate of detection is above 0.80 for values of the SNR greater than $0\,d$B for both $f_s = 12\,kHz$ and $f_s = 3\,kHz$, while the false alarm rate is always below 0.01 and 0.06, respectively. The other two diagrams, Figure 5.11(c) and Figure 5.11(d), show the percentage of unknowns and the accuracy in correctly identifying both the helicopters or at least one of them. For $f_s = 12\,kHz$ and for SNR above $10\,d$B, the two accuracies are $77\,\%$ and $98\,\%$, respectively, which in absolute terms (that is, multiplying them for the rate of detection) become $69\,\%$ and $88\,\%$. In the same range of noise level, but when the lower sampling frequency is used, the accuracies reduces to $59\,\%$ and $94\,\%$, which in absolute terms are $50\,\%$ and $80\,\%$. In terms of percentage of unknowns, when the SNR is above $0\,d$B, it is approximately $2,4\,\%$ and $6.8\,\%$ for

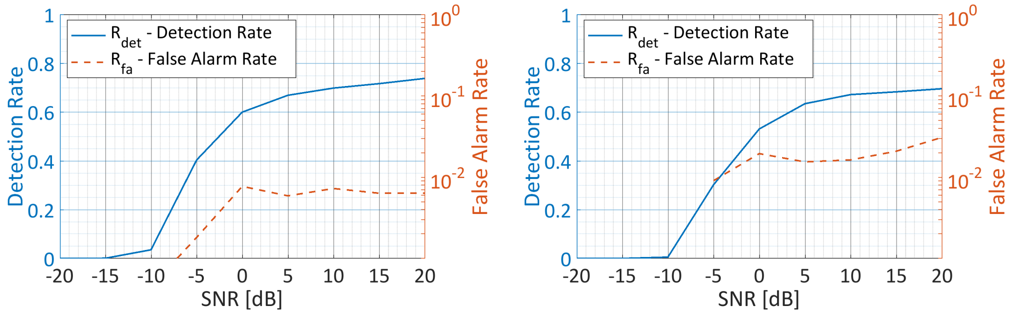

(a) $f_s = 12\,kHz$. (b) $f_s = 3\,kHz$.

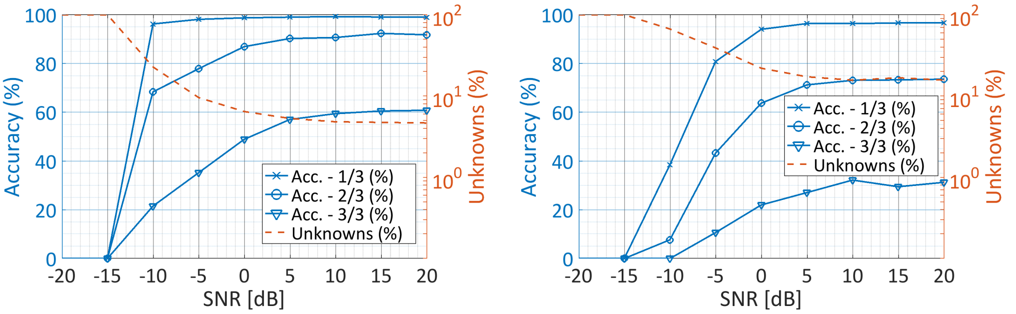

(c) $f_s = 12\,kHz$. (d) $f_s = 3\,kHz$.

Figure 5.12: Performance in terms of (a), (b) detection rate, false alarm rate, (c), (d) identification accuracy and unknowns for the multi-target algorithm tested on the presence of three targets on the scene, on varying the SNR and for two values of the sampling frequency.

$f_s = 12\,kHz$ and $f_s = 3\,kHz$, respectively.

Lastly, the same analysis is also performed while assuming that three helicopters are flying in formation. Results are shown in terms of detection and false alarm rate in Figure 5.12(a) and Figure 5.12(b), for $f_s = 12\,kHz$ and $f_s = 3\,kHz$, respectively. Detection rates are lower with respect to the previous analyses, reaching a maximum of 0.74 and 0.67, for the highest and the lowest sampling frequency, while the false alarm rate is below 0.004 and 0.05, respectively. Moreover, when 3 targets are estimated, in the $99\,\%$ of the cases and for SNR greater than $5\,d$B, at least one of them is correctly identified. This percentage reduces to $90\,\%$ and $58\,\%$ when identifying at least 2, or all the 3 targets, respectively, as shown in Figure 5.12(c) for $f_s = 12\,kHz$. These percentages are equivalent to $67\,\%$, $61\,\%$ and $40\,\%$ in terms of absolute accuracy. When $f_s = 3\,kHz$, the relative accuracy decreases to $96\,\%$, $68\,\%$ and $26\,\%$ as shown in Figure 5.12(d), which, in absolute terms is equivalent to $64\,\%$, $46\,\%$ and $17\,\%$. Furthermore, the percentage of unknowns is much higher in this last evaluated scenario, being of about $5\,\%$ and $17\,\%$ for SNR above $5\,d$B and for $f_s = 12\,kHz$ and $f_s = 3\,kHz$, respectively.

5.7 Performance Evaluation on Real Data

The validity of the algorithms is proved on real data. The dataset is a collection of signals acquired in an anechoic chamber with a $24\,GHz$ CW radar and scattered from a two-bladed helicopter scale model GAUI X3, whose main rotor is made to rotate at three different speeds in order to simulate as many targets H_1, H_2 and H_3. The actual values of the speed are not available, hence they are evaluated by inspection of the time domain signals and the obtained values are shown in Table 5.3, along with the standard deviations of the estimates. The GAUI X3's main blade length is $36\,cm$, which corresponds to a full-size helicopter with blade length of about $660\,cm$ in a real scenario with an L-band radar. However, the availability of signals recorded from only one target, does not allow to validate the multi-sensor fusion framework, since no diversity is available in terms of length of the blades.

Table 5.3: Helicopters' Parameters - Real Data

Target	**Average Speed** ($\tilde{\omega}/2\pi$)	**Standard Deviation**
H_1	$8.58\,rps$	0.13
H_2	$9.85\,rps$	0.18
H_3	$11.41\,rps$	0.34

Four acquisitions are made for each speed, at four different aspect angles $\beta_L = 0°, 15°, 30°, 45°$[34]. From each signal, whose total length is approximately 40 seconds, 90 segments of 0.40 seconds are extracted, filtered to remove the stationary clutter, and downsampled with a factor of 2 in order to match the sampling frequency of $11\,kHz$. Considering that the observation time is selected equal to $0.25\,s$, $N = 2750$ samples.

Both the single-target and the multi-target algorithms are tested, even if the latter is only evaluated in presence of single helicopters to assess the accuracy in estimating the number of targets. The dictionary is built assuming that the actual rotation speeds

---

[34] The pitch angle $\pi/2 - \beta_H$ is zero.

can vary within a range of three times the standard deviation of the estimates. Moreover, six confusers are introduced, having the same rotation speeds shown in Table 5.3, with either 3 or 4 blades. All the parameters are set as for the analysis performed on simulated data.

The results for the single-target algorithm are summarised in Table 5.4, for each target and on varying the aspect angle. The overall accuracy is above $95\,\%$, and the worst performance is obtained with signals acquired with aspect angle $\beta_L = 0°$. This is probably due to the small RCS of the blades in this geometry.

Table 5.4: Real data performance evaluation. Single-target algorithm, accuracy ($\%$).

Target	**Aspect Angle** (β_L)			
	$0°$	$15°$	$30°$	$45°$
H_1	85.6	100	96.7	100
H_2	98.9	100	100	100
H_3	67.8	100	97.8	97.8

Table 5.5 and Table 5.6 show the results for the multi-target algorithm, in terms of detection rate and percentage of accuracy, respectively. The detection rate is above 0.90 in all the analysed case, while the overall accuracy is of about $96.7\,\%$.

Table 5.5: Real data performance evaluation. Multi-target algorithm, detection rate.

Target	**Aspect Angle** (β_L)			
	$0°$	$15°$	$30°$	$45°$
H_1	0.94	0.89	0.89	0.89
H_2	0.82	0.85	0.86	0.97
H_3	0.92	0.94	0.90	1.00

Table 5.6: Real data performance evaluation. Multi-target algorithm, accuracy ($\%$).

Target	**Aspect Angle** (β_L)			
	$0°$	$15°$	$30°$	$45°$
H_1	83.8	100	98.4	100
H_2	98.3	100	100	100
H_3	81.8	100	100	98.6

5.8 Conclusion

A micro-Doppler (mD) model-based algorithm for identification of helicopters was presented in this Chapter, which used a parametric sparse representation of the received signal from the helicopter's rotor in combination with a modified version of a greedy sparse recovery framework, namely the Pruned Orthogonal Matching Pursuit (POMP), to estimate the mD parameters of the target and perform the identification. The algorithm, developed in Section 5.4 for the identification of single-targets and in Section 5.5 for multiple targets, is independent of both the orientation of the aircraft and the initial offset of the blades. Moreover, an information fusion approach was developed with the objective of merging the identification outputs coming from multiple sensors. This allowed to enhance the identification by exploiting the information on the length of the blades, otherwise unused because strongly related on the aspect angle.

Both the variants of the algorithm were tested on simulated data in Section 5.6, on varying the level noise and for high and low Pulse Repetition Frequency (PRF), or sampling frequency f_s, namely $12\,kHz$ and $3\,kHz$ respectively. Results on the single-target algorithm showed that, even at low Signal-to-Noise Ratios (SNRs), for example $-10\,d$B, the estimate was accurate at $85\,\%$ and $75\,\%$, with high and low PRF respectively, achieving a maximum of $92\,\%$ and $85\,\%$ at higher SNRs. When using the multi-target algorithm and two helicopters were flying in formation, the rate of detection was about 0.85 at $SNR = 0\,d$B for both $f_s = 12\,kHz$ and $f_s = 3\,kHz$, with accuracy in identifying 2 out of 2 targets of $70\,\%$ and $50\,\%$ in the two cases; at least one target was correctly identified with an accuracy above $90\,\%$.

In Section 5.7 the performance analysis was extended to data acquired in a controlled environment emulating a real scenario with the presence of one target. Results on both the single-target and the multi-target algorithm validated the concept, with an overall accuracy of $95\,\%$ for the first one, and a detection rate of 0.90 and accuracy of $96.7\,\%$, for the second one.

Chapter 6

FrFT Based CoRadar System

6.1 Introduction

In Chapter 4 and Chapter 5 two Automatic Target Recognition (ATR) algorithms were presented, for the classification of civilian and military vehicles from Synthetic Aperture Radar (SAR) images and for the identification of helicopters through the exploitation of their characteristic micro-Doppler (mD) signatures, respectively. Both these algorithms could exploit the advantage of working in a network of radars spatially distributed, that *see* the target under test from different aspect angles. This diversity was used to enhance the classification performance, provided that the sensors could share their information within the network or with a global fusion centre.

In scenarios like the one described above, dual function radar systems that sense the environment while sending data to one or multiple cooperative systems would be suitable. In Chapter 3, some of the most recent technologies enabling spectrum sharing between communication and radar systems were reviewed, with particular focus on Communicating-Radar (CoRadar) systems (Section 3.3.2), able of embedding data in the transmitted signal while maintaining good radar performance, with the advantage of using the same bandwidth, power and hardware already allocated for the radar task. In this Chapter a novel waveform design framework for CoRadar systems, based on the Fractional Fourier Transform (FrFT) described in Section 3.4, is presented. The framework is highly flexible, since it easily adapts to the bandwidth and pulse length allocated to meet the radar requirements, and to the conditions of the channel. Therefore, depending on the application, the maximum detectable range can vary from few to hundreds of km, while the data rate can be as high as few Mb/s at medium-long distances. Moreover, unlike other approaches, it does not require a phased array antenna, thus not limiting the scope of application.

The remainder of the Chapter is organised as follows. Section 6.2 introduces the proposed waveform design framework, while three optimisation procedures are described in Section 6.3. Section 6.4 presents the implementation of the FrFT CoRadar system on a Software Defined Radio (SDR) device, while radar and communication performance are reported in Section 6.5, both on simulated and real data. Finally, Section 6.6 reports some practical challenges to address, providing direction for further developments.

6.2 Waveform Design

The proposed CoRadar waveform design framework is a multiplexing scheme that uses the FrFT to map the In-phase and Quadrature (IQ) symbols of a selected modulation scheme to different chirp, or LFM, sub-carriers with different time-frequency rates. On transmission the radar is in charge of generating the waveform that embeds the data, while on reception it performs common operations such as matched or mismatched filtering (whose impulse response may change pulse-to-pulse), detection, Doppler processing, etc. The co-operative communication system that receives the sequence of FrFT CoRadar pulses demodulates them and extracts the embedded information. In the following sections, the novel method of information embedding and extraction is presented. Moreover, a pilot waveform is designed aimed at synchronising the pulse and compensating its phase offset at the receiver side.

6.2.1 Information Embedding

The waveform design framework is shown in Figure 6.1. The bits to be embedded in the FrFT CoRadar pulse are divided into $C - 1$ segments of N_b bits each by the serial-to-parallel (S/P) block, where C is the number of chirp sub-carriers to use. The 0-th order sub-carrier is not used to carry information bits. It accommodates a pilot

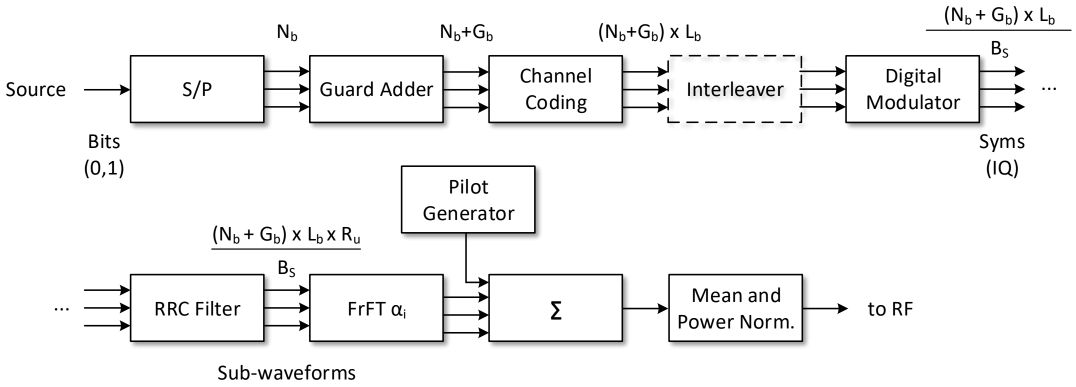

Figure 6.1: Block diagram of the radar transmitter of the FrFT CoRadar system in charge of the waveform generation.

waveform instead, used at the communication receiver for synchronisation and phase compensation. Since each pulse contains $N_b \times (C-1)$ information bits, the final bit rate is $N_b \times (C-1) \times \text{PRF}$ bit per seconds.

In each segment, G_b guard bits are added at the end of the sequence in order to compensate the group delay introduced by the Root Raised Cosine (RRC) filter. Subsequently an Error Correcting Code (ECC) is applied, identified by the couple $(b_{\text{out}}, b_{\text{in}})$. It assigns to each group of b_{in} bits, called dataword, a sequence of b_{out} bits, a codeword, with the aim of detection and correction of errors. The codeword is selected to be an L_b-long Barker code[35], hence $b_{\text{out}} = L_b$, while b_{in} is chosen equal to 1. Therefore, the employed coding technique effectively consists of a repetition ECC and leads to a coded sequence of $(N_b + G_b) \times L_b$ bits. This channel coding technique is able to correct up to $\lfloor L_b/2 \rfloor$ errors per codeword.

An interleaver may be used to mitigate the Inter-Carrier Interference (ICI). This solution is discussed in more detail later in Section 6.3.1.

The digital modulator maps a series of B_S bits to one of the $M_S = 2^{B_S}$ possible complex symbols belonging to the chosen modulation scheme (i.e. QAM, PSK), leading to a $(N_b + G_b) \times L_b/B_S$ long symbol sequence. The modulation scheme and the cardinality of its alphabet, M_S, can be adaptively chosen according to the conditions of the channel.

The RRC filter is used to minimise the Inter-Symbol Interference (ISI) that may

---

[35] The Barker code is selected for its good autocorrelation properties. However any other sequence with similar properties can be used, and even other ECC techniques can be employed.

be caused by the channel. For efficiency, it is implemented as a multirate filter that up-samples the output by a factor R_u, leading to a final sequence of $N = (N_b + G_b) \times L_b \times R_u / B_S$ samples.

The $C - 1$ sub-waveforms obtained after the RRC filter are then mapped to different chirp sub-carriers uniformly spaced in the time-frequency domain. Note that the FrFT is periodic in ϕ with period 2π, however rotations of ϕ and $\phi + \pi$ produce signals that overlap in the time-frequency plane, as demonstrated by equation (3.4). For this reason, only angles in the range $[0, \pi)$ are considered, which, through equation (3.2), leads to $\alpha \in [0, 2)$. Thus, the uniformly spaced sub-carriers are obtained by choosing the i-th fractional order to be equal to $\alpha_i = i\bar{\alpha}, i = 1, \ldots, C - 1$, where $\bar{\alpha} = \frac{2}{C}$. The waveform is then obtained by superimposing the chirp modulated sub-waveforms and the pilot waveform; before sending it to the RF front-end, its mean is removed and the power is normalised such that all the transmitted pulses present the same power.

The spectrogram of a FrFT CoRadar waveform with relatively few sub-carriers ($C = 7$) is shown in Figure 6.2 for clarity, although in practice the spectrogram could appear more crowded. Each sub-carrier (except for the 0-th order sub-carrier that accommodates the pilot waveform) is the rotation by a specific angle, driven by the order of the FrFT, of a phase modulated signal (i.e. PSK). The time axis is normalised to the length of the pulse, τ, while the frequency axis is normalised to its bandwidth:

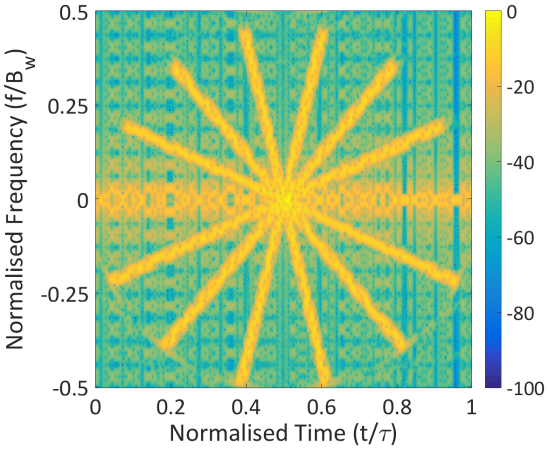

Figure 6.2: Spectrogram of a FrFT CoRadar waveform with 7 sub-carriers.

$$B_w = \frac{N}{\tau} = \frac{(N_b + G_b) \times L_b \times R_u}{\tau B_S} \tag{6.1}$$

6.2.2 Pilot Waveform

As mentioned before, the pilot waveform embedded in the 0-th order sub-carrier is used for both synchronisation and phase estimation and compensation at the communication receiver. The synchronisation is necessary since the pulse could fall anywhere within a PRI due, for example, to the transmitter-receiver distance, and the alignment with the signal on a sample basis is needed to perform the Inverse FrFT (IFrFT). Moreover, the phase offset introduced by the channel has also to be compensated in order to ensure the correct demodulation of the data.

The selected pilot waveform is a bi-phase coded signal run by a Coarse/Acquisition (C/A) code [143] given by:

$$p\left(n\right) = e^{j\pi\left(a(n)-\frac{1}{4}\right)} \tag{6.2}$$

where $a\left(n\right)$ is the selected C/A code properly up-sampled and truncated to match the length, in samples, of the FrFT CoRadar waveform. Figure 6.3(a) shows the autocorrelation of the pilot waveform, which, due to its narrow main lobe and low side lobes, is suitable for the detection and synchronisation of the pulses. The phase estimation and compensation is performed pulse-to-pulse by evaluating the phase of the autocorrelation's peak. Figure 6.3(b) shows how its complex value changes on varying the phase offset. In particular, when the offset is zero the real part reaches its maximum,

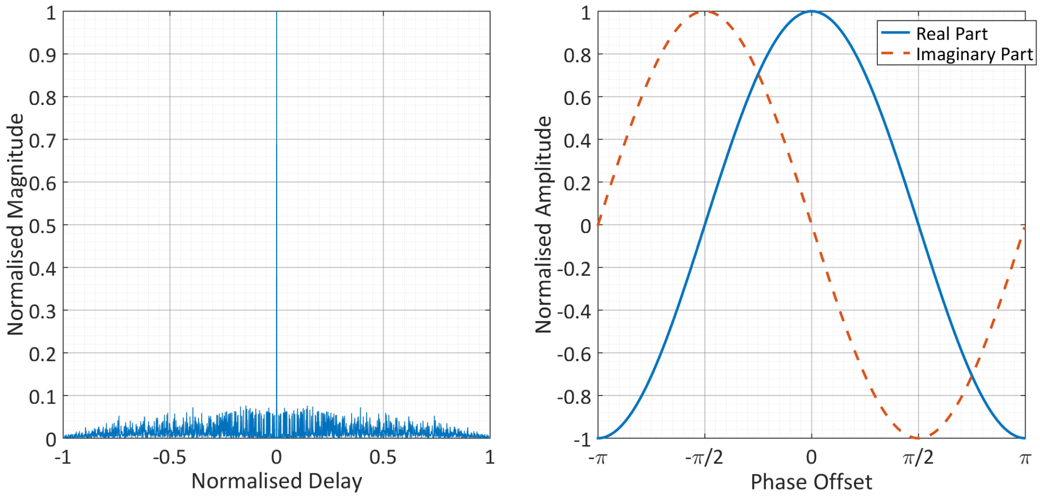

(a) Pilot's autocorrelation.

(b) Peak of the pilot's autocorrelation.

Figure 6.3: Pilot waveform's (a) autocorrelation and (b) its peak's complex value on varying the phase offset.

while the imaginary part is zero. Hence, at the communication receiver, once the peak of the autocorrelation is detected by matched filtering the received signal with the pilot waveform, the phase offset can be firstly estimated by evaluating the phase of such correlation peak, and then compensated accordingly.

6.2.3 Data Extraction

The block diagram of the Communication Receiver of the FrFT CoRadar system is shown in Figure 6.4. Once the synchronisation and the phase compensation are performed as explained above by exploiting the pilot waveform, the pulse can be demodulated. The S/P block splits and redirects the acquired signal, whose length is $(N_b + G_b) \times L_b \times R_u / B_S$ samples, to $C - 1$ different IFrFT blocks. Each sequence is then input of the RRC filter, which also down-samples the sub-waveform by a factor R_u. The digital demodulator translates the $(N_b + G_b) \times L_b / B_S$ long sequence of symbols in a sequence of $(N_b + G_b) \times L_b$ bits, according to the modulation employed. At this point, a de-interleaver may be placed which performs the inverse operation of the interleaver. The channel decoding block correlates the input coded sequence with the L_b-long Barker chip code used in transmission to extract the N_b bits of information, exploiting both the low correlation side lobes and the knowledge that the peaks of the correlation occur every L_b samples. Finally, the guard remover and the P/S blocks reconstruct the original stream by combining the N_b-long bit sequences coming from the $C - 1$ different parallel branches.

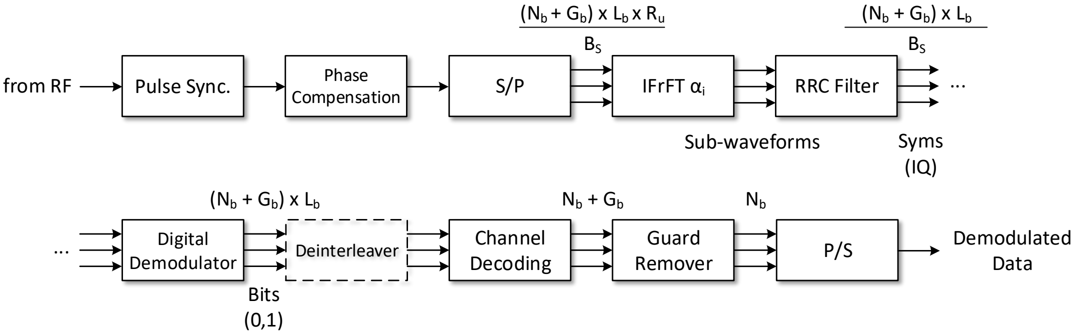

Figure 6.4: Block diagram of the communication receiver of the FrFT CoRadar system, whose task is the demodulation of the received pulses.

6.3 Waveform Optimisation

In this section three waveform optimisation procedures are described. The introduction of either a guard time or an interleaver has the objective of minimising the ICI, caused by the overlap of the chirp sub-carriers. Then, for both these methods, a parameters selection process is presented that maximises the data rate while fixing some parameters that meet the radar requirements. Finally, the adaptive duration of the sub-waveforms that aims to efficiently occupy the available bandwidth is introduced.

6.3.1 ICI Mitigation

Due to the nature of chirps, when more sub-carriers are superimposed there is an overlapping area with centre at the zero frequency and half duration of the pulse that produces ICI. This effect is clear in Figure 6.2, and needs to be mitigated in order to guarantee a reliable communication channel. In this section two ICI mitigation approaches are proposed for the developed waveform design, namely guard time and interleaver.

6.3.1.1 Guard Time

In order to avoid data loss, the time-frequency region affected by ICI is not used for the transmission of bits of information but carries guard bits instead. This can be achieved by slightly modifying the guard adder block in Figure 6.1, such that it adds both G_b'' bits in the middle of the sequence to mitigate the ICI and G_b' bits at the end in order to compensate the group delay introduced by the RRC filter, leading to an overall guard band width of $G_b = G_b' + G_b''$. The ICI guard band width in normalised time unit, called τ_{guard}, is defined as:

$$\tau_{\text{guard}} = \nu_{\text{guard}} Q \tag{6.3}$$

where $\nu_{\text{guard}} \in [0, 1]$ and Q is a measure of the sub-carriers overlap, graphically represented by the diameter of the red circle in Figure 6.5. The value of Q depends on the inter-carrier separation angle $\psi = \phi_{i+1} - \phi_i = \pi/C, \forall i = 0, \dots, C-2$, with ϕ_i be the

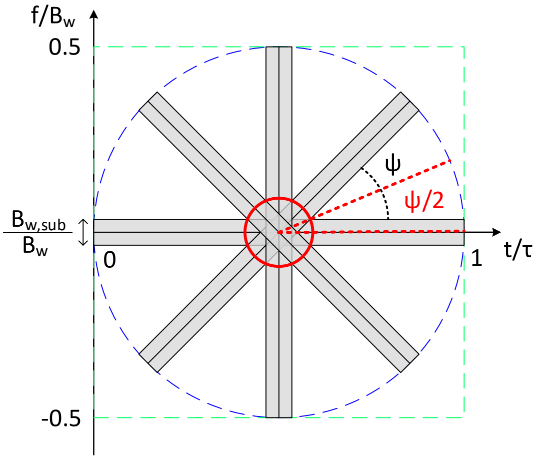

Figure 6.5: Waveform optimisation: representation of the region affected by Inter-Carrier Interference (ICI).

rotation angle of the i-th chirp sub-carrier, and it is equal to:

$$Q = \frac{B_{w,sub}}{B_w} \csc\left(\frac{\pi}{2C}\right) \tag{6.4}$$

where $B_{w,sub}$ is the bandwidth of each sub-waveform:

$$B_{w,sub} = \frac{\left(N_b + G_b' + G_b''\right) L_b}{\tau B_S} (\beta + 1) \tag{6.5}$$

and β is the RRC roll-off coefficient. The guard time τ_{guard} finally translates to a guard band width of G_b'' bits given by:

$$G_b'' = \left\lfloor \left(N_b + G_b'\right) \frac{\tau_{\text{guard}}}{1 - \tau_{\text{guard}}} \right\rfloor = \left\lfloor \left(N_b + G_b'\right) \frac{\nu_{\text{guard}} Q}{1 - \nu_{\text{guard}} Q} \right\rfloor \tag{6.6}$$

6.3.1.2 Interleaver

The second approach to mitigate the ICI is the use of an interleaver. As shown in Figure 6.5, the interference is localised around the centre of rotation of the waveform. This means that it generates a burst of errors, affecting a small group of bits that can be dealt with the use of a suitable interleaving technique.

An interleaver/de-interleaver pair placed before the digital modulator in transmission and after the digital demodulator in reception (Figure 6.1 and Figure 6.4, respectively), and applied only to the N_b bits of information, spreads the burst errors across the entire sequence. Figure 6.6 shows, with an example, the operation of a basic interleaver, implemented as a matrix filled by rows and emptied by columns [144], and how it is used to mitigate the ICI. Let $[a, b, c, d, e]$ be the sequence of $N_b = 5$ bits, or datawords, that is carried by the i-th sub-carrier. After the application of the channel code, each dataword is replaced by a codeword of length $L_b = 3$ as explained above. When combining the different sub-waveforms, the *effect of the overlap* is to corrupt few or all the bits of some codewords: in the example shown, when no interleaver is used the corrupted bits are $[b_3, c_1, c_2, c_3, d_1]$. Since the employed channel coding technique is able to correct up to $\lfloor L_b/2 \rfloor = \lfloor 3/2 \rfloor = 1$ error per codeword, the dataword c cannot be reconstructed. The interleaver is used to deterministically scramble the bits of the codewords: when it is employed as shown in the example, the corrupted bits are $[a_2, b_2, c_2, d_2, e_2]$. Each codeword has one corrupted bit, that can be detected and corrected at the communication receiver during the channel decoding.

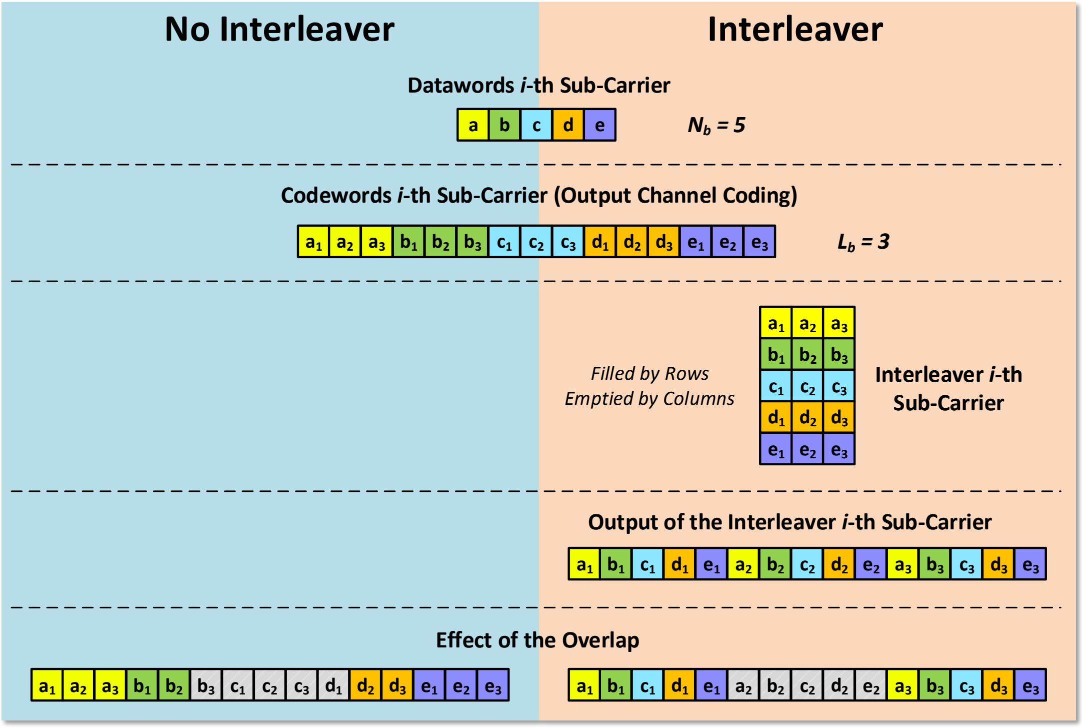

Figure 6.6: Operating principle of the interleaver as Inter-Carrier Interference (ICI) mitigation approach.

6.3.2 Parameters Selection

The parameters of the proposed FrFT CoRadar system that may and must properly be set are several and tightly cross related. For example, in order to increase the data rate per pulse, either the number of bits per sub-carrier, N_b, or the number of sub-carriers, C, needs to be increased. In the former case, this will lead to a larger bandwidth occupancy or a longer pulse width, from equation (6.1), while in the second case it will enlarge the overlapping area, as shown in equation (6.4), with consequences on the selection of G''_b and L_b in order to keep the quality of the transmission, depending on the ICI mitigation approach used.

In this section two procedures for the selection of the parameters are presented, with the assumption that the radar task is prioritised with respect to the communication one. For this reason the following discussion starts from the pulse's bandwidth, B_w, and length, τ, that account for some radar requirements such as range and Doppler resolution and minimum detectable range, and aims to derive the number of sub-carriers, C, of bits per sub-carriers, N_b, and the up-sampling factor, R_u, in order to maximise the bit rate while fixing the number of bits per symbol, B_S, the length of the Barker code, L_b, and the number of guard bits, G'_b, due to the design of the RRC filter. The process differs depending on the ICI mitigation technique used.

6.3.2.1 Guard Time

The number of samples per waveform, N, is bounded by the time-bandwidth product as follows (see equation (6.1)):

$$B_w \times \tau \geq \frac{N_b + G'_b + G''_b}{B_S} L_b R_u = \frac{N_b + G'_b}{(1 - \nu_{\text{guard}} Q)\, B_S} L_b R_u \tag{6.7}$$

where the last analytical step is given by equation (6.6). By rewriting Q in (6.4) by means of (6.1) and (6.5) as:

$$Q = \frac{\beta + 1}{R_u} \csc\left(\frac{\pi}{2C}\right) \tag{6.8}$$

and substituting (6.8) into (6.7), a second degree inequality in R_u can be obtained, such that $R_{u,\min} \leq R_u \leq R_{u,\max}$, which admits real solutions only if the following condition is met:

$$C\left(N_b\right) \leq \frac{\pi}{2} \frac{1}{\sin^{-1}\left(\frac{4\left(N_b+G'_b\right)L_b\nu_{\mathrm{guard}}(\beta+1)}{B_S\tau B_w}\right)} \tag{6.9}$$

where the dependency of C from N_b is highlighted for clarity. Since the greater the number of sub-carriers, the higher the data rate, $C\left(N_b\right)$ is fixed as:

$$C\left(N_b\right) = \left\lfloor \frac{\pi}{2} \frac{1}{\sin^{-1}\left(\frac{4\left(N_b+G'_b\right)L_b\nu_{\mathrm{guard}}(\beta+1)}{B_S\tau B_w}\right)} \right\rfloor \tag{6.10}$$

Thus the parameters selection can be achieved by following this iterative procedure:

(1) Find N_b such that:

$$\max_{N_b} N_b\left(C\left(N_b\right)-1\right) \quad \text{s.t.} \quad N_b \in \mathbb{N} \tag{6.11}$$

while fixing ν_{guard}.

(2) Choose the maximum value of R_u within its range of solutions from the second degree inequality, that is:

$$R_u = \left\lfloor R_{u,\max} \right\rfloor \tag{6.12}$$

subject to:

$$\frac{\left(N_b + G'_b + G''_b\left(R_u\right)\right)L_b}{B_S} \in \mathbb{N} \tag{6.13}$$

where the dependency of G''_b from R_u comes from equations (6.6) and (6.8). This condition guarantees that the number of symbols after the digital modulator is integer.

If the last step has no solution, the procedure is repeated by excluding the previous found solutions for N_b.

6.3.2.2 Interleaver

When an interleaver is used as ICI mitigation approach, the application of the bound of the number of samples leads to a first degree inequality as follows:

$$R_u\left(N_b\right) \leq \frac{B_w \tau B_S}{\left(N_b + G_b'\right) L_b} \Rightarrow R_u\left(N_b\right) = \left\lfloor \frac{B_w \tau B_S}{\left(N_b + G_b'\right) L_b} \right\rfloor \tag{6.14}$$

where, again, the dependency from N_b is highlighted for clarity. Moreover, by forcing the overlap degree, Q, to be less than a threshold, χ, the following constraint on the number of sub-carriers can be obtained:

$$\begin{aligned} C\left(N_b\right) &\leq \frac{\pi}{2} \frac{1}{\sin^{-1}\left(\frac{\beta+1}{R_u(N_b)\,\chi}\right)} \\ &\Rightarrow C\left(N_b\right) = \left\lfloor \frac{\pi}{2} \frac{1}{\sin^{-1}\left(\frac{\beta+1}{R_u(N_b)\,\chi}\right)} \right\rfloor \end{aligned} \tag{6.15}$$

Thus N_b can be found by solving the following problem:

$$\max_{N_b} N_b\left(C\left(N_b\right) - 1\right) \quad \text{s.t.} \quad \frac{N_b + G_b'}{B_S} L_b \in \mathbb{N} \tag{6.16}$$

As before, the condition guarantees that the number of symbols is integer.

6.3.3 Sub-waveform Adaptive Duration

As shown in Figure 6.2, the FrFT CoRadar pulse does not occupy the entire available bandwidth since it is clearly enclosed in a circle of radius 0.5 in normalised units. In order to maximise the bandwidth occupancy, it is possible to consider sub-waveforms with different time durations depending on the fractional order. This also leads to an increase of the bit rate with no effect on the BER, at cost of a slightly higher design complexity.

An example of a longer sub-waveform is shown in Figure 6.7: it has a rotation angle of $\phi_i = \pi/4$ and a bandwidth $B_{w,sub}$. The fraction of additional time with respect to

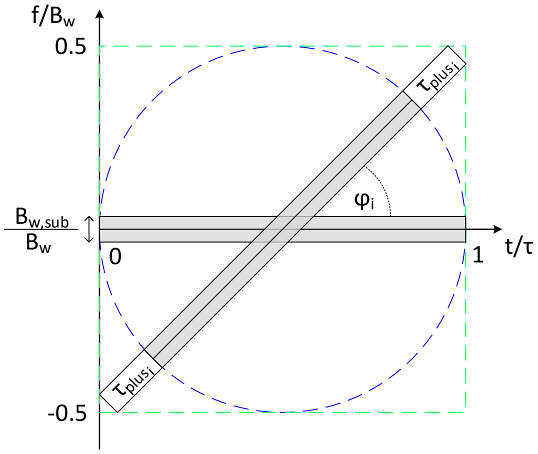

Figure 6.7: Waveform optimisation: representation of sub-waveforms with different duration on varying the fractional order.

the duration of the pulse, τ_{plus_i}, is:

$$\tau_{plus_i} = \frac{\tau_i - \tau}{2\tau} \tag{6.17}$$

where τ_i is the duration of the i-th sub-waveform given by:

$$\tau_i = \begin{cases} \dfrac{\tau}{|\cos(\phi_i)|} & \phi_i \in \left[0, \dfrac{\pi}{4}\right) \cup \left[\dfrac{3\pi}{4}, \pi\right) \\ \dfrac{\tau}{|\sin(\phi_i)|} & \phi_i \in \left[\dfrac{\pi}{4}, \dfrac{3\pi}{4}\right) \end{cases} \tag{6.18}$$

$i = 1, \ldots, C-1$. Thus, the number of bits that the longer i-th sub-waveform can accommodate is given by:

$$N_{b_i} = \left\lfloor \frac{\tau_i B_w}{L_b R_u} B_S \right\rfloor - G_b \quad \text{s.t.} \quad \frac{(N_{b_i} + G_b) \times L_b}{B_S} \in \mathbb{N} \tag{6.19}$$

Equation (3.2) shows a linear relationship between the fractional order α and the rotation angle ϕ. When sub-waveforms with different durations are considered, this equation becomes nonlinear and can be written as (see Appendix A):

$$\begin{cases} \alpha_i = \dfrac{2}{\pi} \tan^{-1}\left[(1 + 2\tau_{plus_i}) \tan\phi_i\right] & \phi_i \in [0, \pi/2) \\ \alpha_i = 1 & \phi_i = \pi/2 \\ \alpha_i = \dfrac{2}{\pi} \tan^{-1}\left[(1 + 2\tau_{plus_i}) \tan(\phi_i - \pi)\right] + 2 & \phi_i \in (\pi/2, \pi] \end{cases} \tag{6.20}$$

An example of spectrograms of a FrFT CoRadar waveform (a) without and (b) with adaptive duration is shown in Figure 6.8. The red circle indicates the time-frequency region occupied by the pulse when no optimisation is applied. In terms of bit rate, the adaptive duration optimisation leads to an improvement of about 10%.

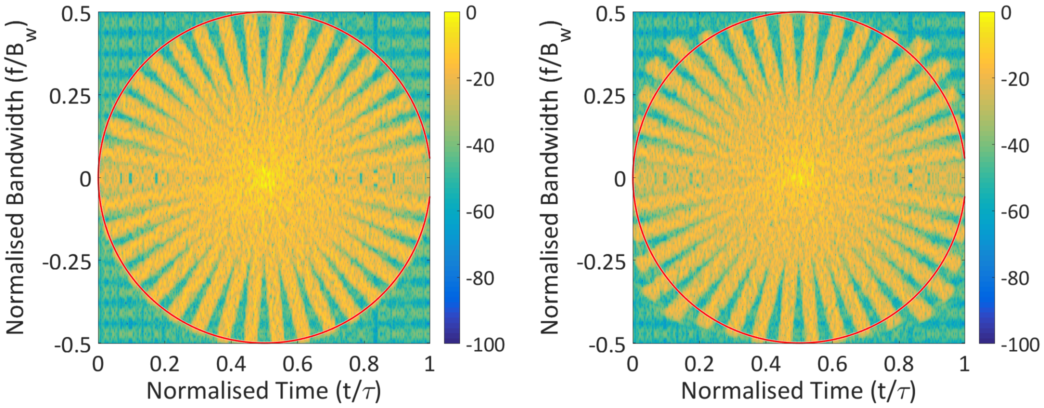

(a) No adaptive duration.
(b) With adaptive duration.

Figure 6.8: Spectrograms of a FrFT CoRadar waveform (a) without and (b) with adaptive duration.

6.4 Implementation on SDR

The prototype of the proposed FrFT CoRadar system consists of a mono-static radar that generates the FrFT waveforms, sends the pulses and performs basic radar tasks, and a separate communication receiver that demodulates the pulses. The entire system is implemented by means of a SDR device, namely the National Instruments Universal Software Radio Peripheral (NI-USRP) 2943r shown in Figure 6.9(a). It has four

(a) NI-USRP 2943r.
(b) Octave horn antenna.

Figure 6.9: Demonstrator of the FrFT CoRadar system: (a) NI-USRP 2943r and (b) an octave horn antenna by A-Info.

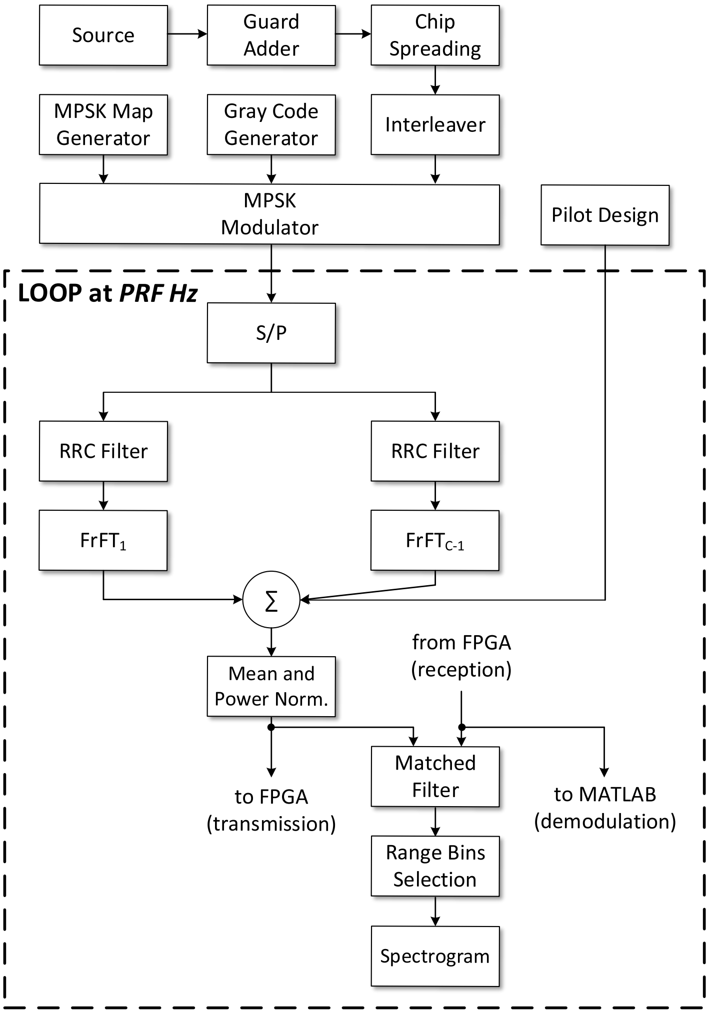

Figure 6.10: High-level block diagram of the FrFT CoRadar system's implementation in LabVIEW.

IQ channels, two receivers and two transmitters/receivers, and its working frequency ranges between $1.2\,GHz$ and $6.6\,GHz$. It is provided with a fully programmable Xilinx Kintex-7 FPGA (Field-Programmable Gate Array) and can be connected to a host computer through a high-speed, low-latency PCI Express x4 ($\sim$800 MB/s). It is used with three wideband LB-2678-15 multi octave horn antennas produced by A-Info, shown in Figure 6.9(b), two for the mono-static radar node and one for the communication receiver.

The USRP 2943r is programmed through NI software LabVIEW, and its high-level block diagram is shown in Figure 6.10. Within the loop that repeats every PRI, the FrFT CoRadar waveform is generated as described in the previous sections[36] and sent

---

[36] Note that the interleaver is selected as ICI mitigation technique.

to the FPGA. The latter up-samples the signal in transmission to meet the $120\,MHz$ data clock frequency of the device and interfaces with the RF front-end. Meanwhile, the received signal, down-sampled and coming from the FPGA, is sent both to a MATLAB session for the real-time pulse demodulation and to a matched filter with the transmitted pulse for further radar processing. Specifically, a real-time spectrogram is computed, showing the results of the radar Doppler processing. This choice is driven by the limited power and bandwidth resources of the employed SDR device, which are not sufficient for more advanced radar operations. Outside the loop, the message to be sent is loaded and all the preliminary steps are performed.

The prototype is highly flexible, since all the parameters described in Section 6.2 can be set, and demonstrates the feasibility of the proposed waveform design framework. However, it suffers from the computation complexity of the discrete FrFT, limiting the PRF and allowing to generate only waveforms with few sub-carriers.

6.5 Performance Analysis

In this section the radar and communication performance of the FrFT CoRadar waveform design framework are evaluated and compared with those obtained with OFDM waveforms, since, as previously showed in Section 3.3.2.2, they are already used in radars and CoRadar systems. Note that, traditional radar processing (matched filtering) is performed on both FrFT and OFDM waveforms. Hence, the technique for OFDM side lobe suppression reviewed in Section 3.3.2.2 is not used in this analysis, since it has the drawback of introducing periodicity, therefore ambiguities, in the range profile. Moreover, a link budget analysis is performed to demonstrate the feasibility of the proposed FrFT waveform design method for CoRadar system. Finally, the system is validated evaluating the performance on laboratory acquired signals.

The OFDM waveforms are generated by using the framework shown in Figure 6.1, where the FrFT block is replaced by an OFDM block, which maps the sub-waveforms into different frequency sub-carriers rather than into chirp sub-carriers, with no addition of the cyclic prefix and in which the interleaver is removed. Furthermore, two parameters selection processes are considered throughout the paper. The first one, FrFT optimised, is the one described above when an interleaver is used; the second one, OFDM optimised, starting from the same parameters, increases the number of sub-carriers, C, in order to optimise the frequency occupancy of the OFDM waveform. Table 6.1 lists the parameters obtained when the two selection processes are used, respectively. The FrFT optimised parameters selection procedure ensures that $Q \leq \chi$, however the OFDM sub-carrier spacing, Δ_f, is greater than $B_{w,sub}$, which means that frequency gaps are present in the OFDM waveform. On the other hand, the OFDM optimised parameters selection process leads to $\Delta_f \approx B_{w,sub}$, but $Q \nleq \chi$.

Table 6.1: List of the parameters obtained when FrFT optimised and OFDM optimised selection processes are used, respectively.

	FrFT Optimised	**OFDM Optimised**
B_w	500 MHz	
τ	9.982 μs	
L_b	7	
B_S	2 (QPSK)	
G_b	3	
β	0.4	
χ	$3/7 = 0.429$	
C	11	16
N_b	59	
Bit/Pulse	590	885
R_u	23	
Q	0.428	0.621
$B_{w,sub}$	30.435 MHz	
Δ_f	45.455 MHz	31.250 MHz

6.5.1 Radar Performance

In order to evaluate the radar performance of the proposed FrFT CoRadar waveform design framework, two analyses are carried out. Firstly, parameters such as range resolution, Doppler resolution and Side Lobe Levels (SLLs) are estimated from its Ambiguity Function (AF). Then, by means of a Monte-Carlo simulation, the Receiver Operating Characteristic (ROC) for a square law detector is derived. A similar analysis is performed for OFDM waveform and LFM pulse for comparison purposes. In particular, the LFM pulse is designed such that it occupies the same bandwidth, B_w, and has the same duration, τ, of the FrFT CoRadar waveform[37].

6.5.1.1 Ambiguity Function

The FrFT's and OFDM's AFs are computed over a Monte-Carlo simulation with 100 iterations, since for both of them the actual pulse is affected by the transmitted sequence of bits. Figure 6.11(a) and Figure 6.11(b) show the average AFs of the FrFT and OFDM, respectively, when the FrFT optimised parameters selection process is used. The FrFT's AF has a much flatter shape than the OFDM's, which, instead, presents very high side lobes caused by spectral peaks and valleys between the OFDM subcarriers. This behaviour is more evident by looking at the zero-Doppler cuts shown in Figure 6.11(c) and Figure 6.11(d), for the FrFT and the OFDM waveform, respectively, while the zero-delay cuts in Figure 6.11(e) and Figure 6.11(f) show a similar trend between FrFT, OFDM and LFM waveform, though this changes at different delay cuts. However, lower side lobes are achieved at cost of a slightly worse resolution of the FrFT waveform with respect to OFDM and LFM, both in range and Doppler. Resolutions and side lobe levels are summarised in Table 6.2, where all the values are taken by assuming a reference level at $-3\,d\mathrm{B}$. Figures 6.11(c)-6.11(f) also report the maximum AF in addition to the average one, obtained by taking the maximum value for each delay/Doppler bin for all the 100 Monte-Carlo iterations. The displacement between the maximum and the average AF is higher for the FrFT waveform than for the OFDM waveform, showing a higher variability of the former due to the sequence of bits embedded.

Table 6.2: Radar Performance Parameters

	FrFT Optimised		**OFDM Optimised**		**LFM**
	FrFT	**OFDM**	**FrFT**	**OFDM**	
Range Resolution	$39.3\,cm$	$26.7\,cm$	$39.3\,cm$	$27.3\,cm$	$26.7\,cm$
Doppler Resolution	$65.4\,kHz$	$45.1\,kHz$	$65.4\,kHz$	$45.1\,kHz$	$44.3\,kHz$
Zero-Doppler SLL	$-16.6\,d\mathrm{B}$	$-4.6\,d\mathrm{B}$	$-16.5\,d\mathrm{B}$	$-9.9\,d\mathrm{B}$	$-13.3\,d\mathrm{B}$
Zero-Delay SLL	$-16.6\,d\mathrm{B}$	$-13.3\,d\mathrm{B}$	$-16.5\,d\mathrm{B}$	$-13.3\,d\mathrm{B}$	$-13.3\,d\mathrm{B}$

---

[37] The LFM pulse is considered as benchmark for the radar performance, since it does not embed any data.

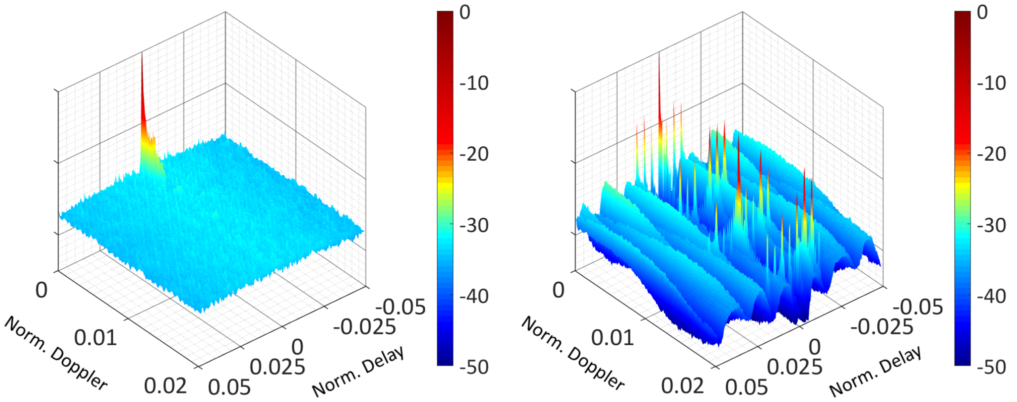

(a) FrFT's ambiguity function. (b) OFDM's ambiguity function.

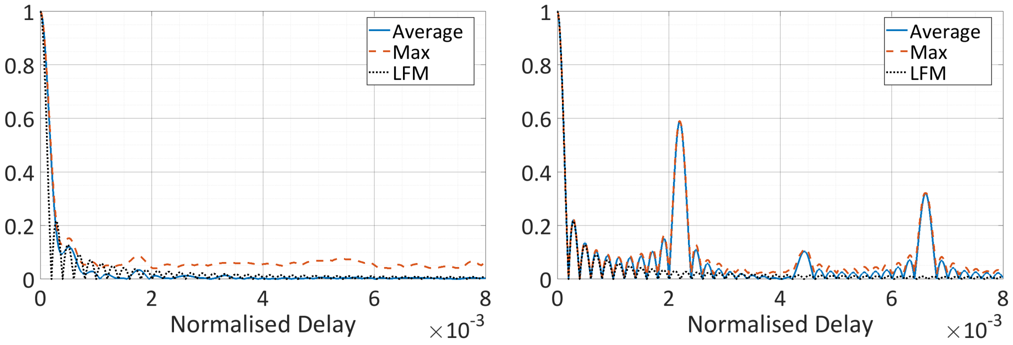

(c) FrFT's zero-Doppler cut. (d) OFDM's zero-Doppler cut.

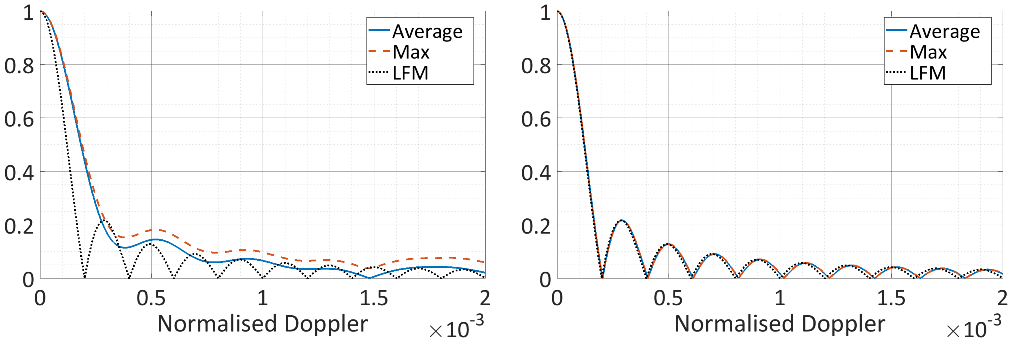

(e) FrFT's zero-delay cut. (f) OFDM's zero-delay cut.

Figure 6.11: Average Ambiguity Functions (AFs) of the (a) FrFT and (b) OFDM waveform when the FrFT optimised parameters selection process is used. Figures (c)-(d) show their zero-Doppler cuts (average, in blue, and maximum, in red) compared to the LFM's zero-Doppler cut. Figures (e)-(f) show their zero-delay cuts (average, in blue, and maximum, in red) compared to the LFM's zero-delay cut.

The results obtained when the OFDM optimised parameters selection procedure is used, confirm that the FrFT waveform presents a general better trend in terms of side lobes, but it is outperformed by the OFDM waveform in range and Doppler resolution, as shown in Figure 6.12 and reported in Table 6.2.

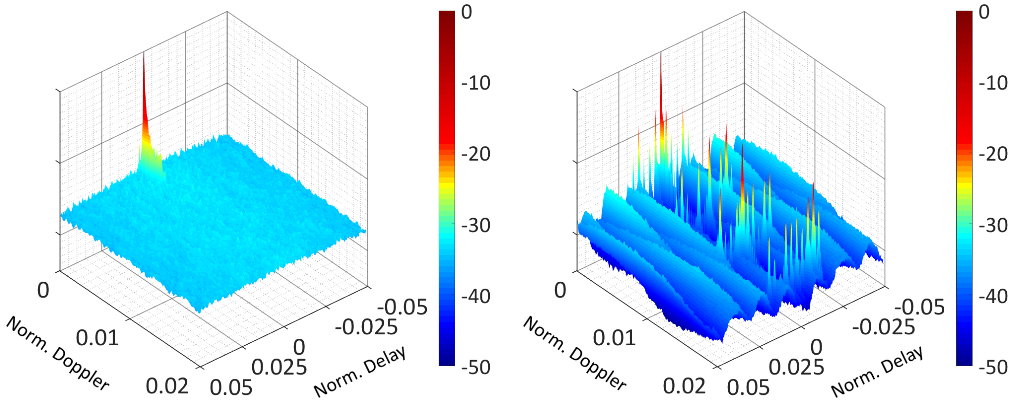

(a) FrFT's ambiguity function. (b) OFDM's ambiguity function.

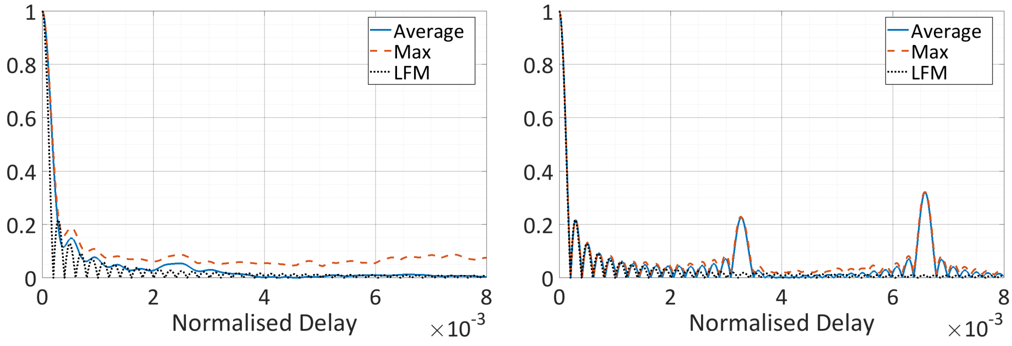

(c) FrFT's zero-Doppler cut. (d) OFDM's zero-Doppler cut.

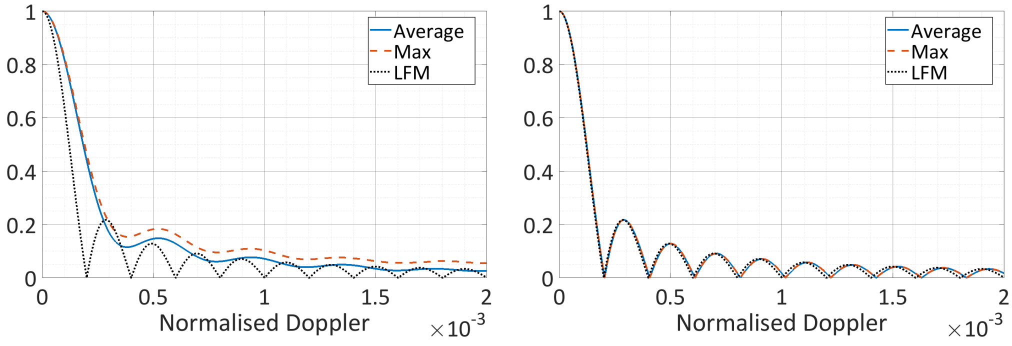

(e) FrFT's zero-delay cut. (f) OFDM's zero-delay cut.

Figure 6.12: Average Ambiguity Functions (AFs) of the (a) FrFT and (b) OFDM waveform when the OFDM optimised parameters selection process is used. Figures (c)-(d) show their zero-Doppler cuts (average, in blue, and maximum, in red) compared to the LFM's zero-Doppler cut. Figures (e)-(f) show their zero-delay cuts (average, in blue, and maximum, in red) compared to the LFM's zero-delay cut.

6.5.1.2 Square Law Detector

The FrFT CoRadar waveform is examined, and compared with OFDM and LFM waveforms, when used for detection purposes with a square law detector, whose threshold is selected based on the noise level, namely the Signal-to-Noise Ratio at the Radar receiver, SNR_r, and the desired Probability of False Alarm (P_{FA}). In order to estimate the Receiver Operating Characteristic (ROC) of the detector, a Monte-Carlo simulation with 10^5 iterations is carried out. In each iteration, a FrFT based pulse is generated which embeds a random sequence of bits; since the length of the pulse, in samples, is approximately of 5×10^3 (time-bandwidth product), the total number of Monte-Carlo tests is equal to 5×10^8. Figure 6.13 compares the performance of the FrFT, OFDM and LFM waveforms when the FrFT optimised parameters selection process is considered, and for (a) $SNR_r = 15\,d\text{B}$ and (b) $SNR_r = 20\,d\text{B}$. In both the cases the FrFT waveform shows performance very close to the LFM, while for the OFDM waveform, once the Probability of Detection, P_D, is fixed to a certain desired level, the P_{FA} results higher compared to FrFT and LFM waveforms, and this is due to the higher range side lobes that its AF presents, as shown in the previous section.

The same analysis is carried out when considering the OFDM optimised parameters selection process. Results, shown in Figure 6.14, confirm the better performance in terms of ROC of the FrFT waveform over the OFDM.

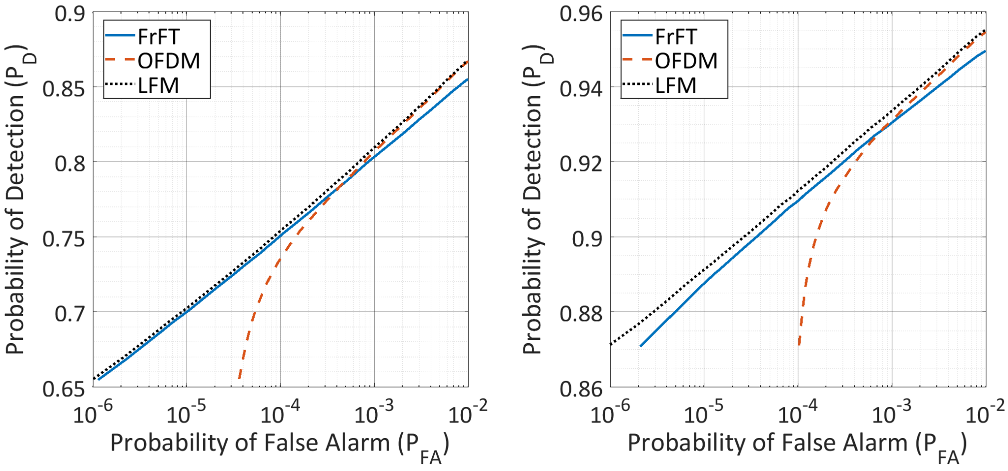

(a) $SNR_r = 15\,d\text{B}$. (b) $SNR_r = 20\,d\text{B}$.

Figure 6.13: Receiver Operating Characteristic (ROC) of the square law detector when FrFT, OFDM (with FrFT optimised parameters) and LFM waveforms are used, and when noise level is (a) $SNR_r = 15\,d\text{B}$ and (b) $SNR_r = 20\,d\text{B}$.

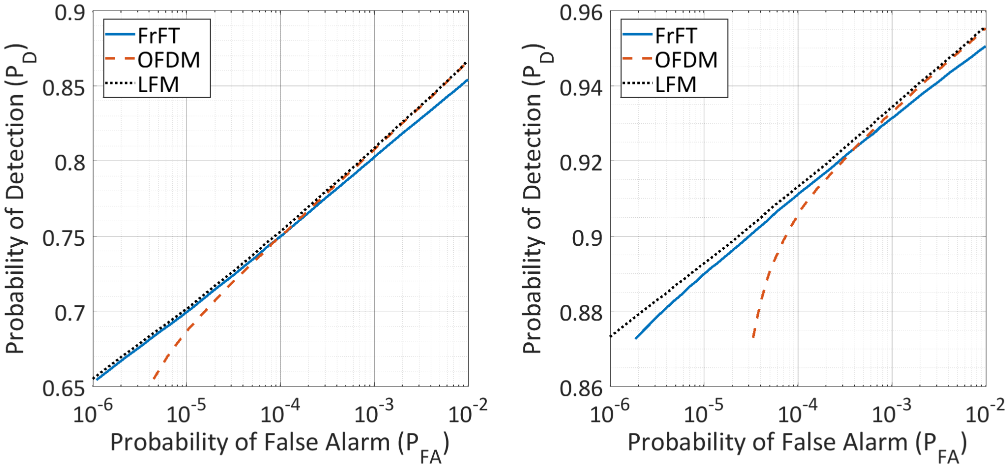

(a) $SNR_r = 15\,d$B. (b) $SNR_r = 20\,d$B.

Figure 6.14: Receiver Operating Characteristic (ROC) of the square law detector when FrFT, OFDM (with OFDM optimised parameters) and LFM waveforms are used, and when noise level is (a) $SNR_r = 15\,d$B and (b) $SNR_r = 20\,d$B.

6.5.2 Communication Performance

In this section, communication performance is expressed in terms of BER, defined as the ratio between the number of bits wrongly decoded and the total number of bits sent, on varying the energy per bit to noise power spectral density ratio, $\gamma_b = E_b/N_0$. The energy per bit is defined as:

$$E_b = \frac{P_s}{R_b} \tag{6.21}$$

where P_s is the power of the transmitted pulse and R_b is the bit rate of an equivalent system designed to send a continuous waveform, defined as the total number of transmitted bits (including overheads) over time:

$$R_b = \frac{(N_b + G_b)\, L_b C}{\tau} = \frac{CB_S}{R_u} B_w \tag{6.22}$$

Then, since N_0 is the noise power in $1\ Hz$ bandwidth, it follows:

$$\gamma_b = \frac{E_b}{N_0} = \frac{P_s}{N_0 B_w}\frac{R_u}{CB_S} = SNR_c \frac{R_u}{CB_S} \tag{6.23}$$

where SNR_c is the Signal-to-Noise Ratio at the Communication receiver.

In the following, two analyses are carried out. Firstly, performance for the two different ICI mitigation approaches is evaluated in AWGN: the objective is to derive conditions for ν_{guard} and χ that ensure the best performance. The second analysis regards the comparison with the OFDM waveform for different channel models. Note that these analyses do not take into account the relative position between transmitter and receiver, and that both the FrFT and the OFDM pulses are assumed to be already synchronised and their phase compensated.

6.5.2.1 Guard Time and Interleaver in AWGN

Communication performance of the FrFT CoRadar waveform design framework subjected to AWGN when guard time and interleaver are used as ICI mitigation approach, respectively, is evaluated and shown in Figure 6.15. The curves are obtained by means of a Monte-Carlo simulation during which 10^8 bits are sent. The parameters selection process described in Section 6.3.2 is used with different values of ν_{guard} and χ, for guard time and interleaver, respectively. The resulting parameters are summarised in Table 6.3.

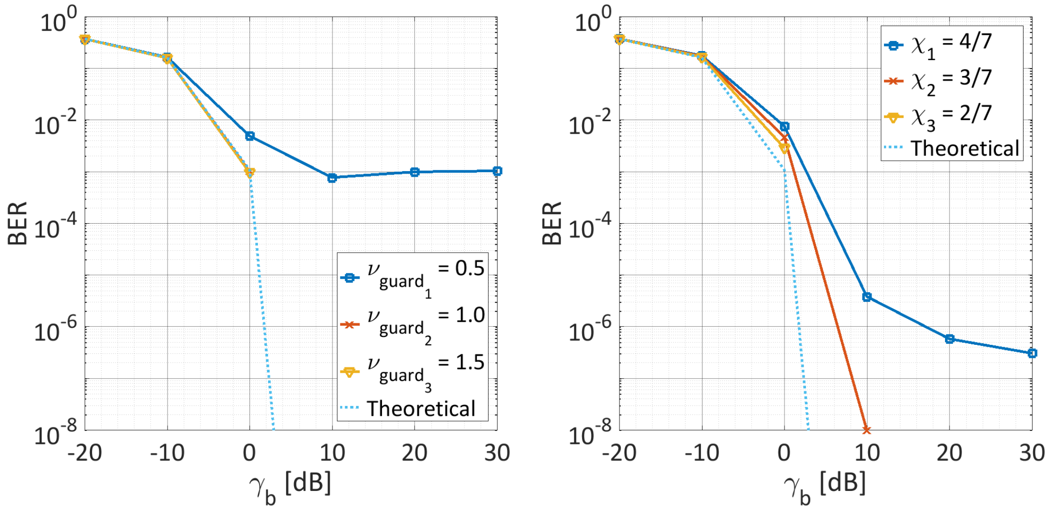

(a) Guard time.

(b) Interleaver.

Figure 6.15: Performance in terms of BER of the FrFT CoRadar waveform design framework in presence of AWGN, when (a) a guard time or (b) an interleaver is used as Inter-Carrier Interference (ICI) mitigation approach.

The lower bound, represented by the light blue dotted line, is the BER obtained when the chirp sub-carriers are considered independent, that is no ICI is present, and the noise that affects each of them is still AWGN. Since the employed channel coding

Table 6.3: List of the parameters for the two different ICI mitigation approaches and on varying ν_{guard} and χ.

Parameters						
			N_b	C	Bit/Pulse	R_u
Guard T.	ν_{guard}	0.5	54	14	756	12
		1.0	30	12	360	22
		1.5	21	11	231	32
Interl.	χ	$4/7$	53	16	848	25
		$3/7$	59	11	649	23
		$2/7$	27	15	405	47

technique is able to correct up to $\lfloor L_b/2 \rfloor$ errors per codeword, the probability that the dataword is wrongly decoded is equal to the probability that the codeword contains more than $\lfloor L_b/2 \rfloor$ errors. This is expressed by the following equation:

$$BER_{lb} = \sum_{k=\lfloor L_b/2 \rfloor+1}^{L_b} \binom{L_b}{k} p_{\text{mod}}^{k} \left(1 - p_{\text{mod}}\right)^{L_b-k} \tag{6.24}$$

where p_{mod} is the probability of error of the employed modulation scheme, Quadrature Phase Shift Keying (QPSK) in the analysed case. When guard time is used as ICI mitigation approach, as expected the BER decreases as the parameters ν_{guard} increases. In fact, $\nu_{\text{guard}} < 1$ means that part of the region affected by ICI is still used to send information bits, thus more errors are expected. In particular a BER floor is visible for $\nu_{\text{guard}_1} = 0.5$. This is due to errors that are independent of the noise level and are only caused by ICI. Conversely, when $\nu_{\text{guard}} > 1$ the guard time is larger than the region affected by ICI, hence the sub-carriers can be considered independent and the BER approaches the lower bound.

Similar results are obtained when the interleaver is used as ICI mitigation method, where the BER decreases as χ decreases, since there is less overlap of the chirp sub-carriers. Interesting is that for $\chi \leq 3/7 = 0.429$, the BER does not present a plateau anymore (which is instead visible for $\chi_1 = 4/7$) and approaches the lower bound. This because the threshold $\chi_2 = \chi^{\star} = 0.429$ is computed as $\lfloor L_b/2 \rfloor / L_b$, and relates to the maximum number of errors per codeword that the employed channel code can correct, while $\chi_1 = \left(\lfloor L_b/2 \rfloor + 1\right) / L_b$ and $\chi_3 = \left(\lfloor L_b/2 \rfloor - 1\right) / L_b$. Thus, selecting $\chi \leq 0.429$

means that the expected errors per codeword are less or equal than $\lfloor L_b/2 \rfloor$, so that the ECC can correct all the errors and the sub-carriers can be considered independent.

6.5.2.2 Comparison with OFDM

In this section the communication performance of the FrFT CoRadar waveform is compared with the performance obtained with the OFDM waveform. The signal is assumed to experience a slow-flat fading, therefore a time-invariant narrowband channel model is considered. Let $\boldsymbol{s}_{T_x}$ be the vector which contains the transmitted signal samples. The received signal can be written as:

$$\boldsymbol{s}_{R_x} = \boldsymbol{c}_h \circ \boldsymbol{s}_{T_x} + \boldsymbol{\xi} \tag{6.25}$$

where $\boldsymbol{c}_h$ is the vector that contains the channel coefficients, $\boldsymbol{\xi}$ is the white Gaussian noise and the operator $\circ$ indicates the Hadamard, or entrywise, product.

The complex elements of the vector $\boldsymbol{c}_h$ are drawn from a statistical distribution whose parameters depend on the propagation path. In addition to the AWGN only scenario for which $c_h = 1$, three other cases are considered. In case of existence of the LoS path, the channel is modelled as Rician with a Rice factor of $4\,d\mathrm{B}$. Conversely, when no LoS path exists, the channel coefficients $\boldsymbol{c}_h$ are drawn from a Rayleigh distribution with scale parameter $\sqrt{2}/2$. Finally, in order to take into account shadowing and diffraction that can occur in bad weather conditions, a combination of Rice and Lognormal is considered [145]. In this case the channel coefficients are obtained as the product of a Rice process normalised in power and a Lognormal variable, whose associated Gaussian variable has a standard deviation of 4 (this is often referred to as the "dB spread").

Assuming that the received signal has been equalised, the communication performance is evaluated in terms of BER vs $\gamma_b\,[d\mathrm{B}]$ in Figure 6.16. As before, a Monte-Carlo simulation is run during which 10^7 bits are sent. The blue lines refer to the FrFT waveform, while the red lines to the OFDM. Solid lines and dotted lines refer to the cases in which FrFT optimised and OFDM optimised parameters selection processes are used, respectively. In presence of AWGN only, as shown in Figure 6.16(a), the

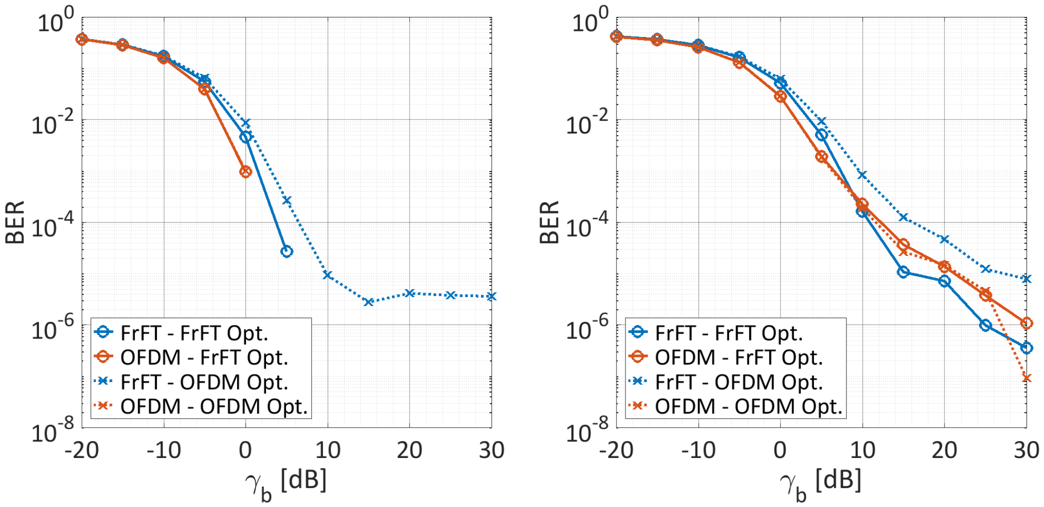

(a) AWGN.

(b) Rice plus AWGN channel.

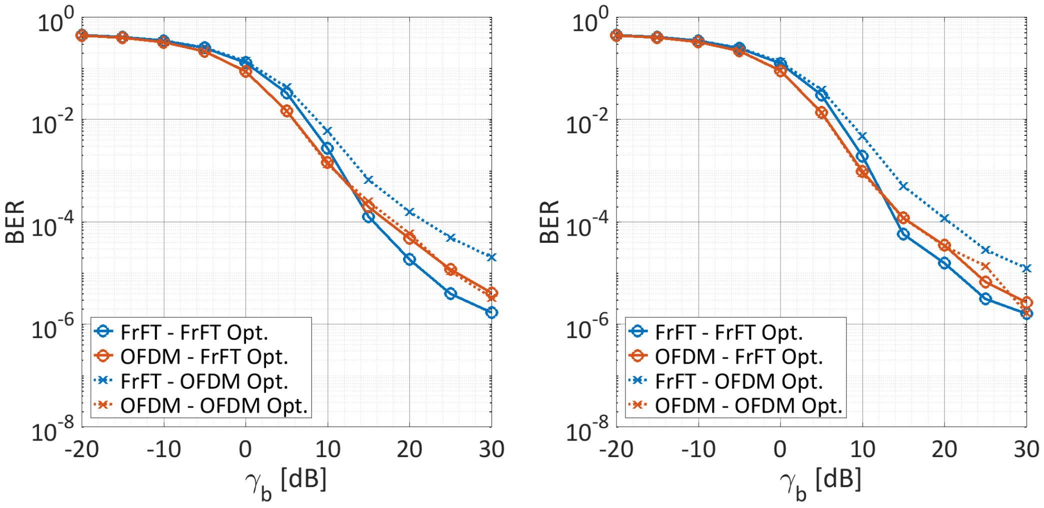

(c) Rayleigh plus AWGN channel.

(d) LogNormal - Rice plus AWGN channel.

Figure 6.16: Communication performance. Comparison between FrFT waveform and OFDM waveform on varying the parameters selection process and for four different channel models: (a) AWGN only, (b) Rice channel, (c) Rayleigh channel and (d) LogNormal-Rice channel.

FrFT waveform is outperformed by the OFDM. Moreover, a plateau can be observed for the FrFT waveform when OFDM optimised parameters are used, which confirms the results obtained in the previous section since $Q \nleq \chi^{\star}$. For all the analysed channel models, the OFDM is not affected by the parameters selection process, while the FrFT, as expected, shows better performance when FrFT optimised parameters are used, as they ensure that the overlap is lower than $\chi^{\star} = 0.429$. However, even when OFDM optimised parameters are used, for which $Q = 0.621 > \chi^{\star}$ but at the same time more information bits are sent, the FrFT's BER is still comparable with the OFDM's.

6.5.3 Link Budget

In order to validate the feasibility of the proposed FrFT waveform design framework for CoRadar system, a link budget analysis is carried out. Signal-to-Noise Ratio at the Radar receiver, SNR_r, and energy per bit to noise power spectral density, γ_b, are chosen depending on the desired radar and communication performance, as shown in the previous sections. Then, assuming that a $PRF = 3\,kHz$ is used, an average power of $P_{T_x} = 50\,W$ is sent, and by fixing the parameters as in Table 6.1 for the FrFT optimised selection process, the maximum radar range, $r_{\max}$, and the maximum radar-communication receiver distance, $d_{\max}$, are obtained. For this specific analysis, the radar link budget is obtained by rearranging the radar range equation as follows:

$$r_{\max} = \sqrt[4]{\frac{P_{T_x}}{\tau PRF} \frac{G_{T_x,\text{main}} G_{R_x,\text{radar}} \lambda^2 \sigma L_s}{F_{\text{radar}} \left(4\pi\right)^3 kT_0 B_w \, SNR_r} n_{\text{int}}^{0.5} G_{sp}} \tag{6.26}$$

while the communication link budget is:

$$d_{\max} = \sqrt{\frac{P_{T_x}}{\tau PRF} \frac{G_{T_x,\text{side}} G_{R_x,\text{comms}} \lambda^2}{F_{\text{comms}} \left(4\pi\right)^2 kT_0 B_w \, SNR_c}} \tag{6.27}$$

All the parameters are listed in Table 6.4. It is worth noting that the communication link budget is evaluated assuming that the communication receiver is placed in the side lobe of the radar's antenna beam.

With this configuration, a target with a radar cross section of $1\,m^2$ can be detected at a maximum range of $r_{\max} = 22.14\,km$ with a probability of detection of about 0.9. In the same time, a data stream of $1.947\,Mb/s$ can be directed to a communication receiver placed in the radar antenna's side lobe at a distance of $d_{\max} = 22.26\,km$, ensuring a BER lower than 10^{-4}.

Table 6.4: Link Budget Parameters.

Parameter	Description	Value
PRF	Pulse Repetition Frequency.	3 kHz
P_{T_x}	Transmitted average power.	50 W
λ	Wavelength.	3 cm
k	Boltzmann's constant.	1.38×10^{-23} J/K
T_0	Noise reference temperature.	290 K
SNR_r	SNR at Radar receiver.	$20\, d$B
$G_{T_x,\text{main}}$	Radar transmitting antenna's gain in the main lobe.	$35\, d$B
$G_{R_x,\text{radar}}$	Radar receiving antenna's gain.	$35\, d$B
σ	Radar cross section.	$1\,\text{m}^2$
L_s	Loss factor.	0.4
n_{int}	Number of pulses combined incoherently.	64
G_{sp}	Signal processing gain.	$37\, d$B
F_{radar}	Radar's noise figure.	$4\, d$B
$r_{\max}$	Maximum radar range.	22.14 km
γ_b	Energy per bit to noise power spectral density.	$20\, d$B
SNR_c	SNR at Communication receiver.	$19.81\, d$B
$G_{T_x,\text{side}}$	Radar transmitting antenna's gain in the side lobe.	$5\, d$B
$G_{R_x,\text{comms}}$	Communication receiving antenna's gain.	$15\, d$B
F_{comms}	Communication receiver's noise figure.	$10\, d$B
$d_{\max}$	Maximum radar-communication receiver distance.	22.26 km

6.5.4 Laboratory Validation

The FrFT CoRadar system demonstrator, described in Section 6.4, is used in a controlled laboratory environment to acquire data and assess its communication and radar capability. The acquisition geometry is shown in Figure 6.17. The mono-static radar is placed at the bottom left, the communication receiver at the top right, while within the light blue area a person is walking towards and away from the radar to generate a

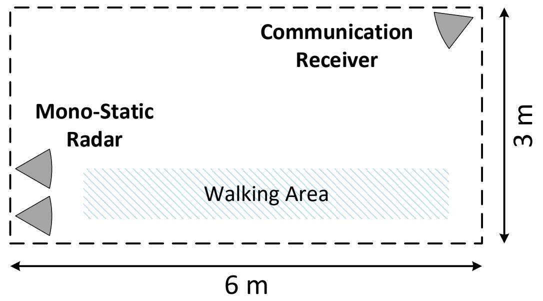

Figure 6.17: Acquisition geometry of the laboratory-based experimental campaign.

Doppler signal.

The transmitted message is a 64×64 black and white image with a bit depth 5. Carrier frequency is $3\,GHz$ and the bandwidth is $1\,MHz$. The number of information bits per carrier, N_b, is 3, the length of the Barker code is $L_b = 7$ and QPSK is the employed modulation scheme, hence $B_S = 2$. The RRC filter is designed to span $S_{\text{RRC}} = 8$ symbols, with an up-sampling factor $R_u = 18$ and a roll-off factor $\beta = 0.4$. This leads to a guard of $G_b = 3$ bits. The total number of samples per waveform is 378, which means that the duration of the pulse is $\tau = 378\,\mu s$. The PRF is fixed to $83.33\,Hz$, giving a duty cycle of $3.15\,\%$.

Different configurations are analysed by changing the number of sub-carriers, $C = 6, 8, 10$, and modifying the transmitted power. The SNR is estimated both at the mono-static radar and the communication receiver.

Communication performance is shown with solid lines in Figure 6.18, in terms of BER averaged over 10 realisations vs the energy per bit to noise power spectral density ratio, γ_b. The dotted lines in Figure 6.18 show the results obtained by running Monte-Carlo simulations with 10^5 iterations with the same parameters listed above, assuming the channel to be Rician with K-factor equal to $6\,d\text{B}$ (indoor channel). They are used as comparison to validate the results on the acquired data. As expected, as γ_b increases, the BER decreases. However, no significant further improvements are observed for γ_b greater than $15\,d\text{B}$, and this trend is confirmed by the results from the Monte-Carlo simulations, which clearly show plateaus. They are due both to the distortion introduced by the channel, and the overlap of the sub-carriers, which causes errors independently of the noise level. For the same reason, performance improves by reducing the number of sub-carriers.

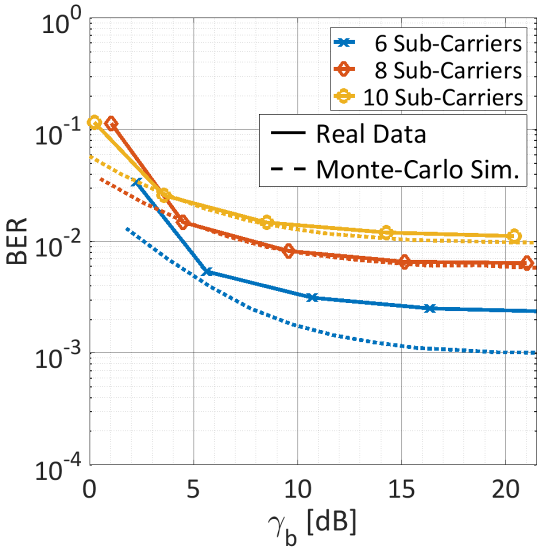

Figure 6.18: Communication performance on real data, on varying γ_b and for different number of chirp sub-carriers.

The radar capabilities of the FrFT CoRadar are presented by showing spectrograms from the signals acquired during the laboratory-based experimental campaign. Figure 6.19 shows spectrograms when FrFT CoRadar pulses with $C = 8$ sub-carriers are used for two different values of SNR_r. In both the cases the Doppler and mD signature of the person walking towards and away from the radar is clearly visible.

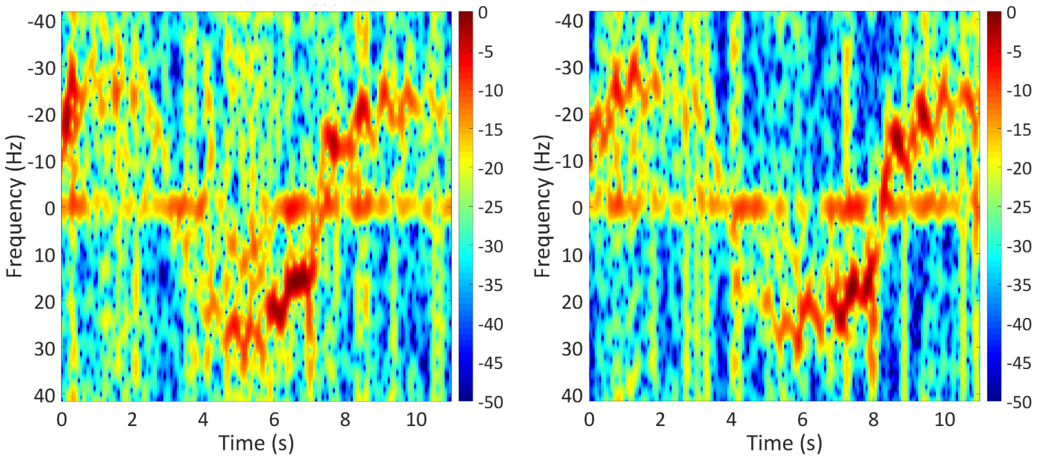

(a) $SNR_r = 3.11\,d\text{B}$. (b) $SNR_r = 14.32\,d\text{B}$.

Figure 6.19: Spectrograms obtained from FrFT CoRadar pulses with $C = 8$ and different SNR_r. Window length 0.36 seconds, overlap $80\,\%$. Person walking towards the radar approximately between 4-8 seconds, and away from it between 0-4 seconds and 8-11 seconds.

6.6 Practical Challenges

Despite demonstrating the feasibility of the proposed FrFT CoRadar framework in Section 6.5, some practical challenges still have to be addressed in order to obtain a full working system. In this Section a non-comprehensive list of them is presented.

The first one concerns the computation of the discrete FrFT. This topic has been widely investigated in the literature [146, 147] but, even if algorithms with complexity $O\left(N\log N\right)$ (with N length of the signal) have been proposed [148], they approximate the continuous FrFT rather than representing fast algorithms for the computation of the discrete FrFT (as the FFT algorithm is for the ordinary discrete FT). A method for the discrete FrFT computation with complexity $O\left(U^2\right)$ was presented in [149], and has been used in Section 6.4 for prototype development. However, as mentioned earlier, due to its high computational cost this implementation of the discrete FrFT limits the generation of waveforms with either a high number of sub-carriers or a high time-bandwidth product. For this reason, either a new formulation of discrete FrFT is sought or an ad-hoc and clever hardware implementation of an existing algorithm is performed. The mitigation of the Range Side lobe Modulation (RSM) effect that occurs because of the transmission of different pulses each PRI represents another practical challenge. Common matched filter processing at the radar receiver would produce range side lobes that are different for each waveform, leading to the problem of clutter dispersion for which standard clutter cancellation techniques are ineffective. Different approaches have been proposed for pulse agility radars and may be adapted to the proposed FrFT CoRadar system. In [150] the RSM effect was mitigated by mismatch filtering the different waveforms sent in a Coherent Processing Interval (CPI) in order to obtain similar range side lobe responses. In particular an iterative procedure for the joint design of multiple receiver filters was presented. This technique is also recalled in [151], where the authors proposed a closed-form rather than iterative solution specifically adapted for Moving Target Indication (MTI) radars. A more general framework for dealing with the problem of RSM was proposed in [152], whose aim was the optimisation of the Cross Ambiguity Function (CAF) at cost, however, of a higher computational complexity.

6.7 Conclusions

A novel concept of Communicating-Radar (CoRadar) system based on the Fractional Fourier Transform (FrFT) was presented in this Chapter. The proposed waveform design technique, described in Section 6.2, directly embedded data into the radar waveform, allowing the two operations, radar and communication, to run simultaneously while sharing bandwidth, power and hardware resources. The method exploited the FrFT to map modulated signal, i.e. QPSK signals, into chirp sub-carriers with different chirp rates. This also made the system fully scalable, since its configuration could be adapted to the available bandwidth, pulse length and condition of the channel. In particular, procedures for parameters selection driven by the radar requirements were explained in Section 6.3, along with two waveform optimisation techniques aiming at minimising the effect of the Inter-Carrier Interference (ICI) and maximising the data rate. A prototype of the proposed FrFT CoRadar system on a Software Defined Radio (SDR) device was also presented in Section 6.4, and used for validation.

In Section 6.5 radar and communication performance of the proposed waveform design framework were assessed and compared with an OFDM CoRadar system, that presented a comparable bit rate. Results showed that the FrFT waveform slightly traded range and Doppler resolutions with much lower side lobe levels, which also led the proposed method to outperform the OFDM waveform when used for detection purposes. Communication performance confirmed the goodness of the proposed waveform design framework, showing comparable Bit Error Rates (BERs) with the OFDM waveform in all the analysed cases. A link budget analysis was also conducted to prove the feasibility of the FrFT based waveform design for CoRadar systems. Finally, the proposed system was validated by assessing its radar and communication performance through data acquired in a real controlled laboratory environment.

The FrFT based CoRadar system is suitable for a wide range of applications, but it needs to be further investigated. Stress analyses simulating a multi-path environment and in presence of clutter are necessary in order to definitely validate the concept, and an investigation of possible clutter cancellation techniques needs to be carried out. Furthermore, some practical problems introduced in Section 6.6 must be addressed, such as the fast computation of the discrete FrFT and the mitigation of the Range Side lobe Modulation (RSM) effect.

Chapter 7

Conclusion and Future Works

This Thesis investigated advanced signal processing solutions for target recognition and spectrum sharing in distributed radar systems. Chapter 2 offered a review of most recent Automatic Target Recognition (ATR) techniques for Synthetic Aperture Radar (SAR) images. The attention was focused on model-based and feature-based techniques. The former used features that were directly extracted from the SAR image of the target of interest, such as bright points, corners, line segments. The latter either computed the features by projecting the SAR image into domains invariant with respect to rotation and/or translation, or left their computation and selection to the algorithm itself. This Chapter also provided an overview of recent micro-Doppler (mD) based ATR algorithms, with particular attention given to techniques aimed at identifying helicopter's models.

Chapter 3 introduced the problem of spectrum congestion and described a collection of methods and techniques for allowing spectrum sharing between radar and communication systems. Discussion was particularly focussed on technologies able of enabling a communication channel in a radar system, exploiting the resources already allocated to meet the radar requirements.

Two SAR ATR algorithms, that enhanced and improved a previously developed framework, were described in Chapter 4. The first one further exploited the information provided by the full-polarimetric SAR image of the target by extracting pseudo-Zernike (pZ) moments based features from both the polarimetric components and the Krogager components. Combining the rotation and translation invariance properties of the pZ moments, and the roll invariance properties of the Krogager components, the proposed algorithm was robust with respect to both the orientation of the target on the scene and the acquisition elevation angle. The framework could also be easily extended to accommodate multiple images provided, for example, by sensors in a distributed radar system. Results from the stress analyses performed on real full-polarimetric circular SAR images of the GOTCHA dataset, showed the effectiveness of the integrated Krogager pseudo-Zernike (Kr/pZ) approach, that outperformed the original algorithm in all the considered cases. The pZ moments, however, being defined in a continuous domain, suffered from the discretisation error. This was more severe as the moments order increased, limiting their capability in representing small differences between different targets. For this reason, the second proposed approach used the discrete defined Krawtchouk moments. Performance, evaluated on the real MSTAR dataset, confirmed the superior capability of these moments in characterising even small details.

A mD model-based algorithm for identification of helicopters was presented in Chapter 5. Based on the sparse representation of the received signal from the helicopter's rotor blades, the algorithm estimated the helicopter's mD parameters through the resolution of a sparse recovery problem. The resolution of such a problem was achieved by means of a modified version of a greedy sparse recovery framework, namely the Pruned Orthogonal Matching Pursuit (POMP). The algorithm, independent on both the orientation of the aircraft and the initial position of its blades, was developed for the identification of both single and multiple targets in the radar cell of interest, and was extensively tested on both simulated and real data. This Chapter also presented an information fusion method, whose objective was the combination of the decisions made by several sensors in order to enhance the identification accuracy. This approach, based on the parametric sparse representation of mD signal, used in conjunction with adapted versions of the POMP, or other optimisation techniques for the resolution of sparse recovery problem, can be used for the classification of other rigid bodies, such as Ballistic Missiles (BMs) or Unmanned Aerial Vehicles (UAVs). The framework could potentially be used also for monitoring and anomaly detection in turbines operation, both in wind and tidal power farms.

Chapter 6 presented a novel waveform design framework for Communicating-Radar (CoRadar) system based on the Fractional Fourier Transform (FrFT). The proposed waveform resulted by the superimposition of chirp sub-carriers modulated by data symbols. The structure of the waveform, composed by chirps with different chirp rates, guaranteed high-level radar performance while allowing the transmission of data. Moreover, the two tasks, radar and communication, could be performed simultaneously while sharing bandwidth, power and hardware resources. The description of a prototype of the proposed system implemented through a Software Defined Radio (SDR) device was also provided. The capabilities of the FrFT CoRadar were tested and compared with a similar system that used OFDM waveforms through extensive simulations, and were validated on real data. The FrFT CoRadar technology is opened to a variety of applications, but it needs to be further investigated. Some practical challenges, arisen in Section 6.6, need to be explored and, eventually, solved, and additional stress analyses are necessary in order to definitely validate the concept. Meanwhile, this technique could potentially be applied to radar systems different from pulsed, such as Frequency Modulated Continuous Waveform (FMCW) radars.

Appendix A

FrFT CoRadar: Nonlinear Relationship Order-Angle

In [121], the relationship between FrFT order and chirp rate is demonstrated. With reference to Figure A.1, that shows a time-frequency plane in normalised units, this relation for the signal in green is equal to:

$$\phi = \frac{\pi}{2}\alpha = \tan^{-1}\left(\frac{y_s}{x_s}\right) \tag{A.1}$$

where y_s and x_s are normalised bandwidth and duration, respectively, of the chirp. The green signal can be seen as a CoRadar sub-waveform to which a FrFT of order α has been applied. Its bandwidth and duration in normalised units, after the application of the transform, can be evaluated as:

$$\begin{cases} x_s = \dfrac{1}{2}\cos\phi \\ y_s = \dfrac{1}{2}\sin\phi \end{cases} \tag{A.2}$$

which graphically means that the signal is rotating on a circumference of radius one half. When a longer sub-waveform is generated, for example with duration $1/2 + \tau_{plus}$ as consequence of the application of the adaptive duration, its rotation is graphically represented by the ellipse of major axis $1/2 + \tau_{plus}$ and minor axis $1/2$, as shown in

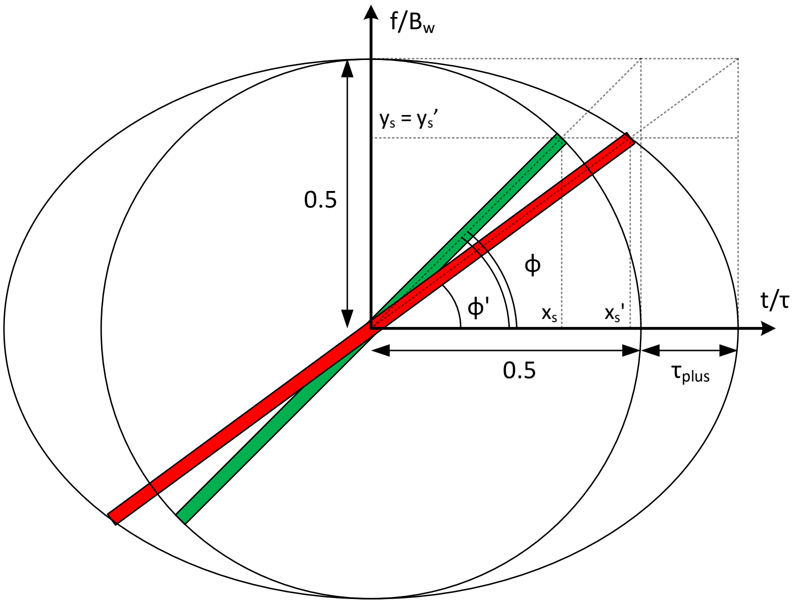

Figure A.1: Derivation of the non linear relationship between order and angle in the Fractional Fourier Transform (FrFT).

Figure A.1 for the signal in red, that is:

$$\begin{cases} x'_s = \left(\frac{1}{2} + \tau_{plus}\right)\cos\phi \\ y'_s = \frac{1}{2}\sin\phi \end{cases} \tag{A.3}$$

However, because of the effect of stretching of the time axis, the actual rotation angle of the sub-waveform in the normalised time-frequency plane, ϕ', is smaller than ϕ. Specifically:

$$\tan\phi' = \frac{y'_s}{x'_s} = \frac{\tan\phi}{1 + 2\tau_{plus}} \tag{A.4}$$

Therefore, in order to maintain the chirp sub-carriers equally spaced, this difference needs to be compensated. Therefore, from (A.1) and (A.4) it follows:

$$\begin{cases} \alpha = \frac{2}{\pi}\tan^{-1}\left[(1 + 2\tau_{plus})\tan\phi'\right] & \phi' \in [0, \pi/2) \\ \alpha = 1 & \phi' = \pi/2 \\ \alpha = \frac{2}{\pi}\tan^{-1}\left[(1 + 2\tau_{plus})\tan(\phi' - \pi)\right] + 2 & \phi' \in (\pi/2, \pi] \end{cases} \tag{A.5}$$

The different cases account for the discontinuity of the tangent function in $\pi/2$.

Author's Publications

Journals

- **D. Gaglione**, *"Student Research Highlights: MACHe - Model-Based Algorithm for Classification of Helicopters"*, IEEE Aerospace and Electronic Systems Magazine, vol. 31, no. 8, pp. 38-40, August 2016.

- **A. R. Persico, C. Clemente, D. Gaglione, C. V. Ilioudis, J. Cao, L. Pallotta, A. De Maio, I. K. Proudler, J. J. Soraghan**, *"On Model, Algorithms and Experiment for Micro-Doppler Based Recognition of Ballistic Targets"*, IEEE Transactions on Aerospace and Electronic Systems, 2017.

- **C. Clemente, L. Pallotta, D. Gaglione, A. De Maio, J. J. Soraghan.**, *"Automatic Target Recognition of Military Vehicles with Krawtchouk Moments*, IEEE Transactions on Aerospace and Electronic Systems, 2017.

Conferences

- **C. Clemente, C. V. Ilioudis, D. Gaglione, K. Thompson, S. Weiss, I. K. Proudler, J. J. Soraghan**, *"Reuse of Fractional Waveform Libraries for MIMO Radar and Electronic Countermeasures"*, 2014 6th International Symposium on Communications, Control and Signal Processing (ISCCSP), pp. 505-508, Athens, Greece, May 2014.

- **D. Gaglione, C. Clemente, L. Pallotta, A. De Maio, I. K. Proudler, J. J. Soraghan**, *"Krogager Decomposition and Pseudo-Zernike Moments for Polarimet-*

ric Distributed ATR", 2014 Sensor Signal Processing for Defence (SSPD), Edinburgh, UK, September 2014.

- **C. Clemente, T. Parry, G. Galston, P. Hammond, C. Berry, C. V. Ilioudis, D. Gaglione, J. J. Soraghan**, *"GNSS Based Passive Bistatic Radar for Micro-Doppler Based Classification of Helicopters: Experimental Validation"*, 2015 IEEE International Radar Conference (RadarCon), pp. 1104-1108, Arlington, VA, USA, May 2015.

- **D. Gaglione, C. Clemente, F. K. Coutts, G. Li, J. J. Soraghan**, *"Model-Based Sparse Recovery Method for Automatic Classification of Helicopters"*, 2015 IEEE International Radar Conference (RadarCon), pp. 1161-1165, Arlington, VA, USA, May 2015 - First Prize in the Best Student Paper Competition.

- **F. K. Coutts, D. Gaglione, C. Clemente, G. Li, I. K. Proudler, J. J. Soraghan**, *"Label Consistent K-SVD for Sparse Micro-Doppler Classification"*, 2015 IEEE International Conference on Digital Signal Processing (DSP), pp. 90-94, Singapore, July 2015.

- **A. R. Persico, C. Clemente, C. V. Ilioudis, D. Gaglione, J. Cao, J. J. Soraghan**, *"Micro-Doppler Based Recognition of Ballistic Targets Using 2-D Gabor Filters"*, 2015 Sensor Signal Processing for Defence (SSPD), Edinburgh, UK, September 2015.

- **C. Clemente, L. Pallotta, D. Gaglione, A. De Maio, J. J. Soraghan**, *"On The Use of Image Moments for ATR from SAR Images"*, NATO SET on Radar Imaging for Target Identification, Pisa, Italy, October 2015.

- **D. Gaglione, C. Clemente, C. V. Ilioudis, A. R. Persico, I. K. Proudler, J. J. Soraghan**, *"Fractional Fourier Based Waveform for a Joint Radar Communication System"*, 2016 IEEE Radar Conference (RadarCon), pp. 811-816, Philadelphia, PA, USA, May 2016.

- **D. Gaglione, C. Clemente, A. R. Persico, C. V. Ilioudis, I. K. Proudler, J. J. Soraghan**, *"Fractional Fourier Transform Based Co-Radar Waveform: Experimental Validation"*, 2016 Sensor Signal Processing for Defence (SSPD), Edinburgh, September 2016.

Submitted Papers

- **D. Gaglione, C. Clemente, C. V. Ilioudis, A. R. Persico, I. K. Proudler, J. J. Soraghan, A. Farina**, *"Waveform Design for Communicating Radar Systems Using Fractional Fourier Transform"*, submitted to IEEE Transactions on Aerospace and Electronic Systems.

References

[1] P. Tait, *Introduction to Radar Target Recognition*, ser. IEE Radar Series. Institution of Engineering and Technology, 2005. 1, 6, 29, 63

[2] T. K. Sarkar, M. S. Palma, and E. L. Mokole, “Echoing Across the Years: A History of Early Radar Evolution,” *IEEE Microwave Magazine*, vol. 17, no. 10, pp. 46–60, Oct 2016. 1

[3] M. Richards, J. Scheer, and W. Holm, *Principles of Modern Radar: Basic Principles*. SciTech Pub., 2010. 1, 11

[4] C. A. Wiley, “Synthetic Aperture Radars,” *IEEE Transactions on Aerospace and Electronic Systems*, vol. AES-21, no. 3, pp. 440–443, May 1985. 1

[5] I. Cumming and F. Wong, *Digital Processing of Synthetic Aperture Radar Data: Algorithms and Implementation*, ser. Artech House Remote Sensing Library. Artech House, 2005, no. v. 1. 1, 9

[6] V. C. Chen, W. J. Miceli, and D. Tahmoush, *Radar Micro-Doppler Signatures: Processing and Applications*. The Institution of Engineering and Technology, 2014. 2

[7] V. Chen, “Analysis of Radar Micro-Doppler with Time-Frequency Transform,” in *2000 10th IEEE Workshop on Statistical Signal and Array Processing*, Pocono Manor, PA, USA, 2000, pp. 463–466. 2, 23

[8] M. Vespe, C. J. Baker, and H. D. Griffiths, “Radar Target Classification Using Multiple Perspectives,” *IET Radar, Sonar Navigation*, vol. 1, no. 4, pp. 300–307, Aug 2007. 2

[9] C. J. Baker and A. L. Hume, “Netted Radar Sensing,” *IEEE Aerospace and Electronic Systems Magazine*, vol. 18, no. 2, pp. 3–6, Feb 2003. 2

[10] R. Cager, D. LaFlame, and L. Parode, “Orbiter Ku-Band Integrated Radar and Communications Subsystem,” *IEEE Transactions on Communications*, vol. 26, no. 11, pp. 1604–1619, Nov 1978. 2

[11] C. Clemente, L. Pallotta, I. Proudler, A. D. Maio, J. J. Soraghan, and A. Farina, “Multi-Sensor Full-Polarimetric SAR Automatic Target Recognition Using Pseudo-Zernike Moments,” in *2014 International Radar Conference (Radar)*, Lille, France, Oct 2014, pp. 1–5. xi, 3, 5, 18, 19, 20, 21, 47, 49, 61

[12] C. Clemente, L. Pallotta, I. Proudler, A. D. Maio, J. J. Soraghan, and A. Farina, “Pseudo-Zernike-Based Multi-Pass Automatic Target Recognition from Multi-Channel Synthetic Aperture Radar,” *IET Radar, Sonar Navigation*, vol. 9, no. 4, pp. 457–466, 2015. xi, 3, 5, 18, 19, 20, 21, 22, 47, 49, 52, 61

[13] G. Li and P. K. Varshney, “Micro-Doppler Parameter Estimation via Parametric Sparse Representation and Pruned Orthogonal Matching Pursuit,” *IEEE Journal of Selected Topics in Applied Earth Observations and Remote Sensing*, vol. 7, no. 12, pp. 4937–4948, Dec 2014. 5, 27, 29, 78

[14] D. E. Dudgeon and R. T. Lacoss, “An Overview of Automatic Target Recognition,” *The Lincoln Laboratory Journal*, vol. 6, no. 1, pp. 3–10, 1993. 8

[15] C. Ning, W. Liu, G. Zhang, J. Yin, and X. Ji, “Enhanced Synthetic Aperture Radar Automatic Target Recognition Method Based on Novel Features,” *Appl. Opt.*, vol. 55, no. 31, pp. 8893–8904, Nov 2016. 8

[16] I. Hajnsek, J. Mittermayer, and K. Papathanassiou, “Polarization Capabilities and Status of TERRASAR-X,” in *4th International Workshop on Applications of Polarimetry and Polarimetric Interferometry (Pol-InSAR)*. Frascati, Italy: European Space Agency, Apr 2009. 10

[17] J.-S. Lee and E. Pottier, *Polarimetric Radar Imaging: From Basics to Applications*. CRC press, 2009. 11, 12, 13

[18] V. Alberga, E. Krogager, M. Chandra, and G. Wanielik, “Potential of Coherent Decompositions in SAR Polarimetry and Interferometry,” in *2004 IEEE International Geoscience and Remote Sensing Symposium (IGARSS)*, vol. 3. Anchorage, AK, USA: IEEE, 2004, pp. 1792–1795. 12, 14

[19] P. Srikanth, K. Ramana, U. Deepika, P. K. Chakravarthi, and M. S. Sai, “Comparison of Various Polarimetric Decomposition Techniques for Crop Classification,” *Journal of the Indian Society of Remote Sensing*, pp. 1–8, 2016. 12, 14

[20] R. Touzi, A. Bhattacharya, and K. Mattar, “Multi-Resolution Target Scattering Decomposition for Urban Feature Characterization Using Polarimetric SARs,” in *2009 IEEE International Geoscience and Remote Sensing Symposium (IGARSS)*, vol. 4, Cape Town, South Africa, Jul 2009, pp. 857–860. 12

[21] V. Turkar and Y. Rao, “Applying Coherent and Incoherent Target Decomposition Techniques to Polarimetric SAR Data,” in *International Conference on Technology Systems and Management (ICTSM)*, Mumbai, India, 2011. 12

[22] W. L. Cameron, N. N. Youssef, and L. K. Leung, “Simulated Polarimetric Signatures of Primitive Geometrical Shapes,” *IEEE Transactions on Geoscience and Remote Sensing*, vol. 34, no. 3, pp. 793–803, May 1996. 13

[23] M. Hellmann and E. Krogager, “Comparison of Decompositions for pol-SAR Image Interpretation,” in *2000 IEEE International Geoscience and Remote Sensing Symposium (IGARSS)*, vol. 3. Honolulu, HI, USA: IEEE, 2000, pp. 1313–1315. 14

[24] E. Krogager, “Properties of the Sphere, Diplane, Helix (Target Scattering Matrix) Decomposition,” *Proc. of JIPR-3, Mar. 1995*, 1995. 14

[25] M. A. Saville, J. A. Jackson, and D. F. Fuller, “Rethinking Vehicle Classification with Wide-Angle Polarimetric SAR,” *IEEE Aerospace and Electronic Systems Magazine*, vol. 29, no. 1, pp. 41–49, Jan 2014. 15

[26] L. M. Novak, S. D. Halversen, G. J. Owirka, and M. Hiett, "Effects of Polarization and Resolution on SAR ATR," *IEEE Trans. on Aerospace and Electronic Systems*, vol. 33, no. 1, pp. 102–116, Jan 1997. 15

[27] C. Duan, W. Hu, and X. Du, "Three-Dimensional Geometrical Feature Estimation for Ship Classification Through SAR Images," in *2012 IEEE 6th International Conference on Information and Automation for Sustainability (ICIAfS)*, Beijing, China, Sep 2012, pp. 181–184. 15

[28] J. I. Park and K. T. Kim, "Modified Polar Mapping Classifier for SAR Automatic Target Recognition," *IEEE Transactions on Aerospace and Electronic Systems*, vol. 50, no. 2, pp. 1092–1107, Apr 2014. 15

[29] K.-T. Kim, D.-K. Seo, and H.-T. Kim, "Efficient Classification of ISAR Images," *IEEE Transactions on Antennas and Propagation*, vol. 53, no. 5, pp. 1611–1621, May 2005. 15

[30] T. Ross, S. Worrell, V. Velten, J. Mossing, and M. Bryant, "Standard SAR ATR Evaluation Experiments Using the MSTAR Public Release Data Set," *Proc. SPIE,*, vol. 3370, pp. 566–573, 1998. 16, 60

[31] MSTAR Image Database. [Online]. Available: https://www.sdms.afrl.af.mil/index.php?collection=mstar 16, 60

[32] G. Jones and B. Bhanu, "Recognition of Articulated and Occluded Objects," *IEEE Transactions on Pattern Analysis and Machine Intelligence*, vol. 21, no. 7, pp. 603–613, Jul 1999. 16

[33] M. Cetin, W. C. Karl, and D. A. Castanon, "Feature Enhancement and ATR Performance Using Nonquadratic Optimization-Based SAR Imaging," *IEEE Transactions on Aerospace and Electronic Systems*, vol. 39, no. 4, pp. 1375–1395, Oct 2003. 16

[34] S. H. Doo, G. Smith, and C. Baker, "Reliable Target Feature Extraction and Classification Using Potential Target Information," in *2015 IEEE International*

Radar Conference (RadarCon), Arlington, VA, USA, May 2015, pp. 0628–0633. xi, 16

[35] S. H. Doo, G. E. Smith, and C. J. Baker, "Aspect Invariant Features for Radar Target Recognition," *IET Radar, Sonar & Navigation*, 2016. 16

[36] Y. Jiang, X. Zhao, Y. Zhang, B. Hu, and Y. Zhuang, "Pose Estimation Based on Exploration of Geometrical Information in SAR Images," in *2016 IEEE Radar Conference (RadarCon)*, Philadelphia, PA, USA, May 2016, pp. 1–4. 17

[37] U. Srinivas, V. Monga, and R. Raj, "SAR Automatic Target Recognition Using Discriminative Graphical Models," *IEEE Trans. on Aerospace and Electronic Systems*, vol. 50, no. 1, pp. 591–606, Jan 2014. 17

[38] S. Chen, H. Wang, F. Xu, and Y. Q. Jin, "Target Classification Using the Deep Convolutional Networks for SAR Images," *IEEE Transactions on Geoscience and Remote Sensing*, vol. 54, no. 8, pp. 4806–4817, Aug 2016. 17

[39] S. Wagner, "Combination of Convolutional Feature Extraction and Support Vector Machines for Radar ATR," in *17th International Conference on Information Fusion (FUSION)*, Salamanca, Spain, Jul 2014, pp. 1–6. 17

[40] F. Yan, W. Mei, and Z. Chunqin, "SAR Image Target Recognition Based on Hu Invariant Moments and SVM," in *2009 Fifth International Conference on Information Assurance and Security (IAS)*, vol. 1, Xi'an, China, Aug 2009, pp. 585–588. 18

[41] M.-K. Hu, "Visual Pattern Recognition by Moment Invariants," *IRE Transactions on Information Theory*, vol. 8, no. 2, pp. 179–187, Feb 1962. 18

[42] Z. Huang and J. Leng, "Analysis of Hu's Moment Invariants on Image Scaling and Rotation," in *2010 2nd International Conference on Computer Engineering and Technology (ICCET)*, vol. 7, Apr 2010, pp. V7–476–V7–480. 18

[43] W. Chen, K. Ji, X. Xing, H. Zou, and H. Sun, "Ship Recognition in High Resolution SAR Imagery Based on Feature Selection," in *2012 International Con-*

ference on Computer Vision in Remote Sensing (CVRS), Xiamen, China, Dec 2012, pp. 301–305. 18

[44] M. Amoon and G. a. Rezai-rad, “Automatic Target Recognition of Synthetic Aperture Radar (SAR) Images Based on Optimal Selection of Zernike Moments Features,” *IET Computer Vision*, vol. 8, no. 2, pp. 77–85, Apr 2014. 18

[45] A. Bhatia and E. Wolf, “On the Circle Polynomials of Zernike and Related Orthogonal Sets,” in *Proc. Cambridge Philos. Soc*, vol. 50, no. 1. Cambridge Univ Press, 1954, pp. 40–48. 18

[46] C. H. Teh and R. Chin, “On Image Analysis by the Methods of Moments,” *IEEE Trans. on Pattern Analysis and Machine Intelligence*, vol. 10, no. 4, pp. 496–513, Jul 1988. 18, 59

[47] S. K. Ranade and N. Kaur, “Empirical Analysis of Scale Invariance in Moment Coefficients,” *International Journal of Computer Science and Technology*, vol. 6, no. 2, pp. 237–242, Jun 2015. 18

[48] C. Clemente, D. Gaglione, L. Pallotta, A. D. Maio, and J. Soraghan, “On the Use of Image Moments for ATR from SAR Images,” in *NATO SET on Radar Imaging and Target Identification*, 2015. 18

[49] S. K. Ranade and S. Anand, “Empirical Analysis of Rotation Invariance in Moment Coefficients,” *International Journal of Computer Applications*, vol. 119, no. 15, pp. 19–26, Jun 2015. 18

[50] S. Kumar, “Comparative Results of Zernike Moments and Pseudo-Zernike Moments,” in *2016 3rd International Conference on Computing for Sustainable Global Development (INDIACom)*, New Delhi, India, Mar 2016, pp. 1254–1259. 18

[51] P. Nassery and K. Faez, “Signature Pattern Recognition Using Pseudo Zernike Moments and a Fuzzy Logic Classifier,” in *3rd IEEE International Conference on Image Processing*, vol. 2, Lausanne, Switzerland, Sep 1996, pp. 197–200. 19

[52] A. Nabatchian, E. Abdel-Raheem, and M. Ahmadi, “Human Face Recognition Using Different Moment Invariants: A Comparative Study,” in *2008 Congress on Image and Signal Processing (CISPs)*, vol. 3, Sanya, China, May 2008, pp. 661–666. 19

[53] M. Ahmady, R. Ghasemi, and H. R. Kanan, “Local Weighted Pseudo Zernike Moments and Fuzzy Classification for Facial Expression Recognition,” in *2013 13th Iranian Conference on Fuzzy Systems (IFSC)*, Qazvi, Iran, Aug 2013, pp. 1–4. 19

[54] M. Sultana, M. Gavrilova, and S. Yanushkevich, “Expression, Pose, and Illumination Invariant Face Recognition Using Lower Order Pseudo Zernike Moments,” in *2014 International Conference on Computer Vision Theory and Applications (VISAPP)*, vol. 1, Lisbon, Portugal, Jan 2014, pp. 216–221. 19

[55] L. Pallotta, C. Clemente, A. De Maio, J. Soraghan, and A. Farina, “Pseudo-Zernike Moments Based Radar Micro-Doppler Classification,” in *2014 IEEE Radar Conference (RadarCon)*, Cincinnati, OH, USA, May 2014. 19

[56] H. Shu, L. Luo, and J. l. Caatrieux, “Moment-Based Approaches in Imaging. 1. Basic Features [A Look At ...],” *IEEE Engineering in Medicine and Biology Magazine*, vol. 26, no. 5, pp. 70–74, Sep 2007. 19

[57] K. Fukunaga, *Introduction to Statistical Pattern Recognition*, ser. Computer Science and Scientific Computing. Elsevier Science, 1990. 21

[58] Q. Zhao and J. C. Principe, “Support Vector Machines for SAR Automatic Target Recognition,” *IEEE Transactions on Aerospace and Electronic Systems*, vol. 37, no. 2, pp. 643–654, Apr 2001. 21

[59] V. C. Chen, F. Li, S. S. Ho, and H. Wechsler, “Micro-Doppler Effect in Radar: Phenomenon, Model, and Simulation Study,” *IEEE Transactions on Aerospace and Electronic Systems*, vol. 42, no. 1, pp. 2–21, Jan 2006. 23, 28

[60] V. C. Chen, *The Micro-Doppler Effect in Radar*. Artech House, 2011. 23, 29, 73, 74

[61] R. Allen and D. Mills, *Signal Analysis: Time, Frequency, Scale, and Structure*. Wiley, 2004. 24, 26

[62] F. Fioranelli, M. Ritchie, and H. Griffiths, "Aspect Angle Dependence and Multistatic Data Fusion for Micro-Doppler Classification of Armed/Unarmed Personnel," *IET Radar, Sonar Navigation*, vol. 9, no. 9, pp. 1231–1239, 2015. xi, 24, 25

[63] Y. Kim and B. Toomajian, "Hand Gesture Recognition Using Micro-Doppler Signatures with Convolutional Neural Network," *IEEE Access*, vol. 4, pp. 7125–7130, 2016. 24

[64] C. Clemente, L. Pallotta, A. Maio, J. Soraghan, and A. Farina, "A Novel Algorithm for Radar Classification Based on Doppler Characteristics Exploiting Orthogonal Pseudo-Zernike Polynomials," *IEEE Transactions on Aerospace and Electronic Systems*, vol. 51, no. 1, pp. 417–430, Jan 2015. xi, 25

[65] A. R. Persico, C. Clemente, L. Pallotta, A. D. Maio, and J. Soraghan, "Micro-Doppler Classification of Ballistic Threats Using Krawtchouk Moments," in *2016 IEEE Radar Conference (RadarCon)*, Philadelphia, PA, USA, May 2016, pp. 1–6. 26

[66] L. Stankovic, "A Method for Time-Frequency Analysis," *IEEE Transactions on Signal Processing*, vol. 42, no. 1, pp. 225–229, Jan 1994. 26

[67] F. H. C. Tivive, S. L. Phung, and A. Bouzerdoum, "Classification of Micro-Doppler Signatures of Human Motions Using Log-Gabor Filters," *IET Radar, Sonar Navigation*, vol. 9, no. 9, pp. 1188–1195, 2015. 26

[68] R. I. A. Harmanny, J. J. M. de Wit, and G. P. Cabic, "Radar Micro-Doppler Feature Extraction Using the Spectrogram and the Cepstrogram," in *2014 European Radar Conference (EuRAD)*, Rome, Italy, Oct 2014, pp. 165–168. xi, 26, 27

[69] D. L. Donoho and X. Huo, "Uncertainty Principles and Ideal Atomic Decomposition," *IEEE Transactions on Information Theory*, vol. 47, no. 7, pp. 2845–2862, Nov 2001. 28

[70] M. Elad and A. M. Bruckstein, “A Generalized Uncertainty Principle and Sparse Representation in Pairs of Bases,” *IEEE Transactions on Information Theory*, vol. 48, no. 9, pp. 2558–2567, Sep 2002. 28

[71] D. L. Donoho, “Compressed Sensing,” *IEEE Transactions on Information Theory*, vol. 52, no. 4, pp. 1289–1306, Apr 2006. 28

[72] J. A. Tropp and A. C. Gilbert, “Signal Recovery From Random Measurements Via Orthogonal Matching Pursuit,” *IEEE Transactions on Information Theory*, vol. 53, no. 12, pp. 4655–4666, Dec 2007. 29

[73] J. Misiurewicz, K. Kulpa, and Z. Czekala, “Analysis of Recorded Helicopter Echo,” in *Radar 97 (Conf. Publ. No. 449)*, Edinburgh, UK, Oct 1997, pp. 449–453. 29, 30

[74] J. Martin and B. Mulgrew, “Analysis of the Theoretical Radar Return Signal form Aircraft Propeller Blades,” in *1990 IEEE International Radar Conference (RadarCon)*, Arlington, VA, USA, May 1990, pp. 569–572. 29

[75] C. Rotander and H. Von Sydow, “Classification of Helicopters by the L/N-Quotient,” in *Radar 97 (Conf. Publ. No. 449)*, Edinburgh, UK, Oct 1997, pp. 629–633. 30

[76] S.-H. Yoon, B. Kim, and Y.-S. Kim, “Helicopter Classification Using Time-Frequency Analysis,” *Electronics Letters*, vol. 36, no. 22, pp. 1871–1872, Oct 2000. 31

[77] L. Zuo, M. Li, and X. Zhang, “Helicopter Classification with a High PRF Radar,” in *2012 International Conference on Systems and Informatics (ICSAI)*, Yantai, China, May 2012, pp. 1682–1686. xii, 31

[78] J. Muoz-Ferraras, F. Perez-Martinez, and M. Burgos-Garcia, “Helicopter Classification with a High Resolution LFMCW Radar,” *IEEE Transactions on Aerospace and Electronic Systems*, vol. 45, no. 4, pp. 1373–1384, Oct 2009. 31

[79] R. Zhang, G. Li, C. Clemente, and P. K. Varshney, "Helicopter Classification via Period Estimation and Time-Frequency Masks," in *2015 IEEE 6th International Workshop on Computational Advances in Multi-Sensor Adaptive Processing (CAMSAP)*, Cancun, Mexico, Dec 2015, pp. 61–64. 32

[80] A. Cilliers and W. Nel, "Helicopter Parameter Extraction Using Joint Time-Frequency and Tomographic Techniques," in *2008 International Conference on Radar*, Adelaide, Australia, Sep 2008, pp. 598–603. xii, 32, 33

[81] C. Sturm and W. Wiesbeck, "Waveform Design and Signal Processing Aspects for Fusion of Wireless Communications and Radar Sensing," *Proceedings of the IEEE*, vol. 99, no. 7, pp. 1236–1259, Jul 2011. 35, 42

[82] S. Quan, W. Qian, J. Guq, and V. Zhang, "Radar-Communication Integration: An Overview," in *2014 IEEE 7th International Conference on Advanced Infocomm Technology (ICAIT)*, Fuzhou, China, Nov 2014, pp. 98–103. 35

[83] M. Fossi and M. Gherardelli, "OFDM Radar Signals for both Surveillance and Navigation Aids to Landing Aircrafts," in *2012 Tyrrhenian Workshop on Advances in Radar and Remote Sensing (TyWRRS)*, Naples, Italy, Sep 2012, pp. 46–52. 35

[84] H. Griffiths, L. Cohen, S. Watts, E. Mokole, C. Baker, M. Wicks, and S. Blunt, "Radar Spectrum Engineering and Management: Technical and Regulatory Issues," *Proceedings of the IEEE*, vol. 103, no. 1, pp. 85–102, Jan 2015. 36

[85] B. D. Cordill, S. A. Seguin, and L. Cohen, "Electromagnetic Interference to Radar Receivers due to In-Band OFDM Communications Systems," in *2013 IEEE International Symposium on Electromagnetic Compatibility*, Denver, CO, USA, Aug 2013, pp. 72–75. 36

[86] S. Kodituwakku, T. Lamahewa, and T. Dissanayake, "Impact on Radar Probability of Detection due to Interference from 4G Communication Signals," in *2015 IEEE Global Electromagnetic Compatibility Conference (GEMCCON)*, Adelaide, Australia, Nov 2015, pp. 1–5. 36

[87] I. Pasya, A. Mahyuni, S. F. S. Adnan, and Z. Awang, "Analysis of Interference from UWB Radar Signals on a Digital OFDM Transmission System," in *2011 IEEE International Conference on System Engineering and Technology (ICSET)*, Shah Alam, Malaysia, Jun 2011, pp. 91–95. 36

[88] M. Juskauskas, J. Krivochiza, J. Aleksandravicius, K. Svirskas, B. Dzindzeleta, R. Aleksiejunas, and M. Zilinskas, "Experimental Investigation of Radar Interference into LTE System at 1800 MHz Frequency Band," in *2013 21st Telecommunications Forum Telfor (TELFOR)*, Belgrade, Serbia, Nov 2013, pp. 28–30. 36, 37

[89] J. Chapin, "Shared Spectrum Access for Radar and Communications (SSPARC)," DARPA, BAA-13-24, Tech. Rep., 2012. 37

[90] G. M. Jacyna, B. Fell, and D. McLemore, "A High-Level Overview of Fundamental Limits Studies for the DARPA SSPARC Program," in *2016 IEEE Radar Conference (RadarCon)*, Philadelphia, PA, USA, May 2016, pp. 1–6. 37

[91] A. Aubry, A. D. Maio, M. Piezzo, and A. Farina, "Radar Waveform Design in a Spectrally Crowded Environment via Nonconvex Quadratic Optimization," *IEEE Transactions on Aerospace and Electronic Systems*, vol. 50, no. 2, pp. 1138–1152, Apr 2014. 37

[92] A. Aubry, V. Carotenuto, A. D. Maio, and S. Iommelli, "Cognitive Radar Waveform Design for Spectral Compatibility," in *2016 Sensor Signal Processing for Defence (SSPD)*, Edinburgh, UK, Sep 2016, pp. 1–5. xii, 38

[93] A. Aubry, A. D. Maio, and M. M. Naghsh, "Optimizing Radar Waveform and Doppler Filter Bank via Generalized Fractional Programming," *IEEE Journal of Selected Topics in Signal Processing*, vol. 9, no. 8, pp. 1387–1399, Dec 2015. 38

[94] K.-W. Huang, M. Bică, U. Mitra, and V. Koivunen, "Radar Waveform Design in Spectrum Sharing Environment: Coexistence and Cognition," in *2015 IEEE*

International Radar Conference (RadarCon), Arlington, VA, USA, May 2015, pp. 1698–1703. 38

[95] M. R. Bell, “Information Theory and Radar Waveform Design,” *IEEE Transactions on Information Theory*, vol. 39, no. 5, pp. 1578–1597, Sep 1993. 39

[96] M. L. Manna, P. Stinco, M. Greco, and F. Gini, “Design of a Cognitive Radar for Operation in Spectrally Dense Environments,” in *2013 IEEE Radar Conference (RadarCon)*, Ottawa, ON, Canada, Apr 2013, pp. 1–6. 39

[97] P. Stinco, M. Greco, F. Gini, and M. L. Manna, “Compressed Spectrum Sensing in Cognitive Radar Systems,” in *2014 IEEE International Conference on Acoustics, Speech and Signal Processing (ICASSP)*, Florence, Italy, May 2014, pp. 81–85. 39

[98] W. Wiesbeck, L. Sit, M. Younis, T. Rommel, G. Krieger, and A. Moreira, “Radar 2020: The Future of Radar Systems,” in *2015 IEEE International Geoscience and Remote Sensing Symposium (IGARSS)*, Milan, Italy, Jul 2015, pp. 188–191. 39

[99] A. Turlapaty and Y. Jin, “A Joint Design of Transmit Waveforms for Radar and Communications Systems in Coexistence,” in *2014 IEEE Radar Conference (RadarCon)*, Cincinnati, OH, USA, May 2014, pp. 0315–0319. 40

[100] S. C. Surender and R. M. Narayanan, “UWB Noise-OFDM Netted Radar: Physical Layer Design and Analysis,” *IEEE Transactions on Aerospace and Electronic Systems*, vol. 47, no. 2, pp. 1380–1400, Apr 2011. 40

[101] L. Han and K. Wu, “Joint Wireless Communication and Radar Sensing Systems - State of the Art and Future Prospects,” *IET Microwaves, Antennas Propagation*, vol. 7, no. 11, pp. 876–885, Aug 2013. 40

[102] J. Moghaddasi and K. Wu, “Multifunctional Transceiver for Future Radar Sensing and Radio Communicating Data-Fusion Platform,” *IEEE Access*, vol. 4, pp. 818–838, 2016. 40

[103] S. J. Xu, Y. Chen, and P. Zhang, "Integrated Radar and Communication Based on DS-UWB," in *2006 3rd International Conference on Ultrawideband and Ultrashort Impulse Signals*, Sevastopol, Ukraine, Sep 2006, pp. 142–144. 40

[104] M. Roberton and E. R. Brown, "Integrated Radar and Communications Based on Chirped Spread-Spectrum Techniques," in *2003 IEEE MTT-S International Microwave Symposium Digest*, vol. 1, Philadelphia, PA, USA, Jun 2003, pp. 611–614. 40

[105] W. Gugler, A. Springer, and R. Weigel, "A Robust SAW-Based Chirp - $\pi/4$ DQPSK System for Indoor Applications," in *2000 IEEE International Conference on Communications*, vol. 2, New Orleans, LA, USA, Jun 2000, pp. 773–777. 41

[106] G. N. Saddik, R. S. Singh, and E. R. Brown, "Ultra-Wideband Multifunctional Communications/Radar System," *IEEE Transactions on Microwave Theory and Techniques*, vol. 55, no. 7, pp. 1431–1437, Jul 2007. 41

[107] X. Chen, X. Wang, S. Xu, and J. Zhang, "A Novel Radar Waveform Compatible with Communication," in *2011 International Conference on Computational Problem-Solving (ICCP)*, Chengdu, China, Oct 2011, pp. 177–181. 41

[108] Z. Zhao and D. Jiang, "A Novel Integrated Radar and Communication Waveform Based on LFM Signal," in *2015 5th International Conference on Electronics Information and Emergency Communication (ICEIEC)*, Beijing, China, May 2015, pp. 219–223. 41

[109] F. Hu, G. Cui, W. Ye, L. Kong, Y. Huang, and L. Yuan, "Integrated Radar and Communication System Based on Stepped Frequency Continuous Waveform," in *2015 IEEE International Radar Conference (RadarCon)*, Arlington, VA, USA, May 2015, pp. 1084–1087. 41

[110] N. Levanon and E. Mozeson, *Radar Signals*. John Wiley & Sons, 2004. 41

[111] B. J. Donnet and I. D. Longstaff, “Combining MIMO Radar with OFDM Communications,” in *2006 European Radar Conference (EuRAD)*, Manchester, UK, Sep 2006, pp. 37–40. 41

[112] B. J. Donnet and I. D. Longstaff, “MIMO Radar, Techniques and Opportunities,” in *2006 European Radar Conference (EuRAD)*, Manchester, UK, Sep 2006, pp. 112–115. 41

[113] C. Sturm, T. Zwick, and W. Wiesbeck, “An OFDM System Concept for Joint Radar and Communications Operations,” in *2009 69th Vehicular Technology Conference (VTC)*, Barcelona, Spain, Apr 2009, pp. 1–5. 41

[114] J. Euziére, R. Guinvarc’h, I. Hinostroza, B. Uguen, and R. Gillard, “Optimizing Communication in TMA for Radar,” in *2016 IEEE International Symposium on Antennas and Propagation (APSURSI)*, Fajardo, Puerto Rico, Jun 2016, pp. 705–706. 42

[115] W. Kummer, A. Villeneuve, T. Fong, and F. Terrio, “Ultra-Low Sidelobes from Time-Modulated Arrays,” *IEEE Transactions on Antennas and Propagation*, vol. 11, no. 6, pp. 633–639, Nov 1963. 42

[116] A. Hassanien, M. G. Amin, Y. D. Zhang, and F. Ahmad, “Dual-Function Radar-Communications: Information Embedding Using Sidelobe Control and Waveform Diversity,” *IEEE Transactions on Signal Processing*, vol. 64, no. 8, pp. 2168–2181, Apr 2016. 42

[117] A. Hassanien, M. G. Amin, Y. D. Zhang, and F. Ahmad, “Dual-Function Radar-Communications Using Phase-Rotational Invariance,” in *2015 23rd European Signal Processing Conference (EUSIPCO)*, Nice, France, Aug 2015, pp. 1346–1350. 42

[118] V. Namias, “The Fractional Order Fourier Transform and its Application to Quantum Mechanics,” *IMA Journal of Applied Mathematics*, vol. 25, no. 3, pp. 241–265, 1980. 43

[119] H. M. Ozaktas, Z. Zalevsky, and M. A. Kutay, *The Fractional Fourier Transform with Applications in Optics and Signal Processing*. Wiley, Chichester, 2001. 43

[120] L. B. Almeida, "The Fractional Fourier Transform and Time-Frequency Representations," *IEEE Transactions on Signal Processing*, vol. 42, no. 11, pp. 3084–3091, Nov 1994. 43

[121] C. Capus and K. Brown, "Short-Time Fractional Fourier Methods for the Time-Frequency Representation of Chirp Signals," *The Journal of the Acoustical Society of America*, vol. 113, no. 6, pp. 3253–3263, 2003. 44, 149

[122] Y. Chen, P. Cai, and Y. Wang, "A New Underwater Acoustic Communication System Based on Fractional Fourier Transform," in *2010 IEEE International Conference on Information and Automation (ICIA)*, Harbin, China, Jun 2010, pp. 413–418. 45

[123] X.-J. Sha, R. hui Wen, and X. Qiu, "A New Multiple-Access Method Based on Fractional Fourier Transform," in *2009 Canadian Conference on Electrical and Computer Engineering (CCECE)*, St. John's, NL, Canada, May 2009, pp. 856–859. 45

[124] S. A. Elgamel, C. Clemente, and J. J. Soraghan, "Radar Matched Filtering Using the Fractional Fourier Transform," in *Sensor Signal Processing for Defence (SSPD 2010)*, London, UK, Sep 2010, pp. 1–5. 45

[125] C. Clemente and J. J. Soraghan, "Range Doppler and Chirp Scaling Processing of Synthetic Aperture Radar Data Using the Fractional Fourier Transform," *IET Signal Processing*, vol. 6, no. 5, pp. 503–510, Jul 2012. 45

[126] H.-B. Sun, G.-S. Liu, H. Gu, and W.-M. Su, "Application of the Fractional Fourier Transform to Moving Target Detection in Airborne SAR," *IEEE Transactions on Aerospace and Electronic Systems*, vol. 38, no. 4, pp. 1416–1424, Oct 2002. 45

[127] C. Pang, Y. Han, H. Hou, S. Liu, and N. Zhang, “Micro-Doppler Signal Time-Frequency Algorithm Based on STFRFT,” *Sensors*, vol. 16, no. 10, 2016. 45

[128] M. Martone, “A Multicarrier System Based on the Fractional Fourier Transform for Time-Frequency-Selective Channels,” *IEEE Transactions on Communications*, vol. 49, no. 6, pp. 1011–1020, Jun 2001. 45

[129] C. Clemente, I. Shorokhov, I. Proudler, and J. J. Soraghan, “Radar Waveform Libraries Using Fractional Fourier Transform,” in *2014 IEEE Radar Conference (RadarCon)*, Cincinnati, OH, USA, May 2014, pp. 855–858. 45

[130] C. Clemente, C. Ilioudis, D. Gaglione, K. Thompson, S. Weiss, I. Proudler, and J. J. Soraghan, “Reuse of Fractional Waveform Libraries for MIMO Radar and Electronic Countermeasures,” in *2014 6th International Symposium on Communications, Control and Signal Processing (ISCCSP)*, Athens, Greece, May 2014, pp. 505–508. 45

[131] C. V. Ilioudis, C. Clemente, I. Proudler, and J. J. Soraghan, “Performance Analysis of Fractional Waveform Libraries in MIMO Radar Scenario,” in *2015 IEEE International Radar Conference (RadarCon)*, Arlington, VA, USA, May 2015, pp. 1119–1124. 45

[132] E. Ertin, C. Austin, S. Sharma, R. Moses, and L. Potter, “GOTCHA Experience Report: Three-Dimensional SAR Imaging with Complete Circular Apertures,” vol. 6568, 2007, pp. 656 802–656 802–12. 49

[133] E. Conte and M. Longo, “Characterisation of Radar Clutter as a Spherically Invariant Random Process,” *IEE Proceedings Communications, Radar and Signal Processing*, vol. 134, no. 2, pp. 191–197, Apr 1987. 51

[134] M. Greco and F. Gini, “Statistical Analysis of High-Resolution SAR Ground Clutter Data,” *IEEE Trans. on Geoscience and Remote Sensing*, vol. 45, no. 3, pp. 566–575, Mar 2007. 51

[135] M. Krawtchouk, “On Interpolation by Means of Orthogonal Polynomials,” *Memoirs Agricultural Inst. Kyiv*, vol. 4, pp. 21–28, 1929. 58

[136] P. T. Yap, R. Paramesran, and S.-H. Ong, "Image Analysis by Krawtchouk Moments," *IEEE Transactions on Image Processing*, vol. 12, no. 11, pp. 1367–1377, Nov 2003. 58, 59

[137] M. E. Patil and M. V. Borole, "Signature Recognition Using Krawtchouk Moments," in *2012 Third International Conference on Computing Communication Networking Technologies (ICCCNT)*, Jul 2012, pp. 1–5. 60

[138] B. Kaur, G. Joshi, and R. Vig, "Analysis of Shape Recognition Capability of Krawtchouk Moments," in *International Conference on Computing, Communication Automation*, Coimbatore, India, May 2015, pp. 1085–1090. 60

[139] S. M. Rahman, T. Howlader, and D. Hatzinakos, "On the Selection of 2D Krawtchouk Moments for Face Recognition," *Pattern Recognition*, vol. 54, pp. 83–93, 2016. 60

[140] R. Prouty, *Helicopter Aerodynamics Volume I.* Lulu.com, 2009, vol. 1. 75

[141] R. Zhang, G. Li, C. Clemente, and J. J. Soraghan, "Multi-Aspect Micro-Doppler Signatures For Attitude-Independent L/N Quotient Estimation and its Application to Helicopter Classification," *IET Radar, Sonar & Navigation*, Dec 2016. 86

[142] T. L. King, "Hardware Interface to Connect an AN/SPS-65 Radar to an SRC-6E Reconfigurable Computer," DTIC Document, Tech. Rep., 2005. 102

[143] GPS ICD, "Global Positioning Systems Directorate System Engineering & Integration Interface Specification IS-GPS-200H," *Navstar GPS Space Segment/Navigation User Interfaces*, 2013. 117

[144] A. Goldsmith, *Wireless Communications.* Cambridge UniversityPpress, 2005. 121

[145] G. Corazza, C. Ferrarelli, and F. Vatalaro, "A Rice-Lognormal Terrestrial and Satellite Channel Model," in *1994 Third Annual International Conference on Universal Personal Communications*, San Diego, CA, USA, Sep 1994, pp. 155–159. 137

[146] X. Yang, Q. Tan, X. Wei, Y. Xiang, Y. Yan, and G. Jin, “Improved Fast Fractional-Fourier-Transform Algorithm,” *J. Opt. Soc. Am. A*, vol. 21, no. 9, pp. 1677–1681, Sep 2004. 143

[147] A. Koc, H. M. Ozaktas, C. Candan, and M. A. Kutay, “Digital Computation of Linear Canonical Transforms,” *IEEE Transactions on Signal Processing*, vol. 56, no. 6, pp. 2383–2394, Jun 2008. 143

[148] A. Bultheel and H. E. M. Sulbaran, “Computation of the Fractional Fourier Transform,” *Applied and Computational Harmonic Analysis*, vol. 16, no. 3, pp. 182–202, 2004. 143

[149] C. Candan, M. A. Kutay, and H. M. Ozaktas, “The Discrete Fractional Fourier Transform,” *IEEE Transactions on Signal Processing*, vol. 48, no. 5, pp. 1329–1337, May 2000. 143

[150] S. D. Blunt, M. R. Cook, and J. Stiles, “Embedding Information Into Radar Emissions via Waveform Implementation,” in *2010 International Waveform Diversity and Design Conference*, Niagara Falls, ON, Canada, Aug 2010, pp. 195–199. 143

[151] A. C. O’Connor, J. M. Kantor, and J. Jakabosky, “Joint Equalization Filters that Mitigate Waveform-Diversity Modulation of Clutter,” in *2016 IEEE Radar Conference (RadarCon)*, Philadelphia, PA, USA, May 2016, pp. 1–6. 143

[152] D. P. Scholnik, “Range-Ambiguous Clutter Suppression with Pulse-Diverse Waveforms,” in *2011 IEEE Radar Conference (RadarCon)*, Kansas City, MO, USA, May 2011, pp. 336–341. 143